High Fidelity Quantum Gates with Ions in Cryogenic Microfabricated Ion Traps

by

Jarosław Łabaziewicz

M.A. Physics
Harvard University, 2003

B.A. Physics and Mathematics
Harvard College, 2003

Submitted to the Department of Physics
in partial fulfillment of the requirements for the degree of

Doctor of Philosophy in Physics

at the

MASSACHUSETTS INSTITUTE OF TECHNOLOGY

September 2008

Author .....
Department of Physics
July 24, 2008

Certified by .....
Isaac L. Chuang
Associate Professor, Departments of Physics and EECS
Thesis Supervisor

Accepted by .....
Thomas J. Greytak
Lester Wolfe Professor of Physics, Associate Department Head for Education

High Fidelity Quantum Gates with Ions in Cryogenic Microfabricated Ion Traps

by

Jarosław Łabaziewicz

Submitted to the Department of Physics
on July 24, 2008, in partial fulfillment of the
requirements for the degree of
Doctor of Philosophy in Physics

Abstract

While quantum information processing offers a tantalizing possibility of a significant speed-up in execution of certain algorithms, as well as enabling previously unmanageable simulations of large quantum systems, it remains extremely difficult to realize experimentally. Recently, fundamental building blocks of a quantum computer, including one and two qubit gates, teleportation and error correction, were demonstrated using trapped atomic ions. Scaling to a larger number of qubits requires miniaturization of the ion traps, currently limited by the sharply increasing motional state decoherence at sub-100 µm ion-electrode distances. This thesis explores the source and suppression of this decoherence at cryogenic temperatures, and demonstrates fundamental logic gates in a surface electrode ion trap.

Construction of the apparatus requires the development of a number of experimental techniques. Design, numerical simulation and implementation of a surface electrode ion trap is presented. Cryogenic cooling of the trap to near 4 K is accomplished by contact with a bath cryostat. Ions are loaded by ablation or photoionization, both of which are characterized in terms of generated stray fields and heat load.

The bulk of new experimental results deals with measurements of electric field noise at the ion's position. Upon cooling to 6 K, the measured rates are suppressed by up to 7 orders of magnitude, more than two orders of magnitude below previously published data for similarly sized traps operated at room temperature. The observed noise depends strongly on fabrication process, which suggests further improvements are possible. The measured dependence of the electric field noise on temperature is inconsistent with published models, and can be explained using a continuous spectrum of activated fluctuators.

The fabricated surface electrode traps are used to demonstrate coherent operations and the classical control required for trapped ion quantum computation. The necessary spectral properties of coherent light sources are achieved with a novel design using optical feedback to a triangular, medium finesse, cavity, followed by electronic feedback to an ultra-high finesse reference cavity. Single and two qubit operations on a single ion are demonstrated with classical fidelity in excess of 95%. Magnetic field gradient coils built into the trap allow for individual addressing of ions, a prerequisite to scaling to multiple qubits.

Thesis Supervisor: Isaac L. Chuang
Title: Associate Professor, Departments of Physics and EECS

Acknowledgments

Countless people have helped me in my personal journey from a small Polish town to writing a PhD in U.S.

First off, I would like to thank Professor Isaac Chuang, my research advisor at MIT. Working in his lab was a unique experience, and I benefited immensely from it. Ike combines a great sense of what is interesting in physics with the courage to go ahead and do it. Somehow, he managed to push the lab towards a common goal while giving us freedom to develop our own ideas. What I know about running an experiment and collaborating with people, I owe in large part to him.

I am indebted to Professors Vuletic and Shor for serving on my committee, providing valuable advice and help throughout the process of writing. Professor Vuletic, in particular, provided countless ideas, and a large amount of equipment we borrowed from his lab. His background, ways of thinking about physics and lab management style left a strong impression on me.

I have had a lot of teachers of physics, both here and at my undergraduate institution, Harvard. Prof. Ketterle runs a very successful AMO class at MIT, which provided me with a good background on problems and methods used in atomic physics. I still refer to his lecture notes whenever I need to understand atomic shifts. Most of my knowledge of quantum mechanics comes from Prof. Halperin's course at Harvard, which I enjoyed for two semesters. The groundwork he provided served me well throughout my PhD. Dr. Markovic and Prof. Hau were my undergraduate research advisors, and spent inordinate amount of time explaining to me the basics of experimental physics. The experience in microfabrication, digital feedback loops and lasers systems was necessary for my graduate work, and I'm glad I received it so early. Prof. Hayasaka from NICT in Kansai was kind enough to let me join his lab for a month after my second year at MIT. His ideas about optical feedback were the seeds that grew into a large fraction of chapter 4 of this thesis.

Benedykt Lubiszewski deserves a mention of his own, being the first and maybe the most influential of my teachers. An extremely gifted teacher, he developed a number of bright students, always staying in the background, claiming to serve just a supporting role. He spent hours after classes, going over problems and his lecture notes, taking me from a complete philistine to an ardent student of physics. In his own words, he gave me the wings necessary to fly beyond what he could teach. Those wings are what allowed me to move to U.S. and study at Harvard and MIT.

Despite my claims to the contrary, I would not accomplish a fraction of this work but for the help of my lab mates. Josh Folk and Andrew Houck were my lab partners when I first joined the group. Under their supervision, I have learned a great deal about condensed matter, literature search, experimental techniques and sensitivity of Al_2O_3 gates to static electricity. The frustrating hours we spent fabricating, characterizing, and failing to understand our devices taught me patience, perseverance and disregard for working hours. Both remain good friends to this day.

After their departure, I moved on to what would become my thesis project, ion traps. Initial work progressed much more smoothly thanks to Robert Clark and Kenneth Brown. Ken brought in a strong theoretical background in atomic physics, and a house we would all hang out at. Rob had good hands, and the patience to take large quantities of data. He is a great guy all around, with a good sense of humor, which made the initial set-up work much more bearable. While all of us were relative ignorants of the black arts of ion trapping, with our forces combined we trapped ions relatively quickly. Later on, I collaborated with

Dave Leibrandt on some of the room temperature experiments. Dave and Liz George also introduced me to climbing, which I hope to continue, and caving, which I hope to avoid.

The cryogenic apparatus was built, and operated, with the help of a number of other students. Paul Antohi and Waseem Bakr put together a lot of the hardware, and their experience running the cryostat allowed me to focus on the science. Phil Richerme put together the first implementation of the qubit laser, saving me much time. Shannon Wang and Ruth Shewmon helped out with laser work and day to day responsibilities towards the end of my PhD.

None of the microfabricated traps would have ever existed without Yufei Ge. After an initial period when we worked together, she took over all fabrication responsibilities completely. I have watched her at work a few times, and am still amazed at how precise and careful she is in the cleanroom. The amount of work she put into this project, going through revisions after revisions of traps and processes, should not be underestimated.

The MIT Sport Tae Kwon Do club, and my sabumnim, Dan Chuang, provided an outlet for frustration, and excellent company. The time I spent with them in the gym and on the tournament circuit provided much needed relief and perspective that kept me sane. While I may forget how to compute g-factors, I will never forget the blood, tears and victories against all odds.

Last, my family. My parents have given me all the support and love a child could ask for, and accepted my early departure from home with grace. I do not think there is an appropriate thank you for their efforts.

Yi Xu, thank you.

Dedicated to my OCD.

Contents

1 Fundamentals of Ion Trap Quantum Computing **15**
- 1.1 History of Ion Trapping . . . 17
- 1.2 Demonstrations of Fundamental Operations . . . 17
- 1.3 Requirements for Quantum Computation - DiVincenzo Criteria . . . 18
- 1.4 Surface Electrode Ion Traps . . . 19
- 1.5 Challenges to Scalability . . . 20
- 1.6 Main Contributions of the Dissertation . . . 21
- 1.7 Structure and Organization of the Dissertation . . . 21
- 1.8 Contributions of Co-workers and Published Papers . . . 22

2 Sr^+ Ion Qubit **25**
- 2.1 Motional State . . . 25
- 2.2 Laser-atom interactions . . . 26
- 2.3 Quantum Operations . . . 30
  - 2.3.1 Carrier Transitions . . . 30
  - 2.3.2 Sideband Transitions . . . 31
  - 2.3.3 Stark Shifts . . . 32
  - 2.3.4 Full gate simulation - CNOT . . . 32
- 2.4 Laser Cooling . . . 35
  - 2.4.1 Doppler Cooling in a 2-level system . . . 35
  - 2.4.2 Doppler Cooling in a Λ system . . . 37
  - 2.4.3 Sideband Cooling . . . 38
- 2.5 State Measurement . . . 41
  - 2.5.1 Atomic State Measurement . . . 41
  - 2.5.2 Motional State Measurement . . . 43
  - 2.5.3 State Tomography . . . 44
- 2.6 Sr^+ Structure and Qubit . . . 45
  - 2.6.1 Zeeman Splitting and Selection Rules . . . 47

3 Experimental Apparatus **49**
- 3.1 Surface Electrode Ion Trap Design And Operation . . . 49
  - 3.1.1 Electrode Geometry . . . 51
  - 3.1.2 Trapping Potential . . . 52
  - 3.1.3 Arcing . . . 53
  - 3.1.4 Fabrication Summary . . . 54
  - 3.1.5 Packaging . . . 56
- 3.2 Cryostat . . . 56

3.3 In-Vacuum RF Resonator . . . 58
3.4 Ion Source . . . 60
3.4.1 Ablation . . . 60
3.4.2 Photoionization . . . 61
3.5 Imaging and Scatter Detection . . . 63
3.6 Laser Delivery Optics . . . 65

4 Coherent Control System **67**
4.1 Monolithic Laser System . . . 67
4.1.1 Wavelength Selectivity and Linewidth . . . 68
4.1.2 Design and Construction . . . 71
4.1.3 Cavity Lock . . . 73
4.1.4 Spectral Filtering . . . 74
4.1.5 Laser Linewidth . . . 75
4.2 Qubit Laser Stabilization . . . 75
4.2.1 ULE Cavity . . . 77
4.2.2 Feedback Loop . . . 78
4.2.3 Temperature Stabilization . . . 78
4.3 Pulse Sequencing . . . 81
4.3.1 Sequencing . . . 81
4.3.2 RF Generation . . . 82
4.4 Achieved Coherence Time . . . 83
4.4.1 Ramsey Spectroscopy . . . 83
4.4.2 Spin-Echo . . . 84

5 Heating Rates Out of Motional Ground State **87**
5.1 Heating Rates and Electric Field Noise . . . 87
5.2 Measurement Methods . . . 88
5.2.1 Heating Rate Measurements of Cold Ions . . . 89
5.2.2 Heating Rate Measurements of Hot Ions . . . 91
5.3 Silver Traps . . . 93
5.3.1 Measured Field Noise at Room Temperature . . . 93
5.3.2 Comparison with Published Values . . . 95
5.3.3 Measured Field Noise at Cryogenic Temperatures . . . 95
5.3.4 Conclusions of Experiments with Silver Traps . . . 96
5.4 Gold Traps . . . 96
5.4.1 Measured Field Noise at Room Temperature . . . 97
5.4.2 Measured Field Noise at Cryogenic Temperatures, Temperature Dependence . . . 97
5.4.3 Conclusions of Experiments with Gold Traps . . . 100
5.5 Other Measurements . . . 101
5.5.1 Superconductive Materials . . . 101
5.5.2 Nickel Trap . . . 102
5.5.3 Lucent Trap . . . 103
5.6 Comments on Heating Rate Measurements . . . 104
5.6.1 RF Voltage Dependence . . . 104
5.6.2 DC Voltage Dependence . . . 104
5.6.3 Contamination with Sr . . . 105

6 Sources of Electric Field Fluctuations **107**
6.1 Models of Noise Sources . . . 108
6.1.1 Thermal Sources . . . 108
6.1.2 Patch Potentials . . . 109
6.2 Estimates of Physical Sources . . . 113
6.2.1 Johnson Noise . . . 113
6.2.2 Electric Field Noise from Adsorbates . . . 113
6.2.3 Electric Field Noise from Patch Potentials . . . 114
6.3 Connection to Other Experiments . . . 114
6.3.1 Measurements of Static Fields . . . 114
6.3.2 Measurements of Fluctuating Fields . . . 116
6.4 Conclusions and Impact of the Results . . . 117

7 Demonstrations of Quantum Operations Using Cryogenic Surface Electrode Traps **119**
7.1 Continuous Qubit Rotations . . . 120
7.1.1 Carrier Rotations - X axis . . . 120
7.1.2 Carrier Rotations - Z axis . . . 121
7.1.3 Composite Rotations - BB1 . . . 121
7.1.4 Sideband Rotations . . . 122
7.2 Process Tomography - Truth Table . . . 124
7.2.1 Single Pulse Gates . . . 124
7.2.2 Controlled-NOT Gate . . . 126
7.2.3 Conclusions . . . 127
7.3 Individual Ion Addressing . . . 128
7.3.1 Magnetic Field Stabilization . . . 128
7.3.2 Magnetic Field Gradient . . . 129
7.3.3 Individual Addressing of Ions . . . 131

8 Conclusions and Future Work **133**

A How to Run an Entire Lab on Python and Field Programmable Gate Arrays **147**
A.1 DAQ . . . 147
A.2 FPGA Control . . . 148
A.2.1 Pulse Sequencer Software Stack . . . 149

B Ion State Simulation Codes **151**

List of Figures

2-1 Λ system of atomic states . . . 37
2-2 Steady state populations of the excited state for a Λ system and a two level system . . . 39
2-3 Steady state populations of the excited state as a function of laser detuning 39
2-4 Sideband cooling scheme in a Λ system . . . 40
2-5 Expected state measurement error as a function of integration time . . . 42
2-6 Atomic level structure of the Sr^+ ion . . . 46

3-1 Schematic of trap electrodes and image of fabricated trap . . . 52
3-2 Computed pseudo-potential above the trap surface . . . 53
3-3 Trap glow due to field emission . . . 54
3-4 SEM images of silver and gold traps . . . 55
3-5 Annealing oven . . . 55
3-6 Packaged traps . . . 57
3-7 Cryostat schematic and work area . . . 57
3-8 CPGA mounting socket . . . 59
3-9 RF resonator reflected power . . . 59
3-10 Ion signal as a function of the number of ablation pulses . . . 61
3-11 Strontium oven for the cryogenic environment . . . 62
3-12 Imaging optics . . . 63
3-13 Histogram of the detected photon numbers in 250 µs integration time . . . 64
3-14 Characterization of an image of a single ion . . . 64
3-15 Laser delivery optics . . . 65

4-1 External grating modification of diode facet reflectivity . . . 70
4-2 Schematic of the laser set-up with optical feedback from a triangular cavity 72
4-3 Schematic of the digital lock system . . . 73
4-4 Spectrum of the laser light at the ECDL and after the filter cavity . . . 74
4-5 Spectrum of the $S_{1/2} \leftrightarrow P_{1/2}$ transition of Sr^+ . . . 75
4-6 Shelving probability spectrum demonstrating 30 kHz laser linewidth . . . 76
4-7 Mechanical mount for the optical reference cavity . . . 77
4-8 Optical reference cavity ring-down measurement . . . 78
4-9 PDH lock loop . . . 79
4-10 Noise spectral density of the PDH error signal . . . 79
4-11 Quartz oscillator temperature sensor . . . 80
4-12 Reference cavity drift . . . 81
4-13 Schematic of the RF drive for AOM control . . . 82
4-14 Decay of Ramsey fringes with Ramsey pulse separation time . . . 84

4-15 Recovery of the phase coherence with spin echo 85
4-16 Measurement of T_2 using repeated spin-echo pulses 85

5-1 Rabi flop on sidebands in a thermal state 89
5-2 Heating rate measurement with a broad laser 90
5-3 Heating rate measurement with a narrow laser 91
5-4 Boil-off time in silver traps at room temperature 94
5-5 Doppler re-cooling estimates of $\bar{n}$ in a silver trap 94
5-6 Measured noise values in silver traps 95
5-7 Measured noise values versus secular frequency 96
5-8 Resistivity of the RuO_2 resistor as a function of temperature 98
5-9 Typical temperature dependence of field noise values in cryogenic gold traps 99
5-10 Frequency dependence of field noise values in cryogenic gold traps 100
5-11 Anomalous temperature dependence of field noise observed in one trap . . . 101
5-12 Reflected RF power from the superconductive trap 102
5-13 SEM image of the Lucent Trap 103
5-14 RF voltage dependence of electric field noise 104
5-15 DC voltage dependence of electric field noise 105
5-16 Sr contamination dependence of electric field noise 106

6-1 Resistivity of electroplated gold 109
6-2 Expected Johnson noise above electroplated gold 110

7-1 Rabi flop on the carrier transition 120
7-2 BB1 composite pulses and pulse-length errors 122
7-3 Demonstration of the BB1 composite pulse algorithm 123
7-4 Rabi flop on the blue sideband transition 123
7-5 Truth table measurements of simple rotations of the qubit 125
7-6 Truth table measurement of a CNOT gate 127
7-7 Magnetic field stabilization 129
7-8 Magnetic field gradient coil design 130
7-9 Observed magnetic field gradient 130
7-10 Rabi oscillations on one of two co-trapped ions 132

A-1 Schematic of DAQ 148

List of Tables

2.1 Schematic depiction of gate simulation 33
2.2 Expected measurement results in 2 qubit state tomography 44
2.3 Saturation fields and intensities for Sr^+ transitions 47
2.4 Landé g-factors for the internal states of the ion 47

5.1 Field noise values measured in cryogenic gold traps 99

Chapter 1

Fundamentals of Ion Trap Quantum Computing

Computation has been a part of human culture for millennia, becoming the driving force behind modern technology over the last few decades. The theoretical foundation of modern information processing was established by Church [Chu36] and Turing [Tur36] in 1930s, and has developed into a mature science since then. All the more surprising was the recent claim that there is a more efficient way of computing, which, at least in certain cases, can result in exponentially faster algorithms. The new methods depend on quantum mechanical description of information, and gained the appropriate name of quantum computing.

While a classical bit of information can assume one of two states, the quantum mechanical description of an equivalent two level system, a qubit, is represented by a unit vector in a 2-dimensional complex plane. The qubits combine via a tensor product, with n qubits represented by a unit vector in a 2^n-dimensional complex plane. The exponential growth of the description size is necessary to capture the correlations between amplitudes and phases of different qubits. These correlations offer a natural way of efficient modeling of other quantum systems, which also require an exponentially large description on a classical computer, but also results in new computing algorithms, which use the qubit correlations to solve problems more efficiently.

Quantum Cryptography was one of the earliest, and so far the most developed application of quantum information. Bennett and Brassard have proposed a communication method which relied on the impossibility of measuring a quantum system without disturbing it [BB84]. Amazingly, the protocol can be proven to be secure, regardless of resources available to a potential eavesdropper. There are already commercial implementations of this protocol, and it has been used to build secure networks and transmit election data.

Quantum Simulations, proposed by Feynman [Fey82] and Deutsch [Deu85], provided the initial impulse for studying quantum computation. A full description of a quantum system consisting of n 2-level systems requires $\mathrm{O}(2^n)$ complex numbers. Simulations can be performed only for small systems, due to the memory requirements involved in tracking the variables. However, if the information is encoded in qubits, only $O(n)$ are required, reducing the complexity exponentially. The ability to simulate quantum systems could help resolve a number of important problems in condensed matter, including the origin of high temperature superconductivity.

Quantum Algorithms, such as the Shor's factoring algorithm [Sho94] and Grover's database search algorithm [Gro96], pushed quantum computation into the mainstream of

physics and computer science. The best known classical algorithms for factoring a large number N need $O(e^{\sqrt[3]{\log N}})$ operations, while the quantum equivalent uses only $(\log N)^3$, an exponential improvement in speed. Factoring turns out to be very important for cryptography, and a realization of a polynomial time factoring code would render most of current encryption schemes useless. The computational speed-up of factoring resulted in a search for other problems which would benefit from quantum computation. So far, this search has not returned as impressive results, underlying the difficulty in understanding the intrinsic properties of quantum computers.

Precision Spectroscopy and the growing demand for improved clock references provide yet another application for quantum information. Current implementations of clock standards, such as the cesium fountain clock, rely on the measurement of the phase of an ensemble of atoms. Due to shot noise, the error of such measurement performed on N atoms, or, equivalently, N times on a single atom, scales as $1/\sqrt{N}$. However, by imposing appropriate correlations on a system of N qubits, the error of the phase measurement can be reduced N fold, as compared to a single qubit measurement. The $\sqrt{N}$ improvement over classical methods can provide a significant boost in precision of spectroscopy and atomic clocks.

These advantages do not come without a cost. As mentioned earlier, the increased size of the description required for quantum bits is a result of the importance of relative qubit phases. In an experimental realization of quantum information processing, these phases must be carefully preserved throughout all performed operations. However, any interaction with the environment may alter the energy states of the qubits, resulting in uncontrolled phase shifts, or decoherence. Such interactions are inevitable, though, and for a while it seemed that complex computations would not be accessible. The discovery of quantum error correction has dramatically altered the landscape, demonstrating that as long as the errors are small enough, they can be reduced further by constructing "logical qubits" out of a number of physical ones [Ste96, Sho95]. The current theoretical estimates place this threshold failure probability at $O(10^{-3})$, which is likely within experimental reach [Ste03].

There are a number of physical systems which have been proposed for the realization of a quantum computer. Enormous progress has been made in implementing qubits using Josephson junctions [MNAU02, MOL+99, NPT99], semiconductor quantum dots [LD98, PJT+05, KBT+06], neutral atoms [BCJD99, MGW+03, ALB+07], nuclear spins [Kan98, VSB+01, CVZ+98], polar molecules [ADD+06], nitrogen vacancy centers [CDT+06] and many others. However, as discussed in Section 1.3, the system which has met most of the requirements deemed necessary for a functional quantum computer uses trapped atomic ions. In particular, state readout, high fidelity one and two qubit gates, teleportation and error correction have all been demonstrated. Motivated by these advances, this thesis will focus on methods and challenges associated with extending the demonstrated trapped ion quantum computation experiments to a larger number of qubits.

The reminder of this chapter is structured as follows. Sections 1.1 - 1.2 present the history of ion trapping, including a review of demonstrated operations and requirements for a successful quantum computing architecture. Section 1.4 and 1.5 review the current approaches to scaling, and known challenges. Finally, Section 1.7 outlines the structure and organization of the reminder of this dissertation.

1.1 History of Ion Trapping

Trapped ions provided a fertile ground for experimental investigations for half a century prior to their application in quantum computing. This section provides a brief overview of the history of ion traps.

The impossibility of confining a charged particle in a static electric field is a textbook problem; two methods were developed to circumvent that restriction. Wolfgang Paul developed the Paul traps, which made use of oscillating electric fields to create a dynamic equilibrium, even though a static one is impossible [PS53, Pau90]. Hans Dehmelt developed Penning traps, which relied on an additional magnetic field to stabilize the motion of an ion [Deh67]. Both were recognized for this contribution with the Nobel prize in 1989. Two properties of ion traps are worth highlighting. First, the strong interaction of the unshielded charge allows for much higher trap depths as compared to neutral atom traps, allowing for long storage times and relatively easy loading. Second, the charges are confined in free space, far away from nearest surface, undisturbed except for collisions with the residual background gas. The ion state and its interactions can be very precisely controlled, allowing for experiments with unparalleled accuracy.

For the two decades after conception ion traps remained dark. Experiments relied on radio-frequency excitations to interact with ions, and the excited motion of ions to detect them [DW68]. With such techniques, the charge, mass and spin of trapped particles could be investigated. These experiments continue to provide precise measurements of mass [DNBP94, GPQ$^+$95] and fundamental physical constants [JPD87, OHDG06]. The advent of laser cooling [WDW78, NHTD78], and laser spectroscopy [WI81, BSW82] spelled a new era of interrogation of trapped ions. Newly accessible meta-stable states, and sub-μK temperatures of the ions allowed for precise spectroscopic studies [WIBH87, RYB$^+$00], fundamental tests of quantum mechanics [BHI$^+$89, SNBT86, For93] and cosmology [RHS$^+$08].

Due to the unparalleled isolation of the ion from its surroundings and the very long storage time of up to months, ion traps were quickly adopted for atomic clocks [BPIW85]. All other things being equal, the precision of a clock is limited by the Q factor of the oscillator. However, it is also desirable for the oscillator frequency to be very high, allowing for shorter averaging times to reach the required accuracy. The issue is non-trivial, as the necessary averaging period to measure the frequency of best atomic clocks can be as long as a day. The optical transitions to meta-stable states satisfy both requirements, with oscillator frequencies in the 10^{15} Hz regime, and intrinsic transition Q factors larger than 10^{17} in certain cases. These favorable properties spurred implementations using Sr^+ [MBH$^+$04], Hg^+ [DUB$^+$01] and Al^+ [RHS$^+$08] ions.

1.2 Demonstrations of Fundamental Operations

The technology involved in constructing precise frequency references turns out to be very similar to that necessary to create a qubit. The similarity was first recognized by Cirac and Zoller in their proposal to implement a quantum computer using trapped ions, creating the field of trapped in quantum computing [CZ95]. Soon, a number of experimental implementations of fundamental components of a quantum computer followed. Some of these experiments are reviewed here.

Control over the atomic state of the ion was extensively developed for clocks, reaching coherence times in excess of 10 minutes [BHI$^+$91]. Motional state control requires initial-

ization to a well defined state. Fortunately, the ion motion can be cooled to its ground state using laser cooling in the resolved sideband limit [DBIW89]. With the use of properly tuned laser pulses, an arbitrary motional state can be generated, completing the necessary control over any single ion [MMK$^+$96]. Currently, single ion rotations can be routinely performed with $> 99\%$ fidelity.

Quantum logic gates involving two or more qubits pose a much harder challenge. Two qubit gates were initially demonstrated with one ion, using the atomic and motional state of the trapped ion [MMK$^+$95]. The first demonstration required the use of an auxiliary state, such as a third atomic level selectively coupled to one of the two qubit levels. The requirement for the auxiliary level was removed by a clever pulse sequence, extending the technique to ions without easily accessible auxiliary states [CC01]. Ions trapped in the same ion trap interact via Coulomb repulsion, strongly coupling their motional states. The coupled motional state allows one to perform two qubit interactions between the ions, by mapping the state of the first ion onto the motional bus and performing the gate between the motional state and the second ion [SKHR$^+$03]. Alternatively, two qubit gates can be performed using the distinct response to light fields for ions in different atomic states [SM99]. Laser beams are applied so that a differential light force drives the coupled motional state if and only if the coupled ions are in different atomic states. This force generates a phase shift conditional on the product of the atomic states, resulting in a two qubit gate [LDM$^+$03]. The fidelity of such gates can be carefully studied using process tomography, which completely characterizes the gates [RKS$^+$06]. The constant improvements in experimental implementation, together with noise insensitive gate designs, result in two qubit gates with fidelities of $> 99\%$, rivaling the single qubit rotations [BKRB08].

Arbitrary single qubit rotations, together with an appropriate two qubit gate constitute a complete set of operations, in principle allowing for an arbitrary computation on the qubits. The high fidelities obtained allow for experimental verification of complex gates and algorithms. Large entangled states, involving up to 8 ions, can be created, demonstrating the possibility of large entangled systems, and enabling improved signal to noise in precision spectroscopy [LKS$^+$05, HHR$^+$05]. Simple algorithms, such as the Deutsch-Jozsa algorithm for deciding whether a given function is constant or balanced, have also been demonstrated using a single ion and its motional state [RLCB$^+$03].

In addition to these demonstrations, ion traps provide a fertile ground for studying and improving robustness of quantum computation. By encoding one quantum of information in three physical qubits, error rates can be substantially reduced, a result demonstrated with three trapped ions [CLS$^+$04]. A number of schemes for simplifying quantum computers relies on teleportation of quantum information, rather than physically moving the qubits into proximity. Entire logic gates can be teleported as well, allowing for generation of gates prior to computation. Deterministic teleportation of quantum informations has been achieved for the first time in ion traps [RHR$^+$04, BCS$^+$04].

1.3 Requirements for Quantum Computation - DiVincenzo Criteria

While the fundamental operations required for quantum computation have been demonstrated, the efforts to scale these experiments to a large scale quantum computer are still in their infancy. Useful algorithms require thousands of qubits, with possibly larger numbers depending on error correction codes used [Ste03]. Even the most modest applications of

quantum computation, namely quantum simulations, require tens of qubits.

DiVincenzo stated the necessary and sufficient criteria for a successful implementation of a quantum information processor [DiV95], which can be re-phrased as

I. Well defined, extensible qubit array

II. Initialization of qubits in a well defined state

III. Universal set of quantum gates

IV. State specific readout

V. Decoherence times much longer than gate duration

The last four requirements have been well demonstrated in ion traps, as discussed in section 1.2. The first requirement, however, has only been partially demonstrated.

Ion chains trapped in an ion trap provide a well defined qubit array, but a single ion chain will not be able to support the large number of ions required for meaningful quantum computations [WMI+98]. First, as the number of ions increases, the motional state becomes more susceptible to decoherence. Second, the number of motional eigenmodes is equal to $3N$, where N is the number of ions. With increasing number of modes, the frequency spacing between adjacent modes is reduced. Off-resonant excitations must be avoided, thus reducing the gate speed to much less than the frequency spacing to the nearest mode. Reduction of higher order cross-couplings may require cooling of all the motional modes, significantly increasing the time required to initialize the motional states. These limitations constrain the number of ions trapped in a single trap to $O(10)$, necessitating a different approach to scaling of current experiments to a large number of ions.

1.4 Surface Electrode Ion Traps

Instead of adding more ions to the same ion trap, one could conceive of using a large number of individual traps or zones, interconnected to allow shuttling of ions between separate traps [WMI+98, KMW02]. Such multiplexed architecture also allows for massively parallel gate execution, as each zone supports independent motional modes. However, each trapping zone requires a number of DC and RF electrodes to create appropriate confining potentials. Current ion traps are constructed out of macroscopic elements, with hand-made electrical connections. This approach was successful in demonstrating ion traps with a small number of zones, on the order of 10 [HOS+06]. Increasing this number to hundreds and thousands requires new methods, allowing for reliable and repeatable fabrication of identical traps with a high density.

Other approaches, which do not require interconnected ion traps, have also been proposed. In particular, ion-ion interactions using optical photons have been demonstrated, and a scheme which makes use of superconductive interconnects has been proposed [MMO+07, TRBZ04]. Both of these schemes would benefit from integrated ion traps.

An equivalent fabrication challenge has already been solved by the established semiconductor industry. The exponential increase in computing power over the last 30 years, known as Moore's law, can be traced to the advent of large and very large scale integration. The first semiconductor devices were fabricated from grown crystal junctions, and held only one functional element each. Development of a planar process, where each device was defined by optical masking and selective doping of parts of the substrate, revolutionized the

industry. With the new process, integration of multiple devices on the same substrate became possible, simplifying wiring and drastically reducing costs. The exponential increase of component density lead to processors holding as many as 1 billion transistors each.

Similar progress can be envisioned for trapped ion quantum computing. Appropriate planar ion trap technology has been proposed [CBB+05] and experimentally demonstrated at the National Institute of Standards and Technology [SCR+06], Michigan University [SHO+06] and MIT [PLB+06, BCL+07, LGA+08]. These designs make use of microfabrication methods to define trap electrodes on a substrate, or out of bulk material. Photo-lithography allows for scaling of trap sizes well below 100 µm, while maintaining sub-µm precision of the electrode alignment and size. The complexity of electrode wiring can be reduced using vertical interconnects, or even by integrating the necessary voltage supplies and control electronics with the trap [KPM+05].

1.5 Challenges to Scalability

The progress to multi-zone arrayed ion traps is obstructed by a number of challenges. Some, including laser delivery to the multiple processing zones, control electronics of the thousands of electrodes or classical control, pulse sequencing and feedback required for operations and error correction, remain actively researched but are not thought to pose a fundamental limitation to scalability [KPM+05]. The unexpectedly rapid decoherence of the ion's motional state in sub-100 µm sized ion traps, however, is very poorly understood and calls the fundamental idea of microfabricated arrays of ions traps into question [TKK+00].

Johnson noise, black body radiation and other fundamental sources drive the motional state towards thermal equilibrium, with theoretical decoherence rate of the ground state smaller than 1 s^{-1}. Experimental values, however, are much higher, up to 10^4 s^{-1} at trap frequencies of 1 MHz. The speed of a single two-qubit gate mediated by the motional state is limited by the trap frequency, and takes approximately 100 µs in current implementations. At the high rates observed, the motional state would be destroyed during the gate time, rendering it useless.

The source of this so-called "anomalous" noise is still not understood, but a number of characteristic features has been measured. By adjusting the motional frequency of the ion, it is possible to measure the noise spectrum over a decade of frequencies around 1 MHz. The results are consistent with $1/f$ scaling, or pink noise. Experiments with an adjustable size traps [DOS+06, TKK+00] demonstrated that the noise increases rapidly at small distances, approximately as $1/d^4$. The rapid scaling implies that ions trapped in traps with ion-electrode distance smaller than 20 µm would exhibit decoherence rates in excess of 10^7 s^{-1}, precluding ground state cooling or quantum gates mediated by motional state.

The strong distance dependence of the heating rate suggests that the electric field noise is generated by surface charge fluctuations with spatial correlation length small compared to the distance to the ion. Charge noise is also observed in condensed matter systems, where device fabrication has proven critical in reducing the problem [SLH+04, OCK+06]. Similarly, in the trapped ion experiments, proper choice of materials and fabrication process allows the noise to be suppressed by > 2 orders of magnitude [ESL+07]. The anomalous noise power has also been demonstrated to be thermally driven, providing another plausible route to reduce the heating. Modest cooling of the electrodes to 150 K has been shown to decrease the decoherence rate by about an order of magnitude [DOS+06].

1.6 Main Contributions of the Dissertation

The question of viability of micron scale ion traps for large scale trapped ion quantum computation provides much of the motivation for this dissertation. This rather broad question is divided into three parts.

At the beginning of this work, surface electrode ion traps were still an untested technology. There are at least as many proposed electrode geometries and fabrication methods as groups implementing the traps. The search for a functional geometry and a reliable fabrication process inspired the initial experimental work.

The anomalous noise observed in close proximity to the surface is the least understood property of the ion traps, and is extensively studied. Although both the temperature and fabrication methods have been demonstrated to affect the observed values, there is no systematic data on either effect. In particular, the questions of how sensitive the noise values are to fabrication, how much can it be suppressed by cryogenic cooling and what the exact temperature is remain completely open. Measurements of these dependences, and evaluation of theoretical models in light of the experimental data constitute the bulk of this thesis.

It is possible, however unlikely, that the developed microfabricated surface electrode traps suffer from other sources of decoherence, not observed previously. The suitability of such traps for quantum computation can be asserted fully only after a complete set of quantum operations is demonstrated. Experimental implementation of single qubit rotations and two qubit CNOT gate is investigated at the end of the thesis. Successful demonstration of these operations provides a spring board for future experiments in trapped ion quantum computation at MIT.

1.7 Structure and Organization of the Dissertation

The reminder of the thesis is conceptually divided into three distinct parts. The first part, including Chapters 2 and 3, describes in detail the cryogenic ion trap apparatus used in this project. The second, consisting of Chapters 4 and 7, covers in detail the classical control system and demonstrated quantum gates. The final part, Chapters 5 and 6, covers the electric field noise and decoherence rates observed in cryogenic ion traps.

Chapter 2 presents an experimentalist view of quantum computation with ions, including Sr^+ ion transitions and energy states, state preparation and readout, and physical implementation of gate operations. A model for the ion, including stark shifts, is presented, allowing for software compensation of accumulated phase error.

Chapter 3 describes the experimental apparatus constructed for this experiment. The cryogenic environment and the design and fabrication method of the first operational symmetric surface electrode ion trap is presented. Details of these traps were published in References [LGA+08] and [BCL+07]. Photo-ionization of a neutral vapor and laser ablation, a novel ion source for loading in cryogenic environments, are characterized; these experiments were later published in Reference [LCL+07].

Chapter 4 demonstrates the steps necessary to achieve coherent control of the ion's state. Four lasers required to perform ion gates are implemented using laser diodes prestabilized by optical feedback to an external medium-finesse cavity. The chapter includes the laser design and measurements of stability and spectral purity, also published in Reference [LRB+07]. The classical control system and achieved coherence times are also included.

Chapter 5 presents experimental measurements of the noise fields at cryogenic temperatures in microfabricated ion traps. The chapter includes the first measurements of decoherence rates at 6 K, later published in Reference [LGA+08], as well as the first controlled measurements of the temperature dependence of these noise fields, later published in Reference [LGL+08]. The effect of changes in the fabrication process and handling are studied.

Chapter 6 analyzes proposed physical models of the noise source in light of the experimental data. The measured temperature and frequency dependence is compared with theoretical predictions of two general models of the noise origin, and also included in Reference [LGL+08]. Field noise measurements performed in other precision experiments are compared with ion trap data in search of a possible common origin. Finally, the relevance of the experimental results to scalability of trapped ion quantum computing is discussed.

Chapter 7 presents the implementation and experimental fidelity of fundamental quantum gates in a single Sr^+ held in a microfabricated trap. Single ion gates, as well as the first controlled-NOT gate in a surface electrode trap are implemented, highlighting the reduced noise fields achieved at cryogenic temperatures. The feasibility of frequency addressing of ions using magnetic field gradients is studied, offering a new alternative to shuttling or precise focusing of the laser beams. These results will be included in a future publication.

Chapter 8 concludes the thesis with a discussion of exciting scientific goals made possible by the development of cryogenic surface electrode ion traps.

1.8 Contributions of Co-workers and Published Papers

While most of the work presented in this thesis constitutes my contribution, a number of other people assisted me at various stages of the project. In particular, Paul Antohi and Waseem Bakr constructed the cryogenic ion trap apparatus and its support structure. Phil Richerme helped with the construction of the laser system and early investigations of the qubit transition. Ruth Shewmon put together the reference cavity and Pound-Drewer-Hall lock used to stabilize the qubit laser, described in Chapter 4. Except for a few prototypes, all of the surface electrode ion traps were fabricated by Yufei Ge. Shannon Wang developed the magnetic field stabilization and gradient structures, described in Chapter 7.

The following list summarizes the publications I have co-authored during my PhD studies. The research described in the first two papers, while unrelated to ion trapping, provided me with experience in cryogenic techniques, microfabrication and low noise electronics. These skills proved invaluable in the thesis work presented here.

- A. A. Houck , J. Labaziewicz, E. K. Chan, J. A. Folk and I. L. Chuang, "Kondo effect in electromigrated gold break junctions," *Nano Lett.*, **5**, 1685 (2005)
- H. B. Heersche et al., A. A. Houck, J. Labaziewicz and I. L. Chuang, "Kondo effect in the presence of magnetic impurities," *Phys. Rev. Lett.*, **96**, 017205 (2006)
- K. R. Brown, R. J. Clark, J. Labaziewicz, P. Richerme, D. R. Leibrandt and I. L. Chuang, "Loading and characterization of a printed-circuit-board atomic ion trap," *Phys. Rev. A*, **75** 015401 (2007)
- D. R. Leibrandt, R. J. Clark, J. Labaziewicz, P. Antohi, W. Bakr, K. R. Brown and I. L. Chuang, "Laser ablation loading of a surface-electrode ion trap," *Phys. Rev. A*, **76**, 055403 (2007)

- J. Labaziewicz, P. Richerme, K. R. Brown, I. L. Chuang and K. Hayasaka, "Compact, filtered diode laser system for precision spectroscopy," *Opt. Lett.*, **32**, 572 (2007)
- J. Labaziewicz, Y. Ge, P. Antohi, D. Leibrandt, K. R. Brown and I. L. Chuang, "Suppression of heating rates in cryogenic surface-electrode ion traps," *Phys. Rev. Lett.*, **100**, 013001 (2008)
- J. Labaziewicz, Y. Ge, D. Leibrandt, S. X. Wang, R. Shewmon and I. L. Chuang, "Temperature Dependence of Electric Field Noise above Gold Surfaces," submitted for review

The following list summarizes undergraduate theses which overlap with the research described in this document.

- Waseem Bakr, "Towards a Cryogenic Planar Ion Trap for Sr-88," B.S. thesis, Massachusetts Institute of Technology, 2006
- Philip J. Richerme, "Depletion, Quantum Jumps, and Temperature Measurements of $^{88}Sr^{+}$ Ions in a Linear Paul Trap," B.S. thesis, Massachusetts Institute of Technology, 2006
- Ruth Shewmon, "Coherent Manipulations of Trapped $^{88}Sr^{+}$ using the $4D_{5/2} \rightarrow 5S_{1/2}$ Transition," B.S. thesis, Massachusetts Institute of Technology, 2008

Chapter 2

Sr^+ Ion Qubit

This chapter presents the general theory of cooling and operations, common to all ion qubits, and its application to Sr^+. Section 2.1 begins with discussion of the motional state of the ion and its quantization. Quantum operations on the internal states of an ion can be performed with coherent light pulses; the theory of this interaction is developed in Section 2.2. Section 2.3 describes the effect of these laser pulses on the ion state. Erroneous phase shifts, resulting from off-resonant couplings, are quantified and removed with appropriate corrections. Corrected sequences of laser rotations promise high fidelity in excess of 99% for realistic trap parameters. Initialization of ion motion requires cooling, with two approaches described in Section 2.4. The Doppler cooling rate and temperature limit for a bound oscillator, as well as further cooling in the limit of resolved oscillator states, are theoretically described. In Section 2.6, these theoretical results are applied to Sr^+ ion. Appropriate cooling and qubit transitions are identified. Experimental complications resulting from the Zeeman structure are discussed.

2.1 Motional State

Ion traps have a typical depth of approximately 1 eV, or 10^4 K. The oscillation frequencies are on the order of 1 MHz $\approx$ 50 μK. Therefore, a trapped ion in a low lying vibrational state samples only the bottom of the potential, allowing the trap to be approximated with good accuracy by an infinite 3-dimensional harmonic well. Let us constrain our attention to a single mode of oscillation.

The Hamiltonian for an oscillator vibrating at frequency ω_v is

$$H = \hbar\omega_v \left(a^\dagger a + \frac{1}{2}\right) \tag{2.1}$$

The raising and lowering operators, $a^\dagger$ and a, satisfy the usual commutation relations

$$[a, a^\dagger] = 1 \tag{2.2}$$

The eigenbasis of H is the set of states $|n\rangle$ which satisfy

$$a|n\rangle = \sqrt{n}|n-1\rangle \tag{2.3}$$

$$H|n\rangle = \hbar\omega_v \left(n + \frac{1}{2}\right)|n\rangle \tag{2.4}$$

Connection to position space is made by

$$x = x_0\left(a + a^\dagger\right) \tag{2.5}$$

$$x_0 = \sqrt{\frac{\hbar}{2m\omega_v}} \tag{2.6}$$

where x is the position coordinate of the oscillator, x_0 is the ground state extent of the oscillator, and m is its mass.

The ground state wavefunction of the oscillator satisfies $a|0\rangle = 0$, or, in coordinate space,

$$\langle 0|x\rangle = \left(\frac{m\omega_v}{\hbar\pi}\right)^{\frac{1}{4}} e^{-\frac{x^2}{4x_0^2}} \tag{2.7}$$

2.2 Laser-atom interactions

Consider a two-level atom interacting with a single mode of coherent light at frequency ω_L, trapped in a harmonic trap with frequency ω_v. The spontaneous decay due to interactions with vacuum fields will be ignored. Let the ground state of the atom be $|g\rangle$, and the excited state be $|e\rangle$, with energy splitting $\hbar\omega_{eg}$. Define $\sigma^z \equiv \frac{1}{2}\left(|e\rangle\langle e| - |g\rangle\langle g|\right)$, $\sigma^+ \equiv |e\rangle\langle g|$. Then, the noninteracting Hamiltonian is equal to

$$H_0 = \hbar\omega_{eg}\sigma^z + \hbar\omega_v\left(a^\dagger a + \frac{1}{2}\right) \tag{2.8}$$

The light field at position $\vec{r}$ can be described classically by

$$\vec{A}\,(r,t) = \frac{c\hat{\epsilon}E_0}{2\imath\omega_L}\left(e^{\imath\left(\vec{k}\cdot\vec{r}-\omega_L t+\phi\right)} - c.c.\right) \tag{2.9}$$

where $\hat{\epsilon}$ is the light polarization, E_0 the peak electric field and $\vec{k}$ the propagation direction. Let $\vec{r}_e$ be the position of the valence electron with respect to the nucleus, and $\vec{R}$ be the position of the atom with respect to the trap. The atom-field interaction, assuming Coulomb gauge, is

$$H_{int} = \frac{e}{m_e c}\vec{A}\left(\vec{R}+\vec{r}_e,t\right)\cdot\vec{p} = \frac{eE_0 e^{\imath\vec{k}\cdot\vec{r}_e}\hat{\epsilon}\cdot\vec{p}}{2\imath m_e\omega_L} \times e^{\imath\left(\vec{k}\cdot\vec{R}-\omega_L t+\phi\right)} + c.c. \tag{2.10}$$

Assuming $\omega_L \approx \omega_{eg}$, the electric dipole (E1) and electric quadrupole (E2) interactions can be written as [Jam98]

$$H_{int}^{(E1)} = \frac{1}{2}\hbar\Omega^{(E1)}\left(|e\rangle\langle g| + |g\rangle\langle e|\right)e^{\imath\left(\vec{k}\cdot\vec{R}-\omega_L t+\phi\right)} + h.a. \tag{2.11}$$
$$H_{int}^{(E2)} = \frac{\imath}{2}\hbar\Omega^{(E2)}\left(|e\rangle\langle g| + |g\rangle\langle e|\right)e^{\imath\left(\vec{k}\cdot\vec{R}-\omega_L t+\phi\right)} + h.a.$$

with the Rabi frequencies Ω equal to

$$\Omega^{(E1)} = \frac{eE_0}{\hbar}\left|\langle e|\vec{r}_e\cdot\hat{\epsilon}|g\rangle\right| \tag{2.12}$$
$$\Omega^{(E2)} = \frac{eE_0\omega_{eg}}{2\hbar c}\left|\langle e|(\vec{r}_e\cdot\hat{\epsilon})(\vec{r}_e\cdot\hat{k})|g\rangle\right|$$

It is usual to specify transition strengths in terms of lifetime, rather than the dipole or quadrupole moments of the transition. The connection can be made by writing spontaneous emission and Rabi frequencies in terms of the reduced dipole or quadrupole moments [Jam98]. Assuming that $J = L + S$ is a good quantum number for atomic states, define $|g\rangle \equiv |j_g m_g\rangle$, $|e\rangle \equiv |j_e m_e\rangle$, where $j_{g,e}$ denotes the angular momentum of the state, and $m_{g,e}$ its projection on the z axis.

$$\langle e|\vec{r}_e\cdot\hat{\epsilon}|g\rangle = \langle e||r_e||g\rangle\sum_{q=-1}^{1}\begin{pmatrix} j_g & 1 & j_e \\ -m_g & q & m_e\end{pmatrix}cD^{(q)}\cdot\hat{\epsilon} \tag{2.13}$$
$$\langle e|(\vec{r}_e\cdot\hat{\epsilon})(\vec{r}_e\cdot\hat{k})|g\rangle = \langle e||r_e^2||g\rangle\sum_{q=-2}^{2}\begin{pmatrix} j_g & 2 & j_e \\ -m_g & q & m_e\end{pmatrix}cQ^{(q)} : \hat{\epsilon}\hat{k}$$

where cD^q, cQ^q are spherical basis vectors in Cartesian coordinates, defined as

$$cD^{(1)} = -\frac{1}{\sqrt{2}}(1, -\imath, 0)$$
$$cD^{(0)} = (0, 0, 1)$$
$$cD^{(-1)} = \frac{1}{\sqrt{2}}(1, \imath, 0)$$
$$cQ_{ij}^{(q)} = \sqrt{\frac{10}{3}}(-1)^q\sum_{m_1,m_2=-1}^{1}\begin{pmatrix} 1 & 1 & 2 \\ m_1 & m_2 & -q\end{pmatrix}cD_i^{(m_1)}cD_j^{(m_2)}$$

Transition lifetimes can be similarly written in terms of reduced multipole moments, to give

$$\Gamma_{eg}^{(E1)} = \frac{e^2\omega_{eg}^3}{3\pi\epsilon_0\hbar c^3}\frac{\langle e||r_e||g\rangle^2}{2j_e+1} \tag{2.14}$$
$$\Gamma_{eg}^{(E2)} = \frac{e^2\omega_{eg}^5}{60\pi\epsilon_0\hbar c^5}\frac{\langle e||r_e^2||g\rangle^2}{2j_e+1}$$

Using Equations 2.12, 2.13 and 2.14 yields the Rabi frequencies in terms of laser light

amplitude, lifetime of the excited state and geometric factors.

$$\Omega^{(E1)} = E_0 \sqrt{\frac{4\pi\epsilon_0 c^3 \Gamma_{eg}}{\hbar\omega_{eg}^3}} \sqrt{\frac{3\left(2j_e+1\right)}{4}} \left| \sum_{q=-1}^{1} \begin{pmatrix} j_g & 1 & j_e \\ -m_g & q & m_e \end{pmatrix} cD^{(q)} \cdot \hat{\epsilon} \right| \tag{2.15}$$

$$\Omega^{(E2)} = E_0 \sqrt{\frac{4\pi\epsilon_0 c^3 \Gamma_{eg}}{\hbar\omega_{eg}^3}} \sqrt{\frac{15\left(2j_e+1\right)}{4}} \left| \sum_{q=-2}^{2} \begin{pmatrix} j_g & 2 & j_e \\ -m_g & q & m_e \end{pmatrix} cQ^{(q)} : \hat{\epsilon}\hat{k} \right| \tag{2.16}$$

Assume the laser k-vector has significant projection on one oscillation mode only. Substituting Equation 2.5 for $\vec{R}$ in Equation 2.11, using the usual substitution $\eta \equiv kx_0$ (Lamb-Dicke parameter), and dropping the dipole/quadrupole designations gives a simple interaction Hamiltonian in laboratory frame

$$H_{int} = \frac{1}{2}\hbar\Omega\left(\sigma^+ + \sigma^-\right) e^{\imath\left(\eta\left(a+a^\dagger\right)-\omega_L t+\phi\right)} + h.a. \tag{2.17}$$

$$\tag{2.18}$$

Using completeness of vibrational basis states $\sum_n |n\rangle\langle n| = 1$,

$$H_{int} = \frac{1}{2}\hbar \sum_{n,m=0} \Omega_{m,n} e^{\imath(\phi-\omega_L t)} \left(\sigma^+ + \sigma^-\right) |m\rangle\langle n| + h.a. \tag{2.19}$$

where $\Omega_{n,m} = \Omega\langle n|e^{\imath\left(\eta\left(a+a^\dagger\right)\right)}|m\rangle$. Expanding the exponent $e^{\imath\left(\eta\left(a+a^\dagger\right)\right)}$, and making use of generalized Laguerre polynomials L_n^α [WMI+98],

$$\Omega_{n,m} = \Omega_{m,n} = \Omega e^{-\eta^2/2} \eta^{m-n} \left(\frac{n!}{m!}\right)^{\frac{1}{2}} L_n^{m-n}\left(\eta^2\right) \qquad n \le m \tag{2.20}$$

Of particular interest are the $\Omega_{n,n}$ and $\Omega_{n\pm1,n}$ transitions, which, for small values of $\eta^2 n$ can be approximated to lowest order by

$$\Omega_{n,n} = \Omega\left(1 - \frac{\eta^2}{2}\left(2n+1\right)\right) \tag{2.21}$$

$$\Omega_{n+1,n} = \Omega\eta\sqrt{n+1} \tag{2.22}$$

$$\Omega_{n-1,n} = \Omega\eta\sqrt{n} \tag{2.23}$$

In particular, Equation 2.21 demonstrates that the number of motional state quanta n modifies the Rabi frequency on the internal atom states.

The interaction Hamiltonian 2.19 contains terms rotating at $O(\omega_{eg})$, which can be removed by transformation to an appropriate frame. In the frame defined by H_0 (see Equation 2.8), the new states and Hamiltonian are

$$\Psi_{QC}(t) = e^{\imath H_0 t/\hbar}\Psi(t) \tag{2.24}$$

$$\begin{aligned} H_{QC} &= e^{\imath H_0 t/\hbar}\left(H_0 + H_{int}(t) - H_0\right)e^{-\imath H_0 t/\hbar} \\ &= \frac{\hbar}{2}\sum_{n,m=0}\Omega_{m,n}e^{\imath(\phi-\omega_L t)}\left(e^{\imath\omega_{eg}t}\sigma^+ + e^{-\imath\omega_{eg}t}\sigma^-\right)e^{\imath(m-n)\omega_v t}|m\rangle\langle n| + h.a. \end{aligned} \tag{2.25}$$

Close to resonance $\omega_L \approx \omega_{eg}$, terms rotating at $\omega_{eg}+\omega_L$ become insignificant compared to those rotating at $\omega_{eg}-\omega_L$, and can be dropped

$$H_{QC} = \frac{\hbar}{2}\sum_{n,m=0}\Omega_{m,n}e^{\imath(\phi-\delta t)}\sigma^+|m\rangle\langle n| + h.a. \qquad \delta \equiv \omega_L - \omega_{eg} - (m-n)\omega_v \tag{2.26}$$

It is clear that in this frame, the states of the atom are stationary when no interaction is applied ($\Omega = 0$). For this reason, the information encoded in the states of the ion and quantum gates performed on those states are easiest to describe in this frame, from now on referred to as the "quantum computing" (QC) frame. The interaction is resonant whenever $\delta = 0$, or $\omega_L = \omega_{eg} + \Delta n\omega_v$, for integer Δn. The $\Delta n = 0$ transition is called the carrier transition, and does not change the motional state. The $\Delta n = 1$, $\Delta n = -1$ transitions are the blue and red sideband transitions, respectively.

While the states are stationary, the Hamiltonian is still time dependent, preventing a simple exponentiation. In the laser frame, defined by $H_L = \hbar\omega_L\sigma^z + \frac{1}{2}\hbar\omega_v$, the states and Hamiltonian are

$$\Psi_{LSR}(t) = e^{\imath H_L t/\hbar}\Psi(t) \tag{2.27}$$

$$\begin{aligned} H_{LSR} =& e^{\imath H_L t/\hbar}\left(H_0 + H_{int}(t) - H_L\right)e^{-\imath H_L t/\hbar} \\ =& \hbar(\omega_{eg}-\omega_L)\sigma^z + \hbar\omega_v a^\dagger a \\ &+ \frac{\hbar}{2}\left(\sum_{n,m=0}\Omega_{m,n}e^{\imath(\phi-\omega_L t)}\left(e^{\imath\omega_L t}\sigma^+ + e^{-\imath\omega_L t}\sigma^-\right)|m\rangle\langle n| + h.a.\right) \end{aligned} \tag{2.28}$$

Again, dropping fast rotating terms, and defining $\delta \equiv (\omega_L - \omega_{eg})$,

$$H_{LSR} = -\hbar\delta\sigma^z + \hbar\omega_v a^\dagger a + \frac{\hbar}{2}\left(\sum_{n,m=0}\Omega_{m,n}e^{\imath\phi}\sigma^+|m\rangle\langle n| + h.a.\right) \tag{2.29}$$

The Hamiltonian is time independent, simplifying evaluation of the interaction. The different pictures differ only by a phase on the states, and can be connected by a unitary transform, defined by $\Psi_{QC}(t) = U_{LSRtoQC}(t)\Psi_{LSR}$,

$$U_{LSRtoQC}(t) = e^{\imath H_0 t/\hbar}e^{-\imath H_L t/\hbar} \tag{2.30}$$

$$= e^{-\delta t\sigma^z + \omega_v t a^\dagger a} \tag{2.31}$$

2.3 Quantum Operations

The two states $|g\rangle$ and $|e\rangle$ considered in Section 2.2 form a single qubit, called the atomic qubit. Define $|\downarrow\rangle \equiv |g\rangle$ and $|\uparrow\rangle \equiv |e\rangle$. The two lowest motional states, $|0\rangle$ and $|1\rangle$, can be used as another qubit, called the motional qubit. Unfortunately, other motional states are separated by the same frequency ω_v, and may become excited by an interaction which couples $|0\rangle$ and $|1\rangle$. Such excitation takes the ion out of the computational space, and has to be avoided by careful design of the operations. In this section, quantum gates on these two qubits are described.

2.3.1 Carrier Transitions

Transitions on the carrier allow us to perform any unitary gate on the atomic qubit. To demonstrate that ability, it is sufficient to demonstrate arbitrary rotations $R_x(\theta)$, $R_y(\theta)$ of the Bloch sphere around the $\hat{x}$ and $\hat{y}$ axes (Theorem 4.1, Reference [NC00]). Then, for any U, there are angles α, β, γ, δ such that

$$U = e^{-\alpha} R_x(\beta) R_y(\gamma) R_x(\delta) \tag{2.32}$$

The rotations R_x, R_y can be explicitly derived from Equation 2.26. On resonance, ignoring off-resonant interactions, this Hamiltonian is

$$H_{QC} = \frac{\hbar}{2} \sum_{n=0}^{\infty} \Omega_{n,n} e^{\imath\phi} \sigma^+ |n\rangle\langle n| + h.a. \tag{2.33}$$

Provided that $\eta^2 n \ll 1$ for all occupied n, $\Omega_{n,n} = \Omega(1 - \frac{\eta^2}{2}(2n+1)) \approx \Omega$, and

$$\begin{aligned} H_{QC} &= \frac{\hbar}{2} \Omega e^{\imath\phi} \sigma^+ \sum_{n=0}^{\infty} |n\rangle\langle n| + h.a. \\ &= \frac{\hbar}{2} \Omega \left(e^{\imath\phi} \sigma^+ + e^{-\imath\phi} \sigma^- \right) \end{aligned} \tag{2.34}$$

In particular, for $\phi = 0$, the unitary matrix describing the action of the Hamiltonian is

$$\begin{aligned} e^{-\imath H_{QC} t/\hbar} &= e^{\frac{-\imath\Omega t}{2}\sigma^x} \\ &= R_x(\Omega t) \end{aligned} \tag{2.35}$$

Similarly, for $\phi = \frac{\pi}{2}$,

$$\begin{aligned} e^{-\imath H_{QC} t/\hbar} &= e^{\frac{-\imath\Omega t}{2}\sigma^y} \\ &= R_y(\Omega t) \end{aligned} \tag{2.36}$$

These two rotations can be composed to execute an arbitrary rotation on the Bloch sphere.

The Z rotation $R_z(\theta)$ can be explicitly performed using $R_x(\frac{-\pi}{2})R_y(\theta)R_x(\frac{\pi}{2})$ rotations if necessary. However, in a sequence of gates, such rotation is equivalent to a phase shift $\Delta\phi = \theta$ of the subsequent laser pulses, thus reducing the required number of gates.

2.3.2 Sideband Transitions

Manipulations of the motional state can be achieved by mapping that state onto the atomic state of the ion, performing an appropriate rotation on the atomic state, and mapping the result back onto the motional state. The mapping operation requires the use of a sideband transition. The red sideband transition, on resonance, is described by (cf. Equation 2.26),

$$H_{QC} = \frac{\hbar}{2}\sum_{n=1}^{\infty}\Omega_{n-1,n}e^{\imath\phi}\sigma^{+}|n-1\rangle\langle n| + h.a. \tag{2.37}$$

The above equation holds only when $\Omega, \Omega\eta\sqrt{n} \ll \omega_v$. Otherwise, off-resonant excitation must be included in the Hamiltonian. This condition motivates the use of very tight traps, with high ω_v, to achieve high gate speeds Ω.

If the initial atomic state is $|\downarrow\rangle$, the motional state can be mapped onto the internal state. Let the initial state of the ion be $\psi = |\downarrow\rangle(a|0\rangle + b|1\rangle)$. The Hamiltonian acting on these states is

$$\begin{aligned} H_{QC} &= \frac{\hbar}{2}\Omega_{0,1}e^{\imath\phi}\sigma^{+}|0\rangle\langle 1| + h.a. \\ &= \frac{\hbar\eta\Omega}{2}\left(e^{\imath\phi}\sigma^{+}|0\rangle\langle 1| + e^{-\imath\phi}\sigma^{-}|1\rangle\langle 0|\right) \end{aligned} \tag{2.38}$$

Defining $U(t) = e^{-\imath H_{QC}t/\hbar}$, and setting $\phi = 0$,

$$\begin{aligned} U\left(\frac{\pi}{\eta\Omega}\right) &= e^{\frac{\imath\pi}{2}\left(\sigma^{+}|0\rangle\langle 1| + \sigma^{-}|1\rangle\langle 0|\right)} \\ &= -\imath\left(\sigma^{-}|1\rangle\langle 0| + \sigma^{+}|0\rangle\langle 1|\right) + \left(|e\rangle\langle e||1\rangle\langle 1| + |g\rangle\langle g||0\rangle\langle 0|\right) \end{aligned} \tag{2.39}$$

Define $S \equiv ZU\left(\frac{\pi}{\eta\Omega}\right)$, with $Z \equiv R_z(-\pi/2)$ on the atomic qubit. The action of S on ψ is, up to a global phase,

$$S\psi = S|\downarrow\rangle(a|0\rangle + b|1\rangle) = a|\downarrow\rangle|0\rangle + b|\uparrow\rangle|0\rangle \tag{2.40}$$

$$= (a|\downarrow\rangle + b|\uparrow\rangle)|0\rangle \tag{2.41}$$

S performs the desired mapping of the motional state onto the atomic state. The operation $S^{\dagger}$ performs the reverse map.

Any desired rotation U_v of the motional state can therefore be accomplished by $S^{\dagger}U_aS$, where U_a is the equivalent rotation of the atomic states. This scheme does not work, however, if the ion is not initialized to the $|\downarrow\rangle$ state. Certain non-trivial operations, such as Controlled-NOT gate between motional and atomic state, are still possible through clever design of qubit rotations.

2.3.3 Stark Shifts

In the preceding derivations, we obtained simple results by neglecting all off-resonant excitations. These interactions, to first order, induce level shifts of the atomic and vibrational states, and a corresponding phase increment. Maintaining the proper phase of the qubit states necessitates computation and removal of these phases [RLCB$^+$03, HGR$^+$03].

Consider a simple 2-level system. The light interaction Hamiltonian in the laser frame is (cf. Equation 2.29)

$$H_{LSR} = -\hbar\delta\sigma^z + \frac{\hbar}{2}\left(\Omega e^{\imath\phi}\sigma^+ + \Omega e^{-\imath\phi}\sigma^-\right) \tag{2.42}$$

$$= \frac{\hbar}{2}\begin{pmatrix} -\delta & \Omega e^{\imath\phi} \\ \Omega e^{-\imath\phi} & \delta \end{pmatrix} \tag{2.43}$$

The eigenvalues of this Hamiltonian are $\pm\frac{1}{2}\sqrt{\delta^2+\Omega^2}$, with the plus sign corresponding to the state which is mostly $|\uparrow\rangle$ ($|\downarrow\rangle$) for $\delta < 0$ ($\delta > 0$). The shift of these states, as compared to the energies for $\Omega = 0$, is

$$\Delta E_g = \frac{\delta}{2|\delta|}\left(\sqrt{\delta^2+\Omega^2} - |\delta|\right) \tag{2.44}$$

$$\Delta E_e = -\frac{\delta}{2|\delta|}\left(\sqrt{\delta^2+\Omega^2} - |\delta|\right) \tag{2.45}$$

In the case of a single trapped ion, operations on the sideband transitions induce an energy shift of the $|\downarrow\rangle$ and $|\uparrow\rangle$ levels, moving the carrier and sideband transitions, as well as modifying the relative rotation rate of these states. One possible solution is to shift the levels back, with another laser beam, tuned at approximately $-\delta$ [HGR$^+$03]. The same effect can also be achieved by an appropriate laser phase adjustments, as shown in Section 2.3.4.

2.3.4 Full gate simulation - CNOT

Exact simulation of the action of the lasers on the computational space requires the use of both laser and QC frames. The full Hamiltonian is time independent in laser frame, suggesting that gate operations should be computed in that frame. The states used in quantum computation are defined in the QC frame, where they are stationary without the interaction applied. Simulation of a gate sequence will therefore require frequent switching between the frames using $U_{LSRtoQC}(t)$.

The schematic of gate computation in QC frame is shown in Table 2.1. Computation is performed by moving to laser frame, exponentiating H_{LSR}, and moving back to QC frame. For example, a gate performed by applying an interaction starting at time t_0 for time τ, can be computed in QC frame to be

$$U = U_{LSRtoQC}(t_0+\tau)e^{-\imath H_{LSR}\tau/\hbar}U_{LSRtoQC}(t_0)^\dagger \tag{2.46}$$

where H_{LSR} and $U_{LSRtoQC}$ depend on laser detuning, phase and Rabi frequency as well as the trap parameters. Note that each laser detuning and trap frequency defines a separate laser frame. The operator $U_{LSRtoQC}$ moves between the unique QC frame, and one of the infinite number of laser frames.

		$e^{-\imath H_{LSR}t_0/\hbar}$		$e^{-\imath H_{LSR}t_1/\hbar}$	
LSR frame:	$\Psi_{LSR}(0)$	$\longrightarrow$	$\Psi_{LSR}(t_0)$	$\longrightarrow$	$\Psi_{LSR}(t_1+t_0)$
	$\uparrow$		$\uparrow$		$\uparrow$
	$U_{LSRtoQC}(0)$		$U_{LSRtoQC}(t_0)$		$U_{LSRtoQC}(t_0+t_1)$
	$\downarrow$	U_0	$\downarrow$	U_1	$\downarrow$
QC frame:	$\Psi_{QC}(0)$	$\longrightarrow$	$\Psi_{QC}(t_0)$	$\longrightarrow$	$\Psi_{QC}(t_1+t_0)$

Table 2.1: Schematic depiction of the computation of a gate in the QC frame. Unitaries U_0, U_1 are of interest, but cannot be computed directly from the time dependent Hamiltonian H_{QC}. These operations can be computed by moving to the laser frame, exponentiating H_{LSR}, and moving back to QC frame.

Gates performed on the carrier transition do not suffer from any phase shifts (there is no stark shift at resonance), and are correct as described by Equation 2.46. Gates on the sideband transitions, however, suffer from a stark shift on the nearby carrier transition and require appropriate corrections. Consider an interaction with laser detuning $\delta \gg \Omega$, carrier Rabi frequency Ω and phase ϕ applied for time τ starting at time t_0. There are two separate phase shifts which need to be cancelled.

- **Stark Shift** of the ground and excited state, computed in Section 2.3.3 can be removed by rotating the phase of the $|e\rangle$ state by $\phi_s = -\left(\delta - \sqrt{\delta^2+\Omega^2}\right)\tau$, equivalent to applying $e^{-\imath\sigma^z\phi_s}$, following the offending gate. As noted before, Z rotations can be performed by changing the phases of all subsequent laser pulses by ϕ_s.
- **Frame Shift** is a more subtle effect. Resonant excitation of sidebands is applied at the stark shifted frequency. The laser frame corresponding to that frequency will rotate with respect to the unshifted states at a rate proportional to the stark shift. To bring the laser frame and unshifted states in phase, the laser phase has to be shifted by $\phi_f = \left(\delta - \sqrt{\delta^2+\Omega^2}\right)t_0$. Such phase shift is equivalent to applying $e^{-\imath\sigma^z\phi_f}$ before the gate, and $e^{\imath\sigma^z\phi_f}$ after.

In a multi-level atom, there can be other transitions, in addition to the carrier and sidebands, which are off-resonantly coupled to the laser. In such case, additional phase shifts may be required to correct for these perturbations. In case of Sr^+, the additional shift was found to equal approximately $\delta_{other} = 0.025 \pm 0.005 \times \frac{\Omega^2}{\mathrm{MHz}^2}\frac{2\pi}{\mu\mathrm{s}}$. Both carrier and sideband transitions are shifted by δ_{other}. However, the sum of carrier gate times is typically sufficiently short that this shift can be ignored for carrier gates. Defining $\delta_{corr} = \left(\delta - \sqrt{\delta^2+\Omega^2}\right) + \delta_{other}$, the corrected gates at carrier and sideband transitions can be written as

$$U_c = U_{LSRtoQC}(t_0+\tau)e^{-\imath H_{LSR}\tau/\hbar}U_{LSRtoQC}(t_0)^\dagger \tag{2.47}$$

$$U_{sb} = e^{\imath\sigma^z\delta_{corr}(\tau+t_0)}\ U_{LSRtoQC}(t_0+\tau)e^{-\imath H_{LSR}\tau/\hbar}U_{LSRtoQC}(t_0)^\dagger\ e^{-\imath\sigma^z\delta_{corr}t_0} \tag{2.48}$$

$$\delta_{corr} \equiv \left(\delta - \sqrt{\delta^2+\Omega^2}\right) + \delta_{other}$$

Correctness of this approach is verified by simulating a full Controlled-NOT (CNOT) gate between ion and the motional state. The gate is similar to a classical XOR gate; the value of the target qubit is flipped iff the control qubit is 1. The choice of the gate is not accidental — CNOT can be shown to allow for arbitrary quantum computation when coupled with single qubit rotations, and is therefore considered to be one of the basic building blocks of such a computer.

Let $R(\theta, \phi)$, $R^+(\theta, \phi)$ denote the carrier and blue sideband ($\delta = \omega_v$) rotations by angle θ with phase ϕ. The CNOT sequence can be written as [CC01, SKHR$^+$03]

$$CNOT = ZR(\frac{\pi}{2}, -\frac{\pi}{2})R^+(\frac{\pi}{\sqrt{2}}, \frac{\pi}{2})R^+(\frac{\pi}{2}, 0)R^+(\frac{\pi}{\sqrt{2}}, \frac{\pi}{2})R^+(\frac{\pi}{2}, 0)R(\frac{\pi}{2}, -\frac{\pi}{2}) \tag{2.49}$$

The precision of the correction can be demonstrated by evaluating the gate numerically in the subspace spanned by the internal states $|\uparrow\rangle$, $|\downarrow\rangle$ and the motional states $|0\rangle$, $|1\rangle$, $|2\rangle$. Defining the basis states as $\{|\uparrow\rangle|0\rangle, |\uparrow\rangle|1\rangle, |\uparrow\rangle|2\rangle, |\downarrow\rangle|0\rangle, |\downarrow\rangle|1\rangle, |\downarrow\rangle|2\rangle\}$, the matrix elements of the unitary gate can be computed explicitly. Ideally, the gate would be represented by a matrix

$$CNOT = \begin{pmatrix} 1 & 0 & 0 & 0 & 0 & 0 \\ 0 & 0 & 0 & 0 & 1 & 0 \\ 0 & 0 & 1 & 0 & 0 & 0 \\ 0 & 0 & 0 & 1 & 0 & 0 \\ 0 & 1 & 0 & 0 & 0 & 0 \\ 0 & 0 & 0 & 0 & 0 & 1 \end{pmatrix} \tag{2.50}$$

where the state of the atomic qubit ($|\uparrow\rangle$, $|\downarrow\rangle$) is flipped when the motional qubit is in state $|1\rangle$.

For sample parameters $\omega_v = 2\pi$, $\Omega = \frac{\pi}{10}$ and $\eta = .05$, the uncorrected CNOT gate evaluates to (dropping terms smaller than $\sqrt{.001}$, numbers in bold should be 1, while all others should be 0)

$$CNOT = \begin{pmatrix} \mathbf{0.895} & -0.0321 & 0 & 0.441\imath & 0 & 0.0321 \\ 0 & 0.0579{+}0.437\imath & 0 & 0 & \mathbf{0.894{-}0.0527}\imath & 0 \\ 0 & 0.036 & -0.897 & 0 & 0 & -0.438\imath \\ 0.441\imath & 0 & 0 & \mathbf{0.895} & -0.0365 & 0 \\ 0 & \mathbf{0.895{+}0.0421}\imath & 0 & 0 & -0.0528{+}0.438\imath & 0 \\ 0 & 0 & -0.438\imath & 0 & 0 & -0.896{+}0.0399\imath \end{pmatrix} \tag{2.51}$$

which shows significant errors on the order of $\sqrt{0.2}$. The corrected pulse sequence, using corrections from Equations 2.47, 2.48 is (dropping terms smaller than $\sqrt{.001}$, numbers in bold should be 1, while all others should be 0)

$$CNOT = \begin{pmatrix} \mathbf{0.998} & 0 & 0 & 0 & 0 & 0 \\ 0 & 0.0697 & 0 & 0.0321 & \mathbf{0.995{-}0.0338\imath} & 0 \\ 0 & 0.0333 & -0.998 & 0 & 0 & 0 \\ 0 & 0 & 0 & \mathbf{0.998} & -0.0336 & 0 \\ 0 & \mathbf{0.996} & 0.0321 & 0 & -0.0699 & 0 \\ 0 & 0 & 0 & 0 & 0 & -0.997{+}0.0443\imath \end{pmatrix} \tag{2.52}$$

which, with gate fidelity $> 99\%$ [NC00], equals to a CNOT gate with the motional qubit controlling the X operation on the internal state qubit. Appendix B presents the derivation and full calculations leading to this result.

2.4 Laser Cooling

The ion initially starts in an undefined motional state, with the number of motional quanta in hundreds of thousands. In order to generate a known motional state, we have to cool the motion of the ion to near ground state. The temperatures required are very low, on the order of µK, necessitating the use of laser cooling techniques.

Two methods will be described, applicable in different temperature regimes. Initially, when the ion temperature is high, > 1 K, the quantization of the motional state plays a negligible role, and we may consider the motion to be classical. However, after the ion is cooled below > 1 mK, there are only a few motional quanta left in the oscillator, necessitating a discretized approach. These two regimes correspond to the Doppler and resolved sideband cooling limits, respectively.

2.4.1 Doppler Cooling in a 2-level system

When the excited state is coupled to vacuum, it will decay at rate Γ, the natural lifetime. The relaxation channel requires a density matrix description. Letting $L \equiv \sqrt{\Gamma}|g\rangle\langle e|$, the equation of motion for the density matrix in Lindblad form is

$$\frac{d\rho}{dt} = \frac{-\imath}{\hbar}[H, \rho] + L\rho L^\dagger - \frac{1}{2}\left(\rho L^\dagger L + L^\dagger L\rho\right) \tag{2.53}$$

where H is the Hamiltonian of Equation 2.29, evaluated in the ground motional state (the motion will be treated classically),

$$H = -\hbar\delta\sigma^z + \left(\frac{\hbar}{2}\Omega e^{\imath\phi}\sigma^+ + h.a.\right) \tag{2.54}$$
$$\delta \equiv \omega_L - \omega_{eg}$$

The population of the excited state can be expressed in terms of the Rabi frequency Ω, laser detuning δ as [MvdS99]

$$\rho_{ee} = \frac{1}{2}\frac{s_0}{1 + s_0 + (2\delta/\Gamma)^2} \qquad\qquad s_0 \equiv \frac{2\Omega^2}{\Gamma^2} \tag{2.55}$$

The force exerted by the light is proportional to the average momentum difference of the incoming and scattered photons. Assuming scattering is symmetric with respect to the origin,

$$\vec{F} = \hbar k \Gamma \rho_{ee} \tag{2.56}$$

The laser detuning as seen by the scatterer depends on the atom velocity $\vec{v}$ due to Doppler shift, $\delta = \omega_L - \omega_{eg} - \vec{k} \cdot \vec{v}$. This dependence results in velocity dependent force $\vec{F} = F_0 \hat{k} - \beta \left(\vec{v} \cdot \hat{k} \right) \hat{k}$ (to lowest order in v), with the damping coefficient [MvdS99]

$$\beta = -\hbar k^2 \frac{4 s_0 \left(\delta / \Gamma \right)}{\left(1 + s_0 + \left(2\delta / \Gamma \right)^2 \right)^2} \tag{2.57}$$

The maximum damping rate is achieved for $s_0 = 2$ and $\delta = -\Gamma/2$ and equals

$$\beta = \frac{\hbar k^2}{4} \tag{2.58}$$

The static force is compensated by the trapping potential, and the damping reduces the velocity towards zero. The atoms do not equilibrate to zero velocity, however, as the scattering events impart a discrete momentum kick. Let k_s be the k-vector of scattered photons. The average squared momentum change is $|\Delta p|^2 = |\hbar \vec{k} - \hbar \vec{k_s}|^2 \approx 2 \left(\hbar k \right)^2$, with exact value dependent on the distribution of scattered photon directions. The energy gained in this process is

$$\frac{dE}{dt} = \frac{|\Delta p|^2}{2M} \Gamma \rho_{ee} = \frac{\left(\hbar k \right)^2}{M} \Gamma \rho_{ee} \tag{2.59}$$

The energy removed from the scatterer per unit time is

$$\frac{dE}{dt} = \langle \vec{F} \cdot \vec{v} \rangle = -\beta \left| \vec{v} \cdot \hat{k} \right|^2 \tag{2.60}$$

Equating the two, we arrive at the Doppler limit for the component of the velocity along the laser beam,

$$k_b T_D = M \left| \vec{v} \cdot \hat{k} \right|^2 = \frac{\left(\hbar k \right)^2 \Gamma \rho_{ee}}{\beta} \tag{2.61}$$

$$= \hbar \Gamma \frac{1 + s_0 + \left(2\delta / \Gamma \right)^2}{8\delta / \Gamma} \tag{2.62}$$

The temperature T_D assumes its lowest value for $s_0 \ll 1$ and $\delta = -\frac{\Gamma}{2}$, equal to

$$k_B T_D = \frac{\hbar \Gamma}{2} \tag{2.63}$$

While the final temperature achievable on narrow transitions is lower, the cooling is only effective for detuning δ on the order of Γ below the atomic transition, and scales as $\left(\frac{\Gamma}{2\delta} \right)^3$ for $|\delta| \gg \Gamma$. A scatterer at 300 K and a typical atomic mass of 50 a.u. has velocity of ≈ 200 m/s, and a Doppler shift of an optical transition of 300 MHz. Efficient cooling of

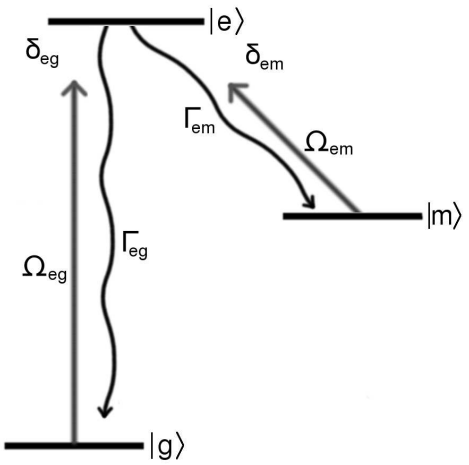

Figure 2-1: Λ system of atomic states. The excited state $|e\rangle$ is coupled to both the true ground state $|g\rangle$, and to a metastable excited state $|m\rangle$.

an initially hot scatterer requires either sweeping the laser frequency to match the Doppler detuning of the particle, or large enough Γ to achieve significant damping at large detuning.

2.4.2 Doppler Cooling in a Λ system

Heavy, hydrogen-like elements such as Sr^+ usually have a Λ-like structure for excited states, such as the one presented in Figure 2-1. In such system, the excited state $|e\rangle$ can decay to both ground state $|g\rangle$ and a metastable state $|m\rangle$. Once the atom decays to $|m\rangle$, it ceases to interact with the light field resonant with the $|e\rangle \leftrightarrow |g\rangle$ transition. Continuous cooling requires repumping of the $|m\rangle$ state with a second laser Ω_{em}.

Using the state $|e\rangle$ as the energy reference, the non-interacting Hamiltonian is $H_0 = -\hbar\omega_{eg}|g\rangle\langle g| - \hbar\omega_{em}|m\rangle\langle m|$. Define δ_{eg} and δ_{em} to be the detunings of the lasers from the resonance, $\delta_{nm} = \omega_{L,nm} - \omega_{nm}$. Define σ operators as usual, with $\sigma^z_{nm} = \frac{1}{2}\left(|n\rangle\langle n| - |m\rangle\langle m|\right)$, $\sigma^+_{nm} = |n\rangle\langle m|$.

In the laser frame, defined by

$$H_L = -\hbar\left(\omega_{eg} + \delta_{eg}\right)|g\rangle\langle g| - \hbar\left(\omega_{em} + \delta_{em}\right)|m\rangle\langle m| \tag{2.64}$$

the Hamiltonian can be expressed analogously to Equation 2.54,

$$H = \hbar\delta_{eg}|g\rangle\langle g| + \hbar\delta_{em}|m\rangle\langle m| + \frac{\hbar}{2}\left(\Omega_{eg}e^{\imath\phi_{eg}}\sigma^+_{eg} + \Omega_{em}e^{\imath\phi_{em}}\sigma^+_{em} + h.a.\right) \tag{2.65}$$

The phases ϕ_{eg}, ϕ_{em} of the beams are not significant for laser cooling, and will be dropped. Let $L_0 \equiv \sqrt{\Gamma_{eg}}|g\rangle\langle e|$, $L_1 \equiv \sqrt{\Gamma_{em}}|m\rangle\langle e|$. The equation of motion for the density matrix ρ in Lindblad form is

$$\frac{d\rho}{dt} = \frac{-\imath}{\hbar}[H,\rho] + \sum_{i=0,1}\left(L_i\rho L_i^\dagger - \frac{1}{2}\rho L_i^\dagger L_i - \frac{1}{2}L_i^\dagger L_i\rho\right) \tag{2.66}$$

This equation can be integrated numerically. Define a vector form of density matrix

$$\vec{v}(\rho) = (\rho_{gg}, \rho_{ee}, \rho_{mm}, \mathrm{Re}(\rho_{ge}), \mathrm{Im}(\rho_{ge}), \mathrm{Re}(\rho_{gm}), \mathrm{Im}(\rho_{gm}), \mathrm{Re}(\rho_{em}), \mathrm{Im}(\rho_{em})) \tag{2.67}$$

Let a propagator A be defined by $\partial_t\vec{v}(\rho) = A\cdot\vec{v}(\rho)$. Straightforward calculation shows that

$$A = \begin{pmatrix}
0 & \Gamma_{eg} & 0 & 0 & -\Omega_{eg} & 0 & 0 & 0 & 0 \\
0 & -\Gamma_{eg}-\Gamma_{em} & 0 & 0 & \Omega_{eg} & 0 & 0 & 0 & -\Omega_{em} \\
0 & \Gamma_{em} & 0 & 0 & 0 & 0 & 0 & 0 & \Omega_{em} \\
0 & 0 & 0 & \frac{\Gamma_{eg}+\Gamma_{em}}{-2} & \delta_{eg} & 0 & \frac{\Omega_{em}}{-2} & 0 & 0 \\
\frac{\Omega_{eg}}{2} & \frac{\Omega_{eg}}{-2} & 0 & -\delta_{eg} & \frac{\Gamma_{eg}+\Gamma_{em}}{-2} & \frac{\Omega_{em}}{2} & 0 & 0 & 0 \\
0 & 0 & 0 & 0 & \frac{\Omega_{em}}{-2} & 0 & \delta_{eg}-\delta_{em} & 0 & \frac{\Omega_{eg}}{2} \\
0 & 0 & 0 & \frac{\Omega_{em}}{2} & 0 & \delta_{em}-\delta_{eg} & 0 & \frac{\Omega_{eg}}{-2} & 0 \\
0 & 0 & 0 & 0 & 0 & 0 & \frac{\Omega_{eg}}{2} & \frac{\Gamma_{eg}+\Gamma_{em}}{-2} & -\delta_{em} \\
0 & \frac{\Omega_{em}}{2} & \frac{\Omega_{em}}{-2} & 0 & 0 & \frac{\Omega_{eg}}{-2} & 0 & \delta_{em} & \frac{\Gamma_{eg}+\Gamma_{em}}{-2}
\end{pmatrix} \tag{2.68}$$

The null space of A gives the steady state solution. In particular, we can show that for $\delta_{eg} = \delta_{em}$, the steady state solution is

$$\vec{v}(\rho) = \frac{1}{\Omega_{em}^2 + \Omega_{eg}^2}\left(\Omega_{em}^2, 0, \Omega_{eg}^2, 0, 0 - \Omega_{em}\Omega_{eg}, 0, 0, 0\right) \tag{2.69}$$

The zero population in ρ_{ee} state indicates that the ion is no longer scattering light, but is trapped in a coherent superposition of $|g\rangle$ and $|m\rangle$ states. These dark states must be avoided by an appropriate adjustment of laser frequencies. The method outlined above can be extended to any number of systems, including, for instance, Zeeman sub-levels of atomic states [BB02]. Aside from this complication, Doppler cooling in a Λ system proceeds similarly to that in a two-level system.

Figure 2-2 shows the comparison between the $|e\rangle$ state population in a Λ system and a simple 2-level system. The detuning δ_{em} and Rabi frequency Ω_{em} were chosen as to optimize the peak excited state population. The damping force is proportional to $\partial_v F \propto \partial_\delta \rho_{ee}$, and quite similar in both cases.

Figure 2-3 shows the population of the $|e\rangle$ state as a function of the detuning of the lasers, δ_{eg} and δ_{em}, for $\Omega_{eg} = \frac{\sqrt{2}}{2}\ \Gamma$, $\Omega_{em} = 1\ \Gamma$. Appendix B presents the derivation of the formulas and results used in this section.

2.4.3 Sideband Cooling

The Doppler cooling limit on a strong transition with a typical decay rate $\Gamma = 10^8\ \mathrm{s}^{-1}$ is 400 µK. The trap oscillation frequencies are on the order of 1 MHz $\approx$ 50 µK. A Doppler

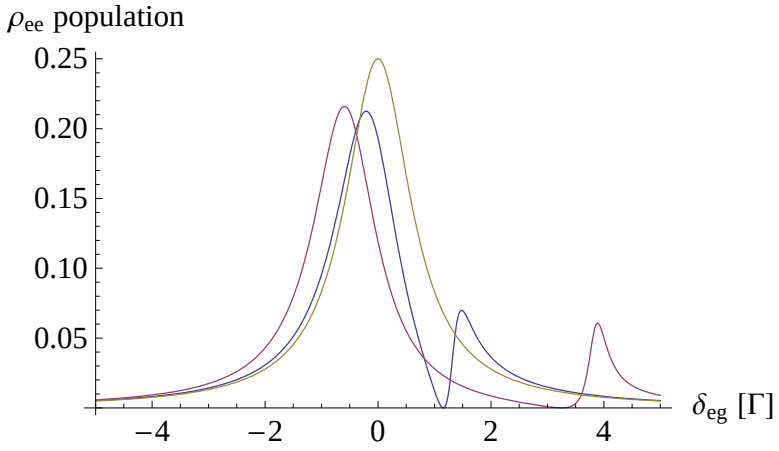

Figure 2-2: Steady state populations of the $|e\rangle$ state for a Λ system (blue, red) and a two level system (yellow). The detuning and Rabi frequency are in units of $\Gamma_{eg} = \Gamma$, and equal $\Gamma_{em} = .05\ \Gamma$, $\Omega_{em} = 1\ \Gamma, 3\ \Gamma$ (blue, red) , $\Omega_{eg} = \frac{\sqrt{2}}{2}\ \Gamma$, $\delta_{em} = 1.15\ \Gamma, 3.25\ \Gamma$ (blue, red).

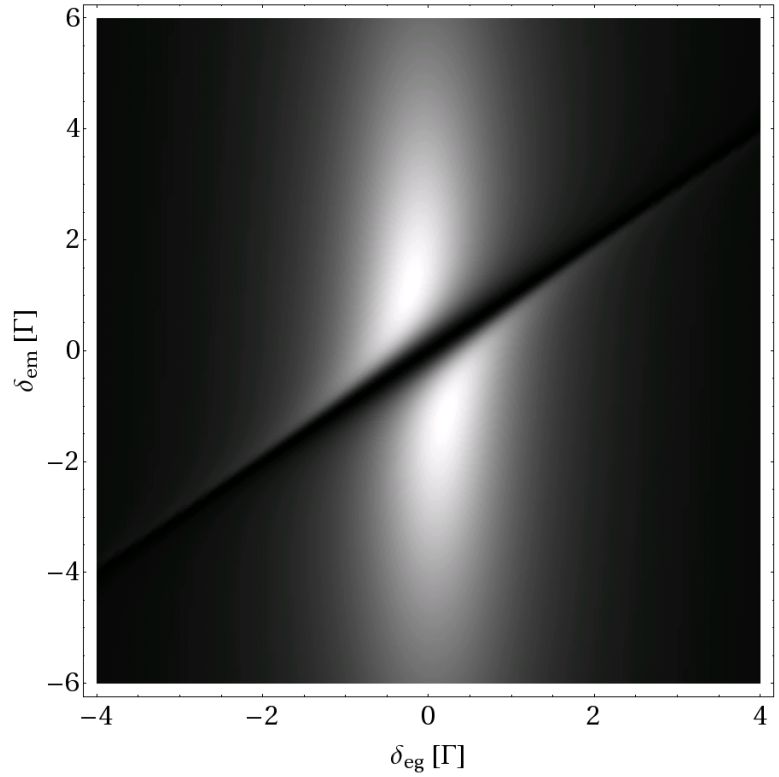

Figure 2-3: Steady state populations of the $|e\rangle$ state as a function of laser detuning. The detuning and Rabi frequency are in units of $\Gamma_{eg} = \Gamma$, and equal $\Gamma_{em} = .05\Gamma$, $\Omega_{em} = 1\ \Gamma$, $\Omega_{eg} = \frac{\sqrt{2}}{2}$. The dark state at $\delta_{em} = \delta_{eg}$ is clearly visible.

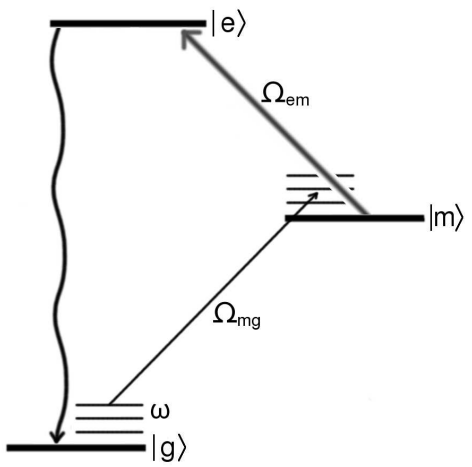

Figure 2-4: Sideband cooling scheme in a Λ system. Ω_{mg} induces transitions which remove a single quantum at a time. The long lifetime of the $|m\rangle$ state is reduced by coupling to the $|e\rangle$ state with Ω_{em} laser.

cooled ion will therefore have on average 8 vibrational quanta. Further cooling to ground state can be achieved using resolved sideband cooling [DBIW89].

Let $\Psi = |n\rangle|m\rangle$ denote an ion in atomic state $|n\rangle$ and motional state $|m\rangle$. Let the states $|g\rangle$ and $|m\rangle$ be connected by a weak transition, with a natural lifetime Γ_{em}. Let the states $|g\rangle$ and $|e\rangle$, and $|e\rangle$ and $|m\rangle$ be connected by strong transitions with very short lifetimes, similarly to Section 2.4.2. As discussed in Section 2.2, for a laser detuned to the red of the transition, $\omega_L = \omega_{mg} - \omega_v$, the resonant part of the Hamiltonian in QC frame is

$$H_{QC} = \frac{\hbar}{2} \sum_{n=0}^{\infty} \Omega\eta\sqrt{n} \left(\sigma^+ |n-1\rangle\langle n| + h.a.\right) \tag{2.70}$$

Provided that $\Omega, \Omega\eta\sqrt{n} \ll \omega_v$, no other terms are significant to the dynamics. Note that η depends on the transition frequency. The above interaction allows us to make a transition from state $|g\rangle|n\rangle$, to $|m\rangle|n-1\rangle$, removing a single phonon. The transition time is equal to $\pi/\left(\eta\Omega\sqrt{n}\right)$, which increases with decreasing number of motional quanta. Subsequently, $|m\rangle$ can be mixed with $|e\rangle$ using light at Ω_{em}, causing it to decay to $|g\rangle$. The cycle is repeated until the ion is sufficiently cooled.

Ground state cooling requires two conditions to be satisfied.

- $|g\rangle|0\rangle$ should not interact with the laser. This condition is equivalent to $\Omega \ll \omega_v$ (the transition is not excited off-resonantly on the carrier) and $\Gamma_{mg} \ll \omega_v$ (the sidebands spectrum is resolved). This is the so-called "strong binding" limit, and it guarantees that an ion cooled to the ground state will remain in it.

- $|e\rangle|n\rangle$ decays preferentially to $|g\rangle|n\rangle$ state. The ratio of decay rates to states $|g\rangle|n\pm1\rangle$ and $|g\rangle|n\rangle$ is proportional to $\left(\frac{\Omega_{n,n+1}}{\Omega_{nn}}\right) \approx \eta^2 n$. Provided that $\eta^2 n \ll 1$, the motional state energy will be decreased by 1 after each cooling cycle. Otherwise, the decay from $|e\rangle$ can increase the number of motional quanta, thus reducing the cooling efficiency.

If the second condition is satisfied, the temperature limit is set by the first, and equal to $\langle n \rangle = \frac{5\Gamma_{em}^2}{16\omega_v^2}$, which can be much less than 10^{-6} for narrow optical transitions [WI79]. The rate of the cooling process is also limited by the first condition, $\Omega \ll \omega_v$. The n-th quanta can be removed in time $\pi/(\eta\Omega\sqrt{n})$. The entire cooling process, starting at n_0 quanta, will necessarily take longer than $\pi\sqrt{n_0}/(\eta\Omega)$.

Typical operating parameters in ion traps are $\omega_v \approx 1$ MHz, $\eta \approx 0.1$ and $\Omega \approx 0.1\ \omega_v$. For a harmonic oscillator in thermal state with a given expected number of quanta $\langle n \rangle$, the probability of n quanta being measured is $P_n = \frac{\langle n \rangle^n}{(\langle n \rangle + 1)^{n+1}}$. There are more than n_0 quanta with probability $\frac{\langle n \rangle^{n_0}}{(\langle n \rangle + 1)^{n_0}}$. The Doppler limited number of quanta is $\langle n \rangle \approx 10$, and with $p = 99\%$ probability the actual number of quanta is less than $\frac{-\log(1-p)}{\log\langle n \rangle - \log(\langle n \rangle + 1)} \approx 50$. The required time to cool from $n_0 \approx 50$ to ground state using the method described in this section is 0.4 ms. Imperfect pumping to the $|m\rangle$ state due to, for example, incorrect pulse lengths, extends the time and the required number of cycles.

2.5 State Measurement

Quantum computation requires efficient measurement of the state of the system. In an ion trap quantum computer, the measurement may need to be able to discern the internal state of the atoms, as well as the motional state. In this section, we describe measurement methods for both states.

Assume the internal states used for computation are the ground state $|\downarrow\rangle \equiv |g\rangle$ and a metastable excited state $|\uparrow\rangle$, outside of the $|g\rangle, |e\rangle, |m\rangle$ Λ system.

2.5.1 Atomic State Measurement

Internal state detection can be performed by illuminating the ion with resonant laser light at ω_{eg} and ω_{em} frequencies. If the ion is initially in $|\uparrow\rangle$, it will not scatter any photons. However, if the ion is initially in $|\downarrow\rangle$ state, it will undergo transitions, as described in Section 2.4.2, scattering incoming ω_{eg} photons at a rate equal to $\Gamma_{eg}\rho_{11}$ (See Figure 2-1). These photons can be counted using a photo-multiplier tube, and the recorded number used to distinguish the states. Detection efficiency and speed are limited by the light collection efficiency and background count rate. The cases of a single ion and multiple ion require different detection times, and will be discussed separately.

Single Ion

Assume the count rate for light scattered from the ion is R_i, and the background count rate is $R_b \ll R_i$. Let the decision threshold be n_0, that is, if observed photon number n satisfies $n < n_0$, the ion is measured to not interact with light, but if $n \geq n_0$, the ion is considered to have scattered. The observed count n, at average count rate R and integration time τ, follows Poisson statistics, with probability distribution $P(n, R\tau) = \frac{(R\tau)^n}{n!}e^{-R\tau}$. The fidelity of the measurement is limited by two errors. Using Γ to denote the Euler Gamma function, these can be expressed as follows.

- $R = R_i$, $n < n_0$. The probability for that event is $P(n < n_0, R_i\tau) = \frac{\Gamma(n_0, R_i\tau)}{\Gamma(n_0)}$. If $R_i\tau \gg 1$, $P(n < n_0, R_i\tau) \approx \frac{(R_i\tau)^{n_0-1}e^{-R_i\tau}}{\Gamma(n_0)}$. This error source increases with increasing n_0, starting at value 0 at $n_0 = 0$.

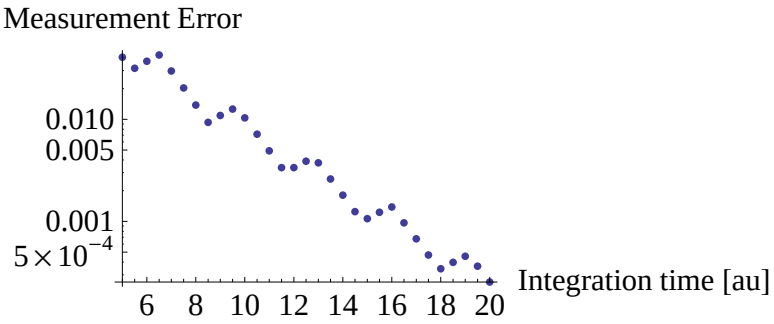

Figure 2-5: Expected state measurement error as a function of integration time, in arbitrary units [au]. Parameters are $R_i = 1$ [1/au], $R_b = 0.05$ [1/au]. The measurement errors are below 0.5% for $\tau R_i > 12$. The plot is not smooth due to the discrete nature of threshold value n_0.

- $R = R_b$, $n \geq n_0$. The probability for this event is $P(n \geq n_0, R_b\tau) = 1 - \frac{\Gamma(n_0, R_b\tau)}{\Gamma(n_0)}$. If $R_b\tau \ll 1$, $P(n \geq n_0, R_b\tau) \approx \frac{(R_b\tau)^{n_0}}{n_0\Gamma(n_0)}$. This error source decreases with increasing n_0, and tends to 0 as $n_0 \to \infty$.

We can find the optimal threshold setting by equating these two error sources. Setting

$$\frac{(R_b\tau)^{n_0}}{n_0\Gamma(n_0)} = \frac{(R_i\tau)^{n_0-1}\, e^{-R_i\tau}}{\Gamma(n_0)} \tag{2.71}$$

results in

$$n_0 \left(\frac{R_i}{R_b}\right)^{n_0} = R_i\tau e^{R_i\tau} \tag{2.72}$$

which can be solved numerically. If $R_i \gg R_b$ and $R_i\tau \gg 1$, an approximate solution is obtained by dropping the factors in front of the exponentials, which gives

$$\left(\frac{R_i}{R_b}\right)^{n_0} = e^{R_i\tau} \tag{2.73}$$

$$n_0 \approx \frac{R_i\tau}{\log\left(R_i/R_b\right)} \tag{2.74}$$

The measurement error can then be estimated from $P(n < n_0, R_i\tau) = \frac{\Gamma(n_0, R_i\tau)}{\Gamma(n_0)}$. Plot of the measurement error for sample scatter rates is shown in Figure 2-5. Note that a measurement with better than 99% fidelity requires around 10 photons to be detected. The time required depends on the scatter rate and the light collection efficiency, necessitating the use of strong transitions with fast decay rates, and optics with a high numerical aperture.

Multiple Ions

When two or more ions are present, discrimination of the number of ions interacting with light requires more time. Assume there are N ions, and the information on whether N, or $N-1$ of these scatter light is of interest. Assuming the scatter rate for a single ion to be

R_i, and the integration time to be τ, the average counts in both cases are $\bar{n}_N = NR_i\tau$ and $\bar{n}_{N-1} = (N-1)R_i\tau$. If $NR_i\tau \gg 1$, the standard deviation of these values is approximately $\sigma_N = \sqrt{NR_i\tau}$ and $\sigma_{N-1} = \sqrt{(N-1)R_i\tau}$. Requiring the difference in counts to be larger than $3\left(\sigma_N + \sigma_{N-1}\right)$ ($< 0.3\%$ error probability),

$$\begin{aligned} R_i\tau &> 3\left(\sqrt{NR_i\tau} + \sqrt{(N-1)\,R_i\tau}\right) \\ R_i\tau &> 9\left(2N + 2\sqrt{N\,(N-1)} - 1\right) \end{aligned} \tag{2.75}$$

The required measurement time scales linearly with the number of scattering ions in the chain. For $N = 2$, $R_i\tau > 52$, significantly longer than the time required for single ion discrimination.

2.5.2 Motional State Measurement

The motional state can not be measured directly, but only through its effect on the atomic transitions. The Rabi frequencies on the red and and blue sidebands are $\Omega_{n-1,n} = \Omega\eta\sqrt{n}$ and $\Omega_{n+1,n} = \Omega\eta\sqrt{n+1}$, both of which depend on the number of motional quanta, allowing for measurement of the motional state.

Consider laser illumination at detuning $\delta = \omega_v$ from the transition $|\downarrow\rangle \leftrightarrow |\uparrow\rangle$, applied for a time t. The transition probability from $|\downarrow\rangle$ to state $|\uparrow\rangle$, in resolved sideband limit, is

$$P(|\downarrow\rangle \rightarrow |\uparrow\rangle, \delta = \omega_v) = \sum_{n=0}^{\infty} P_n \sin\left(\Omega_{n+1,n}t/2\right)^2 \tag{2.76}$$

Similarly, for $\delta = -\omega_v$,

$$P(|\downarrow\rangle \rightarrow |\uparrow\rangle, \delta = -\omega_v) = \sum_{n=1}^{\infty} P_n \sin\left(\Omega_{n-1,n}t/2\right)^2 \tag{2.77}$$

Let the ion be in a thermal state, with occupation probabilities $P_n = \frac{\langle n\rangle^n}{(\langle n\rangle+1)^{n+1}}$. Then

$$\begin{aligned} P(|\downarrow\rangle \rightarrow |\uparrow\rangle, \delta = -\omega_v) &= \sum_{n=0}^{\infty} P_{n+1} \sin\left(\Omega_{n,n+1}t/2\right)^2 \\ &= \frac{\langle n\rangle}{1+\langle n\rangle} \sum_{n=0}^{\infty} P_n \sin\left(\Omega_{n,n+1}t/2\right)^2 \\ &= \frac{\langle n\rangle}{1+\langle n\rangle} P(|\downarrow\rangle \rightarrow |\uparrow\rangle, \delta = \omega_v) \end{aligned} \tag{2.78}$$

Therefore, in a thermal distribution with an average number of quanta $\langle n\rangle$, the transition probability on the blue and red sidebands is related by $\frac{\langle n\rangle}{1+\langle n\rangle}$, regardless of the Rabi frequency Ω and illumination time t.

The population distribution can be measured by scanning the laser pulse time t at a fixed $\delta = \omega_v$, and decomposing the resulting curve into components at frequencies $\Omega\eta\sqrt{n}$ (see Equation 2.76). Provided that the number of occupied motional states is low, such decomposition reveals the population distribution among those states.

	First Measurement		Second Measurement	
	No carrier π pulse	Carrier π pulse	No carrier π pulse	Carrier π pulse
$\|\downarrow\rangle\|0\rangle$	Scatter	No scatter	Undefined	No scatter
$\|\downarrow\rangle\|1\rangle$	Scatter	No scatter	Undefined	Scatter
$\|\uparrow\rangle\|0\rangle$	No scatter	Scatter	No scatter	Undefined
$\|\uparrow\rangle\|1\rangle$	No scatter	Scatter	Scatter	Undefined

Table 2.2: Expected measurement results for the initial states of the 2 qubits. Conditional on the first measurement yielding no scatter, the second measurement can be used to distinguish a pair of states. Optional carrier π pulse allows measurement of all 4 states.

Both of these measurement methods require the atom to initially occupy $|g\rangle$ state. A generalized method which allows for measurements of the internal and motional qubit at the same time is discussed in Section 2.5.3.

2.5.3 State Tomography

The state of both qubits, the internal and motional, can not be measured with the methods discussed above. The measurement of the internal state using light scattering, as outlined in Section 2.5.1, will scramble the motional state if the ion is in $|\downarrow\rangle$ and scatters a number of photons $\approx 1/\eta$, because of photon recoil. However, if the ion is initially in $|\uparrow\rangle$, it will not scatter any photons, leaving its motional state unchanged.

This realization motivates the construction of a novel measurement sequence, which can determine the population in any of the $|\downarrow\rangle|0\rangle$, $|\uparrow\rangle|0\rangle$, $|\downarrow\rangle|1\rangle$, $|\uparrow\rangle|1\rangle$ states. Consider the following algorithm

- Apply an optional π pulse on the carrier transition
- Measure the internal atomic state
- Apply a π pulse on the blue sideband transition
- Measure the internal atomic state

The expected measurement results are tabulated in Table 2.2. Photon recoil scrambles the motional state, and therefore the events where the ion scatters photons during the first measurement provide information about the internal state only. The event when the first measurement does not scatter light, however, allows us to measure the population in a pair of states $|\uparrow\rangle|0\rangle$ and $|\uparrow\rangle|1\rangle$, or $|\downarrow\rangle|0\rangle$ and $|\downarrow\rangle|1\rangle$, depending on whether the initial carrier π pulse was applied or not. Two measurements, with and without the carrier pulse, are sufficient to determine the populations in all 4 states.

The measurements discussed so far measure the state populations only. Equally important are the measurements of the relative phase between the qubit states, which determine coherence properties of the state. These phases can be obtained by appropriate rotations of the qubits prior to measurement, as demonstrated by a simple example. Consider a simple 2-state system. Any general state of such system is described by a density matrix

$$\rho = \frac{1}{2}\left(I + \langle z\rangle Z + \langle x\rangle X + \langle y\rangle Y\right) \tag{2.79}$$

where X, Y, Z are the Pauli matrices.

A projective measurement $P = |0\rangle\langle 0|$ returns $\frac{1}{2}(1 - \langle z \rangle)$, from which we can trivially compute $\langle z \rangle$, the expectation value of the Z operator. To measure the other expectation values, note that

$$Z = R_y\left(\frac{\pi}{2}\right)^\dagger X R_y\left(\frac{\pi}{2}\right)$$
$$Z = -R_x\left(\frac{\pi}{2}\right)^\dagger Y R_x\left(\frac{\pi}{2}\right)$$

Therefore, rotations by $\pi/2$ around the X and Y axes allow us to permute the Pauli matrices in Equation 2.79, and measure the expectation values $\langle x \rangle$ and $\langle y \rangle$, fully describing its state. A similar idea applies to multi-qubit states.

Section 7.2 demonstrates how the described state tomography method can be used to provide characterization of the fidelity of quantum gates.

2.6 Sr^+ Structure and Qubit

The choice of the atomic species determines in large part the coherence properties of the system and the difficulty of achieving coherent control. In our experiments, Sr^+ was chosen for its easily accessible atomic states [Ber02]. In particular, $^{88}Sr^+$ is a hydrogen-like atom, with no nuclear spin, resulting in a simple level structure. The P states have strong transitions to the ground state, allowing for efficient cooling and detection. The metastable D states of the ion have lifetimes of ≈ 400 ms, and are used for encoding quantum information [LWGS05]. All atomic transitions are easily accessible with diode lasers, significantly reducing cost and complexity of the laser system. The wavelength range is within transparency window of typical glasses and optical fibers. $^{88}Sr^+$ is a stable isotope with a natural abundance of 83%, removing the need for isotope selective ion source. These advantages are somewhat balanced by first order magnetic sensitivity of the qubit states, which may result in reduced coherence times. Qubit operations require the use of a very stable optical laser source, which is difficult to construct. There are no stable isotopes of Sr with a nuclear spin of 1/2, necessitating a complete rebuild of the system if such nuclear spin is desired.

The relevant atomic level structure is shown in Figure 2-6. The ground state of the ion is the $5S_{1/2}$ state. The $5P_{1/2}$ excited state is coupled to $5S_{1/2}$ and $4D_{3/2}$ by strong dipole transitions, creating a Λ system with wavelengths of 422 nm and 1091 nm, respectively. The $5P_{3/2}$ excited state is coupled to $5S_{1/2}$, $4D_{3/2}$ and $4D_{5/2}$.

There are two metastable states, $4D_{3/2}$ and $4D_{5/2}$, which are coupled to the ground state by weak quadrupole transitions. The long lifetimes of these states, approximately 400 ms, make them attractive for information storage. If $P_{1/2}$ state is chosen for Doppler cooling and detection, the decay path to $D_{3/2}$ and the required repumping (Section 2.5) would destroy information stored in $D_{3/2}$ during readout. Similarly, if $P_{3/2}$ state is chosen, the decay paths to both $D_{3/2}$ and $D_{5/2}$ would destroy information stored in both of these states. For this reason, the $P_{1/2}$ state is used for cooling and state measurement, and $D_{5/2}$, which does not interact with the transitions to $P_{1/2}$, is used for information storage.

The saturation intensities of these transitions, a useful experimental value defined as the laser power at which $2\Omega^2 = \Gamma^2$, can be derived from Equations 2.15. The electric field values, and laser power densities ($I = \frac{c\epsilon_0}{2}|E|^2$) necessary for saturation and for $\Omega = 2\pi \times 1$ MHz

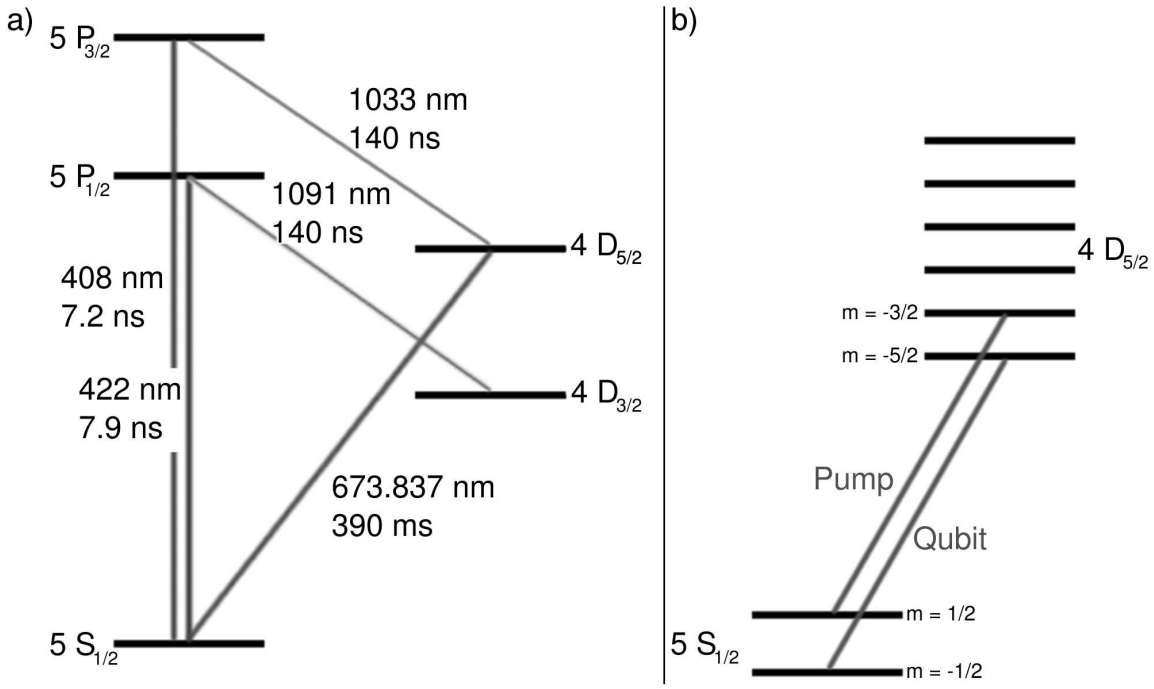

Figure 2-6: a) The relevant atomic level structure of the Sr^+ ion, with air wavelengths indicated next to the transitions. The transition lifetimes are derived from theoretical calculations [GJ91], except for the lifetime of the $D_{5/2}$ state, which is an experimental value [LWGS05]. The 422 nm and 1091 nm transitions are used for Doppler cooling and detection. The 673.837 nm transition couples the qubit levels, and the 1033 nm transition is used to initialize the ion in the $S_{1/2}$ state. b) Detail of the qubit states, with Zeeman levels explicitly drawn. The "qubit" transition connects the qubit states, $S_{1/2}(m = -\frac{1}{2})$ and $D_{5/2}(m = -\frac{5}{2})$. The "pump" transition is used to pump the ion out of the $S_{1/2}(m = \frac{1}{2})$ state during initialization.

	E_{sat} [V/m]	I_{sat} [mW/cm^2]	$E_{1\ \mathrm{MHz}}$ [V/m]	$I_{1\ \mathrm{MHz}}$ [mW/cm^2]
$S_{1/2} \leftrightarrow P_{1/2}$	445	26.3	31	0.13
$D_{3/2} \leftrightarrow P_{1/2}$	25	0.09	32	0.13
$D_{5/2} \leftrightarrow P_{3/2}$	28	0.1	34	0.16
$S_{1/2} \leftrightarrow D_{5/2}$	0.03	0.1×10^{-6}	1.1×10^{5}	1.6×10^{6}

Table 2.3: Saturation fields and intensities for the relevant ion transitions. Also calculated are the values necessary for $\Omega = 1$ MHz.

	$S_{1/2}$	$P_{1/2}$	$P_{3/2}$	$D_{3/2}$	$D_{5/2}$
g_J	2	2/3	4/3	4/5	6/5

Table 2.4: Landé g-factors for the internal states of the ion.

are listed in Table 2.3. The values listed assume the geometric factors dependent on j_g, j_e, m and laser polarization are equal to 1.

2.6.1 Zeeman Splitting and Selection Rules

The atomic structure is further complicated by the Zeeman splitting. Each atomic state X_j with angular momentum j is split into $2j+1$ states, with the projection of the angular momentum on the field axis equal $m = -j, -j+1 \cdots j-1, j$. To avoid degeneracy, these Zeeman sub-states are split in frequency by an applied magnetic field [BB02]. The energy shift in the applied field equals $\Delta E = m g_x \mu_B B$, where g_x is a state specific Landé g-factor. Landé g-factors for different states are shown in Table 2.4.

The dipole and quadrupole transitions couple only specific states, depending on the magnetic field direction, laser $\vec{k}$ vector and polarization $\hat{e}$. These "selection rules" can be derived from the geometric factors in Equation 2.15. Of particular importance are the selection rules on the $D_{3/2} \leftrightarrow P_{1/2}$ and $S_{1/2} \leftrightarrow D_{5/2}$ transitions.

The $D_{3/2}$ state is coupled to $P_{1/2}$ via a dipole transition, which allows $\Delta m = \pm 1, 0$. However, with no magnetic field, we could always pick the angular momentum axis along the laser polarization, which results in $\Delta m = 0$ transitions. In such arrangement, only 2 of the 4 Zeeman states of the $D_{3/2}$ would be coupled to the $P_{1/2}$. An external magnetic field forces an angular momentum quantization axis. If the laser polarization is set at an angle to $\vec{B}$, all transitions with $\Delta m = \pm 1, 0$ are allowed, efficiently repumping the $D_{3/2}$ state. The splitting between the Zeeman states should be on the order of the Rabi frequency of the repumper, or 10 MHz, which corresponds to a field of a few Gauss [BB02]. Alternative method uses polarization rotation of the light beam at MHz frequencies, continuously varying the addressed states.

The $S_{1/2}$ state is coupled to $D_{5/2}$ via a quadrupole transition. For $\vec{k} \perp \hat{e} \perp \vec{B}$, the allowed transitions are $\Delta m = \pm 2$. The states coupled are the $S_{1/2}(m = 1/2) \leftrightarrow D_{5/2}(m = -3/2)$ and the $S_{-1/2}(m = -1/2) \leftrightarrow D_{5/2}(m = -5/2)$ (plus symmetric transitions with $\Delta m = 2$). The latter transition is convenient for sideband cooling, as it forms a closed cycle; the $D_{5/2}(m = -5/2)$ state will necessarily return to $S_{1/2}(m = -1/2)$ after pumping to $P_{3/2}$ via a dipole transition ($\Delta m = \pm 1, 0$), and a decay to $S_{1/2}$ state via, again, a dipole interaction. This does not hold true for very high laser powers on the $D_{5/2} \leftrightarrow P_{3/2}$ transition, which can induce multiple transitions between the $D_{5/2}$ and $P_{3/2}$ states before the decay to the $S_{1/2}$ state. This transition is also the strongest of all the Zeeman lines, and therefore used

as the qubit transition.

The transition $S_{1/2}(m = \frac{1}{2}) \leftrightarrow D_{5/2}(m = -\frac{3}{2})$ can be used to pump the ion into the $S_{1/2}(m = -\frac{1}{2})$ state. Because the transitions starting from $m = \frac{1}{2}$ and $m = -\frac{1}{2}$ have different Zeeman shifts, the population in $m = \frac{1}{2}$ state can be selectively pumped to the $D_{5/2}$ state, and subsequently returned to the $S_{1/2}$ state via the $P_{3/2}$. The decay from the $P_{3/2}$ state is not selective, and returns the electron to either of the $S_{1/2}$ states, with exact ratio dependent on polarization of the 1033 nm laser. After a number of cycles, however, the entire population can be pumped to the $S_{1/2}(m = -\frac{1}{2})$ state.

Chapter 3

Experimental Apparatus

Trapping of Sr^+ ions requires accomplishing a few general steps, which will be discussed in this chapter. First, an appropriate confining potential is required to trap the charge. The design of the recently developed surface electrode ion trap is presented in Section 3.1, with theoretical calculations of the trap potential. The fabrication of these traps presents a significant challenge, and is presented in detail. In order to avoid collisions and chemical loss of ions, an enclosure with vacuum pressures reaching 10^{-10} Torr is necessary. The cryogenic environment, described in Section 3.2, simplifies this requirement significantly by virtue of reduced outgassing of materials and cryopumping of residual gas on an appropriate getter material. The cryogenic cooling of ion traps will also be crucial to the study of electric field noise, described in later chapters. Sr^+ can be formed by either ablation of a Sr-rich target or photo-ionization of a neutral vapor. Both methods are presented and evaluated in terms of simplicity and repeatability, and the results presented in Section 3.4. Lastly, Section 3.5 describes the optics system designed to deliver laser light and gather scattered photons, together with characterization of its performance.

The cryogenic environment, ion sources and optics are straightforward implementations of established ideas. Microfabricated surface electrode ion traps are discussed in Reference [CBB+05]. However, the electrode geometry and fabrication methods constitute original content in this thesis.

3.1 Surface Electrode Ion Trap Design And Operation

A static electric field cannot confine a charged particle, which follows from the required relation $\nabla^2 V = 0$. Ions can be trapped, however, with an addition of a magnetic field (Penning trap) or an oscillating electric field (Paul trap). This section reviews the derivation of the trapping pseudo-potential in a Paul trap.

Consider the following potential, independent of z position,

$$V(t, x, y, z) = V(t)\frac{xy}{R^2} \tag{3.1}$$

generated by an oscillating voltage $V(t) = V_0 \cos(\Omega t)$. The potential in Equation 3.1 can be generated by four electrodes shaped as hyperbolas (the equipotantial surfaces of the potential V) and charged to voltage of $\pm V(t)$, symmetrically about the origin.

Consider the motion of a charge in this potential. If $\vec{r}$ is the position, m the mass and

Q the charge of the particle, the equation of motion is

$$m\ddot{\vec{r}} = Q\nabla V(t,\vec{r}) \tag{3.2}$$

$$= QV(t)\frac{2\vec{e}\,(\vec{r}\cdot\vec{e}) - \vec{r}}{R^2} \tag{3.3}$$

$$\vec{e} \equiv \frac{\hat{x}+\hat{y}}{\sqrt{2}} \tag{3.4}$$

There is no force along $\hat{z}$, so all vectors can be restricted to the $x-y$ plane. Such an equation of motion is known as a Mathieu equation. While difficult to solve exactly, much progress can be made by separating the ion position into a term oscillating with the field, and another slowly varying term. Define two vectors $\vec{r}_\mu$ and $\vec{r}_s$, which are slowly varying compared to $\cos(\Omega t)$

$$\vec{r}(t) = (2\vec{e}\,(\vec{r}_\mu\cdot\vec{e}) - \vec{r}_\mu)\cos(\Omega t) + \vec{r}_s(t) \tag{3.5}$$

After substitution into Equation 3.2,

$$-m\,(2\vec{e}\,(\vec{r}_\mu\cdot\vec{e}) - \vec{r}_\mu)\,\Omega^2\cos(\Omega t) + m\ddot{\vec{r}}_s = QV_0\cos(\Omega t)\,\frac{\vec{r}_\mu\cos(\Omega t) + (2\vec{e}\,(\vec{r}_s\cdot\vec{e}) - \vec{r}_s)}{R^2}$$

$$-(2\vec{e}\,(\vec{r}_\mu\cdot\vec{e}) - \vec{r}_\mu)\,\Omega^2\cos(\Omega t) + \ddot{\vec{r}}_s = \frac{QV_0}{mR^2}\left(\vec{r}_\mu\cos^2(\Omega t) + (2\vec{e}\,(\vec{r}_s\cdot\vec{e}) - \vec{r}_s)\cos(\Omega t)\right)$$

where we neglected the $\ddot{\vec{r}}_\mu$ term, assuming it to be small compared to $\ddot{\vec{r}}_s$ and $\Omega^2\vec{r}_\mu$. Equating the terms proportional to $\cos(\Omega t)$, averaging $\cos^2(\Omega t) \approx \frac{1}{2}$ and equating slowly oscillating terms results in equations in the so-called "pseudo-potential" approximation.

$$\vec{r}_\mu = -\frac{QV_0}{m\Omega^2R^2}\vec{r}_s$$
$$\ddot{\vec{r}}_s = \frac{QV_0}{2mR^2}\vec{r}_\mu$$

Substituting the first equation into the second, and defining $q_m \equiv \frac{2QV_0}{m\Omega^2R^2}$,

$$\vec{r}_\mu = -\frac{q_m\vec{r}_s}{2}$$
$$\ddot{\vec{r}}_s = -\frac{q_m^2\Omega^2}{8}\vec{r}_s \tag{3.6}$$
$$q_m \equiv \frac{2QV_0}{m\Omega^2R^2}$$

This equation of motion describes a harmonic oscillator oscillating at frequency $\frac{q\Omega}{2\sqrt{2}}$, called the "secular frequency" of the trap. The effective potential can be approximated by

$$\Phi(\vec{r}) = \frac{1}{2}\frac{mq_m^2\Omega^2}{8}\left|\vec{r}\right|^2 \tag{3.7}$$

$$= \frac{Q^2V_0^2}{4m\Omega^2R^4}\left|\vec{r}\right|^2 \tag{3.8}$$

Given that $\left|\vec{E}(r)\right|^2 = \frac{V_0^2}{R^4}\left|r\right|^2$, this potential can also be written as

$$\Phi(\vec{r}) = \frac{Q^2}{4m\Omega^2}\left|\vec{E}\right|^2 \tag{3.9}$$

Equation 3.9 depends only on local field, and holds for any shape of the time-dependent potential, allowing for computation of the pseudo-potential based solely on the values of $\left|\vec{E}\right|^2$ in space.

While the above derivation used a z-independent potential, three dimensional confinement can be similarly achieved using an oscillating 3-D hyperbolic potential. Alternatively, two DC electrodes can be added at $z = \pm z_0$, to provide confinement along the $\hat{z}$ direction. The latter solution will be used in traps developed in this work.

The fast oscillating component of $\vec{r}$, proportional to $\vec{r}_\mu$, is called "micromotion", and have amplitude equal to $\frac{q_m}{2}$ of $\vec{r}_s$, called "secular" motion. The amplitude of the micromotion is zero for ion position $\vec{r}_s = 0$. Such arrangement is typically desirable, as it minimizes the velocity and position uncertainty of the ion and maximizes the laser coupling. When the trap is defined by both RF and DC potentials, the DC potentials should be set so that the equilibrium ion position is at the saddle of the RF potential, the so-called "compensated" values.

The pseudo-potential approximation holds as long as $q_m \ll 1$. More careful investigation of the Mathieu equations allows for a derivation of an exact solution, as well as determination of the stability of the particle in the potential, which requires $q_m \lesssim 0.9$ [Gho95].

3.1.1 Electrode Geometry

Equation 3.9 suggests that a local minimum of $\left|\vec{E}\right|$ is a necessary and sufficient condition for a confining potential. The design of the trap, then, becomes a problem of finding a geometry where such a minimum exists. As mentioned in the previous section, hyperbolic electrodes can create a field with the desired minimum, and such arrangement was used in the early ion traps. More recently, it was shown that a minimum of $\left|\vec{E}\right|$ exists in geometries where all electrodes are in the same plane, creating a surface electrode ion trap [CBB$^+$05, JPM90]. Such an arrangement is highly desirable due to the ease of construction and the possibility of using microfabrication techniques developed by the electronics industry to miniaturize the traps.

A schematic of the trap design developed at MIT, in this thesis work, and an image of a fabricated trap are shown in Figure 3-1. The cross-section of the trap along $\hat{x}$ consists of five electrodes, DC-RF-GND-RF-DC. Such design facilitates scalability to multi-zone traps with complex geometries by allowing Y-shaped intersections of trapping zones.

A symmetric trap design results in one of the principal axes of the trapping potential Φ pointing along $\hat{z}$. The lasers used for cooling are confined to the $\hat{x} - \hat{y}$ plane, and would not

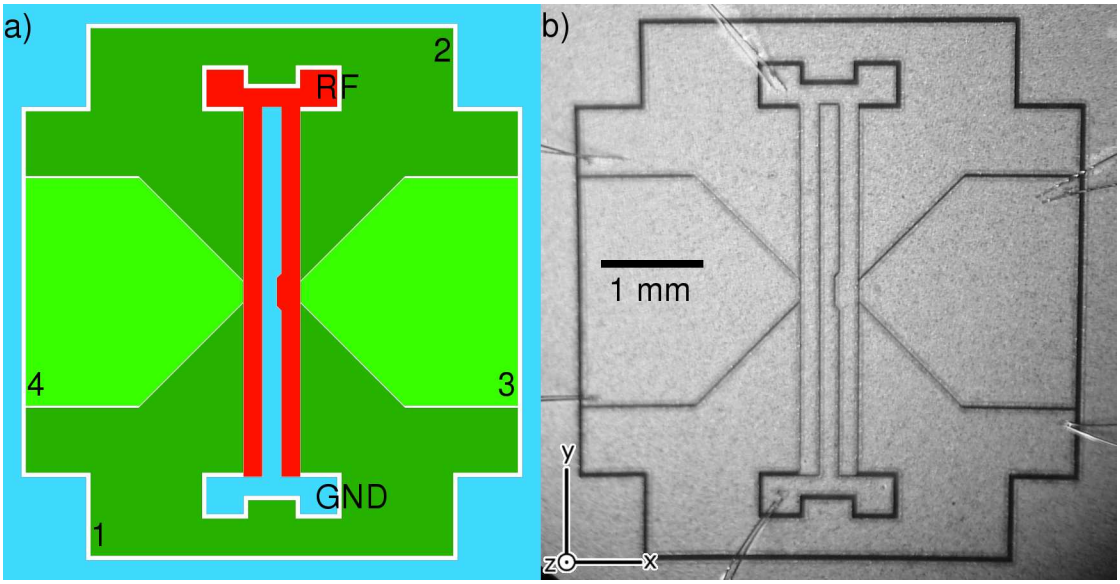

Figure 3-1: a) Schematic of the trap electrodes. DC electrodes (green) are numbered from 1 to 4. The RF (red) and GND (blue) electrodes complete the trap. The notch in the central electrode tilts the principal axes of the trap by 6° to 20°, depending on DC voltages, and defines a point where the RF field is zero. b) Microscope image of a fabricated trap. In this trap, the width of the central electrode at the notch is 136 µm, with RF to GND electrode spacing of 21 µm. The potential minimum is 150 µm above the surface.

cool the motion along the $\hat{z}$ direction (See Section 2.4). To tilt the potential, the central GND electrode is asymmetrically notched, resulting in a 6° to 20° tilt of the principal axis, depending on DC voltages. Additionally, the notch breaks the near invariance of the RF electrode along the $\hat{y}$ axis, and creates a well defined point where the oscillating electric field is zero. Without the notch, this point could be well outside of the center of the chip, due to small fabrication imperfections or RF losses along the electrode. Such behavior was observed in the initial designs which did not utilize the notch, where the zero of the oscillating field was found to be significantly displaced from the geometric trap center.

The design was scaled so that the width of the GND electrode at the notch equaled 150 µm, 100 µm and 75 µm. The intended spacing between electrodes was constant, from 6 to 10 µm, breaking somewhat the symmetry between traps of different sizes. Such small spacings are necessary to reduce exposed dielectric surface, which does not have a well defined potential. The smallest gaps used, 6 µm, were limited by the precision of optical lithography and breakdown voltage considerations.

3.1.2 Trapping Potential

The trapping potential can be derived from the RF electric fields and the DC potential above the surface. The field values can not be computed analytically, however, and a numerical approach is necessary. Charge Particle Optics, a software package from Electron Optics, was used to compute the voltages and electric fields from each electrode independently (assuming all other electrodes are grounded). For any desired electrode voltages, these so called "shape functions" can be added together with appropriate weights to form the total potential. The simulation is scale independent, allowing one to perform a single simulation

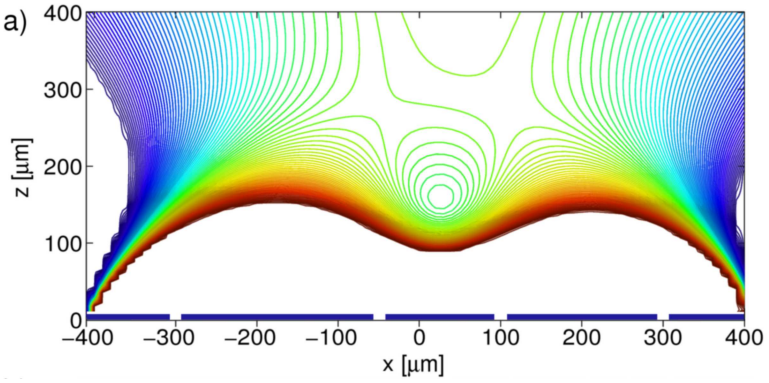

Figure 3-2: (a) Computed pseudo-potential in the $\hat{x} - \hat{z}$ plane at the trap center for $V_1 = V_2 = 16$ V, $V_3 = -16$ V, $V_4 = -13$ V, $V_{RF} = 240$ V_{amp}. Isosurfaces are separated by 50 mV. The trap electrodes are outlined above x axis.

for all traps which are identical up to a scale factor.

The traps are typically operated at a RF voltage of 200 V_{amp} and a frequency of 26 MHz (for electrode width of 150 µm) or 36 MHz (electrode widths of 100 and 75 µm traps). Due to the large inter-electrode spacing, we did not fabricate traps smaller than 75 µm. Numerically calculated trap height above the surface is within 3% of the electrode size. Theoretical compensated DC electrode voltages satisfy $V_1 = V_2 = -V_3 = -\frac{5}{4}V_4$, where V_i is the voltage on electrode i. For $V_1 = 25$ V in the 150 µm trap, the secular frequencies are 1 MHz along $\hat{y}$ and 2.5 MHz and 2.3 MHz in the $\hat{x} - \hat{z}$ plane. Intersection of the simulated potential and the $\hat{x} - \hat{z}$ plane through the trap center is shown in Fig. 3-2. The depth of the trap is ≈ 0.3 eV, or 3000 K.

Experimentally measured radial secular frequencies were found to be within 10% of the theoretically predicted values, using the RF voltage as a free fitting parameter. The axial secular frequency is within 3% of theoretical value, at the same RF voltage.

3.1.3 Arcing

Initial fabrication runs used etched silver films to define the trap electrodes, and were severely compromised by low breakdown voltage of the RF electrode, which reduced the maximum applied voltage, and the possible trap depths and secular frequencies. Breakdown considerations are very common in ion traps - typical operating voltages have values on the order of 100 V applied across electrode gaps just 10 µm wide. The electric fields in the gap exceed 10 MV/m, value comparable to that necessary to cause field emission and dielectric breakdown of the substrate.

The problem was traced to the etching process, which results in rough edges with multiple sharp points. These points emit electrons via Fowler-Nordheim tunneling when driven with voltages in excess of 100 V. The emitted electrons induce stray electric fields, eventually destroying the trapping potential. Such emission can be seen in the visible spectrum as well, as the emitted electrons or the impacts on opposing metal surface generate infrared radiation. Figure 3-3 shows a picture of a trap with multiple "glow" points visible, indicating a large amount of emission.

In order to smooth the electrode edges, the traps are annealed at 720 °C to 760 °C for 1 hour (Figure 3-4). The high temperatures used are necessary to re-flow the silver, but

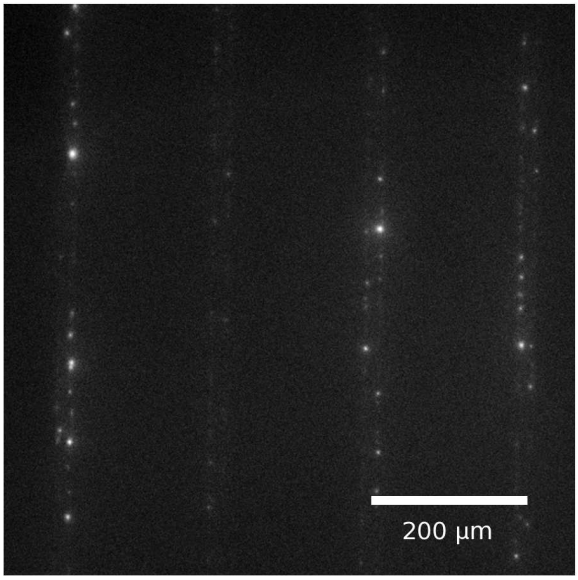

Figure 3-3: Optical picture of a section of the trap, showing glow on the electrode edges due to electron emission or impact. Each white point corresponds to an emitter, or group of emitters. As a rule of thumb, no glow should be visible for up to twice the desired operating voltage for the trap to work properly.

result in an optically roughened surface. After annealing, we find no field emission points for voltages up to 750 V across the gaps.

The annealing process should be performed in vacuum, to avoid oxidation of silver in air at such high temperatures. To satisfy these requirements, a small copper oven heated by a tungsten filament was constructed (Figure 3-5). The oven was placed in a vacuum chamber made out of standard CF pieces and pumped down to 10^{-5} torr. The temperature was monitored using a thermocouple mounted to the inside of the oven. The resistivity of the tungsten filament was 6 Ω at room temperature, and with 30 W dissipated the oven would heat up to 650 °C. The required power increases rapidly with temperature, due to black body radiation, and reaches 50 W for oven temperature of 750 °C.

The electrode edges can also be smoothed by electroplating a layer of metal over the electrodes. The plating is fastest in regions of high electric field, naturally reducing sharpness of edges of the electrodes. The resulting electrodes did not have as high a breakdown as the annealed electrodes, with breakdown voltages on the order of 400 V. However, due to the better repeatability of the plating process, this method was preferred in latter experiments.

3.1.4 Fabrication Summary

Two fabrication methods were developed, which will be referred to as the silver and the gold process. Both processes use single crystal quartz substrate, a high thermal conductivity material at cryogenic temperatures. A brief description of both processes is presented below.

Silver process

- Evaporate 10 nm of a Ti sticking layer, followed by 1 µm of Ag, chosen for its favorable etch properties.
- Coat the wafer with NR9–3000 photoresist.

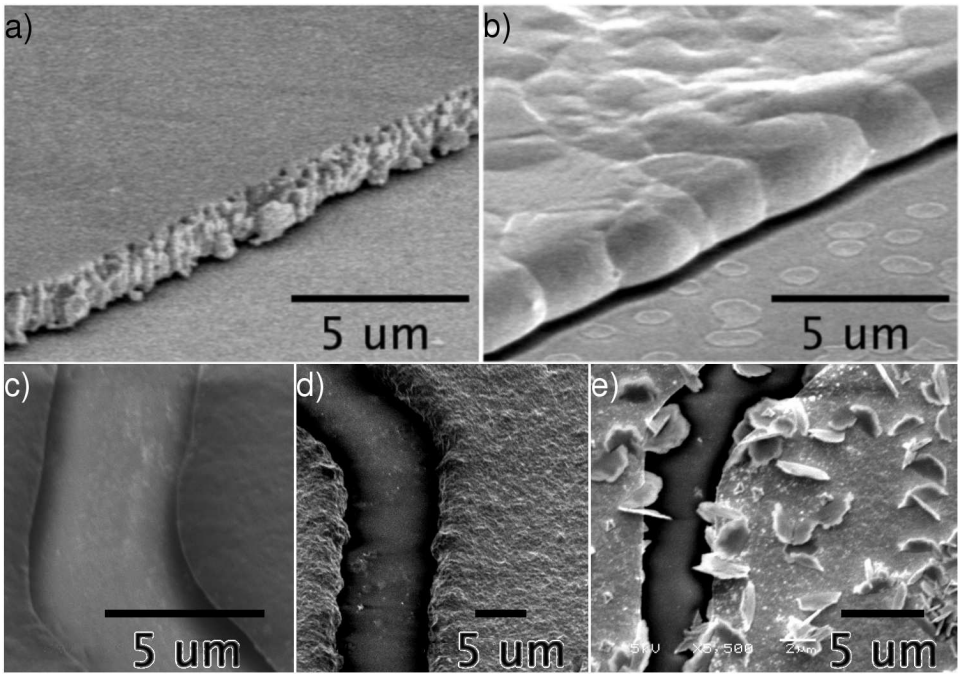

Figure 3-4: (a) SEM image of one of the silver trap electrodes before annealing and (b) after annealing at 760 °C for 1 hour. (c-e) SEM pictures of the gold electroplated edges. The smoothness of the edge varies strongly between fabrication runs, as seen from the images (c) and (d). Trap shown in (e) was observed to grow "flakes" months after fabrication, possibly due to internal stress in the film.

Figure 3-5: (top) Annealing oven designed to heat a sample up to 800 °C in vacuum. (bottom) Heating element, made out of tungsten wire wound on an alumina bar, and contained in the lower part of the oven.

- Expose through a chrome optical mask and wash away the exposed resist.
- Etch away the exposed metal using $NH_3OH : H_2O_2$ Ag etch, followed by HF Ti etch.
- Remove the resist with acetone.
- Anneal the finished trap at $720 - 760$ °C for 1 hour.

Gold process

- Evaporate 10 nm of Ti sticking layer, followed by 0.1 µm of Ag
- Coated the wafer with AZ–4620 photoresist.
- Expose through a chrome optical mask and wash away the exposed resist.
- Plate the exposed silver using TSG-250 gold plating solution.
- Remove the resist with acetone.
- Etch away the exposed Ag and Ti using $NH_3OH : H_2O_2$ Ag etch and HF Ti etch.

In addition to the gold and silver processes, we fabricated a nickel coated trap and superconductive traps made in NbN and Nb. The required fabrication processes will be described in a future publication.

3.1.5 Packaging

The final fabrication stage involves mounting and connecting of the chip. For surface temperature measurement and control, a 1 kΩ heating element and two RuO_2 temperature sensors, on opposite sides of the trap, are soldered to the surface of the trap. A copper or niobium spacer is placed under the trap to elevate the surface, and the entire stack is glued using epoxy (Varian, Torr Seal) in a ceramic pin grid array carrier (CPGA, Global Chip Materials IPKX0F1-8180AB). 1 nF filter capacitors (AVX GH0358102KN6N) connected to the electrodes and mounted on the CPGA reduce RF pickup and noise. Each trap electrode is wirebonded to two pads on the CPGA, which allows for debugging of possible faulty connections.

The amorphous material of the CPGA does not conduct heat well. If good thermal contact is desired, a strip of copper mesh is soldered to the trap surface and connected to the helium bath. However, the weak thermal connection allows for large temperature gradients and regulation of the surface temperature independent of the rest of the cryostat.

The finished trap is cleaned in laboratory solvents, dried at 100 °C and exposed to a UV/ozone lamp, to remove organic residue. Clean traps are transferred to the cryostat vacuum chamber within hours of cleaning.

Figure 3-6 shows some of the fabricated traps already mounted in the CPGA holder.

3.2 Cryostat

There is a number of approaches to cryogenic cooling, including bath, closed cycle and flow cryostats. The simplest is the bath cryostat, consisting of a vacuum enclosure and insulated tanks of cryogens, and it has been previously employed by the ion trapping community to

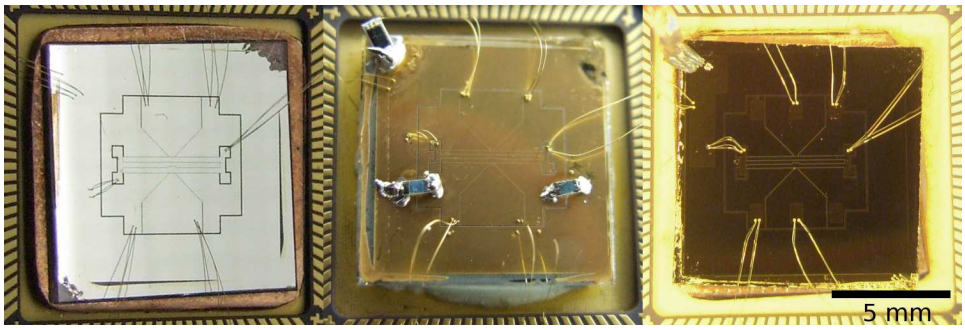

Figure 3-6: (left to right) Picture of the finished silver, gold and NbN traps. The gold trap picture shows the temperature sensing resistors (blue) and the heater resistor (black) soldered to trap surface. The NbN trap requires gold pads for wirebonding.

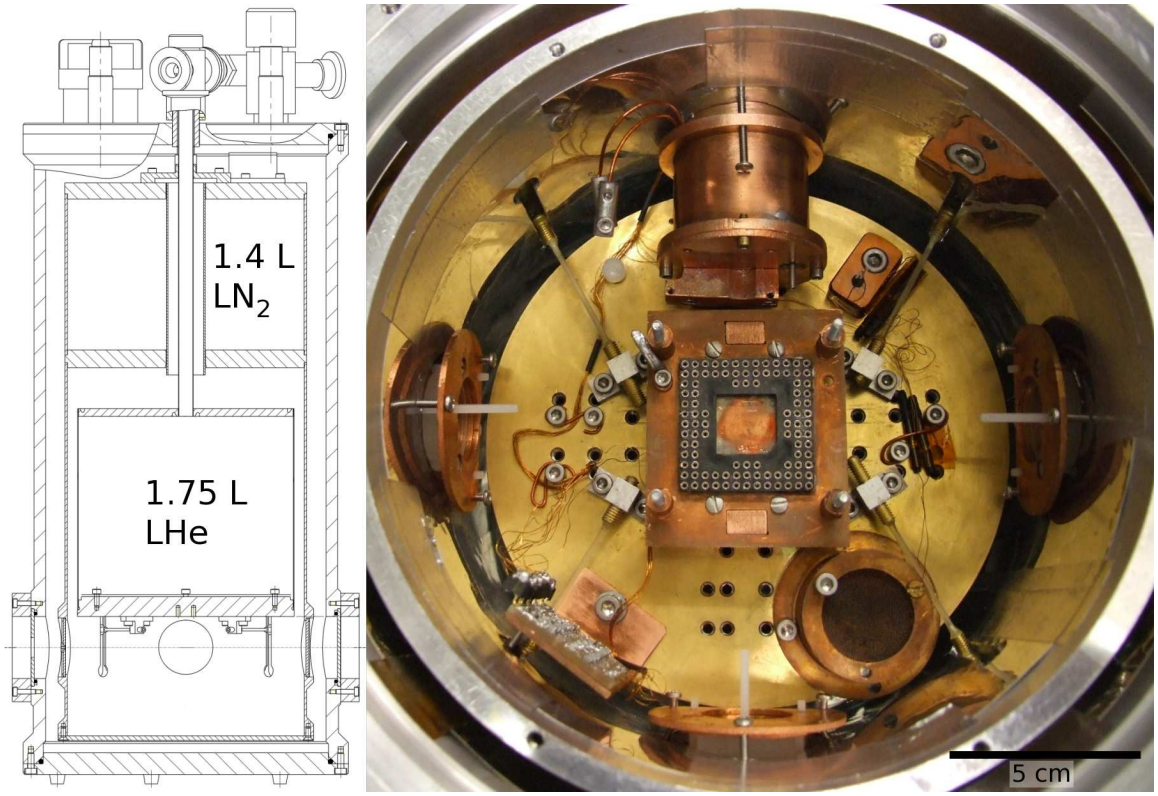

Figure 3-7: (left) Schematic of the cryostat, with liquid helium (LHe) and liquid nitrogen (LN_2) tanks labeled. The 77 K shield attached to the LN_2 tank encloses the 4 K tank and work area. (right) Picture of the work area of the cryostat, with CPGA socket (center), RF resonator (12 o'clock), activated charcoal getter (5 o'clock), laser windows (3, 6, 9 o'clock) and DC low pass filters (7 o'clock). DC connections are routed between the RF resonator and the LN_2 shield. The oven mount is attached to the front of the RF resonator.

improve the lifetime of the trapped particles [PBIW96, OWN+01] The design of the cryostat used in this experiment is depicted in Figure 3-7.

The outer shell of the cryostat is sealed with rubber o-rings, allowing the inside to be pumped to a pressure of $\approx 10^{-5}$ Torr. There are 4 symmetrically spaced, 50 mm openings on the perimeter of the shell, and a single 50 mm opening on the bottom. The bottom opening and three of the perimeter ones are used for optical access, and covered with windows (Melles-Griot 02 WBK 226). The last is used for a 55-pin feedthrough, which provides all the electrical connections to the inside.

The inside of the cryostat consists of a 1.4 L liquid nitrogen (LN_2) tank, 1.75 L liquid helium (LHe) tank and a metal shield attached to the nitrogen tank. The total heat capacity of the stored nitrogen is 0.22 MJ, while the stored helium can absorb only 4.4 kJ, reflecting its much lower density and latent heat. For this reason, the thermal load on the helium tank needs to be kept at minimum. A significant source of heat is the black body radiation, which equals approximately ≈ 45 mW/cm^2 at room temperature, but only 0.2 mW/cm^2 at 77 K. The nitrogen shield serves to absorb this radiation from the vacuum enclosure, and is covered in layers of reflective foil to further minimize the heat loads on the helium tank. The openings in the shield necessary for optical access are covered with BK7 windows, which are opaque to thermal radiation (peaked at ≈ 10 µm). The cryogen hold time is similar for both LN_2 and LHe, and equal to approximately 10 hours.

Two getters, consisting of a metal cylinder filled with activated charcoal and covered with a mesh, are mounted on the nitrogen and helium tanks, and provide large surface area for cryopumping of residual gas. The ion lifetime was measured using a chain of ions and equals to 10 h, providing an upper bound on the pressure of reactive species.

The region between the bottom of the helium tank and the nitrogen shield forms the experimental work space. The 4 K baseplate serves as a mounting surface for a temperature sensor (Lake Shore RX-103A), 2 stage low pass DC filters with cutoffs at 4 kHz, and a charcoal getter. To facilitate replacing of traps, the electrical connections are routed to a 101-pin pin grid array socket (Mill-Max 510-93-101-13-061001), which accepts the CPGA with the ion trap chip (Figure 3-8). The wiring is done with 36 AWG phosphor bronze wires, with room temperature thermal conductivity of $\frac{0.06\Delta T}{L}$ mW/K, where L is the wire length in cm. For a ≈ 100 K temperature gradient and ≈ 10 cm wire, each wire contributes 0.6 mW heat load. The thermal conductivity drops at low temperatures, and therefore the number above should be treated as an upper bound.

The cryostat is suspended in a support structure constructed out of 80/20, which allows for optical access to all four windows. Three breadboards surround the outside, providing a space to mount optics. The camera, PMT and imaging optics are mounted to a separate breadboard, attached below the cryostat. The system is constantly pumped on using a separately mounted turbo pump (Pfeiffer-Balzers TPU270), connected via a long and flexible formed steel bellows to one of the two KF16 ports at the top of the cryostat.

3.3 In-Vacuum RF Resonator

Ion traps require an oscillating voltage on the order of ≈ 200 V_{amp} at frequencies of more than 10 MHz. While such source can be easily realized, the long resistive wires necessary in a cryogenic environment are not compatible with the required low resistance and inductance. To sidestep the issue, the RF is supplied at a low voltage and a helical resonator, mounted on the nitrogen shield, is used to step up the voltage [Fis76]. The RF resonator is connected

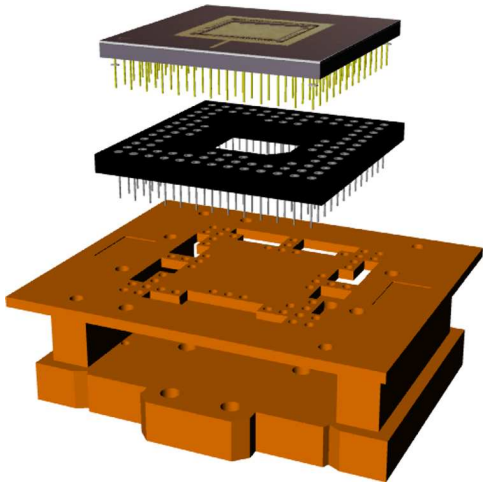

Figure 3-8: Detail of the CPGA mounting socket, with a copper support. The socket is soldered into the support to ensure good thermal contact.

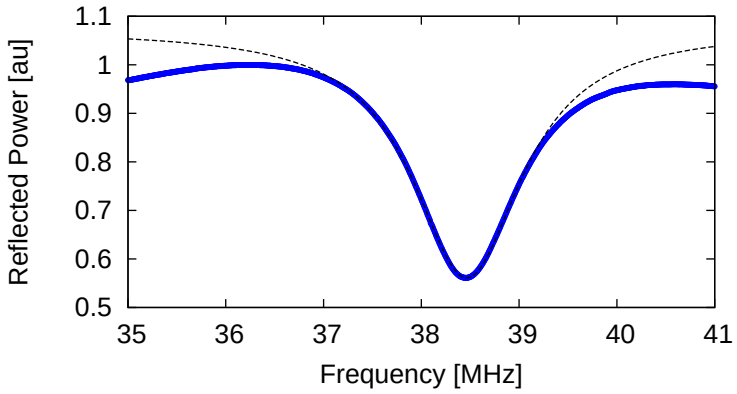

Figure 3-9: Reflected RF power from the helical resonator with a trap attached (thick line), and a fit to a Lorentzian (dashed line). The resonance width (FWHM) is 1.4 MHz, with $\approx 50\%$ of the power reflected at resonance.

to the ion trap with 25 mm of phosphor bronze wire, which is expected to have a resistance of 0.2 Ω, while contributing < 2 mW of heat load.

The resonator is made out of 22 turns of 1 mm copper wire, wound on a Teflon support structure. The resonance with a 3 pF load, similar to that posed by an ion trap, is ≈ 37 MHz with a voltage step-up form input to output of 20. The reflected power and the fit to a Lorentzian are shown in Figure 3-9. The width of the resonance gives a loaded Q factor of the resonator, $Q \approx 30$. The amplitude of the reflected power depends sensitively on the load presented by the trap, and varies from nearly zero for large traps to almost 100% in the case of a superconductive trap.

With the high in-vacuum step-up, the feedthrough wires have to be driven at around 10 V_{amp}, or approximately 1 W, to get the ≈ 200 V_{amp} at the ion trap required for trapping.

3.4 Ion Source

There is a number of established methods of generating ionized species. Three of these, including electron impact ionization of a neutral vapor, photoionization of a neutral vapor and laser ablation of a solid target are commonly used in the ion trapping community. Electron impact ionization relies on collisions between electrons and neutrals to strip an electron from the neutral. The small cross-section for this process dictates the use of a large flux of electrons to achieve good ionization efficiency. These electrons become stuck to dielectric surfaces in the work area, such as windows, generating large electric fields which affect trapping [BCL$^+$07]. In a cryogenic environment, such trapped charge does not dissipate over time, and may permanently affect the ability to trap. For this reason, only ablation and photoionization were tried in the cryostat.

A hybrid method, utilizing photoionization of an ablation plume, has been demonstrated by other groups [HGH$^+$07], providing another way of loading of cryogenic traps. This technique was used briefly; it was abandoned because the high voltages necessary to filter charged particles out of the ablation plume interfered with trapping potentials.

3.4.1 Ablation

Laser ablation of a solid target has been used to load ion traps as early as 1981 [Kni81, Kwo89]. The high powered laser pulse ejects material from the target, including neutrals, ions, molecules and electrons. It has been shown that electrons reach the trap first [HMO$^+$06], and short trap electrodes for a period of $\approx$ 10 µs. The slower moving ions reach the trap as the trapping potential recovers, and can be trapped.

The advantages of laser ablation over other loading methods include its simplicity - it requires a pulsed laser beam, but no extra components in vacuum. The ablation laser is not species specific, and a wide range of ions, including molecular ions and multiply charged ions, can be produced this way. As opposed to most other methods which may require tens of seconds to load an ion, ablation loads in few tens of µs. Such rapid loading rate my be necessary in experiments with large number of ions. Finally, the heat load of ablation pulse is negligible as compared to ionizing a neutral vapor produced by an oven.

To demonstrate loading of ions into a planar trap, a printed circuit board ion trap was used [LCL$^+$07, BCL$^+$07]. Pulsed, frequency-tripled Continuum Minilite ND:YAG laser at 355 nm served as the ablation laser. The pulse duration and energy were $\approx$ 4 ns and $\approx$ 8 mJ at full power. The ablation pulse was focused onto the target using a 200 mm lens, forming an $\approx$ 300 µm spot. The target was positioned approximately 25 mm from trap center.

The choice of target material was found to affect the efficiency of loading of the trap. Five materials were tested, including Sr metal (99% pure, Sigma-Aldrich), Sr/Al alloy (10% Sr, KB Alloys), $SrTiO_3$ single crystal (100 orientation, Sigma-Aldrich), $SrTiO_3$ powder in epoxy matrix and SrCl salt. While each of these materials produced trappable ions, the longevity of the target varied by orders of magnitude, as shown in Figure 3-10. $SrTiO_3$ was found to have the highest longevity, producing ions for $> 10^3$ pulses. Sr/Al alloy and $SrTiO_3$ powder in epoxy, however, would stop producing ions after only 200 and 10 pulses, respectively. Sr metal fell in between, but offered the most stable ion signal from pulse to pulse. The SrCl salt was found to be incompatible with ablation, as it shattered when illuminated with the pulsed laser.

Large static electric fields up to 1 kV/m, similar to those expected with electron impact ionization, were observed in the trapping region after an ablation pulse. These fields

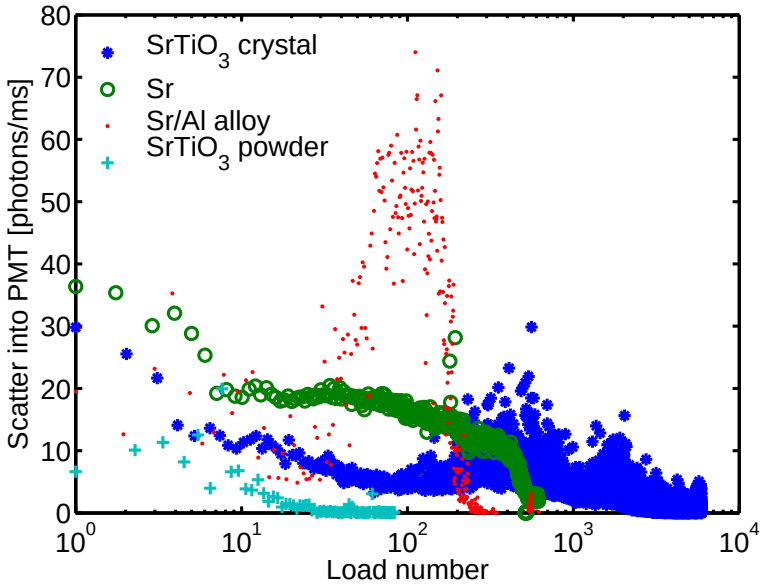

Figure 3-10: Plot of the trapped ion signal as a function of the number of ablation pulses. The ablation laser was focused to a spot size of 300 µm, with pulse energy of 8 mJ. In this set-up, a single ion scatters roughly 2.5 counts/ms at the PMT.

made loading of small, < 100 µm, traps challenging, sometimes requiring as many as 10 ablation pulses to load a single ion into the trap. These stray electric fields changed after every load attempt, requiring a subsequent characterization and cancellation. The stray fields, compounded with unstable loading rates of the method, motivated the switch to photoionization of a neutral vapor.

3.4.2 Photoionization

The large electric fields observed after electron impact and ablation loading result from the large number of charges created, all but a few of which are of no experimental use. A species specific ionization method, such as photoionization, reduces the number of ions produced, stabilizing the electric field environment [BLW+06].

Neutral Sr can be photoionized in a two stage process. The ground state, $(5s^2)^1S_0$, couples strongly to the $(5s5p)^1P_1^0$ excited state via a dipole allowed transition at 650.5035 THz ($\approx$ 460 nm), with linewidth of $\approx$ 30 MHz [MCS75]. The excited state can be ionized to the continuum with a laser at a wavelength less than 413 nm. Alternatively, very high ionization cross-section is possible by coupling to an autoionizing $(5p^2)^1D_2$ state using a 405.5 nm laser [MBK95]. The autoionizing state decays rapidly into an ion and a free electron, resulting in a very broad transition with linewidth in excess of 1 nm.

Implementation of this scheme requires two light sources at 405 nm and 460 nm, and a source of neutral Sr atoms. The first of the two lasers is implemented using a 405 nm laser diode (Photonic Products, DL-5146-152W), stabilized by feedback from an external grating in a Littrow configuration. Further stabilization is not necessary, due to the very wide linewidth of the transition. The laser power after the grating is set at 3 mW (estimated 5 mW at the diode), much below the maximum diode power of 30 mW. Losses on optical components and imperfect mode-matching into an optical fiber reduce the power at the ion

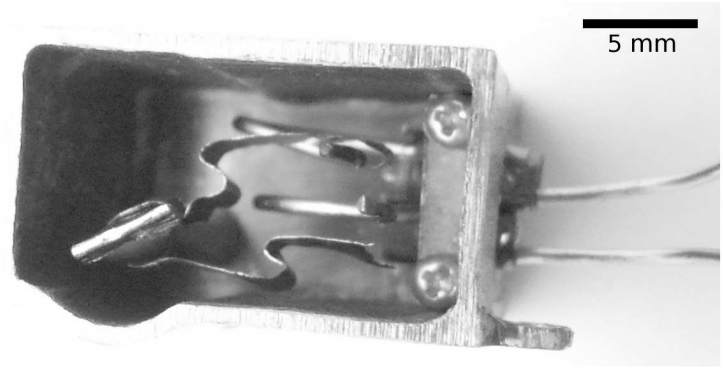

Figure 3-11: Sr oven for the cryogenic environment. Sr metal is confined in a stainless tube, shielded by copper walls from all sides. $0.002''$ stainless foil is used as a heating element, requiring ≈ 5 A to produce neutral Sr vapor.

trap to 1 mW.

Laser light at 460 nm cannot be generated so simply, due to lack of diodes emitting near that frequency. Instead, the appropriate wavelength is generated with a frequency doubled Ti:Sapphire. A 5 W laser at 532 nm (Spectra-Physics, Millennia Pro 5s DPSS) pumps a Ti:Sapphire ring laser (Coherent MBR110) generating 270 mW of 920 nm radiation. Subsequently, the light is frequency doubled using a BBO non-linear crystal in a resonant cavity (Spectra-Physics, WaveTrain CW doubler), resulting in ≈ 3 mW of 460 nm laser light. Approximately half of this light is coupled together with 405 nm into a single mode fiber and delivered to the trap. The Ti:Sapphire can only lase at the ring cavity resonances, or every 300 MHz. After doubling, the frequency can be tuned to modes spaced by 600 MHz, or within 300 MHz of any desired frequency. The atomic transition is power broadened to a similar value, negating the need for finer adjustment. The frequency of the 460 nm light is continuously monitored using a 10 MHz precise wavelength meter (HighFinesse WS-7).

The final piece of the system is a source of neutrals, usually accomplished using a resistive oven. Typical oven set-up is complicated by the necessity to reduce heat deposited to the helium tank. Sr metal is confined in a stainless tube with two $\approx$ 10mm long strips of $0.002''$ stainless foil used as a heating element (See Figure 3-11). The tube is mounted in a copper enclosure, which sinks thermal radiation generated by the heating element. The box itself is mounted to the front of the RF resonator, and heat sunk to the 77 K reservoir. Sr vapor pressure sufficient for loading requires ≈ 5 A of current to be passed through the heating element.

Photoionization was successfully used to load a number of traps, with trap depths as low as 20 meV and sizes down to 60 µm. Repeated loads would not induce a discernible change to the electric field environment of the trap, greatly improving reliability and repeatability of experimental work. However, the heat dissipated by the oven is significant. Despite the effort to shield the inside of the cryostat from the oven, the temperature sensor on the helium tank warms up to ≈ 6 K during loading. Fortunately, the long lifetime of the trapped ions make it unnecessary to run the oven more than a few times a day, which does not reduce the helium hold time perceptibly.

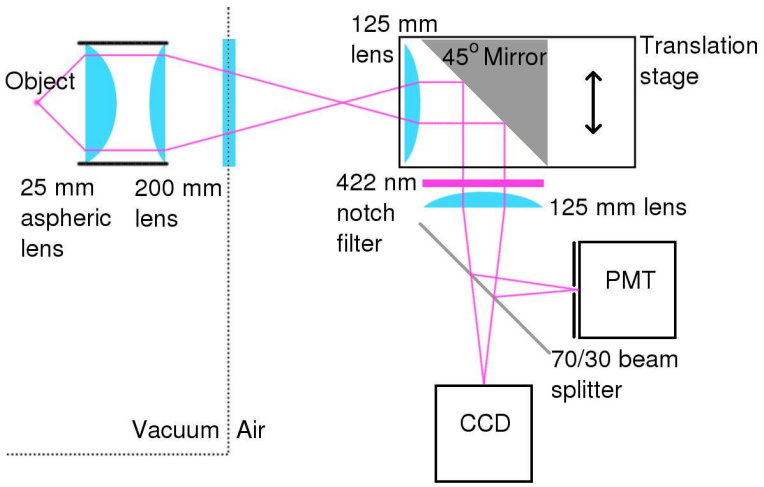

Figure 3-12: Schematic of the imaging optics. A 25 mm asphere collimates the scattered light, which is focused using a 200 mm plano-convex lens. The image is relayed using two identical 125 mm plano-convex lenses. Two 45° mirrors on translation stages (one shown) allow for alignment of the image to the CCD and PMT. A 70/30 beam splitter reflects 70% of the light towards the PMT, while allowing 30% to be imaged by the CCD.

3.5 Imaging and Scatter Detection

Discrimination of qubit states requires detection of approximately 10 photons scattered by the ion (see Section 2.5.1). The necessary integration time is inversely proportional to the efficiency of collection of the scattered light. Fast detection requires optics with a large numerical aperture and a high efficiency photon counting module.

The cryostat windows limit useful diameter of the light gathering optics to 25 mm; large numerical aperture can be achieved only by placing the lens close to the ion, inside the vacuum chamber. The ion light is collimated using a 25 mm focal length aspheric lens (Edmunds TechSpec NT49-102, AR coated), and focused using a 200 mm plano-convex singlet, as shown in Figure 3-12. The percentage of light gathered by the optics is approximately 6.5%. The focusing lens is not in principle necessary, but it simplifies alignment of the optics - the secondary image allows the vacuum and air parts of the optics to be separately tested and aligned for lowest aberration and coma.

The secondary image is refocused on a camera and a photomultiplying tube (PMT) using two matched 125 mm singlets. Two 45° mirrors mounted on translation stages in between of the singlets translate of the image of the ion in the focal plane. Appropriate mounting of the lenses to the mirrors ensures that the optics remains concentric for any position of the translation stages, which is critical to avoid coma. A notch filter (Semrock, FF01-427/10-25, $>$ 98% transmission at 422 nm) mounted in the Fourier plane blocks all light except for 422 ± 5 nm, reducing environmental scatter.

The refocused light is split on a 70/30 beam splitter and directed to a camera (30% of the light, Princeton Instruments PhotonMax512) and a photon counting PMT (70% of the light, Hamamatsu H7360-02). The expected photon counter efficiency at 400 nm is $\approx 20\%$, resulting in overall theoretical photon detection efficiency of 1%. The observed number of counts scattered from a single ion, 1.1×10^5 counts/s at high laser power, is somewhat higher than expected given the maximum scatter rate on the $S_{1/2} \leftrightarrow P_{1/2}$ transition, $\Gamma/2 \approx$

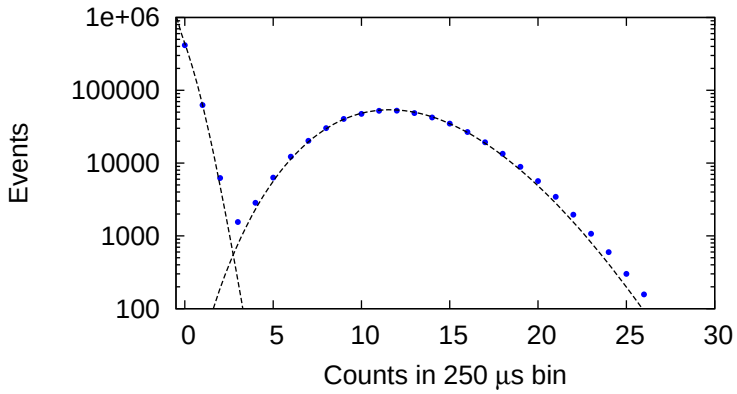

Figure 3-13: Histogram of the detected photon number in a 250 µs integration time(•) and Poisson distribution fits (dashed lines), with expected count per bin of 0.15 and 12.1. Ion is initially prepared in a random state, with a total of 958000 experimental runs. Setting the discrimination threshold at 3, the overlap between the distributions is less than 0.1%.

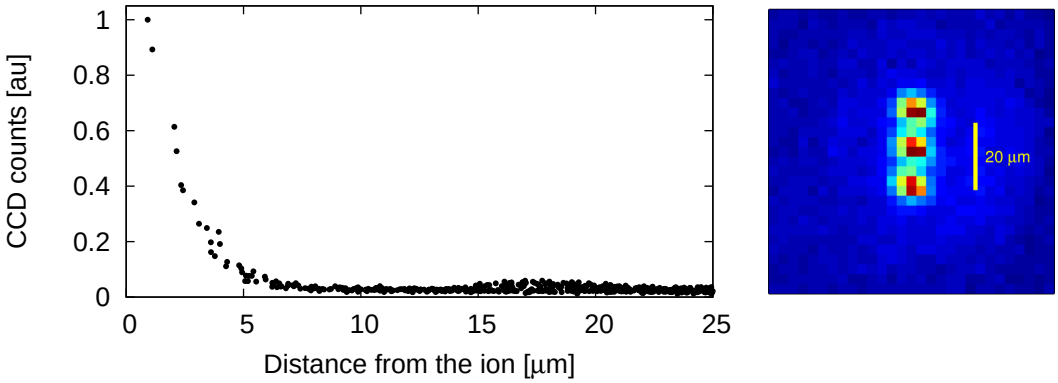

Figure 3-14: (left) Plot of the ion scatter on the camera as a function of the distance from the image center (measured at the object plane), normalized to 1 at center. The half-width of the peak is estimated to be ≈ 2 µm. The significant halo at $15 - 20$ µm is due to the spherical aberration of the optics. (right) Image of three ions trapped in the trap, demonstrating a resolved ion chain.

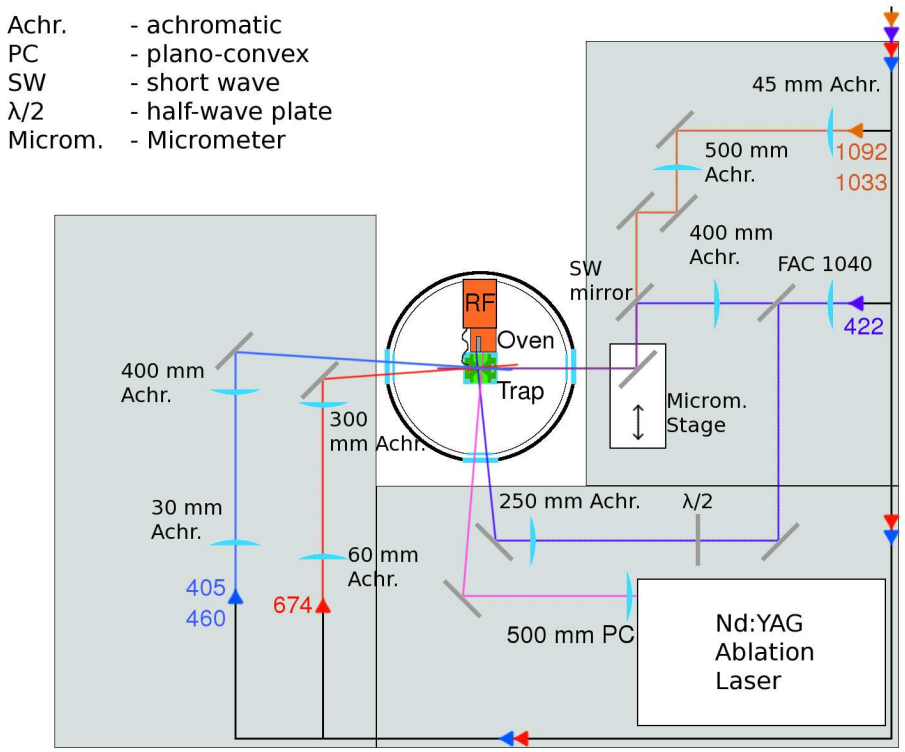

Figure 3-15: Laser delivery optics surrounding the cryostat. Six wavelengths necessary in the experiments are coupled into 4 fibers, with fiber light drawn using colored arrows. In each case, the light out of the fiber is collimated with an achromat, or a compound lens, and focused above the trap using another achromat. The 1091, 1033 and one of the 422 nm laser beams are co-aligned using a short-wave mirror (CVI, LWP-45-RP400-TP670-PW-1025), ensuring overlap. The co-aligned beams can be precisely moved using a periscope on a micrometer stage (only one of the mirrors is shown).

10^7 photons/s. The excess count rate may be due to higher than specified efficiency of the PMT. Typical histogram of counts measured in a 250 µs integration time, with Poisson distribution fits, is shown in Figure 3-13.

The resolution of the optical system is approximately 4 µm (FWHM), as shown in Figure 3-14.

3.6 Laser Delivery Optics

The cryostat and the lasers are supported by separate structures. The alignment is maintained by fiber-coupling all six frequencies into four fibers. The 1033 and 1091 nm laser, as well as the 405 and 460 nm lasers are close enough in frequency, and serve similar enough function to allow these to be fibercoupled into a single fiber. The optics used to deliver the laser beams to the ion is depicted in Figure 3-15.

Doppler cooling requires projection on all major axes of the trap, and therefore the 422 nm laser is split into two orthogonal paths, intersecting at the ion position. Sideband cooling and quantum operations utilize only a single vibrational mode (along $\hat{y}$ direction, see Figure 3-1), and only require a laser beam along that mode. The two IR lasers, as well

as the photoionization beams can come from any direction. For convenience, the IR beams are co-aligned with the 422 nm beam before steering mirrors, to ensure overlap when the beam is scanned during initial alignment. A periscope mounted on two micrometer stages translates the coaligned beams with micrometer precision and repeatability, allowing for precise alignment to the trap center.

Efficient measurement requires high ratio of photons scattered from the ions to background photons. The notch filter in front of the measurement instruments blocks all light except for the 422 nm laser scatter, reducing the problem to minimizing the scatter from that beam. The small ion-surface distance requires focusing of the light beam to < 30 µm to avoid scattering on the trap surface. Aberrations have to be avoided, as a large halo around the laser spot may significantly contribute to the scatter. The aberrations are mostly caused by the collimating optics in front of the fiber tip, due to the large numerical aperture of the fiber output. Standard achromatic and plano-convex lenses did not perform acceptably, but a large numerical aperture compound lens (Thorlabs, FAC 1040) was found to collimate the fiber output without appreciable distortion.

Chapter 4

Coherent Control System

There are two general kinds of metastable states used as qubits in trapped ion quantum computing. The "hyperfine" qubits use two hyperfine ground states of the ion. Typical transition frequencies between such states are on the order of 1 GHz, and can be synthesized using off-the-shelf components with high stability and reliability. Unfortunately, the hyperfine structure of atomic states complicates ion cooling and readout.

The other kind of qubits, called "optical" qubits, uses the ground and excited electronic state of an ion with, usually, zero nuclear spin. The simple level structure allows for use of fewer laser frequencies for cooling and detection, at the cost of very high qubit transition frequency. Typical resonant frequencies of an optical qubits are on the order of 500 THz, and have to be excited with laser fields.

The challenge of coherent control of atoms with light fields stems from the weakness of the interaction. The natural linewidth of a metastable state is typically on the order of 1 Hz, and the Rabi flops between the states can be performed at O(1 MHz) with reasonable amount of laser power (10 mW). To ensure that errors due to phase noise do not interfere with the gates, the laser frequency has to be stabilized to a fraction of the Rabi frequency, preferably to the natural transition linewidth. Such stability equals to 1 part in 10^9 to perform a single Rabi flop, and 1 part in 10^{15} to achieve coherence limited by ion state. Steps taken to approach this level of stability constitute the bulk of this chapter.

Section 4.1 starts by discussing the laser design, implemented using laser diodes prestabilized by optical feedback from an external medium-finesse cavity. The stability and spectral purity of the lasers is sufficient for addressing the dipole transitions. The qubit laser requires further stabilization, accomplished by locking to an ultra-high finesse cavity and described in Section 4.2. Cavity lock, temperature stabilization loop and acoustic noise characteristics are presented. Pulse sequences, necessary to perform qubit operations as described in Chapter 2, are generated using a field programmable gate array chip and direct digital synthesis boards. Finally, in Section 4.4, the coherence of the entire system is characterized using Ramsey spectroscopy and spin-echo revival.

4.1 Monolithic Laser System

Semiconductor lasers provide a convenient source of laser light thanks to their compactness and reliability. A typical extended cavity diode laser (ECDL) set-up, however, has laser linewidth of approximately 1 MHz, insufficient for quantum computation experiments [RWE$^+$95, LLT$^+$06]. Several techniques have been applied to improve the stability,

including negative electronic feedback via current injection [SNY85, OK85], optical feedback [HMJ+90, DHD87], or a combination of the above [SO90].

These schemes, however, do not filter out the large fluorescent background extending by many nanometers from the diode center line, which can pump the sample to a dark state [TMU+01] (though some similar experiments were not affected [HUW00]), or reduce the lifetime of metastable states [BDL+00]. Because of the small emitter area of single-mode diodes, such fluorescence is well collimated and cannot be spatially filtered. An additional step, using a grating and a pinhole [BDL+00, LHW+03], or an interferometric filter [TMU+01] is usually necessary.

The laser design described in this thesis utilizes a single, medium-finesse optical cavity, which provides both the required spectral filtering and the optical feedback used to narrow the linewidth of the laser.

4.1.1 Wavelength Selectivity and Linewidth

Bare Diode

The lasing wavelength of a bare semiconductor diode laser is determined by two factors - the gain profile of the medium and the laser cavity resonances. Typically, the diode cavity is $d \approx 1$ mm long, with an index of refraction $n \approx 3$, resulting in cavity mode spacing (free spectral range, FSR) of,

$$\mathrm{FSR}_{LD} = \frac{c}{2dn} \approx 50 \text{ GHz} \tag{4.1}$$

The cavity finesse is determined by the facet reflectivity. Usually, one facet is coated for high reflectivity, $R_{d,1} \approx 1$, while the other is left uncoated, reflecting $R_{d,2} \approx \left(\frac{n-1}{n+1}\right)^2 \approx 20\%$ of the light. The corresponding cavity finesse is

$$\mathcal{F} = \frac{\pi \left(R_{d,1} R_{d,2}\right)^{\frac{1}{4}}}{1 - \sqrt{R_{d,1} R_{d,2}}} \approx 4 \tag{4.2}$$

The gain profile of a laser diode extends for several nm from the maximum, spanning hundreds of cavity modes. Such weak mode selectivity can result in lasing at a number of frequencies simultaneously, so-called "multimode" operation [Sie86].

Laser diode emission is characterized by a very large natural linewidth. The fundamental limit on the linewidth is due to Schawlow-Townes [ST58, GMS91], and for a laser at frequency ω_L can be expressed as

$$\delta f_{st} = \frac{P_2}{P_2 - P_1} \left(\frac{\hbar \omega_L}{2\pi P_{out}}\right) \gamma_c^2 \tag{4.3}$$

$$\gamma_c \equiv -\left(\frac{c}{2d}\right) \log\left(R_{d,1} R_{d,2}\right) \tag{4.4}$$

where P_{out} is the output power, and P_1, P_2 are the steady state populations of the ground and excited states. The short, low finesse, laser cavity results in a very high cavity photon decay rate, γ_c, which broadens the lasing line. Evaluating this expression at $P_{out} = 1$ mW

and $\omega_L = 400$ THz,

$$\delta f_{st} = 2 \text{ MHz} \tag{4.5}$$
$$\gamma_c = 200 \text{ GHz} \tag{4.6}$$

The actual linewidth exceeds this limit by an order of magnitude, reaching tens of MHz, as explained by Petermann [Pet79] and Henry [Hen82].

Adjustment of the diode gain profile and cavity length can be performed by tuning the current and temperature settings, with sensitivities on the order of 0.1 GHz/mK and 1 GHz/mA. The gain profile moves faster than the cavity mode frequencies, resulting in the laser hopping between different cavity modes to track the peak of the gain profile. Tuning to an arbitrary frequency is not in general possible.

ECDL

The first step in stabilizing the lasing action involves placing a diffraction grating in front of the diode, directing the first order reflection back into the diode (Littrow configuration), and forming the so-called "external cavity diode laser" (ECDL). The grating serves a dual purpose. First, by creating a much longer cavity, on the order of 3 cm, the γ_c in Equation 4.3 is decreased, reducing the Schawlow-Townes limit. Exact calculations are performed by Henry [Hen86] and Tromborg et al. [TOPS87], and to lowest order the linewidth is described by

$$\delta f = \left(\frac{\tau_d}{\tau_e + \tau_d} \right)^2 \delta f_{st} \tag{4.7}$$

where τ_d, τ_e are the times a photon spends in the diode and external grating cavities, respectively. Experimentally, the resulting linewidth is on the order of 1 MHz [LLT+06, RWE+95].

Second, the wavelength dependent reflectivity of the grating improves the frequency selectivity of the laser. For a grating at incident angle θ to the laser beam, with line spacing of a, and spot size on the grating b, the reflected power coupled back to the laser diode is [TOPS87]

$$R_g(\omega_L) = R_{g,0} e^{-\left(\frac{N_{eff}}{4}\right)^2 (\omega_L \rho - 2\pi)^2} \tag{4.8}$$
$$\rho \equiv \frac{2a \cos\theta}{c}$$
$$N_{eff} \equiv \frac{2b}{a \sin\theta}$$

where N_{eff} is the illuminated number of grating lines, and $R_{g,0}$ is the peak reflectivity. The center of the gain is at $\omega_{L,0} = 2\pi/\rho$, with $1/e$ half-width of

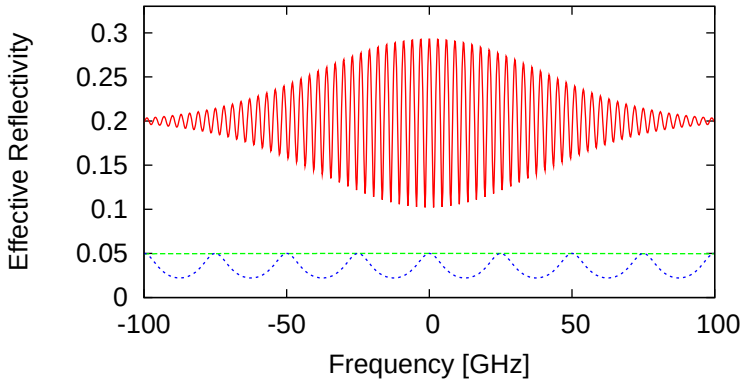

Figure 4-1: (continuous red line) Effective reflectivity of the diode laser facet modified by external grating, assuming $R_{d,2} = 0.2$, $R_{g,0} = 0.1$, and grating to diode distance of 5 cm. For frequency scale reference, the diode gain (dashed green line) and diode cavity modes (dashed blue line) are plotted as well.

$$\begin{aligned} \Delta\omega_L &= \frac{4}{N_{eff}}\frac{1}{\rho} \\ &= \frac{4}{2\pi N_{eff}}\omega_{L,0} \end{aligned} \tag{4.9}$$

For a typical grating with 2000 lines/mm, at angle $\theta \approx 45°$, and laser spot size on the grating of $b \approx 1$ mm,

$$\begin{aligned} N_{eff} &= 5.6 \times 10^3 \\ \Delta\omega_L &= 10^{-4}\omega_{L,0} \end{aligned} \tag{4.10}$$

The effective reflectivity of the facet equals

$$R_{eff} = \frac{R_{d,2} + R_g(\omega_L)e^{-\imath\omega_L\tau_e}}{1 + R_{d,2}R_g(\omega_L)e^{-\imath\omega_L\tau_e}} \tag{4.11}$$

and is plotted in Figure 4-1 [TOPS87]. While the diode gain profile provides frequency selectivity on the 1% level, the grating enhances the gain only for a 10^{-4} fraction of the center frequency. At visible frequencies of around 400 THz, the grating will enhance the gain in a 40 GHz window, which is smaller than the mode spacing of the diode laser cavity, thus forcing the diode to lase in a single diode cavity mode. The comparable reflectivities of the grating and diode facet allow the grating to select any diode mode within $\approx \pm 1$ nm of diode gain center.

The fast oscillation visible in Figure 4-1 are due to multiple reflections between the grating and the diode facet. Using Equation 4.1 again, the FSR of this cavity is

$$\text{FSR}_{GRT} = \frac{c}{2dn} \approx 5 \text{ GHz} \tag{4.12}$$

By tuning the grating distance, the resonance can be continuously tuned within that window. For larger extensions, the lasing mode will hop between grating cavity modes, requiring an adjustment of the grating angle or the diode cavity modes. The exact lasing frequency is determined by the total gain, which depends on the diode gain peak and grating angle, and the requirement that the round-trip length is an integer multiple of wavelength.

ECDL with Cavity Feedback

Linewidth reduction much below 1 MHz could be accomplished by placing the grating far away from the diode, at the cost of the stability of the alignment of optical components. The same goal can be achieved by adding an medium-finesse cavity to the system, and feeding the light coupled into the cavity back to the diode. The linewidth of such systems has been theoretically described by Breant et al. [LCB89], and shown to be equal to

$$\delta f = \frac{\beta \tau_d^2}{\tau_{cav}^2} \delta f_{st} \tag{4.13}$$

where τ_d and τ_{cav} are the resonator storage times in the diode and the cavity, respectively, and β is the attenuation of the feedback from the cavity. The result is similar to that obtained in case of a reflection from a grating (cf. Equation 4.7). The storage time in the cavity, however, can be made orders of magnitude longer than the storage times possible with the grating, due to multiple round trips between cavity mirror surfaces. Therefore, even with a modest feedback, the linewidth can be significantly narrowed, to a few kHz level [OS92, LCB89, DHD87].

4.1.2 Design and Construction

The design of a laser incorporating the three discussed feedback elements is shown in Figure 4-2. In order to provide both the optical feedback and spectral filtering, the design uses a triangular running-wave cavity to provide feedback, instead of the usual confocal cavity. This set-up was implemented at 422, 674, 1033 and 1091 nm, to address all necessary Sr^+ transitions.

The ECDL is quite similar to that described in Reference [RWE+95], and will not be described in detail. Gratings reflectivities are $\approx 20\%$, with the grating angle $\approx 40^\circ$ (3600 lines/mm at 422 nm, 1800 at 674 nm, 1200 at 1033 and 1091 nm). The ECDL laser light is typically elliptical, and requires either an anamorphic prism pair or a pair of cylindrical lenses. The latter was used, to avoid shifting the beam horizontally. Two spherical lenses set the beam size and waist in between the tilted cavity mirrors, for proper mode-matching.

The cavity consists of two 99% reflectivity mirrors at a 42° angle to the cavity axis and a 200 mm concave high reflectivity (HR) mirror. The HR mirror is mounted on a single layer piezo to allow for frequency tuning. Non-confocal arrangement of the cavity separates the resonant frequency for the TEM_{00} mode from higher order modes, allowing us to remove them from the laser beam. The coupling into the cavity is $\approx 60\%$. Significant scatter on the cavity mirrors lowers the cavity efficiency to $\approx 75\%$, resulting in $\approx 45\%$ of the incident light coupling through the cavity. A fraction of the light leaks through the HR mirror, allowing us to measure the power in the cavity. A glass plate reflects 4% of transmitted light, exciting the reverse going mode which provides optical feedback. Slight misalignment

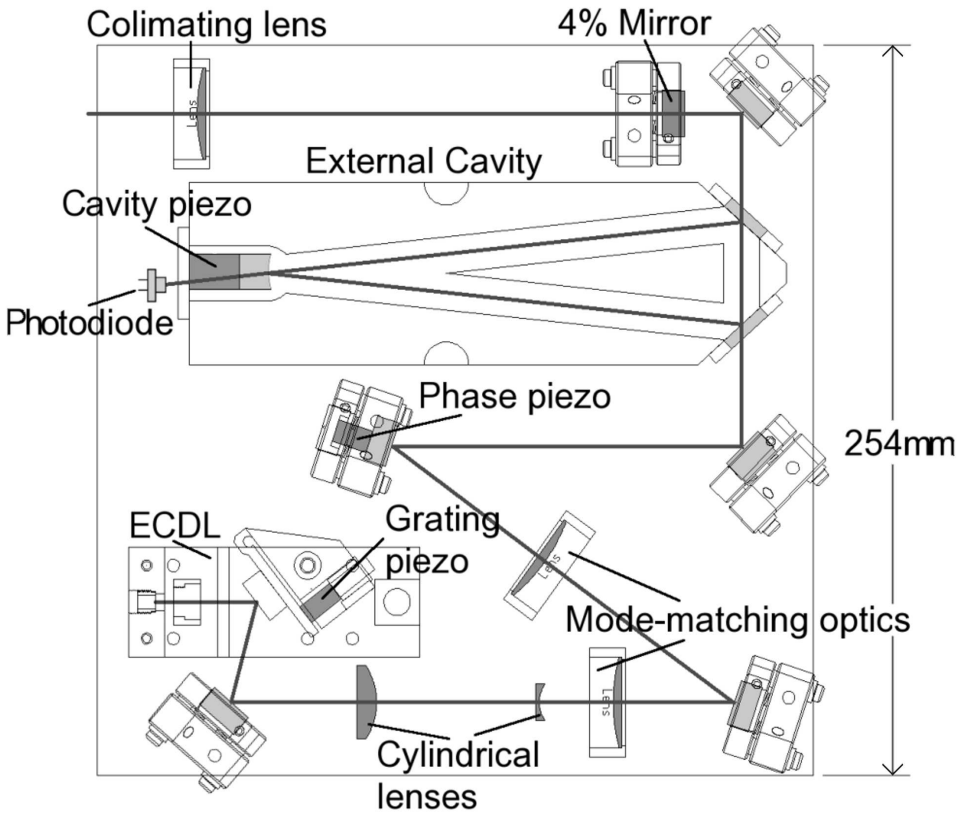

Figure 4-2: Schematic of the laser set-up with superimposed laser beam. The laser light, after reflecting of the grating, is shaped with cylindrical and spherical lenses to match the cavity. 4% of the light coupled through the cavity is reflected of a glass plate, and sent back to the diode, providing optical feedback. The attenuation can be regulated by adjusting the angle of the plate.

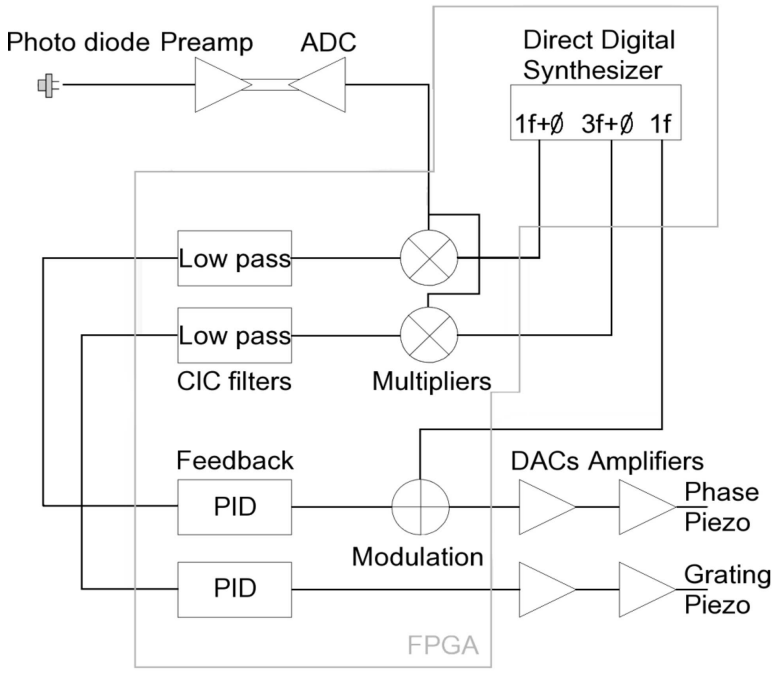

Figure 4-3: Schematic of the digital lock system. The grey box denotes components implemented digitally using a field-programmable gate array.

of this plate allows us to adjust the coupling strength to that mode. A mirror mounted on a piezoelectric transducer (phase piezo) controls the distance to the cavity, and the phase of the optical feedback.

The ECDL and optics are mounted on a custom-machined and temperature stabilized aluminum plate. For increased stability, the entire set-up is placed in a vacuum-tight box and pumped down to $< 10^{-5}$ Torr. The vacuum environment improves pressure and temperature stability, but makes laser alignment significantly harder. In particular, the grating angle is wavelength selective, rather than frequency selective, which is important to keep in mind when adjusting the horizontal grating angle. Based on the drift of the cavity frequency, we estimate the temperature stability of the baseplate to be better than 1 mK over an hour.

4.1.3 Cavity Lock

Optical feedback requires stabilization of both the phase of the returning light and the free-running ECDL frequency. While the phase can be locked by maximizing the power in the cavity using a simple lock-in technique, locking the ECDL frequency requires a measurement of the asymmetry of the cavity power peak [OS92, LCB89, Hay02, TKOU06]. For a phase piezo dither at frequency f, such asymmetry shows up as a $3f$ peak in the spectrum of the cavity power, and can be measured with a lock-in at that frequency. Due to the relative complexity of the locking method, the input is digitized and fed to a field programmable gate array for processing. A schematic of the lock loop is presented in Figure 4-3.

A 600 kHz, 18bit Analog-to-Digital converter (Texas Instruments ADS8382) digitizes the ≈ 3 V photodiode signal with a 100 μV_{pp} precision. This signal is mixed with 10 kHz and

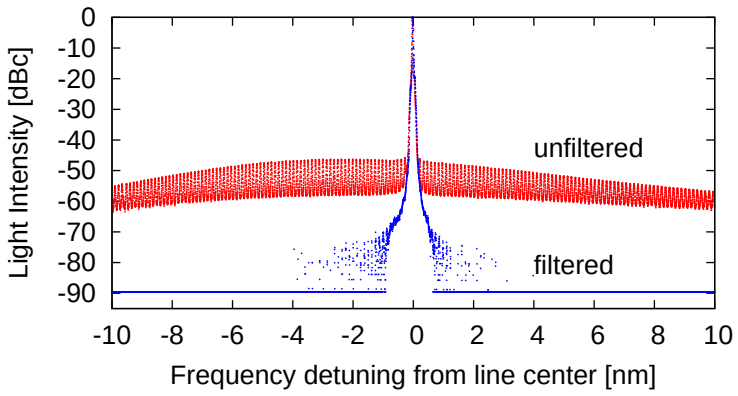

Figure 4-4: Spectrum of the 674 nm laser at the ECDL (top trace) and after the filter cavity (bottom trace). −90 dBc indicates null intensity.

30 kHz variable phase sine waves from a direct digital synthesizer to pick up the respective frequency components. Two low pass, three stage Cascaded-Integrator-Comb filters with cutoff at 100 Hz remove high frequency noise. The filtered signal is fed to Proportional-Integral-Derivative (PID) circuits, the 10 kHz component controlling the phase and the 30 kHz component controlling the free-running ECDL frequency via the grating piezo. The total gain was set to 0.1 (P) and 10 s^{-1} (I) for the 10 kHz circuit, and 10 (P) and 1000 s^{-1} (I) for the 30 kHz one. As the last step, a 10 kHz modulation is added to the phase output. The digital output is converted to analog using two low noise, 100 kHz, 16-bit Digital-to-Analog converters (Linear Technology LTC1592).

The lock is stable with 0.2% modulation of the cavity power ($\approx$ 300 kHz frequency modulation) for more than 10 hours at a time. The passive stability of the system allows the lock to be turned off for $\approx$ 10 minutes before a 1% change in output amplitude is observed. Response time of the lock circuit is 100 Hz and 1 Hz for the phase and grating locks, respectively, allowing for 25 MHz/s scan rate. The slow grating response is caused by very weak third-harmonic signal at the low modulation levels we used. The maximum scan range is 1 GHz, limited by cavity piezo travel range.

4.1.4 Spectral Filtering

The fluorescent background of the 674 nm laser diode (Roithner RLT6715MG) was measured using a grating spectrum analyzer connected via a single mode APC fiber. The observed background was reduced by the filter cavity to below the analyzer's sensitivity of −90 dBc from the initial value of −50 dBc at the ECDL (see Fig. 4-4).

The suppression of coherent background light equals to the average transmission through the cavity, equal $\approx$ 1%. However, if the coherence time is shorter than the cavity ring-down time, the suppression equals to the transmissivity through the two angled mirrors, or 10^{-4}. The strong suppression observed indicates that the fluorescent light has very short coherence times.

The coherent part of the residual background is expected to have a periodicity equal to that of the cavity, or $\approx$ 1 GHz. Because the usual linewidths of strong atomic transitions, which could be affected by this background, have $\approx$ 10 MHz width, the chance of a residual background peak aligning with a parasitic transition is $\approx$ 1%.

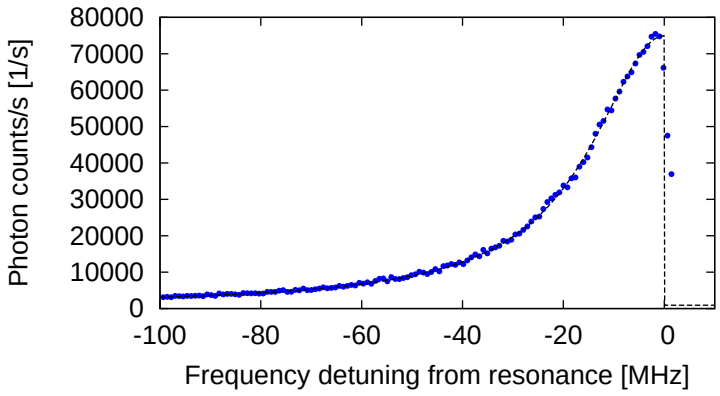

Figure 4-5: Spectrum of the $S_{1/2} \leftrightarrow P_{1/2}$ transition of Sr^+ (blue •) and a fit to a half-Lorentzian curve (dashed line). The FWHM of the fit is 35 MHz, indicating saturation parameter $s = 2$.

Sufficient purity of the 422 nm laser was further verified by Doppler cooling a single Sr^+ ion trapped in a linear Paul trap identical to that described in Reference [FNTU05]. In Reference [TMU+01] it was observed that the broad fluorescent background from a violet laser diode prevented Doppler cooling by shelving the ion to a metastable D state via the $P_{3/2}$ state. Figure 4-5 shows a clean Lorentzian lineshape with no shelving transitions, demonstrating the purity of the laser spectrum.

4.1.5 Laser Linewidth

The linewidth and frequency stability of the 674 nm laser was measured using electron shelving to a metastable $D_{5/2}$ state, with a natural width of 2 Hz [WIBH87]. Ten Zeeman components of the quadrupole-allowed $S_{1/2} \leftrightarrow D_{5/2}$ line and the secular motion sidebands of each component were observed.

The observed relative position of the laser and transition frequencies remained within ± 1 MHz of its initial value over a period of 3.5 hours. Based on the width of the peaks, we put an upper bound on the 674 nm laser linewidth at 30 kHz for a 30 s scan acquisition time (Fig. 4-6). The likely cause of such a broad line is residual acoustic vibrations of the filter cavity; the AC magnetic shifts should be negligible at this level [LGRS04]. The Allan deviation at 60 s averaging time was 1.3×10^{-10}. Given the similar construction of the other lasers, the respective linewidths and drifts should be similar.

4.2 Qubit Laser Stabilization

The residual linewidth of the cavity-stabilized laser has a large component at low frequencies, which can be eliminated by further locking to an ultra-high finesse cavity. Such systems are capable of sub-1 Hz linewidths, a significant improvement over the system in Section 4.1 [SMHS06, LHN+07, AMK+]. The main limitations to stability of such lock are the vibrations and the thermal fluctuations of the cavity material. The latter can be reduced using vertical mounting of the cavity at its center of mass, described in Reference [LHN+07]. The former requires careful thermal isolation and accurate temperature stabilization feedback loop.

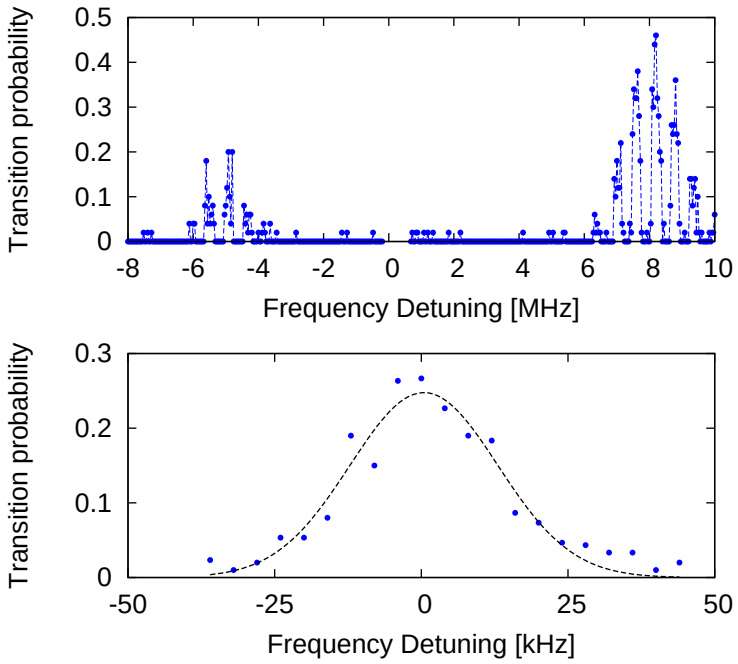

Figure 4-6: (Top) Shelving probability spectrum for the two lowest frequency Zeeman components of the $S_{1/2} \leftrightarrow D_{5/2}$ line, $m = -\frac{1}{2} \leftrightarrow m = -\frac{5}{2}$ and $m = \frac{1}{2} \leftrightarrow m = -\frac{3}{2}$. The splitting indicates a magnetic field of 9 mT. Each peak is further split by the 600 kHz secular motion of the ion in the trap. (Bottom) Detailed scan across the central line of the $m = -\frac{1}{2} \leftrightarrow m = -\frac{5}{2}$ line. The Gaussian fit to the spectrum has a 30 kHz FWHM. The lock circuit was turned off during this scan to avoid line broadening by the phase piezo dither.

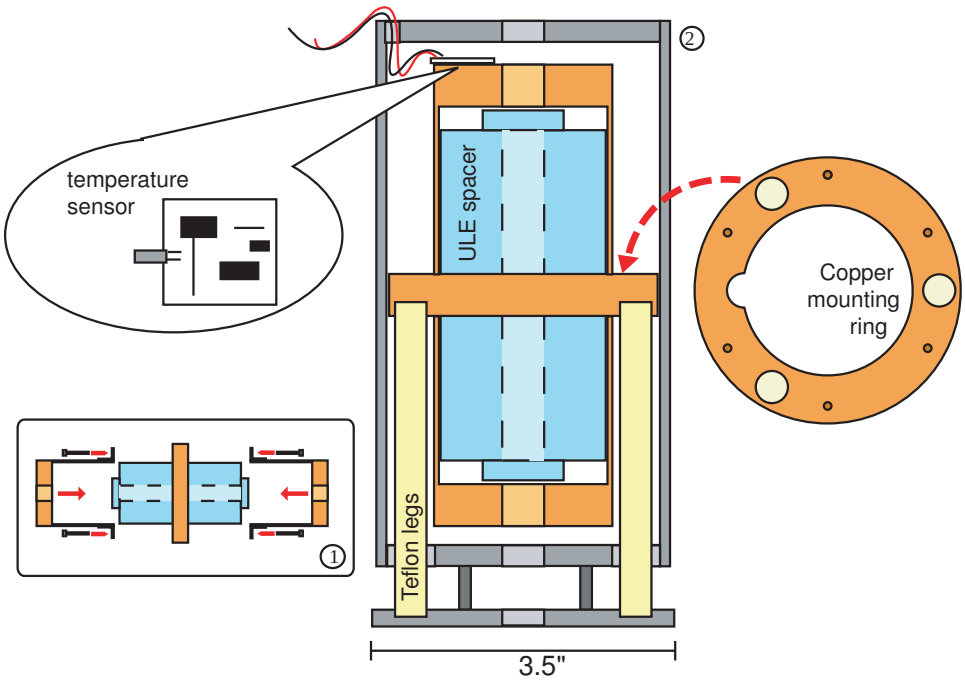

Figure 4-7: Schematic of the mechanical mount. The cavity is housed in two nested metal cans, providing a uniform temperature environment, and mounted vertically on three Teflon supports. The assembly is attached to a con-flat flange and pumped to high vacuum with an ion pump.

4.2.1 ULE Cavity

The cavity is made out of a single, 10 cm long, cylindrical piece of ULE glass, with optically contacted mirrors with transmissivity of 2.3×10^{-6} (AT Films, CO). A copper ring is attached to the midpoint of the cylinder, providing a mounting point (see Figure 4-7). Three hollow Teflon rods attach to the ring and the wall of the UHV enclosure, providing a thermally insulating and vibrationally soft support. A thin copper can encloses the entire cavity and provides a uniform temperature environment for the glass. A temperature sensing board, further discussed in Section 4.2.3, is attached to the top surface of the can. Heater wire, wrapped on an aluminum can surrounding the copper can, allows the cavity to be heated up to 10 °C above room temperature via black body radiation. Pressure fluctuations are removed by pumping the entire assembly to 10^{-7} Torr using an ion pump.

The finesse and linewidth of the cavity can be characterized by measuring the decay time of photons in the cavity. The time dependence of the laser power in the cavity after blocking the incoming beam is shown in Figure 4-8. Based on the photon lifetime $\tau = 75$ µs, the finesse is

$$\mathcal{F} = \frac{2\pi c\tau}{2L} = 700,000 \tag{4.14}$$

where $L = 10$ cm is the cavity length. The experimental mirror reflectivity equals $R = 1 - 4.5 \times 10^{-6}$ ($\frac{\pi\sqrt{R}}{1-R} = \mathcal{F}$), and places an upper bound on losses of 2.2×10^{-6}.

The vacuum chamber is mounted in a wooden box laid with acoustically and thermally insulating material. The box itself sits on 75 mm tall sorbothane supports, which eliminate

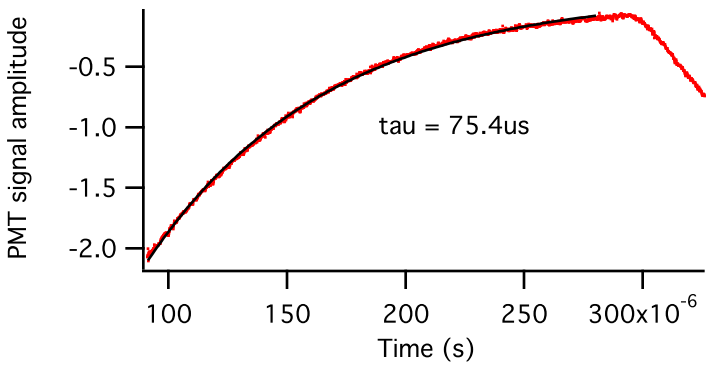

Figure 4-8: Observed transmission through the cavity, as measured on a photomultiplier tube (more negative values indicate higher photon flux). At around 80 µs, the laser light incident at the cavity was blocked. The photon flux decayed exponentially with time constant equal to 75 ± 1µs, indicating finesse of 700,000.

direct vibration coupling from the floor. Despite these precautions, the acoustic noise, coupling through the walls or supports of the box, is believed to be the dominant source of noise in the system.

4.2.2 Feedback Loop

The feedback loop constructed to lock the laser to the cavity is shown in Figure 4-9. The diode laser is isolated from possible external feedback using an optical isolator, and frequency shifted by a double pass, cat's eye configured AOM. Part of the shifted beam (300 µW) is tapped off and coupled into a single mode fiber leading to the ULE cavity box. The error signal is derived using the Pound-Drewer-Hall method, by modulating the laser at 10.24 MHz, and measuring the interference of the sidebands with the light coupled into the cavity. The photodiode signal is demodulated, low-passed and fed into a proportional-integral (PI) feedback controller (Precision Photonics LB1005). The controller's output drives a voltage controlled oscillator (VCO, Crystek CVCO55CL-0184-01909), setting the frequency shift of the laser and closing the feedback loop.

The loop bandwidth was measured to be 500 kHz, limited mostly by the response time of the AOM and the PI controller. The PDH error signal, scaled to frequency deviation from the cavity, is shown in Figure 4-10. The deviation of the laser from cavity resonance remains mostly below 0.1 Hz^2/Hz over the entire spectrum, indicating linewidth of 0.3 Hz. The cavity resonance, however, is not as stable. Vibration analysis performed by measuring frequency deviation versus acoustic noise, and the ambient acoustic noise is also plotted on the same figure. The vibrations of the cavity broaden the laser linewidth to more than 100 Hz.

4.2.3 Temperature Stabilization

The ULE glass used for the cavity has a zero thermal expansion point at around $5 - 10$ °C [Win06]. The temperature control system employed is designed to work above ambient temperature, where the sensitivity of the cavity to temperature drifts is on the order of 30 MHz/K. To obtain sub-10 kHz stability, the temperature control must be precise to

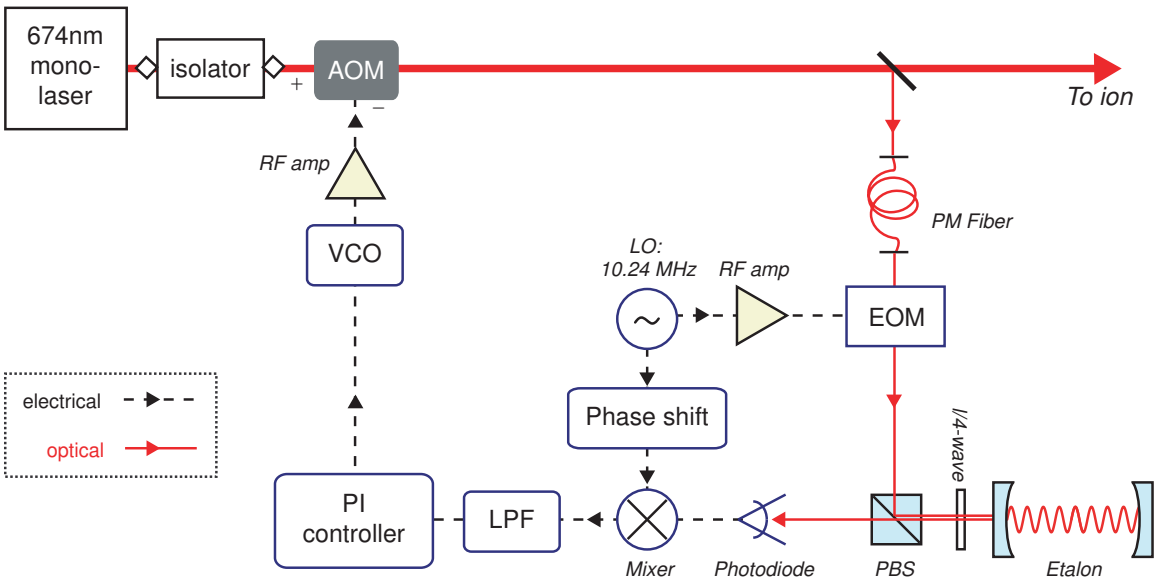

Figure 4-9: Schematic of the lock system employed to lock the laser to the cavity. Pound-Drewer-Hall scheme is used to derive an error signal, which is fed to a PI feedback controller. The PI output adjusts the VCO driving a double pass AOM, locking the laser to the cavity. The bandwidth of the loop is 500 kHz, limited by the response time of the AOM and the PI controller.

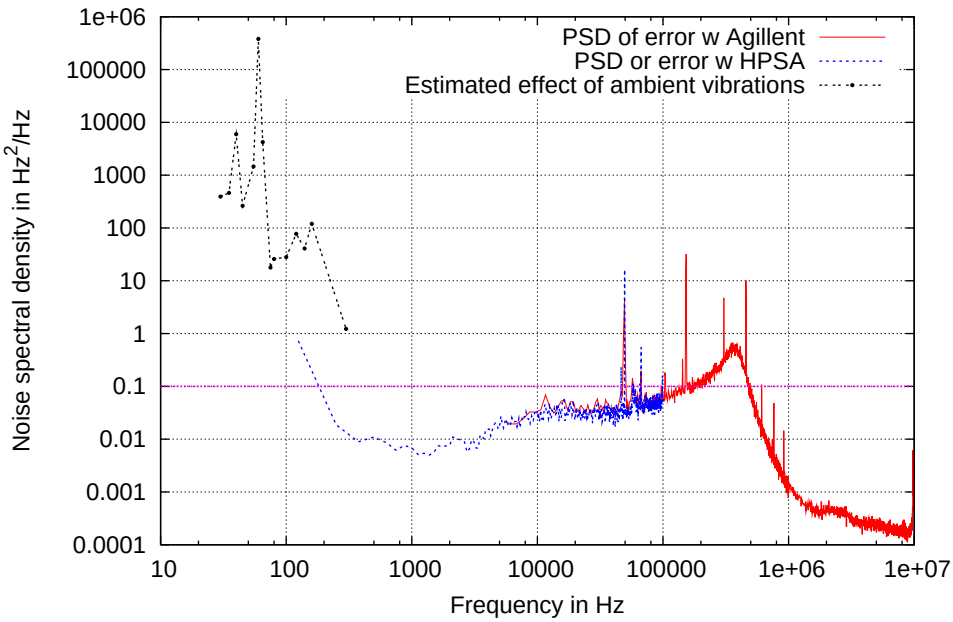

Figure 4-10: The power noise density of the PDH error measured using two spectrum analyzers (blue - HP3562A, red - Agilent E4407B), and converted to frequency units using the measured error signal sensitivity value of 0.12 mV/Hz. The noise remains mostly below the 0.1 Hz^2/Hz line (pink), which would correspond to a 0.3 Hz noise level. Also plotted is the expected fluctuation of the cavity line due to acoustic noise, which dominates the noise due to imperfect lock to the cavity.

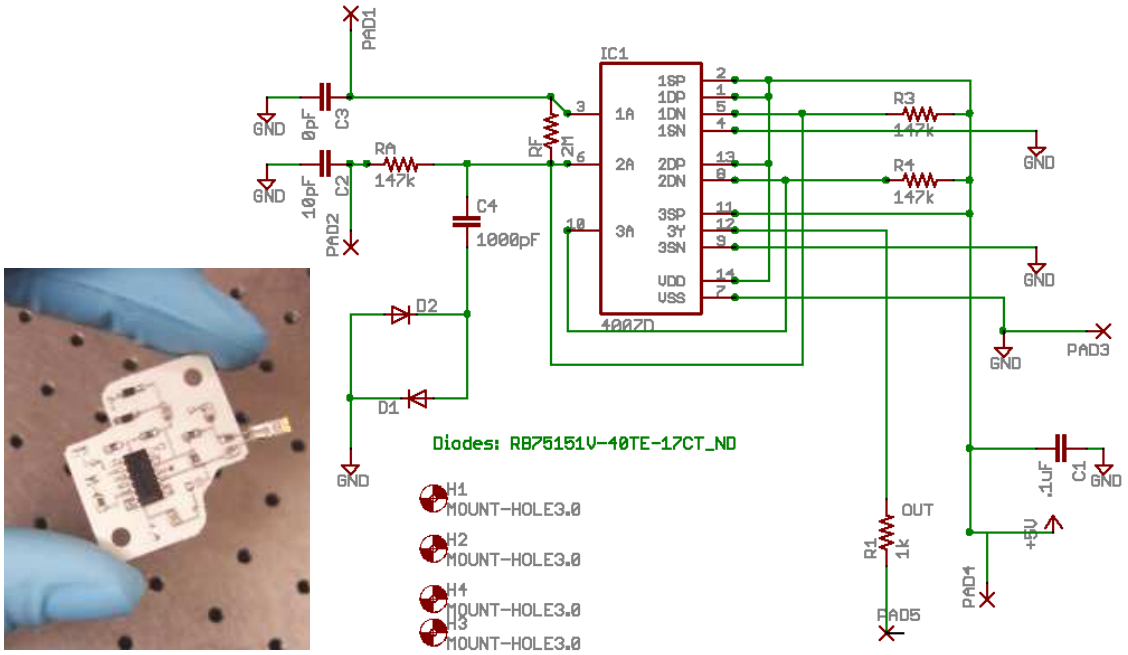

Figure 4-11: Schematic of the Pierce oscillator, based on a CD4007D chip, which drives the temperature sensitive quartz oscillator (similar to design by Statek Inc). The quartz crystal is attached between PAD1 and PAD2. Diodes D1, D2 limit the amplitude of oscillations and improve supply voltage insensitivity of the circuit.

better than 0.3 mK.

Analog temperature sensors are very sensitive to fluctuations in supply voltages and radiofrequency pickup. The latter can be significant, due to a large number of RF sources (AOM, trap drive) present in the experiment. To avoid such issues, the temperature sensor used to measure the temperature of the cavity utilizes a quartz crystal (Statek, CX-1V-03 171kHz), with resonant frequency strongly dependent on temperature (resonant frequency of 172 kHz with temperature coefficient of 8 Hz/K). The crystal is used in a Pierce-type oscillator and mounted to the cavity, generating a 5 V square wave (see Figure 4-11). The output frequency is computed by measuring the duration of 172000 periods ($\approx$ 1 s) with 10 ns accuracy. Good phase stability of the resonator allows for single shot temperature measurement with 0.2 mK of noise. The temperature sensor was found to be insensitive to noise and drifts, with power supply sensitivity at 2 mK/V after an adjustment of capacitive loads C2, C3.

The time constant for the temperature stabilization loop is $\approx$ 4 h. The PID controller is fully digital, and uses bang-bang control to adjust the heater current (20 s total period of the on and off states). The stability of the temperature of the sensor is better than $\pm$0.5 mK over a period of days.

Cavity frequency can be monitored by tracking the narrow $S_{1/2} \leftrightarrow D_{5/2}$ line of Sr^+ using Ramsey spectroscopy, described fully at the end of the chapter. Figure 4-12 shows data gathered over a period of 7 hours, measuring the relative frequency of the cavity and the ion. The cavity-ion frequency difference remains within 5 kHz of the mean for the entire data period.

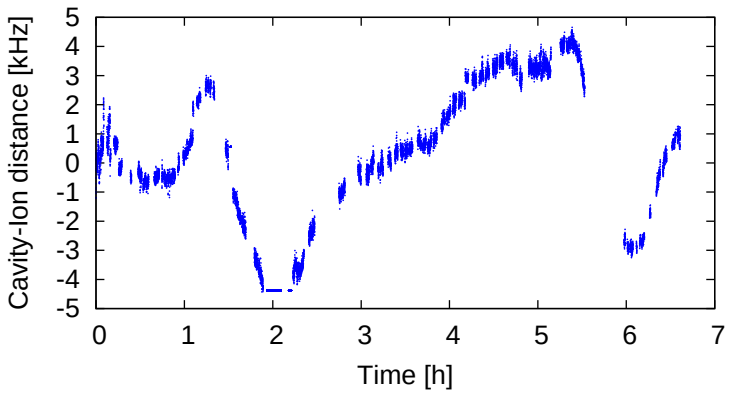

Figure 4-12: Drift of the reference cavity measured by locking to the ion line. The average frequency difference between ion and cavity equaled 385.5816 MHz, and was subtracted from the data.

4.3 Pulse Sequencing

Qubit operations require sequences of laser pulses with precisely controlled phases, amplitudes and lengths. Switching of the beam, and the desired frequency and phase shift is accomplished using an acousto-optic modulator (AOM), which shifts the laser beam frequency and phase by values equal to its RF drive frequency and phase. Frequency tuning range is limited to approximately ± 10 MHz by phase matching requirements of the laser and acoustic waves. The 674 nm AOMs are set up in a double-pass cat's eye configuration, which improves pointing stability over the tuning range [DHL$^+$05]. With such set-up, the problem of laser light control morphes into the problem of generating RF pulses at ≈ 200 MHz with accurate phase, amplitude and frequency.

The solution to this problem is described in two parts. First, the logic and state machine responsible for scheduling the pulses and recording results. Second, the RF generation implemented using direct digital synthesis boards (DDS). Both parts are schematically depicted in Figure 4-13.

4.3.1 Sequencing

The RF pulses have to be applied in a sequence, which may change based on qubit measurement results. The strict timing requirements and large number of digital control lines preclude the use of a PC, but is well suited to implementation on a field programmable gate array (FPGA).

The heart of the sequencer is an XEM3010-1000 (OpalKelly) development board featuring a Spartan-3 FPGA with 1,000,000 logic gates. The board's 100 general I/O pins are used for controlling the DDS modules and the attenuators. Additionally, one of the inputs receives the signal from the photon counter, allowing for readout of the state of the ion. The FPGA is clocked from the SYNC pin of the DDS, which allows for reliable control of the DDS operation.

The sequencing of the pulses is governed by a simple von Neumann-type processor. The design uses 4000 bytes of 32-bit memory, and is clocked at 62.5 MHz. Each instruction takes at least two cycles, with frequency switches taking up to 11. The processor is capable of simple arithmetic, function calls and conditional and unconditional jumps, which allows for

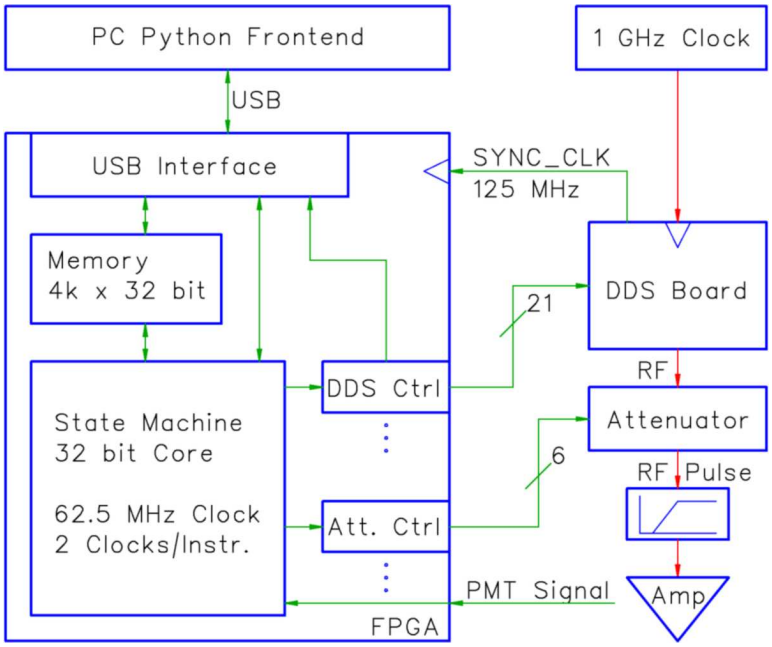

Figure 4-13: Schematic of the pulse sequencer. PC front end, written in python, communicates with the FPGA via USB. The FPGA's state machine controls DDS boards and attenuators to create a sequence of RF pulses. PMT signal on an input pin allows for state measurement and feedback during the sequence.

changes in instruction flow depending on ion's state. The software controlling the sequencer, including the sequence description pseudo-code, Verilog FPGA logic and python front-end are described in detail in Appendix A.2.

4.3.2 RF Generation

RF is synthesized using an Analog Devices AD9858 development board, which allows for a 32-bit frequency and 14-bit phase resolution, controlled by the FPGA using the 21-bit parallel port interface. The board uses phase continuous switching, meaning that the waveform is continuous after a frequency change. This feature, while reducing glitches, is undesired as it results in essentially random phase of the RF after a frequency switch. To circumvent this problem, the expected phase at time t (referenced to a fixed point in the past) for a given frequency f is computed using $\phi_0(t) = f \times t (\mathrm{mod}\ 2\pi)$. Then, after a frequency switch at time T, the absolute phase of the waveform is adjusted to equal $\phi_0(T) + \phi$, where ϕ is any desired phase. This process allows for frequency switching while maintaining phase information referenced to a fixed point in time, the so-called "phase coherent" switching. Proper execution of this correction requires precise knowledge of the time when the AD9858 switches frequency and phase, achieved by synchronizing control commands to the SYNC clock signal of the AD9858.

The output of the AD9858 is attenuated with a 6-bit digital variable attenuator (HRF-AT4610), with 0.5 dB resolution and 31.5 dB range, providing amplitude control. To remove low frequency noise (such as ground bounce, digital switching), the signal is filtered using a 100 MHz high pass filter (MiniCircuits SHP-100). The filtered signal is amplified using a linear RF power amplifier (Motorolla MHW1345) soldered into a custom made PCB,

offering approximately 30 dB of RF power.

The system is replicated three times, providing RF power to the AOMs switching the 674, 422 and 1033 nm lasers. The 1091 nm laser does not require switching.

A precise frequency source (Agilent 8648B) clocks the DDS boards, providing a stable clock used throughout the experiment.

4.4 Achieved Coherence Time

The coherence time of narrow lasers is difficult to measure, usually requiring a beat measurement between two identical systems. An upper bound can be obtained by measuring the decay of Ramsey fringes as a function of the separation of the Ramsey $\pi/2$ rotations [LGRS04]. Such measurement includes the effects of the drift in laser-ion distance, which causes Doppler shifts, and fluctuations of ion frequency due to changing magnetic fields. Experimentally, reducing the magnetic field noise (see Section 7.3.1 for further details) by a factor of 50 did not improve coherence by more than a factor of 2, indicating that magnetic field noise is not a dominant source of decoherence.

4.4.1 Ramsey Spectroscopy

Ramsey spectroscopy can be understood by considering the qubit state as a point on a sphere (Bloch sphere), with the $\pi/2$ rotations corresponding to a 90° rotation of the sphere about the $\hat{x}$ axis. If the laser is detuned from the qubit transition by δ, the increasing phase difference is equivalent to a rotation of the sphere around $\hat{z}$ axis at rate δ. The first $\pi/2$ pulse takes the qubit from its initial position, assumed to be the north pole, to the $-\hat{y}$ point on the equator. Depending on the detuning δ and the time T_R between the two Ramsey $\pi/2$ pulses, the qubit will rotate around the equator by angle δT_R. The second $\pi/2$ pulse performs another rotation around $\hat{x}$, rotating the qubit to the opposite state, back to original state or to a superposition of the two depending on δT_R. For a fixed detuning, the measured population in the original state will trace a sinusoid as a function of T_R, with frequency δ.

Perfectly coherent systems exhibit no variation in δ, and show Ramsey oscillations extending to infinity with no loss in contrast. Uncertainty of the detuning δ results in a weighted average of the sine functions with frequencies δ, reducing the oscillation amplitude at large T_R. The point at which the contrast drops to half of initial value is usually denoted T_2^*, the $*$ indicating the presence of inhomogeneous (varying between experimental runs) decoherence processes. A Gaussian broadened laser, with standard deviation of frequency fluctuations Γ, induces Gaussian decay of the Ramsey oscillations with envelope $\exp - \left(\frac{1}{2}\left(2\pi\Gamma\right)^2 T_R^2\right)$. Given T_2^*, the standard deviation of laser frequency fluctuations is

$$\Gamma = \frac{\sqrt{2\log 2}}{2\pi T_2^*} \tag{4.15}$$

The envelope of the observed Ramsey spectrum fits a Gaussian curve well, and indicates laser width of $\Gamma \approx 400$ Hz (cf. Figure 4-14). The spectrum FWHM equals to $2\sqrt{2\log 2}\,\Gamma \approx 900$ Hz.

The observed 400 Hz detuning could be explained by relative motion of the laser reference cavity and the cryostat at velocity of 3×10^8m/s $\frac{400\text{ Hz}}{447\text{ THz}} = 0.3$ mm/s. The distance

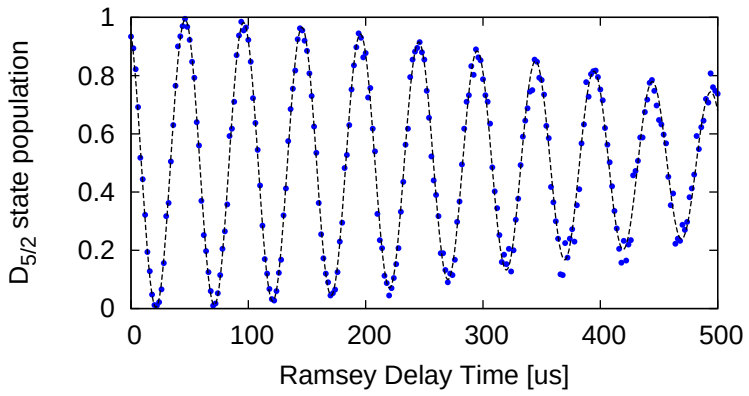

Figure 4-14: Decay of Ramsey fringes with Ramsey pulse separation time (•), and fit to a sine wave with a Gaussian envelope (dashed line). The amplitude of the fit waveform is 0.99 ± 0.01, with oscillation frequency 20.00 ± 0.1 kHz and Gaussian envelope half-width of 490 ± 10 µs.

between the two parts of the experiment is about 3 m; the exceedingly low drift velocities required underscore the technological challenges of quantum computation with optical qubits.

4.4.2 Spin-Echo

Inhomogeneous broadening can be reduced using spin-echo methods. Using the picture from the previous section, a π pulse rotates the sphere by 180° around the $\hat{x}$ axis, effectively reversing the direction of all rotations around $\hat{z}$. Provided that the detuning δ is constant, applying the π pulse at time $T = T_0$ results in the Bloch vector assuming its original position $-\hat{y}$ at time $T = 2T_0$, regardless of δ. The process is called refocusing, as it returns the system to a well understood state even if δ is unknown, or noisy. The method is successful only if δ remains constant over the time T_0; if δ differs in the periods $T < T_0$ and $T > T_0$, the phase rotation cancellation will not be perfect.

Figure 4-15 presents spin-echo data, with the echo pulse applied at $T_0 = 0.5$ ms, $T_0 = 1.0$ ms and $T = 1.5$ ms. In all cases, the fringe contrast recovers at time $2T_0$, but the recovery is only partial for $T_0 > 1$ ms. The almost perfect recovery for spin-echo pulses applied at $T_0 < 1$ ms indicates the dominant sources of noise are constant over that period of time, or equivalently the spectrum is dominated by noise below 500 Hz.

Spin-echo pulses can be used repeatedly, to reduce the low frequency noise in the system. The experimental limit of this technique can be explored by applying a number of π pulses, at times T_0, $3T_0$, $5T_0$ and so on. Such sequence is demonstrated in Figure 4-16. The contrast is well recovered for up to 5 ms, providing a lower bound on the intrinsic coherence time of the system T_2.

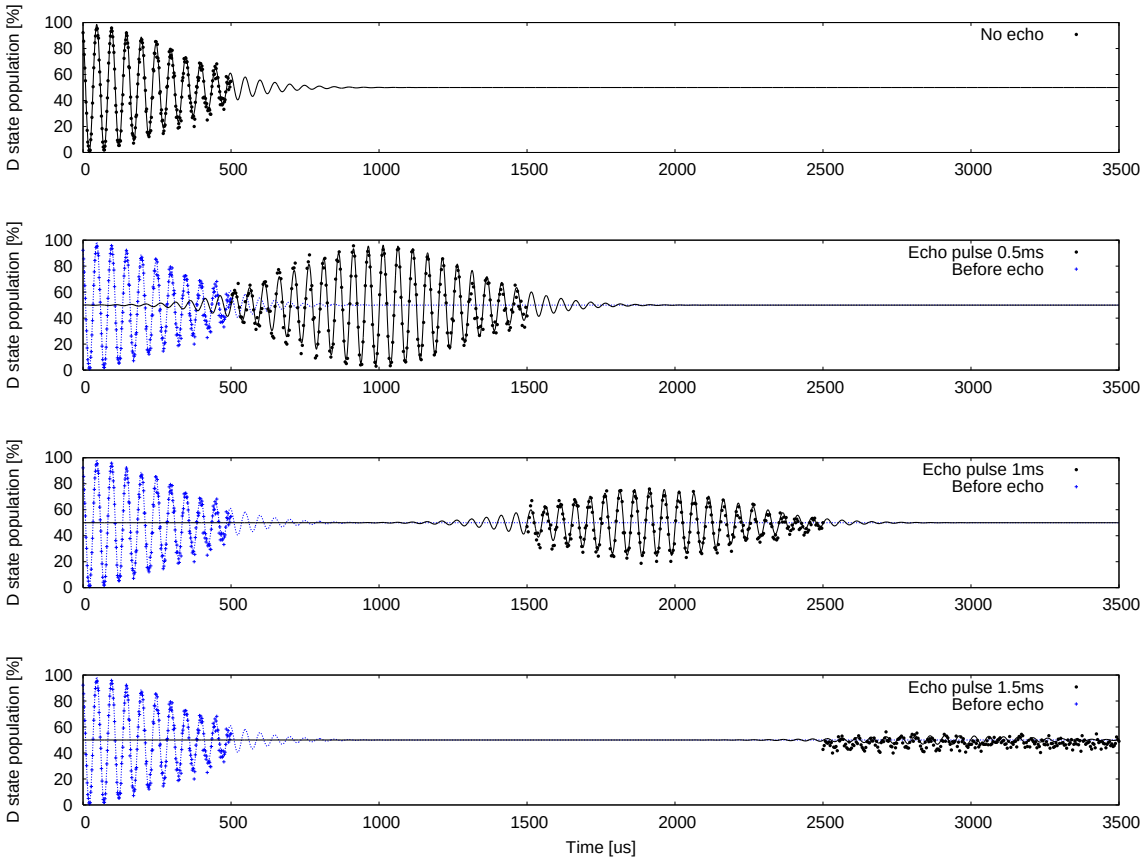

Figure 4-15: Spin-echo recovery of the contrast in Ramsey spectroscopy. (Top to bottom) Ramsey spectroscopy with no spin-echo, with inhomogeneous decay time of 340 µs. Coherence recovery with a spin-echo pulse at 0.5 ms, 1 ms and 1.5 ms.

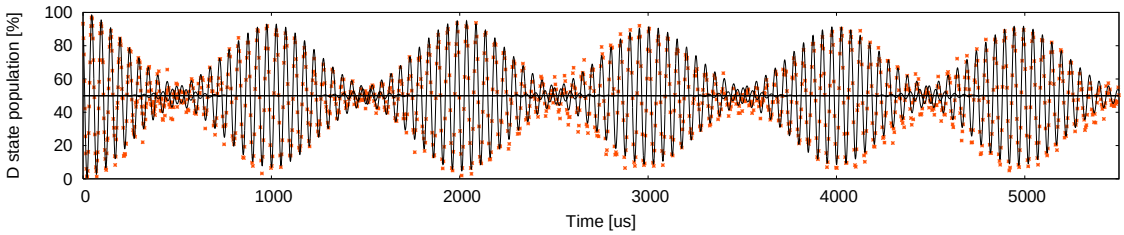

Figure 4-16: Repeated spin echo pulses applied at regular intervals demonstrate coherence for more than 5 ms.

Chapter 5

Heating Rates Out of Motional Ground State

There are two important parameters which characterize an ion trap for quantum computation experiments: the secular frequencies and the heating rates out of the ground state; global characteristics, such as trap depth or the electrode geometry may be important for loading or optical access, but do not affect the behavior of a trapped ion near ground state. While the secular potential can be very accurately computed for any trap geometry and any voltages, there is no such model for the heating rates. This chapter presents a range of experimental data, with particular focus on the measurements of the temperature, frequency and distance dependences of the heating rates.

Sections 5.1 and 5.2 establish a connection between heating and electric field noise, and describe the measurement methods used to acquire data. Two types of traps were investigated in detail, with trap electrodes fabricated out of silver (Section 5.3) and gold (Section 5.4). For silver traps, heating rates at room and cryogenic temperatures are presented, showing a dramatic reduction in decoherence at 6 K. Surprisingly, the measured values are strongly dependent on the annealing temperature. For gold traps, in addition to room temperature and 6 K data, the heating rates are characterized as a function of trap frequency and surface temperature in the $6 - 100$ K. Section 5.5 presents a number of one-off measurements taken in other traps, including the first superconductive ion trap.

The chapter concludes with Section 5.6, on the observed dependence of heating rates on surface contamination with Sr metal, as well as the RF and DC voltages applied to trap electrodes.

5.1 Heating Rates and Electric Field Noise

Heating out of ground state is usually assumed to be caused by electric field fluctuations, $\epsilon(t)$, at the ion position. Other sources, such as acoustic vibrations of the trap, are not expected to have a significant spectral component at the secular frequency of the ion. Taking $H_0 = \hbar\omega_v \left(a^\dagger a + \frac{1}{2}\right)$ (cf. Section 2.1), the noisy Hamiltonian is

$$H = H_0 + q\epsilon(t)x = H_0 + q\epsilon(t)x_0\left(a + a^\dagger\right) \tag{5.1}$$
$$x_0 = \sqrt{\frac{\hbar}{2m\omega_v}}$$

where q is the charge of the ion, m its mass and ω_v the vibrational frequency.

Using first order perturbation theory, the average transition rate to the first excited state is [TKK+00]

$$\Gamma_{0\to1} = \frac{1}{\hbar^2}\int_{-\infty}^{\infty} e^{-\imath\omega_v\tau}\langle\epsilon(t)\epsilon(t+\tau)\rangle\left|\langle 1|x_0\left(a + a^\dagger\right)|0\rangle\right|^2 d\tau \tag{5.2}$$

Defining the spectral density of electric field noise

$$S_E(\omega) = 2\int_{-\infty}^{\infty} e^{-\imath\omega\tau}\langle\epsilon(t)\epsilon(t+\tau)\rangle d\tau \tag{5.3}$$

the formula for transition rate simplifies to

$$\Gamma_{0\to1} = \frac{q^2}{4m\hbar\omega_v}S_E(\omega_v) \tag{5.4}$$

The above derivation is simplified by considering the ion motion in the effective trapping potential. Full derivation, starting with a dynamic trapping potential results in additional terms which couple to noise fields at $\omega_v \pm \Omega$, where Ω is the RF frequency. These, however, are expected to be suppressed by at least the square of Mathieu q parameter, which is typically less than 0.05, and will be dropped here.

The field noise is a better characteristic of the trap than the heating rate, as it is not dependent on charge and mass of the ion, or the secular frequency (except through the frequency dependence of the field noise itself). In case of a Sr^+ ion, the relation between noise S_E and heating rates $\dot{n}$ is

$$S_E(f_v) = \frac{4m\hbar(2\pi f_v)}{q^2}\dot{n} \approx 15\ \dot{n}\ \frac{f_v}{1\text{ MHz}} \times 10^{-15}\ \text{V}^2/\text{m}^2/\text{Hz} \tag{5.5}$$

where $f_v \equiv \omega_v$.

The data presented later in the chapter will be given in terms of field noise.

5.2 Measurement Methods

Measurements of heating are typically done by cooling to the ground state, then disabling the cooling process (described in Section 2.4) for a prescribed time and subsequently measuring the state population. There are a number of methods for determination of the motional temperature of the ion, appropriate in different ion energy regimes. In particular, for low energy ions, sidebands of the $S_{1/2}(m = -\frac{1}{2}) \leftrightarrow D_{5/2}(m = -\frac{5}{2})$ transition provide an

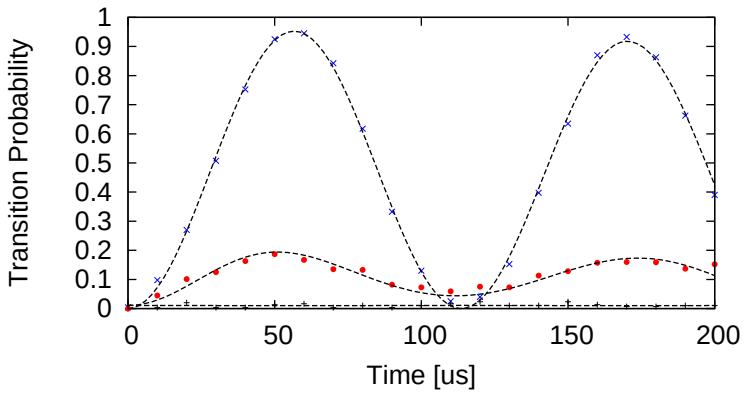

Figure 5-1: Rabi flop on the blue (×) and red (+) sidebands of an ion in the ground motional state and fits to sine waves (dotted line). After allowing the ion to heat up for 10 ms, the red sideband was measured again (•). The new waveform was fitted to a thermal state, with best guess of the average quanta number being $\bar{n} = 0.26 \pm 0.01$ (dotted line).

accurate measurement of motional state. For high energy ions, Doppler cooling, Doppler re-cooling and lifetime analysis can be used [ESL+07].

5.2.1 Heating Rate Measurements of Cold Ions

Low energy ions, with expected number of quanta less than 1, are investigated by observing the strength of the red and blue detuned sideband transitions (cf. Section 2.5.2). Single $^{88}Sr^{+}$ ions are loaded and Doppler cooled to < 1 mK, followed by sideband cooling of the lowest frequency mode on the $S_{1/2}(m = -\frac{1}{2}) \leftrightarrow D_{5/2}(m = -\frac{5}{2})$ transition (cf. Section 2.4). Measurement of transition probability on the sidebands is performed by applying an appropriately detuned laser pulse. The state of the ion is subsequently measured using light scattered on the $S_{1/2} \leftrightarrow P_{1/2}$ transition. The entire process is repeated 100 times, resulting in a transition probability. Laser drifts are eliminated by locking to the transition using Ramsey spectroscopy with 90° phase shift between the two $\pi/2$ pulses [LGRS04]. A single lock cycle is inserted before every measurement cycle.

Measuring the population distribution in all the motional states requires scanning the length of the probe pulse, and gathering enough data to decompose the resulting waveform into components at frequencies $\Omega\sqrt{n}$. Figure 5-1 shows the shelving probability on both blue and red sidebands for an ion in ground state, as well as the shelving probability on the red sideband for an ion which was allowed to heat up. The data and the expected dependence assuming a thermal distribution of motional states are in good agreement, justifying the later assumption that the ion heats up to a thermal state.

Measurement of the average number of quanta, $\bar{n}$, for an ion in a thermal state can be accomplished with just two measurements of sideband transition probabilities. Using Equation 2.78,

$$\bar{n} = \frac{P(|\downarrow\rangle \rightarrow |\uparrow\rangle, \delta = -\omega_v)}{P(|\downarrow\rangle \rightarrow |\uparrow\rangle, \delta = \omega_v) - P(|\downarrow\rangle \rightarrow |\uparrow\rangle, \delta = -\omega_v)} \tag{5.6}$$

While the measurement result is independent of details of the probe pulse power and

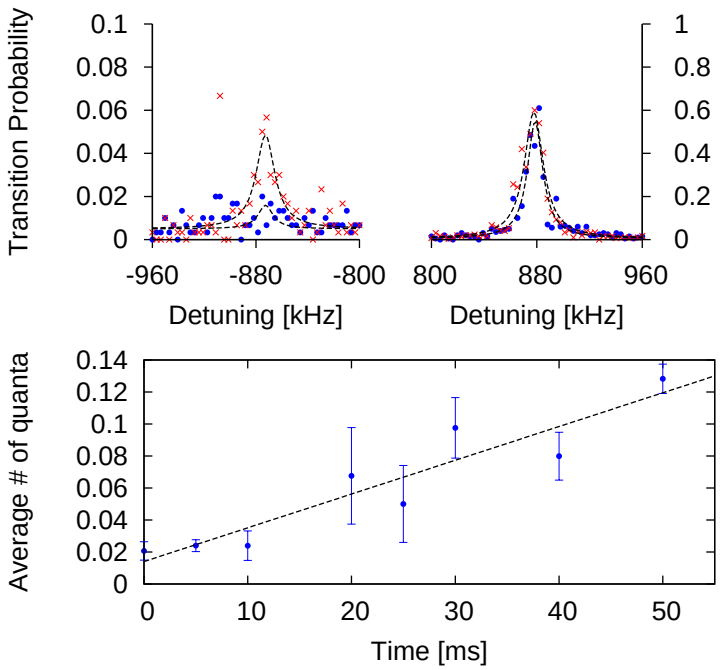

Figure 5-2: Sample data taken in a 150 µm silver trap at 6 K. (top) Sideband spectra after cooling (•) and after a 40 ms delay (crosses). Note that the scale for red (left) sideband is 10 times smaller than the scale for blue (right) sideband. (bottom) Average number of quanta versus delay time, with a linear fit. The slope of the fit line is 2.1 ± 0.2 s^{-1}

duration, the signal-to-noise ratio is best for $P(|\downarrow\rangle \rightarrow |\uparrow\rangle, \delta = \omega_v) \approx 1$. To this end, the laser pulse length is set to $\approx \pi(\eta\Omega)^{-1}$.

Depending on the stability of the laser with respect to the ion, one of two methods was used.

Method A

Prior to stabilization of the qubit laser to the ULE cavity, the uncertainty of the laser frequency was comparable to the Rabi frequency on the sideband. To ensure correct measurement of the transition probability, the probe laser was scanned across both sidebands, and the resulting lineshape fit to a Gaussian line. The amplitudes of the Gaussian are proportional to the transition probabilities, and can be used directly in Equation 5.6. The scans are repeated for a number of delay times between cooling and readout, and the measured $\bar{n}$ plotted versus delay time, yielding heating rates. Figure 5-2 shows a typical result of such a scan.

The necessary number of points taken around each sideband transition makes this measurement somewhat slow, requiring on the order of 10 minutes to measure the heating rate. The issue is compounded once the dependence of heating on another parameter, say RF voltage, is desired.

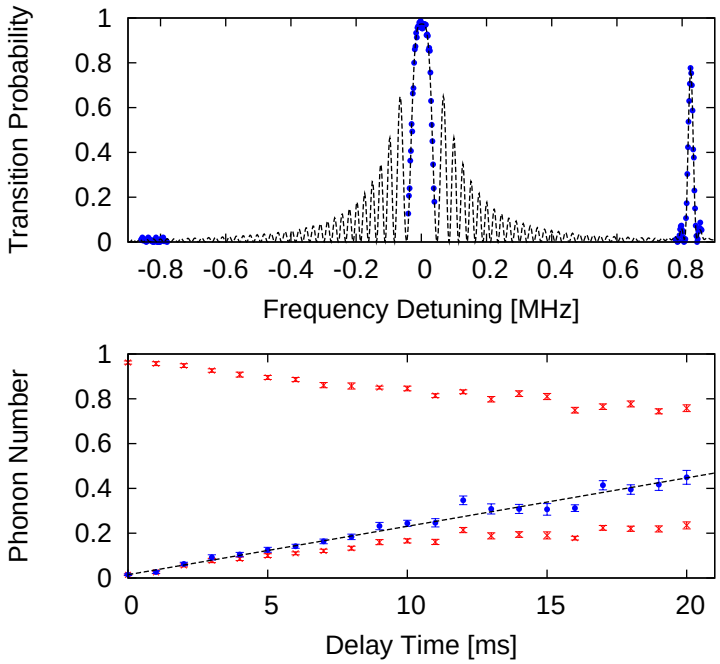

Figure 5-3: (Top) The spectrum (•) and fit line (dashed line) of the metastable $S_{1/2}(m = -\frac{1}{2}) \leftrightarrow D_{5/2}(m = -\frac{5}{2})$ transition immediately after sideband cooling, showing both carrier and the blue motional sideband transition. (bottom) Phonon number (average of 10 scans) as a function of delay time between cooling and measurement (blue •), with a fit line corresponding to heating rate of 21 ± 1 s^{-1}. Also shown are the transition probabilities on the blue (upper red ×) and red motional sideband (lower red ×) of the transition.

Method B

Once the laser is stabilized to better than the sideband Rabi frequency, the measurement can be accelerated by taking only a single probability point on each sideband. The sideband frequency is stable to < 10 kHz for a period of hours. Locking to the carrier removes any slow drifts, and ensures that the points fall on the peaks of the transition. The probability measurements are repeated for a range of delay times. This scan is repeated 10 times in succession, to remove effects of drifts in the cooling and/or heating processes during the measurement. The pulse length is set to $\pi(\eta\Omega)^{-1}$, a π rotation on the blue sideband for a ground state ion, to optimize signal-to-noise ratio. Figure 5-3 depicts typical data run.

Method B has numerous advantages over Method A. The number of data points taken is drastically reduced, resulting in much shorter scans. Repeating the measurement of the dependence of $\bar{n}(t)$ on t 10 times in succession, together with higher transition probability $P(|\downarrow\rangle \rightarrow |\uparrow\rangle, \delta = \omega_v) > .95$ results in lower measurement noise, evident from comparison of the two figures. These features were critical to the success of the later measurements of noise values versus surface temperature.

5.2.2 Heating Rate Measurements of Hot Ions

The methods outlined so far work well only for ion states with a low average number of quanta. Otherwise, the transition probabilities on the two sidebands are almost identical,

and Equation 5.6 becomes very sensitive to measurement noise. However, in traps with very high heating rates it is difficult to reach the motional ground state, due to the relative slowness of sideband cooling. A number of alternative methods has been developed, three of which have been used here.

Boil-off

The conceptually simplest method of estimating heating rates is to measure the time required for the loss of the ion through "boil-off." The measurement proceeds, again, by loading and Doppler cooling an ion to mili-Kelvin temperatures. Subsequently, the cooling laser is turned off for a prescribed interval of time. At the end of the interval, the cooling lasers are turned back on, re-cooling the ion or confirming its loss. Repeated observations at varying time intervals provide an estimate of the time τ_{boil} required for the ion to boil out of the trap.

Taking the trap depth to equal $E_{\text{trap}} = N_{\text{trap}}\hbar\omega_v$, the heating rate for $\omega_v \approx 1$ MHz can be estimated to be

$$\dot{\bar{n}} = N_{\text{trap}}/\tau_{\text{boil}} \tag{5.7}$$

$$= 250 \times 10^8 \times \frac{E_{\text{trap}}}{1 \text{ eV}} \frac{1 \text{ s}}{\tau_{\text{boil}}} \tag{5.8}$$

While simple, the method can be very inaccurate and time consuming, with each measurement potentially requiring a new ion to be loaded. Published data shows that the heating rates estimated from boil-off can exceed those measured near ground state by two order of magnitude [SHO+06]. The estimate of the energy E_{trap} can depend on trap geometry and the re-cooling laser settings, with consequent inaccuracy of the estimate. Lastly, our experiments revealed that even in cases of negligible heating out of ground state, the lifetime of an ion with lasers off can be quite short, on the order of 1 minute, indicating other loss channels (such as collisions with background gas).

Doppler Re-cooling

If the cooling laser is switched on before the ion acquires enough energy to escape, the re-cooling dynamics can be observed. The expected time-dependence of the scatter has been described in detail in Reference [WEL+07]. The equilibrium is reached quickly, after ≈ 1 ms, over which time the ion scatters approximately 10 photons into the PMT. The dependence of the scatter rate on time in that window is measured by repeated the experiment $O(1000)$ times, and creating a histogram of photon arrival times after the cooling laser is switched on. The data is then fitted to the numerical model, yielding the expected initial number of quanta. Significant change to the scatter rate requires as many as 10000 motional quanta, determining the necessary delay before the cooling laser is switched back on.

This method has been successfully used by other groups, reporting a good agreement with measurements made using sideband ratios [ESL+07].

Doppler Cooling Limit

Another estimate of the heating rate relies on balancing the Doppler cooling rate against the trap heating rate. Let the Doppler cooling rate of an ion with energy ϵ equal $R_{\text{D}}(\epsilon, \delta, s)$,

where δ and s are the detuning and saturation parameters of the cooling laser. Let $R_{\mathrm{D,\,max}}(\delta, s)$ be the maximum of $R_{\mathrm{D}}(\epsilon, \delta, s)$ over all ϵ. The ion will be lost once the heating rate exceeds $R_{\mathrm{D,\,max}}(\delta, s)$. The minimum cooling rate can be experimentally determined by measuring the minimum saturation parameter s necessary to retain the trapped ion, at a fixed laser detuning. A numerical model, same as the one used in Doppler re-cooling, allows then for an estimate of the $R_{\mathrm{D,\,max}}(\delta, s)$ values based on the experimental detuning and saturation data.

5.3 Silver Traps

The results of Reference [DOS+06] demonstrated the field noise to be strongly dependent on temperature and distance to the surface. The temperature range explored in those experiments was limited to > 150 K, leaving open the question whether the anomalous noise could be completely suppressed by cooling to sufficiently low temperatures. Measurements of the electric field noise at 6 K comprised the scientific goal of the initial set of experiments in cryogenic ion traps.

The traps used in these experiments were fabricated using the silver process described in Section 3.1.4. In total, 9 traps were fabricated, all except one used a crystal quartz substrate. Out of these, 7 were characterized at 6 K and the other 2 were used at room temperature. In order to determine the distance dependence of the noise, the traps were fabricated at 3 different scales, with ion-trap distances of 75, 100 and 150 µm.

The silver electrodes' properties depend strongly on the annealing temperature. In silver on quartz traps annealed at 760 °C, re-crystallization and void formation was observed in the Ag film. To characterize film roughness, the fraction of power of a 650 nm laser reflected from the surface at normal incidence was measured. The reflectivity of the annealed film was reduced from initial value of $> 90\%$ to $\approx 5\%$. At 720 °C, the Ag film was much smoother, with reflectivity $\approx 75\%$. At temperatures exceeding 760 °C, most of the silver film evaporates during the annealing process. The Ag film did not undergo any chemical reactions observable using x-ray photon spectroscopy during the process.

Silver deposited on sapphire surface exhibited somewhat different annealing behavior, with the film annealed at 760 °C showing similar optical properties to the silver on quartz films annealed at 720 °C.

5.3.1 Measured Field Noise at Room Temperature

Room temperature value of electric field noise was measured in two separate 150 µm silver on quartz traps annealed at 760 °C, in a UHV system. The base pressure in the system was 5×10^{-10} torr, and is not expected to contribute to heating. Single Sr^+ ions were loaded using photoionization of a neutral vapor, and the ion lifetime with cooling lasers on was observed to be on the order of 10 minutes. The field noise was measured using the three methods outlined in Section 5.2.2.

The boil-off time of the ion from the trap was estimated to be 0.46 ± 0.05 s, for a computed trap depth of 0.32 eV (Figure 5-4). Using Equation 5.7, the average heating rate can be estimated to be $(3 \pm 1) \times 10^8$ 1/s.

The ion was observed to leave the trap rapidly when the laser power was lowered. The estimated limit on Doppler cooling rate at the edge of stability was equal to $(6 \pm 2) \times 10^8$ 1/s. The limit, however, depended on the detuning δ, with lower values observed at smaller detuning, highlighting an inadequacy of the theoretical model.

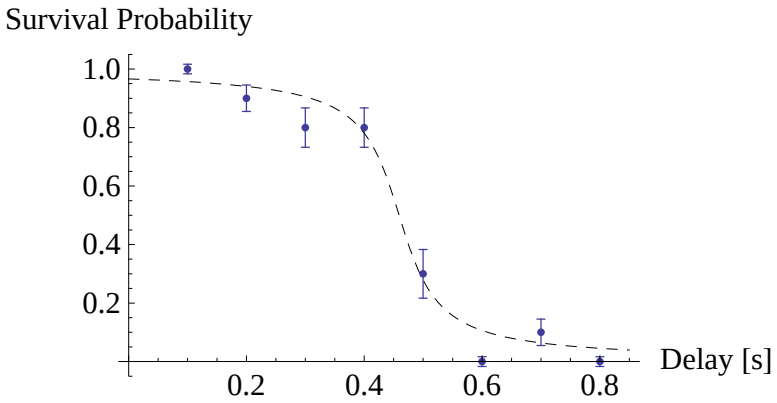

Figure 5-4: Boil-off time out of the trap. The survival probability (points) and a fit to a arctan function (dashed line) versus the length of time the ion is allowed to heat up is shown. The half-life of the ion is 0.46 ± 0.05 s, corresponding to average heating rate of $(3 \pm 1) \times 10^8$ 1/s.

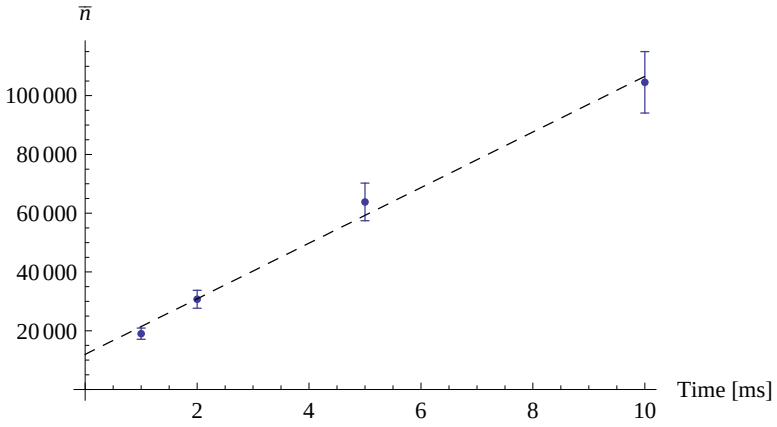

Figure 5-5: (points) Estimates of $\bar{n}$ after prescribed interval of time the cooling laser is off. Linear fit to the data (dashed line) has slope of $(10 \pm 3) \times 10^6$ 1/s

Doppler re-cooling data disagreed with the previous estimates. Turning off the cooling laser for $1 - 10$ ms resulted in an increase of scattered light by $5 - 30\%$ for approximately 500 µs. The rate of re-cooling was inconsistent with the model, taking approximately 10 times as long as expected to reach equilibrium. The disagreement may be caused by the Λ level structure of Sr^+, or the heating concurrent with the re-cooling, both of which are expected to increase the time to reach equilibrium. For this reason only the initial scatter values, within 100 µs of turning the laser on, were used to estimate the average number of quanta. Figure 5-5 shows the estimates as a function of the allowed warm-up time. Linear fit to the points has a slope of $(10 \pm 3) \times 10^6$ 1/s

The disagreement between Doppler re-cooling methods and the other two is somewhat expected in light of similar results reported in literature [SHO+06]. It has been suggested that the heating rates for a hot ion are significantly higher than those in ground state, accounting for the discrepancy. Therefore, the heating rate near ground state is estimated to be equal to that obtained from Doppler re-cooling, or $(10 \pm 3) \times 10^6$ 1/s. The normalized field noise is approximately $15 \pm 5 \times 10^{-8}$ $V^2/m^2/Hz$.

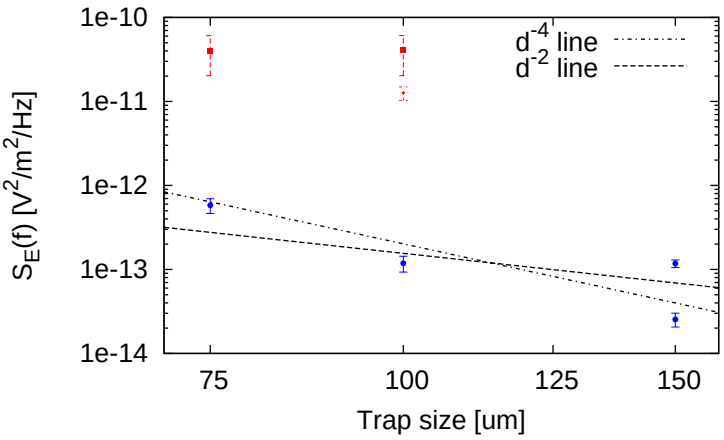

Figure 5-6: Measured noise density in 7 different traps, with secular frequencies in 0.85 − 1.25 MHz range. Each data point is normalized to 1 MHz, assuming the spectrum scales as ω^{-1}. Circles correspond to traps annealed at 760 °C, squares correspond to traps annealed at 720 °C while the triangle corresponds to a trap fabricated on sapphire.

5.3.2 Comparison with Published Values

Field noise measured in the silver traps at room temperature exceeds expected room temperature values by approximately 100 [TKK+00]. However, given the very wide range of observed heating rates in other experiments (exceeding 2 orders of magnitude), these values are not inconsistent with previous experiments. In particular, the microfabricated traps manufactured at Michigan and Sandia both exhibited heating rates on the order of 10^6 quanta/s, indicating that certain microfabrication processes result in very high heating rates [SHO+06, Luc07].

5.3.3 Measured Field Noise at Cryogenic Temperatures

Field noise at cryogenic temperatures was measured in the remaining 7 traps. Each trap was mounted in the cryostat, and thermally coupled to the 4 K bath using a short section of a copper mesh soldered to the trap surface. A temperature sensor was glued to one of the traps, and measured a temperature of 6 K with all voltages applied to the trap. Crystalline quartz has a very high thermal conductivity at low temperatures, ensuring uniform temperature of the trap surface. Ions were loaded by ablation of a $SrTiO_3$ target. Ablation pulses generate strong stray fields, compensated using the photon-correlation method [BMB+98].

The heating rates observed at cryogenic temperatures allowed the use of sideband ratios to measure the average number of quanta; method A was used for all measurements. Figure 5-6 shows the measured field noise densities. Closed circles correspond to traps annealed at 760 °C, squares correspond to traps annealed at 720 °C, while the triangle corresponds to a trap fabricated on a sapphire substrate, using the same process, and annealed at 760 °C.

Figure 5-7 shows the measured electrical noise density as a function of trap secular frequency. Only a narrow range of frequencies was experimentally accessible, due to reduced stability of the trap outside of that range. However, in that range, $S_E(\omega)$ scales as ω^{-1}, and the heating rate $\dot{\bar{n}}$ scales as ω^{-2}. This result is consistent with the literature, and justifies the ω^{-1} scaling used in Figure 5-6.

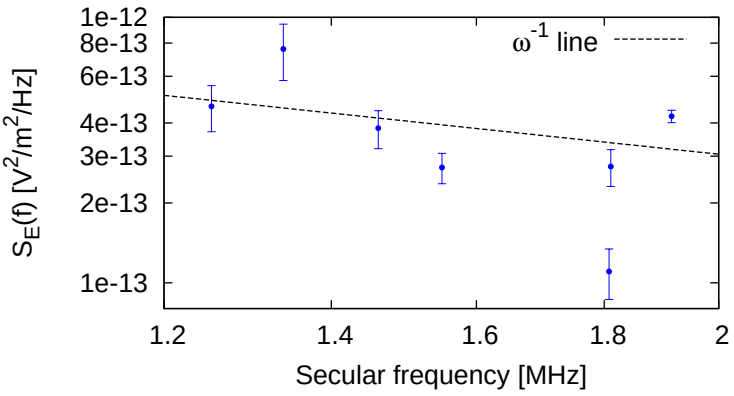

Figure 5-7: Measured field noise density in a 75 µm trap at different frequencies of the ion motion. The dependence is consistent with ω^{-1} scaling.

5.3.4 Conclusions of Experiments with Silver Traps

As expected, cryogenic cooling strongly suppresses heating rates out of ground state. Noise field values observed at 6 K are reduced by 7 orders of magnitude as compared to the values observed at room temperature. The lowest of the values are more than an order of magnitude lower than best values measured at room temperature in similarly sized traps.

Surprisingly, traps with highly reflective surfaces have field noise 2 to 3 orders of magnitude higher than similar traps annealed at 760 °C. This dependence is not at all understood, though the large difference in surface morphology suggests the crystal grain, surface smoothness or adsorption properties of the film are very important to the process. The trap fabricated on sapphire shows similarly high heating rates, implying that the insulating layer is not the dominant source of noise. Measured fields cannot be attributed to any technical source of noise, demonstrating that the mechanism generating these fields does not necessarily freeze out at 6 K. This point will be elaborated on in the next section.

In traps annealed at 760 °C, there is a clear increase of the noise fields in smaller traps. However, due to systematic errors stemming from the use of distinct traps and the low number of points, the exponent of the distance scaling cannot be determined exactly. Plotted in Figure 5-6 are fits to d^{-2} and d^{-4} scaling; both lines are consistent with the data.

Separately fabricated traps, annealed at 760 °C have heating rates which are quite consistent, with the two 150 µm traps showing heating rates within a factor of 5. However, this amount of variation may make it challenging to study the dependence of observed noise on fabrication process, unless a large number of traps can be measured for each process.

5.4 Gold Traps

The challenges presented by the experiments with silver traps, in particular the strong dependences on the annealing temperature and the unexpectedly high heating rates at room temperature, motivated development of a new process. Instead of annealing the traps, thin silver electrodes were electroplated with gold, as described in Section 3.1.4. Gold is known to provide very clean surfaces and does not passivate in air, which is expected to result in more repeatable data between separate traps. The strong suppression and non-zero noise fields measured at 6 K in silver traps suggested the temperature dependence will be of

interest. To that end, temperature sensors and a heating element were added to the trap surface, as described in Section 3.1.5.

The electroplating process turned out to be very sensitive to temperature, current, concentration of the plating solution and the surface plated (see Figure 3-4 for two examples). This variability made it unlikely the distance dependence could be accurately determined. For this reason, out of the 4 traps fabricated, 3 were scaled so that the ion-surface distance equaled 75 µm, while the fourth was scaled to 100 µm. The data from the last trap was normalized by $(4/3)^4$, using scaling from References [TKK+00, DOS+06].

To reduce the stray electric fields, photoionization of neutral vapor was used in all experiments. Despite the cleaner method, stray fields were still observed, with field values markedly different in room temperature and cryogenic traps. At room temperature, the experimental DC voltages necessary to compensate the fields exceeded 10 V, and drifted on a 10 minute time scale. The cryogenic experiments, however, required voltages 2 orders of magnitude lower, and remained fixed for a number of hours, even after reloading of the trap. The fields observed at room temperature seemed more sensitive to laser illumination, suggesting the difference in behavior could be explained by a difference in the photoelectric effect at the two temperatures.

5.4.1 Measured Field Noise at Room Temperature

One of the fabricated traps was used to characterize the room temperature noise fields prior to cooling down in the cryostat. The UHV system used was identical to that described in Section 5.3.1. A heating element was added below the CPGA, allowing the trap to be heated above room temperature to approximately 100 °C.

The heating rates were low enough to allow both Methods A and B from Section 5.2.1 to be used. Similarly to the previously used silver traps, large stray fields were present, which would often change between loading events. The short ion lifetime, on the order of 10 minutes did not allow for proper compensation, and therefore the measurements could be affected by stray electric fields.

The room temperature heating rates were measured to be 4200 ± 300 s^{-1} at 1 MHz, or $60 \pm 5 \times 10^{-12}$ V^2/m^2/Hz, in good agreement with published data [SCR+06, ESL+07]. The observed rate did not change by more than the measurement error as the trap was heated to 50 °C. Upon further heating of the trap, the lifetime was reduced below values necessary for the measurements.

5.4.2 Measured Field Noise at Cryogenic Temperatures, Temperature Dependence

Initial measurements of the field noise at 6 K indicated low, but non-zero, field noise value above the surface. In order to gather more information on the noise source, as well as separate possible technical noise from fundamental sources, the temperature dependence of the noise was studied.

Temperature control of the surface was accomplished using a 1 kΩ heating element, soldered at the edge of the trap. The CPGA's material provides a thermal insulator from the LHe tank, allowing for trap temperature as high as 120 K with less than 1 W of power applied to the resistor. Two RuO_2 resistors (Mouser Electronics) monitor surface temperature. The sizable heating power applied to the trap could result in large temperature gradients. For that reason, the temperature sensors are soldered on the opposite sides of

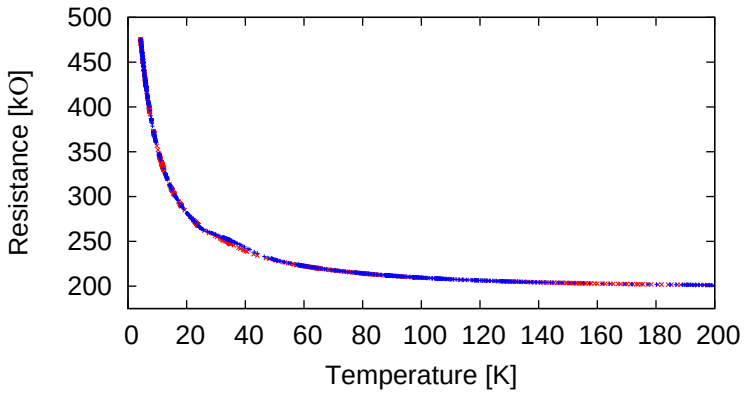

Figure 5-8: Resistivity of the RuO_2 resistor as a function of temperature. The resistor was calibrated against a known temperature sensor (LakeShore, DT400). Two data sets are plotted, acquired when cooling the resistors down (blue +) and warming up (red $\times$), with almost perfect overlap. The experimental errors in the data acquisition are negligible compared to the difference in response when cooling down and warming up, and the differences in response of different resistors.

the trap, and a geometric mean of their readings (typically within 5 K) is taken as the trap temperature.

The resistivity of the RuO_2 is a strong and monotonic function of temperature in $4 - 200$ K range. The resistors were calibrated against a known temperature sensor (LakeShore, DT400). Both sensors were soldered to a copper plate, which was slowly immersed in a tank of LHe, over a period of an hour. The correlation between the readouts during cooldown and warmup is shown in Figure 5-8. The small differences in the calibration for the two curves, together with variations in response of different resistors result in estimated temperature calibration uncertainty of 2%.

In addition to the surface patch potentials, there are a number of other sources of heating, including electrical noise on RF and DC electrodes, coupling to hot vibrational modes of the ion and possible extra heating due to micromotion. All DC sources are low-pass filtered at 4 kHz, and the RF source is high-pass filtered at 10 MHz. Prior to measurements, we minimize the ion micromotion using photon-correlation method, reducing it to < 10 nm in plane of the trap and < 100 nm perpendicular to that plane [BMB+98]. This procedure has to be done only once every few hours, with observed micromotion not affected by loading of ions into the trap. The observed heating rates do not depend strongly on DC and RF voltages near the optimal operating point, indicating that the aforementioned sources of noise do not contribute significantly to the data. Finally, to guard against remaining temperature independent sources, electric field noise data was taken in a non-sequential order of temperatures.

The temperature dependence was characterized in four traps, with one trap measured five separate times, resulting in 8 datasets. Except where noted, data was taken at 0.84 to 0.88 MHz and scaled to 1 MHz assuming $1/f$ scaling.

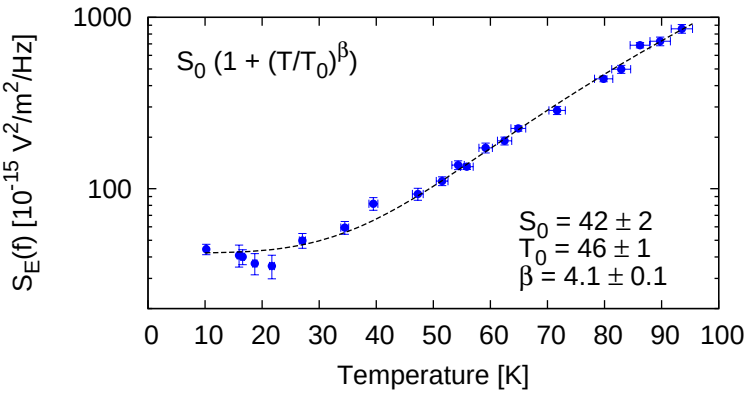

Figure 5-9: Temperature dependence of the measured field noise in trap II (•) and the fit to $S_E(T) = 42\left(1 + (T/46\text{ K})^{4.1}\right) \times 10^{-15}$ V^2/m^2/Hz (dashed line).

Trap	Fit Parameters S_0 [10^{-15} V^2/m^{2}Hz]	T_0 [K]	β [1]	Notes
I	65 ± 3	73 ± 3	3.0 ± 0.2	6^{th} cooldown
II	42 ± 2	46 ± 1	4.1 ± 0.1	Initial cooldown
III a)	167 ± 7	46 ± 1	3.6 ± 0.2	Initial cooldown
b)	120 ± 10	45 ± 3	3.5 ± 0.2	Temperature cycle to 130K
c)	54 ± 3	44 ± 2	3.2 ± 0.1	Temperature cycle to 340K
d)	60 ± 4	49 ± 4	2.1 ± 0.1	Re-cleaning in lab solvents
e)	18 ± 3	17 ± 3	1.8 ± 0.1	Re-cleaning in lab solvents
IV	$3.30 \times 10^3 \pm 40$	73 ± 1	3.2 ± 0.1	Following RT measurements

Table 5.1: Summary of the fit parameters to $S_E(T) = S_0\left(1 + (T/T_0)^{\beta}\right)$ obtained from the measurements. Trap III was measured five times, with in-between processing steps indicated in the notes column. Trap IV was measured in a room temperature system prior to measurements at cryogenic temperatures.

"Typical" Temperature Dependence

Typical temperature dependence curve is shown in Figure 5-9. The observed field noise remains rather flat below 40 K, but increases rapidly with temperature above that point, where it can be modelled accurately by a polynomial T^{β}. Table 5.1 summarizes the parameters of the fits to $S_E(T) = S_0\left(1 + (T/T_0)^{\beta}\right)$. The frequency spectrum of the noise was measured in one trap (trap III), and fitted to $f^{-\alpha}$. At 100 K, the exponent α is very close to 1, consistent with published values [DOS$^+$06, ESL$^+$07]. At lower temperatures, however, $\alpha \approx 0.7$ (Fig. 5-10).

The exponent β varies between the traps, and between separate measurements in the same trap. In trap III, the observed noise amplitude was found to be stable for hours (III a), before abruptly dropping after a temperature cycle to 130 K (III b). Temperature cycling to 340 K, without breaking vacuum, resulted in a further decrease in observed noise (III c). Exposure to air and laboratory solvents did not return the observed fluctuations to initial values (III d,e), indicating that temperature cycling results in an irreversible change. The lowest obtained value (III e) is more than 2 orders of magnitude below best reported

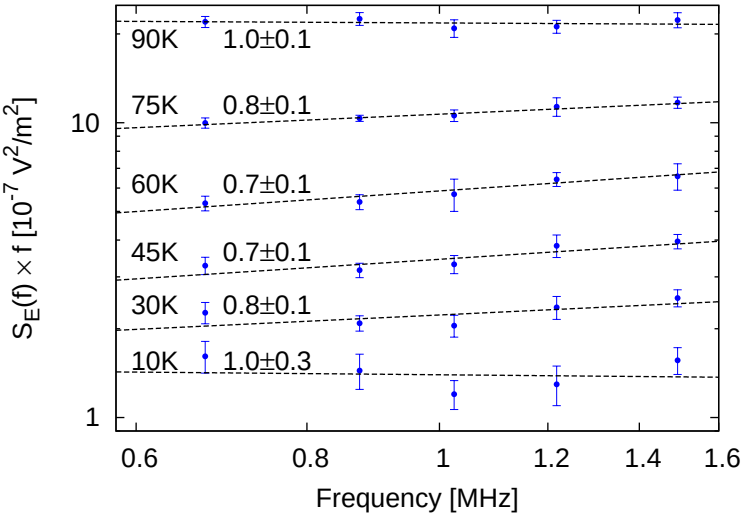

Figure 5-10: Noise spectrum at 6 different temperatures measured in trap III a. Plotted are the values of $S_E(f) \times f$ and fit lines to $S_E(f) \times f = f^{1-\alpha}$. The fit exponent α and the measurement temperature is indicated above fit lines.

values for similarly sized traps operated at room temperature [ESL+07]. Trap IV, used to measure the noise at room temperature, exhibited significantly higher heating rates at cryogenic temperatures, possibly related to temperature cycling between 77 K and 200 °C or cleaning in hot acetone performed when removing the trap from the room temperature system. Despite strong variation in the amplitudes S_0, the turn-on temperatures T_0 are consistent through the dataset. The finite zero-temperature intersect indicates either zero temperature fluctuations, or a thermally activated process with activation energy less than 7 K [SHM08].

"Anomalous" Temperature Dependence

In one instance, we found a dramatically distinct behavior. After trap II was cleaned in an ultrasonic bath, the surface became visibly roughened. The observed heating rates increased from the initial values by 2 orders of magnitude. The temperature dependence could not be fitted to the T^β form, but followed an Arrhenius curve, $S_0 + S_T e^{-T_0/T}$, with the activation energy $T_0 \approx 40$ K (Fig. 5-11). Good agreement of the fit and experimental data suggests that the noise is dominated by a narrow range of activated processes.

5.4.3 Conclusions of Experiments with Gold Traps

The data obtained in gold traps was more repeatable than the measurements in silver traps. All but one data point fell within a factor of 10 of each other, reflecting a more stable process, or lower susceptibility of gold to contamination and chemical reactions. The measured values are also much lower than those measured in silver traps, and reflect the "quietest" traps ever reported. However, the variability of the surface quality with plating parameters, and its influence on noise fields should be carefully characterized.

The measured noise values are very sensitive to the history of the trap, with large changes observed as the trap is thermally cycled and cleaned in laboratory solvents. Interestingly,

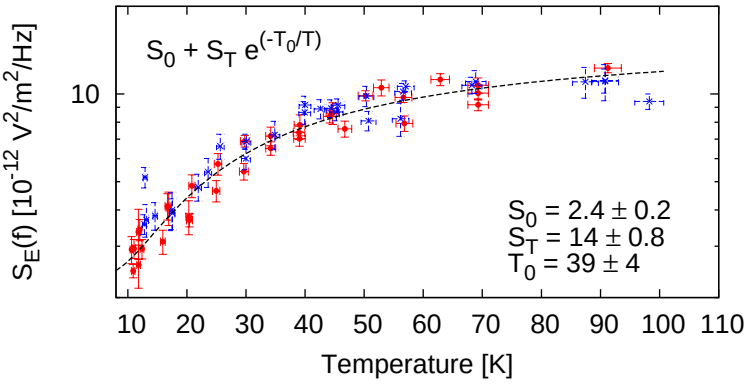

Figure 5-11: Anomalous behavior observed in trap II, after cleaning in an ultrasonic bath. Data points taken at 0.86 MHz (red •) and 1.23 MHz (blue ×) were scaled to 1 MHz assuming $1/f$ scaling and fitted to an Arrhenius curve (dashed line).

temperatures as low as 120 K are sufficient to alter the value and the temperature dependence of the noise. The noise fields seem to reach a steady value at temperatures below 20 K, indicating possible zero-temperature fluctuations. The impact of these measurements on both the experimental implementation of quantum computation in ion traps, and the theoretical models of the sources of the observed noise will be discussed in next chapter.

5.5 Other Measurements

In addition to the systematic measurements in gold and silver traps presented in the previous two sections, three traps using other materials are characterized. These are one-off measurements, and given the strong changes of observed noise levels with process details, do not fully characterize the representative processes. However, due to the very different properties of these traps, these results still provide a useful test for a number of possible noise sources.

The three traps studied are a superconductive trap fabricated out of NbN, a silver trap electroplated with nickel, and a trap fabricated out of aluminum. The first two are of identical design to the gold and silver traps discussed earlier, the last uses a radically different design fully described elsewhere [KPM$^+$05, Slu06]. For each trap, the trap fabrication process is described first, followed by the measured field noise values and other experimental comments.

5.5.1 Superconductive Materials

Superconductive materials may allow for novel ways of coupling quantum information between systems [TRBZ04], but may also shed new light on the sources of the motional heating. The zero resistivity of the material below superconductive transition removes Johnson noise, as well as shielding any sources within the bulk of the material, possibly eliminating the decoherence altogether. To test this hypothesis, a superconductive trap made out of NbN was fabricated.

Fabrication begins by depositing a 200 nm thick NbN film on a sapphire wafer with an RF sputterer. The material thickness should be able to support a 0.5 A current in a

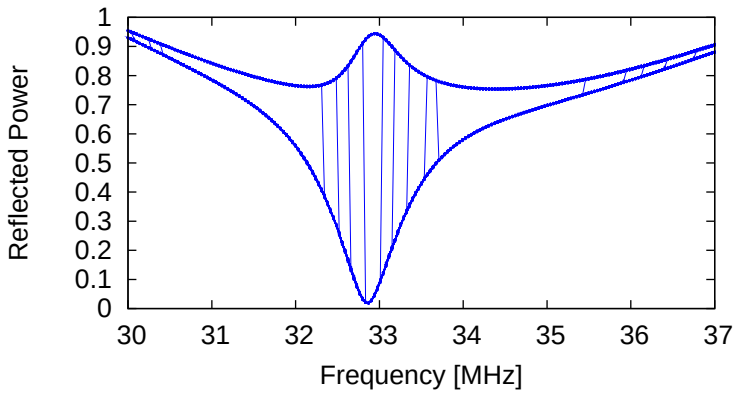

Figure 5-12: Measurement of the reflected RF power versus frequency in the NbN trap during warm-up of the cryostat. The observed value is observed to switch multiple times between two curves (vertical lines) at baseplate temperature of around 13 K. The multiple transitions are due to warm-up and cool-down of the trap as the RF is moved on and off resonant frequency.

100 µm wide electrode, well above the currents used in the traps in operation. NR9-3000P photoresist, exposed through a chrome mask and developed in RD6 developer, defines the electrodes. Reactive ion etch is used to etch exposed NbN, with care taken not to exceed 90 °C during the entire process. The surface is too hard for wirebonding, and requires a secondary evaporation and etch step to define gold bond pads on the NbN surface.

The superconductive transition of the RF electrode can be easily observed by measuring the reflected power from the resonator. The NbN film has a very high resistivity of 2×10^{-6} Ωm above the transition temperature, and zero resistivity below. Figure 5-12 presents the reflected power during warm-up of the cryostat, in the vicinity of 13 K, measured at operating RF voltage. Two easily distinguishable curves are seen, with the bottom one corresponding to higher temperatures. A number of transitions between the two curves was observed, corresponding to multiple transitions to and out of superconductive state, due to a warm-up and cool-down of the trap as the RF is moved on and off the resonant frequency.

The heating rates and corresponding field noise were measured using Method B (see Section 5.2.1) at various RF powers and DC voltages with a consistent value of $S_E(1\text{ MHz}) = 0.25 \pm 0.05 \times 10^{-12}$ V^2/m^2/Hz. The measurement could not be performed in normal state because of the high resistivity of the trap and associated RF gradient along the RF electrode.

5.5.2 Nickel Trap

Initial plating experiments used nickel instead of gold, which can be easily deposited using an electro-less plating solution. A silver trap was plated using a two part plating solution heated to approximately 90 °C (Caswell). While it is well known that certain plating processes have to be "jump started" by contact of the surfaces to be plated with a particular metal, the solution used in our experiments would only be activated by contact with one particular screwdriver. The plated surfaces were typically uneven, and required a number of tries before an acceptable finish was achieved. These difficulties led to abandoning of the nickel plating process.

A single trap was successfully fabricated and cooled in the cryostat to 6 K. Using

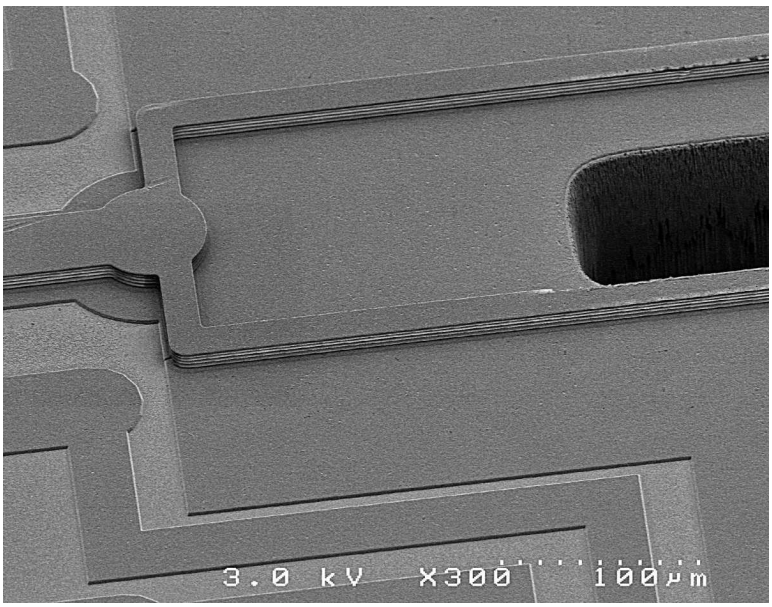

Figure 5-13: The substrate consists of p-doped Si wafer coated with a layer of Si_3N_4 insulator. DC electrodes are fabricated in the plane of the trap, while the RF electrode is elevated on a 10 µm layer of sputtered SiO_2. The hole on the right-hand side goes through the wafer, and does not extend to the experimental zone. Reproduced with permission from David Leibrandt.

Method A (see Section 5.2.1), the field noise was measured at $S_E(1\text{ MHz}) = 0.3 \pm 0.1 \times 10^{-12}\text{ V}^2/\text{m}^2/\text{Hz}$.

5.5.3 Lucent Trap

The last of the three tested traps was developed by R. E. Slusher at Lucent Technologies [KPM+05, Slu06]. The trap is fabricated on p-doped Si wafer coated with a layer of Si_3N_4 insulator. The DC electrodes are evaporated directly onto that insulator, and the RF electrode is elevated on a 10 µm layer of sputtered SiO_2. Both the DC and RF electrodes are made out of 1 µm aluminum. SEM image of a part of the finished trap is shown in Figure 5-13. The predicted ion height equals to 78.7 µm above trap surface.

The heating rate of a vibrational mode along the RF rails was measured at cryogenic temperatures using Method A, at a secular frequency of 550 kHz. The field noise, normalized to 1 MHz equaled $S_E(1\text{ MHz}) = 0.9 \pm 0.1 \times 10^{-12}\text{ V}^2/\text{m}^2/\text{Hz}$. For comparison, the field noise measured at room temperature in another trap of this design was $S_E(1\text{ MHz}) = 77 \times 10^{-12}\text{ V}^2/\text{m}^2/\text{Hz}$ [Win06].

The measured value should be considered as an upper bound. The elevated RF electrode structure did not allow for a laser perpendicular to the RF rails, reducing the effectiveness of Doppler cooling of the two vibrational modes in the plane perpendicular to the electrodes. Large number of quanta in those modes could heat the mode under investigation, resulting in an overestimate of field noise. The heating rates were also observed to decrease with increasing RF voltage, with a 4 fold decrease as the voltage was ramped from 155 to 195 V_{amp}. Further increase in RF was not possible due to breakdown considerations.

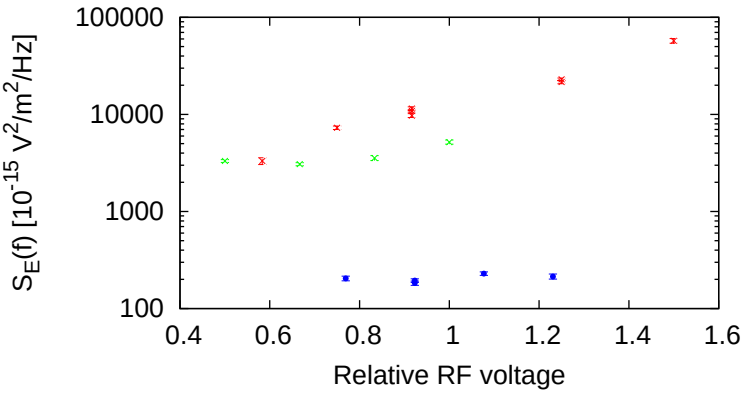

Figure 5-14: Electric field noise dependence on the applied RF voltage. While most traps do not exhibit any significant change (blue •), one of the traps (Trap IV, gold electrodes) showed a strong, almost exponential growth (red ×). Re-cleaning of that trap resulted in a somewhat weaker dependence (green ×).

5.6 Comments on Heating Rate Measurements

We conclude the chapter with some comments regarding the stability of the measured heating rates with respect to changing trap parameters. In particular, the dependence of the heating rate on the RF voltage, compensation voltages and Sr contamination is discussed.

5.6.1 RF Voltage Dependence

The noise process under study could be driven by the large RF fields present near the trap surface. To test such a hypothesis, the heating rate is observed as a function of the RF voltage. The vibrational mode studied is defined by the DC voltages on the electrodes, and its frequency is not significantly affected.

Figure 5-14 show two types of dependences observed in the measurements. Bottom curve (blue •) represents typical data behavior, with little or no dependence on the RF over a factor of 2 in RF voltage. Two top curves are taken in a different sample (Trap IV, gold electrodes), and exhibit a very strong dependence on the RF voltage. The first (red ×) shows an almost exponential increase over the studied range. The second (green ×), acquired after re-cleaning the same trap, shows a weaker dependence, with a fairly stable values attained below a value of 0.8 (all voltages relative to an arbitrary point). The exponential dependence could be explained assuming the noise is dominated by field emission noise from a nearby emission point. Such emission points are known to exist (see Section 3.1.3). Samples which did exhibit strong RF dependence, and could not be used in a region where the heating rate plateaued were discarded.

5.6.2 DC Voltage Dependence

Similar considerations apply to the DC voltages on the trap. Ideally, the trap voltages should be set so that the saddle point of the DC fields and the saddle point of the RF field coincide - the so-called compensated values. In such arrangement, the ion is not influenced by the noise on the RF electrode and its micromotion is minimized, resulting in, possibly,

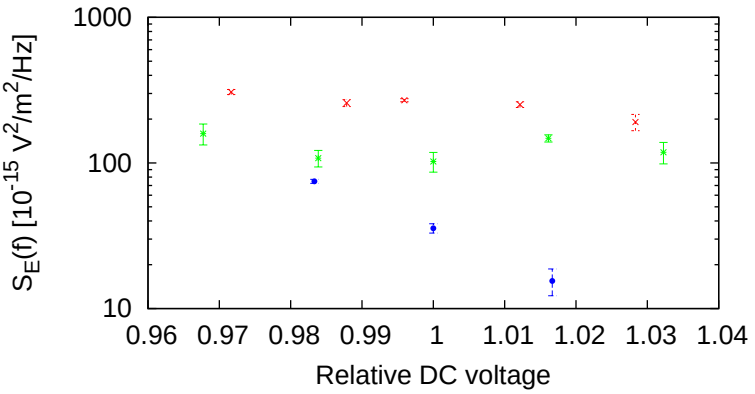

Figure 5-15: Electric field noise dependence on the applied DC voltages. While most traps do not exhibit any significant dependence (red $\times$, green $*$), one of the traps (Trap III e, gold process) showed a strong decrease after an adjustment of the DC voltage (blue $\bullet$).

lowest heating rates. Note that changing DC voltages may change the tilt of the trap axis (which affects the number of quanta in modes perpendicular to the trap axis) and the ion-surface distance, which can complicate the dependence.

Optimum relative voltages on electrode pairs 1 and 2 and 3 and 4 (see Figure 3-1) is established easily by measuring the micromotion amplitude along the $\hat{y}$ and $\hat{x}$ using the photon correlation method. The relative value of the 1, 2 pair with respect to 3, 4 pair is harder to measure, as the lasers do not have a significant projection on the $\hat{z}$ axis. Figure 5-15 shows the result of a scan of the voltage applied to electrode 4 of the trap, while keeping the voltages on electrodes 1 and 2 constant, and minimizing micromotion along $\hat{y}$ using electrode 3. Again, as in the case of RF dependence, most traps do not exhibit any significant dependence on the DC voltages (red $\times$, green $*$). However, in one case (Trap III e, gold process), the heating rate drops significantly (blue $\bullet$) after adjustment of the DC voltages. In typical operation, the DC voltage is scanned about the approximate compensated values to minimize the heating.

5.6.3 Contamination with Sr

Material evaporated from the oven onto trap surfaces has been suggested as a possible source of the noise [TKK$^+$00, ESL$^+$07]. The hypothesis was tested in a 100 µm gold trap, with an initial field noise value of $(220 \pm 10) \times 10^{-15}$ V^2/m^2/Hz. The trap was initially relatively clean, with only a few ions loaded prior to the scan. A large current was applied to the oven, resulting in loading rates on the order of 2 ions/s. Every few minutes, the loading process was interrupted to re-measure the field noise. Figure 5-16 shows the field noise as a function of the cumulative loading time. The fit to the data indicates a change of $(18 \pm 14) \times 10^{-15}$ V^2/m^2/Hz after 1000 s of loading.

Except for the high loading rates, the trap design and voltages used are representative of the experiments in Sections 5.4 and 5.5. In those experiments, the total number of loaded ions is on the order of 10, corresponding to a few seconds in Figure 5-16. Considering the modest increase in noise field observed in this experiment, Sr contamination is not expected to affect measured values. The low impact of loading may be attributed to the high efficiency of photoionization compared to other loading methods, which reduces the

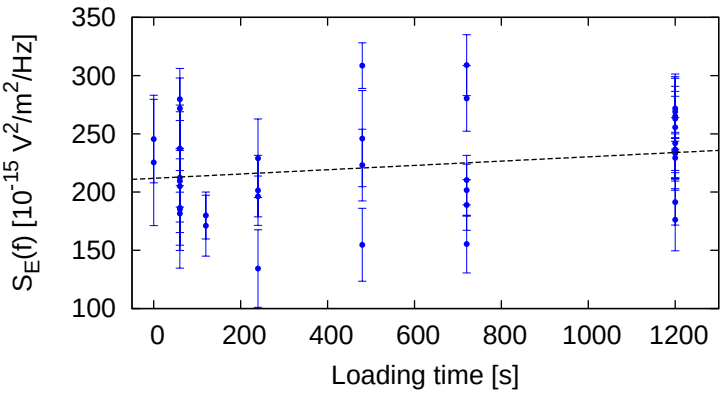

Figure 5-16: Electric field noise dependence on Sr contamination (•) and a linear fit to the data (dashed line). The fit indicates a change of $18 \pm 14 \times 10^{-15}$ $V^2/m^2/Hz$ after a 1000 s of loading.

necessary atomic flux [BLW+06].

In contrast, experiments on the silver traps reported in Section 5.3 relied on ablation as an ion source, with possibly much higher amount of Sr deposited on the surface.

Chapter 6

Sources of Electric Field Fluctuations

In Chapter 5, heating out of the motional ground state was derived as a consequence of electric field noise at the ion position. The fluctuations of the electric field, in turn, have to be generated by fluctuations of the potentials on and around the trap. This chapter focuses on various physical models of such fluctuations, discusses the expected temperature, frequency and distance dependences of the field noise, and relates these expectations to the data presented in Chapter 5. Clear identification of the physical mechanism would greatly facilitate the efforts to suppress this noise further.

Static and fluctuating electric fields above metal surfaces are also observed in many other experiments, including neutral atoms, cantilevers, gravitational forces, nanomechanics and single spin detection. Although these experiments explore a different frequency and distance regime to that important in trapped ions, a meaningful comparison is possible using appropriate scaling laws. These measurements and their impact on models of ion trap noise are reviewed in Section 6.3.

Section 6.1 describes two physical mechanisms typically considered to be the source of the noise. Finite resistances of the trap electrodes and voltage sources cause thermal fluctuations of the voltages on the electrodes. Similar fluctuations can also be caused by time dependent potential patches related to the presence of crystal facets or adsorbates on the surface, with the time variation driven by tunneling or thermally activated processes. Comparison of the expected temperature, frequency and trap size dependences to experimental data allows for refinement of the theoretical models.

In Section 6.2 the magnitude of source necessary to explain the experimental heating data is estimated for various models. In particular, the required resistances are found to be large compared to experimental values. The sizes of thermally activated sources can not be evaluated in general, due to the uncertainty in the actual process. Instead, two example mechanism are considered, a patch potential and an adsorbed polarizable particle, with estimates on patch sizes and particle count.

Section 6.4 concludes the heating rate measurements with a discusses of the relevance of the experimental results to scalability of trapped ion quantum computing.

6.1 Models of Noise Sources

Two general categories of models have been put forth to explain the decoherence measured in ion traps. The fundamental noise sources, caused by thermal fluctuations necessitated by fluctuation-dissipation theory, have been considered extensively in literature [HW99, Lam97, TKK+00, BP01]. Such sources are well-studied and well understood, allowing for calculation of the expected fields above metal surfaces as a function of distance and temperature. Main results relevant to the experiment are summarized below.

Following the discussion of thermal sources, the thermally activated sources are considered. These sources are technical, in the sense that they rely on imperfections of the metal surface which affect the surface potentials. The class of possible imperfections is very broad, and no identification of a particular process will be made. However, very general assumptions about the size and activation energies allow for derivation of scaling laws and comparison with experiment.

6.1.1 Thermal Sources

There are two separate sources of thermal noise. Noisy voltage sources and Johnson noise in the trap leads can be described by a voltage noise spectral density $S_{\mathrm{V,\ source}}(f)$ of the entire electrode. As the traps are scaled down, the shape of the equipotential surfaces remains the same. The expected value of field noise at the ion should satisfy

$$S_{E,source}(f) = S_{\mathrm{V,source}}(f)\,\frac{d_0^2}{d^2} \tag{6.1}$$

where d is a characteristic length scale of the trap, such as ion-electrode distance, and d_0 is a unitless constant, related to the ratio of the actual electrode distance and the characteristic trap size.

The electrode surfaces generate noise as well, having a finite conductivity. Consider an infinite metal surface with conductivity σ. The component of the electric field fluctuations parallel to this plane, at a distance d, is [TKK+00]

$$S_{E,\mathrm{Johnson}}(f) = \frac{k_B T}{8\pi\sigma d^3}\left(\frac{1}{2}+\sqrt{\frac{1}{4}+\frac{d^4}{\delta^4}}\right)^{1/2} \tag{6.2}$$

where δ is the skin depth, $\delta \equiv \frac{1}{\sqrt{\pi f \mu \sigma}}$, which equals to approximately 50 µm at 1 MHZ for a good conductor at room temperature. At cryogenic temperatures, $d \gg \delta$, and we can approximate

$$S_{E,\mathrm{Johnson}}(f) = \frac{k_B T}{8\pi\sigma\delta d^2} \tag{6.3}$$

Both types of Johnson noise scale as the inverse of the square of the distance of ion to the trap. Note that the above equations are valid in cases where the conductor's thickness is greater than the skin depth. While our data is inconclusive regarding the distance dependence (cf. Figure 5-6), published data does not agree with a d^{-2} scaling [DOS+06, TKK+00].

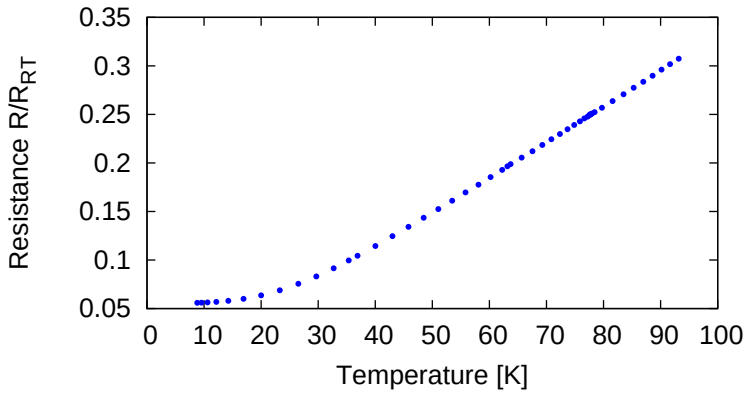

Figure 6-1: Resistivity of electroplated gold. A long gold wire was fabricated on the trap, providing a 3.7 Ω resistance at room temperature, reduced to 0.2 Ω at 6 K. The observed 20-fold decrease in resistivity is smaller than that of bulk gold (equal to approximately 100), and attributed to impurities in the plated film [Mat79].

Frequency Dependence

The spectrum of the Johnson field noise is "white", that is independent of frequency. The experimental evidence presented in Chapter 5 points strongly to a "pink" noise spectrum, with a $1/f$ dependence. Such difference however, could be due to low-pass filtering of the noise, or due to limited applicability of the above model to thin film structures.

Temperature Dependence

Johnson noise sources typically scale as the product of resistivity and temperature of the sample. The resistivity of the gold film forming the electrodes of traps used in the experiments described in Section 5.4 is shown in Figure 6-1. Experimental dependence is linear above 30 K, and almost constant below that temperature.

The expected noise power, proportional to ρT is plotted in Figure 6-2, together with a fit to $S_0(1 + (T/T_0))^\beta$. The best-fit parameters are $\beta = 2.2 \pm 0.01$ and $T_0 = 11.3 \pm 0.4$. No change in resistivity was observed after repeated temperature cycling of the metal film to room temperature.

While consistent with some of the measured dependences (Trap III d, III e, Table 5.1), the exponent is too low to explain the other data sets. The turn-on temperature T_0 is also too low to fit the measured value of ≈ 45 K, except in Trap III e. The T_0 value, however, is sensitive to constant offsets reducing the severity of the disagreement.

6.1.2 Patch Potentials

The inconsistencies of thermal fluctuation model with observed dependencies suggest investigation of a new model. Metal surfaces are known to exhibit "patch potentials", related to crystal facets [CDB91, GGJM$^+$06], material composition [NOW91], charge traps [OCK$^+$06] and surface adsorbates [RO92]. These potential could fluctuate, due to the movement of adsorbates, hopping electric charges or changes in grain sizes. The fluctuations can be driven by a tunneling processes or thermally activated, with different resulting temperature dependences. Despite the lack of precise specification of the physical source, a number of scaling

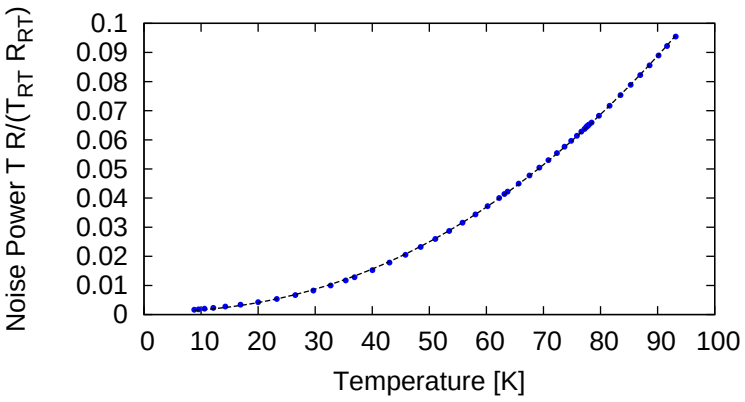

Figure 6-2: Expected Johnson noise resistivity of electroplated gold. The noise is reduced to 2×10^{-3} at 6 K as compared to room temperature values.

laws can be derived based on assumed sizes and activation energies of the fluctuators.

Distance Dependence

Consider a time dependent patch of potential with a characteristic size r_p on a surface of an electrode. This model and derivations are based on similar arguments by Turchette et al. [TKK+00]. For simplicity, assume the electrode forms a spherical shell of radius d around the trapped charge, and that each patch is a circular disk with potential V_p. The electric field of a single patch at the center of the sphere is

$$E_p = -\frac{3r_p^2}{4d^3}V_p \tag{6.4}$$

in the direction of the patch.

There are $N \propto \frac{d^2}{r_p^2}$ patches contributing to the total electric field. Assuming no correlations,

$$\begin{aligned}\langle E_p^2 \rangle &= N\left(\frac{3r_p^2}{4d^3}\right)^2 \langle V_p^2 \rangle \\ &\propto \frac{r_p^2}{d^4}\langle V_p^2 \rangle\end{aligned} \tag{6.5}$$

In frequency space, the field noise is related to voltage noise by the same factor, yielding

$$S_E(\omega) \propto \frac{r_p^2}{d^4} S_{V_p}(\omega) \tag{6.6}$$

Similar distance dependence holds in the case of a distribution of random point dipoles, a model intended to capture noise due to adsorbates. Assume a each particles has a dipole moment $\vec{p}$, randomly oriented up or down, perpendicular to the surface. Consider a point distance d away from the surface. The dipole field from a single particle at a distance

$\vec{r} = x\hat{x} + d\hat{y}$ from the ion is

$$\vec{E} = \frac{1}{4\pi\epsilon_0}\left(\frac{3\left(\vec{p}\cdot\hat{r}\right)\hat{r} - \vec{p}}{r^3}\right) \tag{6.7}$$

The field in the plane of the surface ($\hat{x}$) is

$$\vec{E}\cdot\hat{x} = \frac{1}{4\pi\epsilon_0}\frac{3(\vec{p}\cdot\hat{y})xd}{r^5} \tag{6.8}$$

If the dipole density is ρ, there are $N = 2\pi x\rho\partial x$ dipoles in a ring of radius x and thickness ∂x. The expected magnitude of the electric field from these dipoles, assuming $\langle p\rangle = 0$, is

$$\begin{aligned}\langle\left(\vec{E}\cdot\hat{x}\right)^2\rangle &= N\frac{9\langle p^2\rangle}{\left(4\pi\epsilon_0\right)^2}\frac{x^2d^2}{r^{10}} \\ &= \frac{9\rho\langle p^2\rangle}{\left(4\pi\epsilon_0\right)^2}\frac{2\pi d^2x^3\partial x}{r^{10}}\end{aligned} \tag{6.9}$$

Integrating over all distances x from 0 to infinity, the expected field is

$$\langle\left(\vec{E}\cdot\hat{x}\right)^2\rangle = \frac{3\rho\langle p^2\rangle}{4\left(4\pi\epsilon_0\right)^2}\frac{1}{d^4} \tag{6.10}$$

The same relation holds for the Fourier transformed values, resulting in

$$S_{Ex}(\omega) = \frac{3\rho S_p(\omega)}{4\left(4\pi\epsilon_0\right)^2 d^4} \tag{6.11}$$

with, again, d^{-4} dependence.

The d^{-4} dependence observed in previous calculations stems from the averaging over many patches or dipoles, with no correlations between them. If such correlations were present, due to large patch size or common behavior of the dipoles, the scaling would be much weaker, and equal to d^{-2}. Experimentally, while the data from Section 5.3 was inconclusive, other data suggests a scaling at least as fast as $d^{-3.5}$, consistent with a large number of uncorrelated sources [TKK+00, DOS+06].

Frequency Dependence

To derive a frequency scaling, assume the noise process is generated by two-level fluctuators, i.e. a dipole pointing up or down, or a patch with size and potential assuming one of two values. A random process with a characteristic switching time τ has a spectrum (up to a multiplicative constant)

$$S(\omega) = \frac{\tau}{1+\omega^2\tau^2} \tag{6.12}$$

In a thermally activated process, $\tau = \tau_0 e^{\frac{E}{k_B T}}$, where E is the activation energy and τ_0 is the transition attempt time. For a process with a single activation energy, the expected spectrum is

$$S(\omega, E) = \frac{\tau_0 \exp\left(E/k_B T\right)}{1+\omega^2\tau_0^2 \exp\left(2E/k_B T\right)} \tag{6.13}$$

with a Lorentzian frequency dependence.

In the case of a continuous spectrum of activation energies with density $D(E)$, the noise is an integral of the contributions at each energy. The spectrum of Equation 6.13 peaks at $\bar{E} = -k_B T \log \omega\tau_0$, with a width of $k_B T$. Following Reference [DH81] and Taylor expanding around the peak value $E = \bar{E}$,

$$\begin{aligned} S(\omega, T) &= \int dE D(E) S(\omega, E) dE \\ &= \int \sum_{n=1}^{\infty} \frac{d^n D(E)}{dE^n} \frac{(E-\bar{E})^n}{n!} \frac{\tau_0 \exp\left(E/k_B T\right)}{1+\tau_0^2 \exp\left(2E/k_B T\right)} dE \\ &= \frac{k_B T}{\omega} \left(D(\bar{E}) + \sum_{n=1}^{\infty} \frac{\mathcal{E}_n}{(2n)!} \left(\frac{\pi k_B T}{2}\right)^{2n} \frac{d^{2n} D(E)}{dE^{2n}} \right) \end{aligned} \tag{6.14}$$

where $\mathcal{E}_n$ is the n$^{\text{th}}$ Euler number.

If $D(E)$ is constant around $\bar{E}$, a simple expression emerges

$$S(\omega, T) = \frac{k_B T}{\omega} D(\bar{E}) \tag{6.15}$$

demonstrating an explicit 1/f frequency dependence.

In general, the frequency scaling of $S(\omega, T)$ can be related to its temperature dependence [DH81]

$$\begin{aligned} S(\omega, T) &\propto \omega^{-\alpha} \\ \alpha(\omega, T) &= 1 - \frac{1}{\log\left(\omega\tau_0\right)} \left(\frac{\partial \log S(\omega, T)}{\partial \log T} - 1 \right) \end{aligned} \tag{6.16}$$

The 1/f behavior requires a relatively flat distribution $D(E)$ around $E = \bar{E}$ over an energy scale of $k_B T$. The peak energy, though, equals $\bar{E} = -k_B T \log \omega\tau_0$, which is much greater than $k_B T$ for typical solid-state attempt times of $\tau_0 = 10^{-14}$ s (equal to inverse phonon frequency), and therefore the constraint is not a serious one.

Temperature Dependence

The temperature dependence is a function of the energy density of the activation energies. From Equation 6.15, the noise scales as $TD(\bar{E})$, where $\bar{E} = -k_B T \log \omega\tau_0$. Any temperature dependence T^β can be therefore duplicated assuming $D(E) \propto T^{\beta-1}$ around $\bar{E}$. The model is sufficiently flexible to accommodate all data presented in Section 5.4.

Note that the coefficient α is temperature dependent, and expected to be lower than 1 when S_E grows more slowly than T, and larger than 1 when the growth is faster i.e. above $T \approx T_0$ in the experimental fits. While our data exhibits qualitatively similar behavior, α remains below 1 up to much higher temperatures. A further refinement of this model is necessary to resolve this issue.

6.2 Estimates of Physical Sources

Field noise contributions from the sources mentioned in previous section can be computed explicitly for a realistic set of physical properties. This section considers fields associated with three example sources of noise: Johnson noise, electric fields noise due to oscillating dipoles and fields from patch potentials of given size and voltage noise.

6.2.1 Johnson Noise

Two sources of Johnson's noise are considered: the DC voltages and the trap surface resistivity. Voltage noise on the RF electrode is not expected to contribute to heating, due to a good ground connection at low frequencies. Moreover, when properly compensated, the electric field due to voltage on the RF electrode is zero at the ion position.

At frequencies near 1 MHz, the DC filters used have output impedance around $R_{filter} = 10\ \Omega$. The resistance of the leads from the DC filters to the trap electrodes is $< 1\ \Omega$, with the trap electrodes having a negligible resistance. Using simulation results with the 100 µm scaled trap, the electric field at the trap center due to 1 V difference in voltages on electrodes 1, 2 is 200 V/m, resulting in an effective electrode distance of 5 mm. Assuming the noise is dominated by the Johnson noise of the filters at $T = 4$ K, the expected voltage noise on the DC electrodes is estimated to be $S_V(\omega) = 4k_BTR = 2 \times 10^{-21}$ V^2/Hz. The electric field noise at the ion at 1 MHz is estimated to be $S_E(\omega) = S_V(\omega)\left(200\frac{100\mu m}{d}\right)^2 = 1 \times 10^{-16}\left(\frac{100\mu m}{d}\right)^2$ V^2/m^2/Hz, where d is the ion-trap distance.

Using Equation 6.3, and taking $\rho = 0.1 \times 10^{-8}$ Ωm and $\mu = 4\pi \times 10^{-7}$ J/T for gold resistivity and permeability, the expected noise from the gold surface is $S_E(\omega) = 2 \times 10^{-20}\left(\frac{100\mu m}{d}\right)^2$ V^2/m^2/Hz. The result may be higher if the 2 µm thickness of the film, which is smaller than the 16 µm skin depth at 1 MHz, is taken into account. The correction, however, is expect to be at most an order of magnitude.

Both Johnson noise sources are significantly smaller than the observed noise values measured at cryogenic temperatures.

6.2.2 Electric Field Noise from Adsorbates

Consider an adsorbed atom or molecule, which donates its charge to the metal surface forming a dipole. The typical dipole moment of such particle is on the order of $p =$ 5 Debye = 1 eÅ [OWC07]. Using the two level fluctuator model (cf. Section 6.1.2), the

noise spectral density $S_p(f) = Cp^2/f$, where C is a constant dependent on the frequency spectrum of the oscillating dipoles, with a value less than 1 for broadband 1/f noise [HB97]. Then, using Equation 6.11,

$$\begin{aligned} S_{Ex}(f) &= C\frac{3\rho\, p^2}{4f\,(4\pi\epsilon_0)^2\, d^4} \\ &= C\rho \times 10^{-28}\ \mathrm{V^2/m^2/Hz} \end{aligned} \tag{6.17}$$

Very high dipole densities on the order of $\rho = 10^{17}/\mathrm{m}^2$, or $0.1/\mathrm{nm}^2$, are required to explain the measured room temperature noise $S_E(f) = 10^{-11}\ \mathrm{V^2/m^2/Hz}$ at $d = 100\ \mu\mathrm{m}$.

6.2.3 Electric Field Noise from Patch Potentials

Consider a set of patches of area A_{patch}, with voltage noise of $S_V(\omega)$ on the patch. Using $S_E(f)d^4 \approx S_V(f)A_{patch}$ (See Equation 6.6, also Reference [TKK+00]),

$$\begin{aligned} S_V(f) &= \frac{S_E(f)d^4}{A_{patch}} \\ &= 10^{-16}\frac{(1\ \mu\mathrm{m})^2}{A_{patch}} \end{aligned} \tag{6.18}$$

For a 1 $\mu\mathrm{m}^2$ patch, the required voltage noise at 1 MHz is $S_V(f) = 100\ \mathrm{nV^2/Hz}$.

6.3 Connection to Other Experiments

The field noise above metal surfaces is a very generic problem, observed in a number of experiments in addition to the trapped ion systems. Static fields are measured in experiments with neutral atoms [NRV+87, SBC+93, OWC07], gravitational forces [LWF77, RBB+06], electron emission [HN49] and contact potentials [CDB91, RO92, GGJM+06]. Thanks to the relatively simple set-up required in electron emission or contact potential experiments, static potentials have been extensively characterized for a wide variety of materials and morphologies.

The fast fluctuating component of these fields is, in comparison, poorly studied. These fluctuations have been observed in precision experiments in nanomechanics [DFWG99, SMS+01, KLM06], single spin detection [MBCR03] and measurements of weak forces [ST03, DLC+05].

None of the above measurements are in the frequency and distance range which would allow for immediate comparison to the trapped ion results. In this section, appropriate scaling laws are derived and used to extrapolate trapped ion data to distances and frequencies explored in these systems.

6.3.1 Measurements of Static Fields

While certain types of pink noise have been shown to follow a 1/f scaling to frequencies as low as 1/week, such dependence has been confirmed in trapped ion experiments at

frequencies above 1 MHz only. Nevertheless, assuming the scaling to hold true at all timescales, the high frequency behavior can be extrapolated to static values by integrating the $1/f$ spectrum of the noise. True $1/f$ dependence is not integrable, and needs to be capped at a low and high frequencies. Taking $\tau_l = 10^{-14}$ s (phonon frequency) and $\tau_h = 10^3$ s (longest measurement time) to be the bounds for $1/f$ scaling, the expected value of $\sigma_E^2 = \langle E^2 \rangle$ is [HB97]

$$\sigma_E^2 = S_E(f) \times f \times \ln(\tau_h/\tau_l) \tag{6.19}$$

Using the measured room temperature noise, $S_E(f) = 10^{-11}$ V^2/m^2/Hz at 100 µm, results in estimated fluctuation of the electric field

$$\sigma_E^2 \approx d^{-4} \times 10^{-20} \text{ V}^2\text{m}^2 \tag{6.20}$$

Reference [SBC+93] measured the field value using the stark shift of a neutral atom traveling between gold plates spaced by a variable distance on the order of 1 µm. The square of the electric field scaled as $Ad^{-2} + Bd^{-4}$, with the d^{-4} component equal to $E^2 = 3d^{-4} \times 10^{-17}$ V^{2}m^2, approximately three orders of magnitude higher than the extrapolated value above.

A number of similar measurements have been performed with Rydberg atoms in high excited states, in a metal enclosure of radius $d > 1$ cm. At such distances, the extrapolated fields become insignificant compared to the measured values [NRV+87]. Interestingly, reported values are significantly lower for graphite coated metal surfaces [CDB92, NRV+87], providing a possible way of reducing noise in ion traps as well.

Contact potential experiments provide a different physical characteristic of the static patch fields. Let $\Delta\phi$ be the potential of a patch, r_p be the patch size and L be the probe size. Kelvin probe measurements average over $N = L^2/r_p^2$ patches, and the expected standard deviation of measured contact potential σ is [CDB91].

$$\sigma_V = \sqrt{N} \times \Delta\phi \times \frac{A_{patch}}{A_{probe}} = \Delta\phi \times \frac{r_p}{L} \tag{6.21}$$

Let $S_V = \Delta\phi^2$ be the patch voltage noise. The product of the patch size $A_{patch} = r_p^2$ and the surface potential variance S_V is

$$S_V A_{patch} = \sigma_V^2 L^2 \tag{6.22}$$

Reference [CDB91] reports $\sigma_V = 10^{-3}$ V, giving

$$S_V A_{patch} = (1 \text{ mV})^2 (1 \text{ mm})^2 = 10^{-12} \text{ V}^2\text{m}^2 \tag{6.23}$$

The equivalent quantity extrapolated from the ion trap data is derived from Equation 6.5, $\sigma_V^2 A_{patch} \approx \sigma_E^2 d^4$. Using the room temperature values for S_E, $\sigma_V^2 A_{patch} \approx 10^{-20}$ V^{2}m^2.

The published measurements of static fields are significantly larger than expected by

integration of the $1/f$ spectrum extrapolated from the high frequency values. While it cannot be ruled out that the noise spectrum undergoes a dramatic change at low frequencies, an appealing explanation assumes that only a small fraction, on the order of part per thousand or million of the DC sources fluctuate. Such model is natural in cases such as an adsorbate which moves by a distance small compared to the ion-surface spacing, or patch potential noise which originates only on the grain boundary.

6.3.2 Measurements of Fluctuating Fields

Quantitative measurements of fluctuating fields have been performed using microfabricated cantilevers. The vibrational mode of such cantilever couples to the noise field, resulting in a damping force proportional to the cantilever's charge. This damping is typically observed only at sub-µm distances.

Assume that the surface distance and frequency scalings of the noise are d^{-4} and f^{-1}, over the necessary range. Rewriting the room temperature data as $S_E(f) = f^{-1}d^{-4} \times 10^{-21}\mathrm{V}^2\mathrm{m}^2$, the expected noise at 100 nm and 10 kHz is

$$S_E \approx 10^3 \ \mathrm{V}^2/\mathrm{m}^2/\mathrm{Hz} \tag{6.24}$$

Reference [KLM06] reports a field noise above gold surfaces which scales as d^{-2} with a value at 100 nm (from Figure 3) of

$$S_E = 10^3 \ \mathrm{V}^2/\mathrm{m}^2/\mathrm{Hz} \tag{6.25}$$

Similar measurements from Reference [DFWG99] state that the cantilever damping rate is $\frac{\Gamma}{m_{eff}} = \frac{18\times10^6}{d^4}\ \mathrm{s}^{-1}$, where $m_{eff} = 10^{-11} - 10^{-13}$ kg is the effective mass of the cantilever and d is the distance to the surface in nm. At $d = 100$ nm,

$$\frac{\Gamma}{m_{eff}} = 0.16 \ 1/\mathrm{s} \tag{6.26}$$

Assuming contact voltage of 0.2 V and capacitance 10^{-17} F [CCW+03], the field noise can be written as [SMS+01]

$$\begin{aligned} \frac{S_E}{m_{eff}} &= \frac{4k_BT\Gamma m_{eff}}{C^2V^2} \\ &= 662\frac{m_{eff}}{\mathrm{kg}} \times 10^{12} \ \mathrm{V}^2/\mathrm{m}^2/\mathrm{Hz} \\ &= 66 \times (1 - 100) \ \mathrm{V}^2/\mathrm{m}^2/\mathrm{Hz} \end{aligned} \tag{6.27}$$

where the $1 - 100$ range is the specified uncertainty in cantilever mass m_{eff}.

Reference [SMS+01] reports fields three orders of magnitude smaller, at 0.8 $\mathrm{V}^2/\mathrm{m}^2/\mathrm{Hz}$. However, the tip used in those experiments had a much larger radius of curvature, equal to approximately 1 µm as compared to < 100 nm used in Reference [KLM06]. The large curvature may result in measurement of an average of the field noise, or an overestimated value of tip capacitance.

Notably, the noise fields reported in Reference [SMS+01] are suppressed by a factor of 20 upon cooling to 77 K, and an additional factor of 25 after cooling to 4 K. Both of these factors are within a factor of 2 of those observed in the gold ion traps.

The measurements performed using microfabricated cantilevers are in a very good agreement with noise fields extrapolated from ion trap data, indicating that the d^{-4} scaling law holds down to distances as small as 1 µm, placing an upper bound on the size of the patch sources. The wide variety of materials which can be studied by this method, and the relative simplicity of sample preparation should allow for a significant progress in understanding the material dependence of the observed noise.

6.4 Conclusions and Impact of the Results

The noise process exhibits a complex behavior, with strong dependences on fabrication, cleaning and temperature cycling history of the trap. Such variability makes any attempt at understanding the source of heating extremely challenging. Temperature dependence provides a new way of characterizing the noise, intimately tied to the physical source through activation energies. The observed behavior is not in agreement with previously proposed theoretical models, and is incompatible with a process characterized by a single activation energy. The proposed theoretical model, assuming a continuous spectrum of energies can explain the temperature dependence, but needs refinement to match the frequency dependence of noise.

Measurements of heating in superconductive traps conclusively show the noise to be a surface process, unconnected to the bulk resistivity of the material. Unfortunately, the continuous spectrum of energies and the surface origin of the noise suggests further progress will require a better understanding of surface physics. Measurements of damping of micromechanical cantilevers may provide a better way of characterizing potential fluctuations on surfaces, due to the generality of the method and the simplified sample preparation.

While a large number of questions remain, the demonstrated suppression of the field noise allows for a significant reduction of trap sizes used in demonstrations of quantum gates. Assuming d^{-4} and ω^{-2} scalings, the cryogenically cooled traps would offer decoherence rates smaller than 100 quanta/s in traps as small as 10 µm operating at 10 MHz. Given the achievable 2-ion gate times of $O(10\ \mu\text{m})$, such heating rates would increase gate failure probability by 10^{-3}, comparable to current estimates of the threshold error probability for fault tolerant quantum computation [Ste03].

Chapter 7

Demonstrations of Quantum Operations Using Cryogenic Surface Electrode Traps

The dramatic reduction of the heating rates removes a known source of decoherence, but does not in itself demonstrate the feasibility of executing high fidelity quantum operations. Low heating rates correspond to a long amplitude decoherence time, but do not provide a lower bound on the equally important phase decoherence time. It is conceivable that the trapped ions suffer from an unforeseen noise which dephases the atomic or motional qubit. A successful implementation of one and two-qubit operations, however, fully validates the cryogenic microfabricated ion traps for trapped ion quantum computing experiments.

The demonstrated coherent operations are presented in two parts. In Section 7.1, the atomic state is measured after a continuous qubit rotation on either the carrier or the sideband transition. The resulting data allows for an estimate of the laser amplitude errors and the state preparation fidelity. Section 7.2 focuses on a small number of quantum gates, including identity, π rotations on carrier and sideband transitions and a Controlled-NOT (CNOT) gate on the atomic qubit controlled by the motional qubit. For each of these gates the truth table, or transition amplitudes, for the 4 computational basis states of the atomic and motional qubit are measured. Experimental error sources are discussed based on the achieved similarity of the gates to their respective ideal implementations.

The demonstrated gates are sufficient to perform any operation on a single ion. Scaling to a larger number of ions requires the ability to individually address each of the ions. Section 7.3 is devoted to a new method of distinguishing of ions trapped in an ion trap, using the magnetic field sensitivity of the qubit transitions. Magnetic bias field used to separate the Zeeman sub-states is stabilized using a precisely designed arrangement of superconductive rings. An additional coil microfabricated in the electrode structure imposes a field gradient, allowing for individual addressing of the ions. Simple experiments, such as a controlled rotation of one of the two ions and ion coherence measurement demonstrate the addressing ability.

The experiments in this Chapter are performed on ions trapped 100 µm above the trap surface, which, to our knowledge, constitutes the smallest such distance in experimental demonstrations of quantum operations.

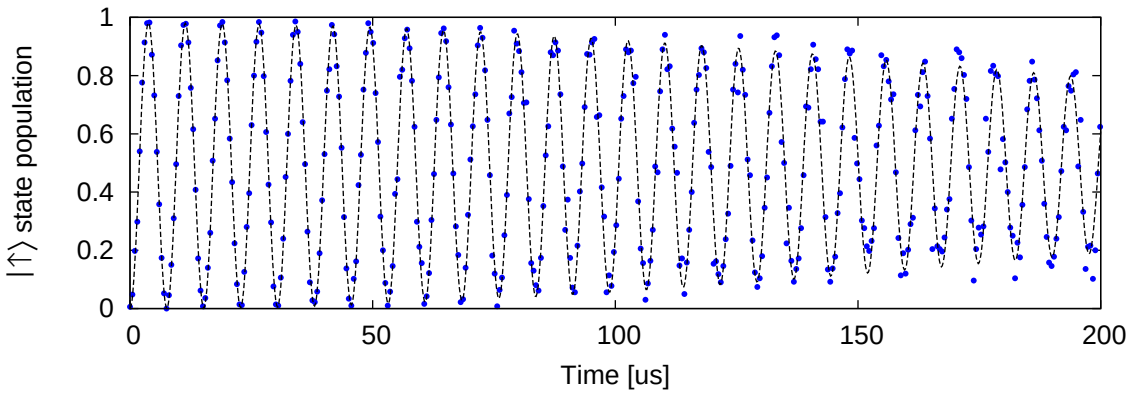

Figure 7-1: Rabi flop on the carrier transition, between the $|\downarrow\rangle|0\rangle$ and $|\uparrow\rangle|0\rangle$ states. The Rabi frequency is $\Omega = 132$ kHz with initial contrast of 98%. The oscillation's envelope is fitted to a Gaussian, yielding HWHM of 240 µs.

7.1 Continuous Qubit Rotations

The theoretical description of the trapped ion and its interaction with laser light is derived in Chapter 2. In particular, rotations in the $|\downarrow\rangle|0\rangle$, $|\uparrow\rangle|0\rangle$ and the $|\downarrow\rangle|0\rangle$, $|\uparrow\rangle|1\rangle$ subspaces are executed using appropriately detuned laser pulses. This section explores the effect of these pulses on the atomic state of an ion initially prepared in the $|\downarrow\rangle|0\rangle$ state.

The motional state of the ion is initialized using sideband cooling (cf. Section 2.4.3). The atomic state of the ion is initialized using optical pumping on the "pump" transition (cf. Section 2.6). Based on the observed transition probabilities on the motional sidebands and the pump transition, the initialization to the the $|\downarrow\rangle|0\rangle$ state is successful $\approx 99\%$ of the time.

The simple carrier and sideband rotations discussed here are a standard part of any trapped ion experiment, and do not constitute a novel contribution. However, deviations from the ideal behavior provide valuable information about the dominant error sources in the system.

7.1.1 Carrier Rotations - X axis

Rotations of the atomic qubit vector on the Bloch sphere about the $\hat{x}$ axis are executed using a laser pulse tuned to the carrier of the qubit transition. For a laser Rabi frequency Ω, illumination time τ, and initial state $\psi_0 \equiv |\downarrow\rangle|0\rangle$, the final qubit state is

$$\begin{aligned}\psi &= R_x(\Omega\tau)\psi_0 = (\cos(\Omega\tau/2)I - \imath\sin(\Omega\tau/2)\sigma_x)\psi_0 \\ &= (\cos(\Omega\tau/2)|\downarrow\rangle - \imath\sin(\Omega\tau/2)|\uparrow\rangle)|0\rangle \end{aligned} \tag{7.1}$$

where I is the identity and σ_x is the Pauli σ matrix. Subsequent measurement of the atomic state is expected to return $|\uparrow\rangle$ with probability $\sin(\Omega\tau/2)^2 = \frac{1}{2}(1 - \cos(\Omega\tau))$.

The experimental probability of the ion being measured in the $|\uparrow\rangle$ state is plotted in Figure 7-1. The data exhibits clear sinusoidal oscillations between the $|\downarrow\rangle$ and $|\uparrow\rangle$ states with a 7.6 µs period. The envelope of the fringes is fitted to a Gaussian, yielding half width at half max (HWHM) of $T_{HWHM} = 237 \pm 7$ µs and initial contrast of $98.1 \pm 0.5\%$.

The Gaussian envelope indicates a Gaussian spectrum of Rabi frequencies, with a standard deviation $\Gamma = \frac{\sqrt{2\log 2}}{2\pi T_{HWHM}} = 790 \pm 25$ Hz, equal to 0.6% of the Rabi frequency. This amount of variability could be explained by a 1.2% change in the laser power, which is not actively stabilized, over the length of the scan. Static measurements of the diode laser power indicate better than 0.1% power stability. However, the laser power at the trap drifts by up to a 1% over minutes, attributed to thermal effects in the AOMs and RF sources, consistent with the observed envelope. Similar amplitude changes can be expected from the fluctuation of the polarization angle at the output of the polarization maintaining fiber, and drifts in the alignment of the laser to the ion. Improvement of the rotation fidelity requires active locking of the laser power, and tracking of the Rabi frequency during the experiment.

The initial contrast of the envelope indicates either imperfect state preparation or slight detuning of the laser with respect to the ion. The peak transition probability for a laser detuned by Δ is $\frac{\Omega^2}{\Omega^2+\Delta^2}$. At a Rabi frequency of $\Omega = 132$ kHz, the peak transition probability decreases to 98% for $\Delta \approx 20$ kHz, much larger than the measured laser FWHM of 900 Hz (cf. Section 4.4). The missing 2% is therefore attributed to imperfect initial state preparation, such as failure to pump to the $|\downarrow\rangle$ qubit state, or failure to cool the ion to a low lying motional state.

Despite these errors, on the order of 60 π rotations can be performed before a 50% loss of contrast.

7.1.2 Carrier Rotations - Z axis

Arbitrary rotations of the qubit's Bloch sphere can be accomplished by performing at most three rotations, around the $\hat{x}$ and $\hat{y}$ directions (cf. Section 2.3). Rotation about the $\hat{z}$ axis are a special case, however, and can be accomplished trivially by commuting the gate through the following gates until the measurement, resulting in a change of the laser phases used in those operations. Rotation about $\hat{z}$ by an angle θ is equivalent to an additional phase shift θ of every subsequent laser pulse. In particular, a π rotation, typically denoted by Z, is equivalent to π shift of the phase of each subsequent laser pulse. The fidelity of these rotations is limited only by the laser frequency fluctuations and the precision of the phase adjustment, equal to 0.04° in our set-up.

7.1.3 Composite Rotations - BB1

The Rabi frequency fluctuations observed in Section 7.1.1 can be removed using composite pulse sequences. One such sequence, called BB1, uses four laser pulses to suppress a small systematic error ϵ in the Rabi rotation rate Ω, reducing the rotation angle error to $O(\epsilon^3)$. BB1 has been extensively employed in NMR, but, to our knowledge, has not been used in ion traps before.

The laser pulses and phases in the BB1 sequence depend on the desired final state. For desired $\pi/2$ rotation about the $\hat{x}$ axis, a $\pi/2$ rotation about $\hat{x}$ is performed first. Subsequently, π, 2π and a π rotations about axes at 97.2°, 291.5°, 97.2° angle to the $\hat{x}$ axis are applied [Wim94]. The intuitive idea behind the sequence is represented pictorially in Figure 7-2. Three cases are shown, with each laser pulse under-rotating the qubit by 25% (left diagram), each pulse performing exact rotation (center) and each pulse over-rotating the qubit by 25% (right). In each case, the final Bloch sphere rotation is closer to the desired after the corrective pulses.

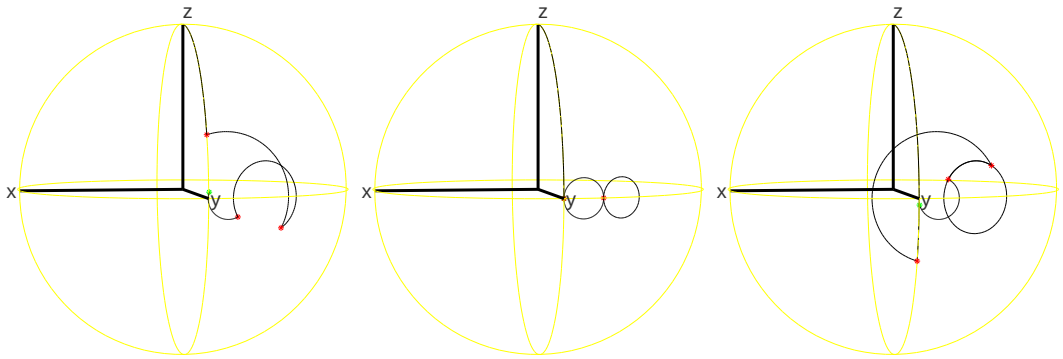

Figure 7-2: The trajectories on a Bloch sphere of a spin driven by a BB1 composite pulse in with 25% under-rotation error (left), no systematic rotation error (center) and a 25% over-rotation error. Reproduced with permission from [VC05].

Figure 7-3 demonstrates the observed state populations for a single pulse rotation, BB1 corrected pulse and the theoretical fits to both. In case of a $\pi/2$ rotation, the desired final state is $|\downarrow\rangle - \imath|\uparrow\rangle$, with 0.5 probability of measuring either state. These state populations, following a single rotation by an angle $\frac{\pi}{2}(1+\epsilon)$ are proportional to ϵ around 0, as seen from the experimental data ($\times$) and theoretical fit (dashed line). The BB1 corrected populations are insensitive to ϵ around $\epsilon = 0$, as expected. Similar effect is observed for a desired π rotation, where the state populations after a BB1 corrected rotation are insensitive to the error ϵ over a wide range.

Despite the demonstrated error correcting capability of the BB1 sequence, the fit amplitude of the BB1 corrected π pulse is 98%, offering no improvement over the initial contrast of a single π rotation. This result strongly supports the previous hypothesis that, for small rotation angles, the contrast is limited by state preparation errors, rather than the rotation angle errors. Current experiments require a total rotation angle of less than 10π, in which case the BB1 sequence is not expected to improve the fidelity.

7.1.4 Sideband Rotations

Sideband rotations are sensitive to the initialization and decoherence of the motional state in addition to the laser power fluctuations. In particular, imperfect motional state cooling reduces the contrast of the fringes, and decoherence of the motional state reduces the envelope half width.

Sideband rotations rotate the qubits between the $|\downarrow\rangle|0\rangle$ and $|\uparrow\rangle|1\rangle$ states (cf. Section 2.3). For a laser Rabi frequency Ω, illumination time τ, and initial state $\psi_0 \equiv |\downarrow\rangle|0\rangle$, the final qubit state is

$$\psi = \cos(\eta\Omega\tau/2)|\downarrow\rangle|0\rangle - \imath\sin(\eta\Omega\tau/2)|\uparrow\rangle|1\rangle \tag{7.2}$$

where η is the Lamb-Dicke parameter. Subsequent measurement of the atomic state is expected to return $|\uparrow\rangle$ with probability $\sin(\eta\Omega\tau/2)^2 = \frac{1}{2}(1-\cos(\eta\Omega\tau))$.

The experimental probability of measuring the $|\uparrow\rangle$ state is plotted in Figure 7-4. The oscillation frequency is reduced by $\eta \approx 0.05$ as compared to the carrier rotations, with a single π rotation taking 68 µs. The envelope of the fringes is fitted to a Gaussian, yielding HWHM of $T_{HWHM} = 1250$ µs and initial contrast of $97.5 \pm 0.3\%$.

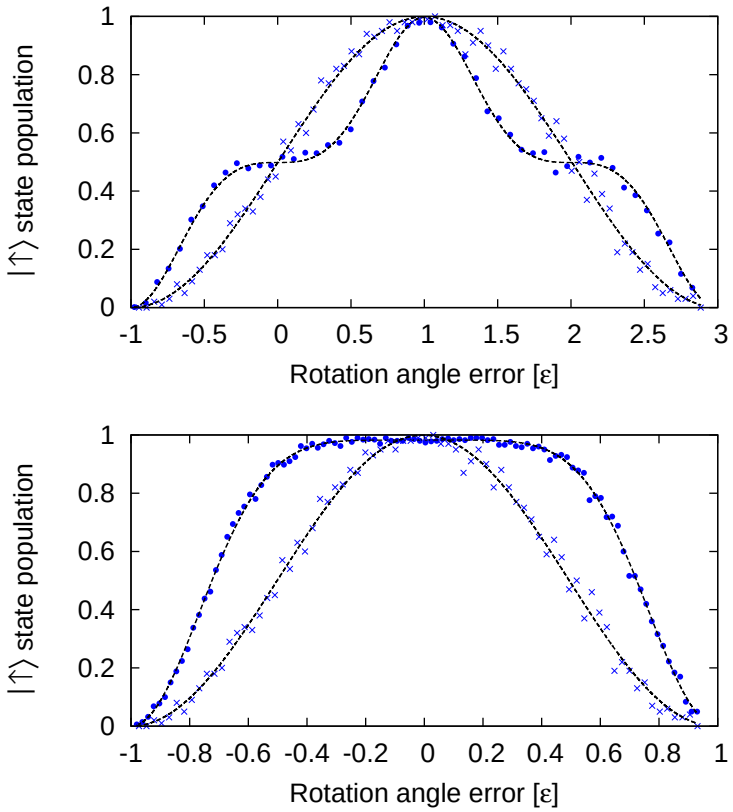

Figure 7-3: Systematic laser amplitude errors and pulse length errors distort all rotation angles from θ to $\theta(1+\epsilon)$. (top) Population after a BB1 sequence designed for a desired $\pi/2$ rotation, as a function of ϵ ($\bullet$) and an uncorrected single pulse rotation ($\times$). (bottom) Population after a BB1 sequence designed for a desired π rotation, as a function of ϵ ($\bullet$) and an uncorrected single pulse rotation ($\times$). Theoretical fits to all curves are plotted as well (dashed lines). The corrected data demonstrates reduced sensitivity to ϵ around $\epsilon = 0$

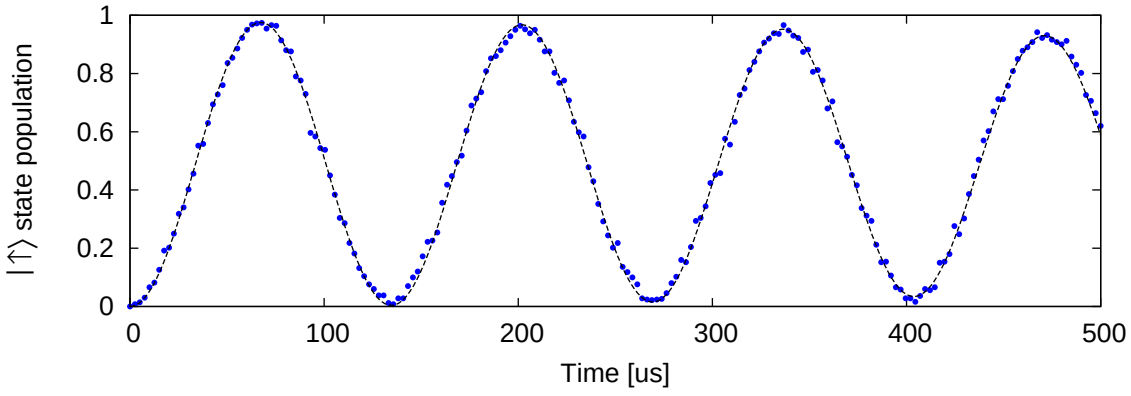

Figure 7-4: Rabi flop on the blue sideband transition, between the $|\downarrow\rangle|0\rangle$ and $|\uparrow\rangle|1\rangle$ states. The Rabi frequency is $\Omega = 7.4$ kHz with an initial contrast of 97.5%. The oscillation's envelope is fitted to a Gaussian, yielding HWHM at 1250 µs.

The Gaussian envelope indicates a Gaussian spectrum of Rabi frequencies, with a standard deviation $\Gamma = \frac{\sqrt{2\log 2}}{2\pi T_{HWHM}} = 150 \pm 10$ Hz, equal to 2% of the Rabi frequency. The increase in fractional fluctuation of the Rabi frequency over that observed in the case of a carrier rotation can be attributed to the 900 Hz FWHM of the laser frequency. The effective Rabi frequency Ω_{eff} for a laser detuned by Δ from the transition equals $\Omega_{eff} = \sqrt{\Omega^2 + \Delta^2} \approx \Omega\left(1 + \frac{\Delta^2}{2\Omega^2}\right)$. For $\Omega = 7.4$ kHz, the laser frequency fluctuations contribute $O(1\%)$ noise to the Rabi frequency for average detuning $\langle\Delta\rangle = 0$, and $O(3\%)$ for average detuning $\langle\Delta\rangle = 900$ Hz. Therefore, without further stabilization of the laser, it can not be concluded that the envelope decay is indicative of motional state decoherence.

The initial contrast, comparable to that observed on the carrier transition, suggests that the motional state initialization is successful with a high probability.

The oscillating behavior of the qubit requires phase coherence between the $|\downarrow\rangle|0\rangle$ and $|\uparrow\rangle|1\rangle$ states. The Gaussian envelope should allow for approximately 20 rotations before a 50% loss of contrast, demonstrating coherence between the $|0\rangle$ and $|1\rangle$ for longer than 1.0 ms.

7.2 Process Tomography - Truth Table

The previous section discussed the population in the $|\uparrow\rangle$ state after a simple rotation starting from the $|\downarrow\rangle|0\rangle$ state, providing a partial characterization of the action of these rotations. For any specified gate operations much more information is available by preparing each of the computational basis states, $|\downarrow\rangle|0\rangle$, $|\downarrow\rangle|1\rangle$, $|\uparrow\rangle|0\rangle$, $|\uparrow\rangle|0\rangle$, applying the desired gate, and reading out the populations in each of the basis states, as described in Section 2.5. The resulting matrix is equivalent to the classical truth table of the chosen gate.

16 experiments are required to create the truth table, with a 1000 repetitions of each measurement performed to obtain the transfer probabilities. Both single rotations and a two-qubit gate are investigated, and the resulting truth tables compared to theoretical expectations.

7.2.1 Single Pulse Gates

The simplest gate to characterize is the identity, with the expected result being a matrix with 1's on the diagonal, and 0's everywhere else. Deviations from the expected result characterize the state preparation and readout. The accuracy of the carrier rotations can be checked by measuring the truth table of a π rotation on the carrier. Similarly, a π rotation on the blue sideband, denoted by π^+, provides the relevant fidelity for sideband rotations.

Figure 7-5 shows the experimental results. The diagonal elements of the identity truth table (top) remain in $92 - 96\%$ range, providing an estimate of the fidelity of the measurement process. Carrier π rotation interchanges amplitudes in the $|\downarrow\rangle$ and $|\uparrow\rangle$ states, as expected, with very little loss of contrast. The π^+ rotation interchanges the $|\downarrow\rangle|0\rangle$ and $|\uparrow\rangle|1\rangle$ states while leaving the $|\uparrow\rangle|0\rangle$ state untouched, as expected. The $|\downarrow\rangle|1\rangle$ does not, however, remain intact. Due to the degeneracy of the motional transition frequencies, the $|\downarrow\rangle|1\rangle$ state is partially transferred to the $|\uparrow\rangle|2\rangle$ state, with expected transfer probability equal to $\sin\left(\pi\sqrt{2}/2\right)^2 = 0.63$. The $|\uparrow\rangle|2\rangle$ state, however, is outside of the qubit space, and erroneously measured as $|\uparrow\rangle|1\rangle$ or $|\uparrow\rangle|0\rangle$, resulting in measured probabilities of approximately 33% in each of the three states.

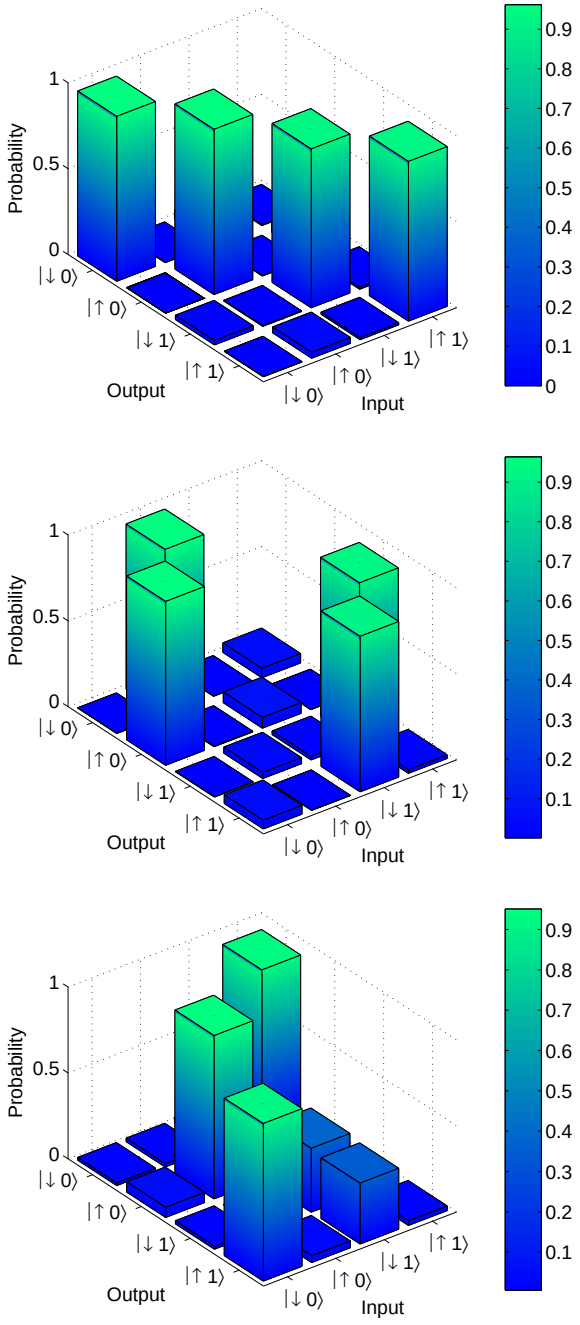

$$\begin{pmatrix} 96.0 & 0.3 & 5.2 & 0.6 \\ 0.0 & 96.2 & 0.3 & 5.1 \\ 2.5 & 0.4 & 92.5 & 1.3 \\ 0.1 & 3.4 & 1.2 & 92.9 \end{pmatrix}$$

$$\begin{pmatrix} 0.1 & 96.4 & 0.3 & 5.5 \\ 95.4 & 0.4 & 6.2 & 0.1 \\ 0.2 & 3.5 & 2.1 & 92.4 \\ 5.0 & 0.1 & 90.5 & 2.1 \end{pmatrix}$$

$$\begin{pmatrix} 1.6 & 2.0 & 3.6 & 93.2 \\ 5.9 & 95.1 & 23.8 & 1.6 \\ 1.8 & 0.6 & 37.2 & 3.7 \\ 91.7 & 3.9 & 35.4 & 2.7 \end{pmatrix}$$

Figure 7-5: Truth table measurements for simple gates: identity (top), a π-pulse (middle), and a π^+-pulse (bottom).

Quantitative characterization of the gate error can be made by defining an appropriate distance measure. Following Reference [CFR+08], define similarity S between the theoretical and experimental truth tables, T and E, to be

$$S = \frac{1}{16}\left(\sum_{i,j=1}^{4}\sqrt{T_{i,j}E_{i,j}}\right)^2 \tag{7.3}$$

This definition is very similar to the definition of classical fidelity, usually given as

$$F = \frac{1}{N}\sum_{i=1}^{N} p(f(|i\rangle) \mid |i\rangle) \tag{7.4}$$

where $|i\rangle$ are the N computational basis states, $f(|i\rangle)$ is the expected state after the gate operation and $p(|a\rangle \mid |b\rangle)$ is the truth table element corresponding to an initial state $|a\rangle$ and a final state $|b\rangle$. In our experiments, both of these distance measures return an essentially equal value.

The similarities of the demonstrated rotations to the ideal implementations are 0.94, 0.94 and 0.93 for the identity, π and π^+ rotations. The approximately equal fidelities of the three gates indicate that the π and π^+ gates are executed with much higher fidelity than the state preparation and readout. This conclusion is, again, in agreement with experiments in Section 7.1 which suggested the state initialization to be the most significant source of error.

7.2.2 Controlled-NOT Gate

The π^+ rotation can take the ion out of the computational space, and does not constitute a useful two qubit gate unless the state is known not to be $|\downarrow\rangle|1\rangle$. Instead, a composite rotation consisting of 4 sideband pulses can be used to change the phase of the atomic qubit by an amount dependent on the motional state qubit, while leaving the ion within the computational space for all initial states. Together with 2 Ramsey pulses, these rotations effect a Cirac-Zoller type CNOT gate, with the motional and atomic qubits serving as control and target, respectively. Successful implementation of this gate is conditional on phase and amplitude coherence of the atomic and motional qubits during the gate operation, making the CNOT a very attractive probe of the coherence of the trapped ion. The gate and the required Stark shift corrections are described in detail in Section 2.3.4.

A similar gate has been implemented as early as 1995 by Monroe et al. using a single $^9Be^+$ ion, with similarities $\approx 80\%$ [MMK+95]. More recently, Riebe et al. demonstrated a CNOT gate with $\approx 92.6(6)\%$ process fidelity [RKS+06] using two $^{40}Ca^+$ ions. Much higher fidelities are possible using the so-called bichromatic gates, based on a scheme by Sørensen and Mølmer [SM99]. The current record fidelity is 99.3(1)% for a bichromatic gate in $^{40}Ca^+$ ions[BKRB08].

The gate discussed in this section is based on Reference [RKS+06], with a number of important differences. The stark shifts are compensated using appropriate shifts of gate phases, rather than by an additional laser beam, simplifying the experimental set-up. No extra phase or frequency corrections above those described in Section 2.3.4 are necessary. The truth table measurements presented do not contain phase information, and can not be

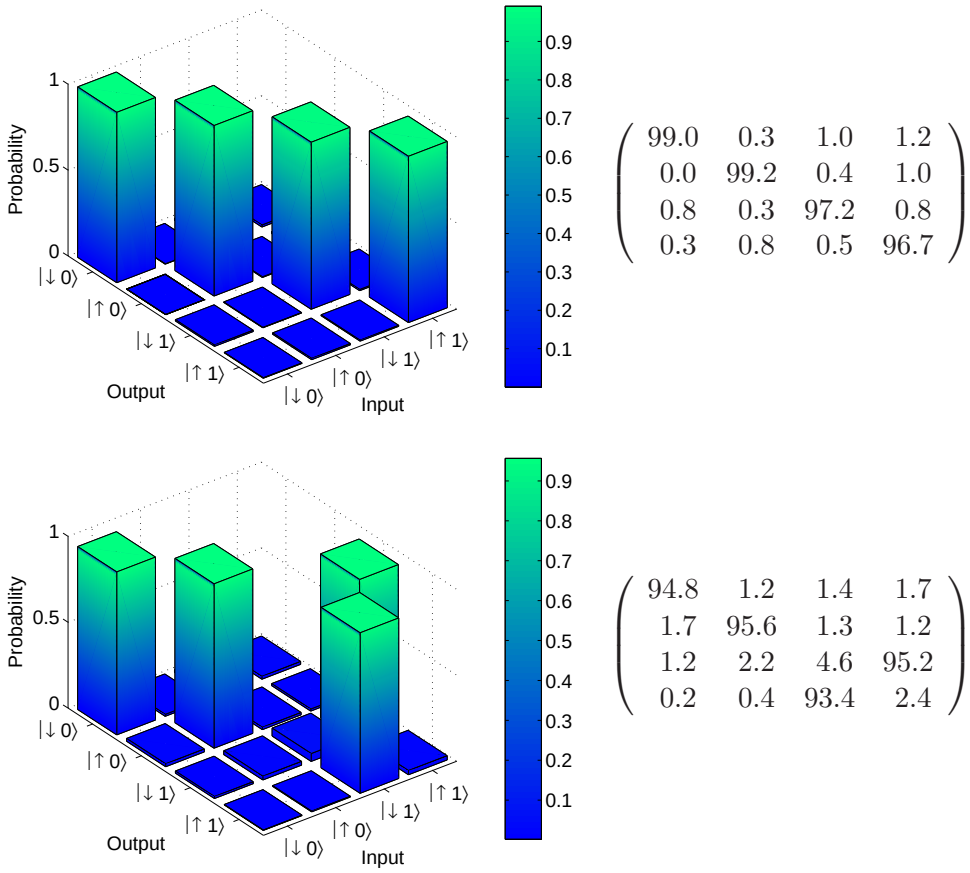

$$\begin{pmatrix} 99.0 & 0.3 & 1.0 & 1.2 \\ 0.0 & 99.2 & 0.4 & 1.0 \\ 0.8 & 0.3 & 97.2 & 0.8 \\ 0.3 & 0.8 & 0.5 & 96.7 \end{pmatrix}$$

$$\begin{pmatrix} 94.8 & 1.2 & 1.4 & 1.7 \\ 1.7 & 95.6 & 1.3 & 1.2 \\ 1.2 & 2.2 & 4.6 & 95.2 \\ 0.2 & 0.4 & 93.4 & 2.4 \end{pmatrix}$$

Figure 7-6: Improved truth table measurement of an identity (top) and a CNOT gate (bottom).

compared directly with the process fidelity values. Finally, the gate is implemented using a single ion only; extension to two ions requires individual addressing of the ions, further discussed in Section 7.3.

Figure 7-6 presents the experimental truth table of the implemented gate CNOT gate, as well as an identity gate measured during the same experimental run. The improvement of the similarity of the identity gate to 0.98 is attributed to a careful determination of the qubit frequencies and active tracking of the laser Rabi frequency during the data acquisition. The similarity of the CNOT gate to an ideal implementation is 0.95, 0.03 lower than the value for the identity gate. This drop is consistent with the ≈ 1 ms Gaussian envelope of the sideband rotations observed in Section 7.1.4, and the $O(0.01)$ drop observed for a single π^+ gate observed in Section 7.2.1. Therefore, the gate error can be fully attributed to technical noise discussed in Section 7.1.4.

7.2.3 Conclusions

The experiments presented in this chapter demonstrate the first coherent operations in an ion trapped 100 µm above the trap surface, with similarity to an ideal implementation in excess of 95%. The demonstrated rotations and CNOT operations do not indicate any non-trivial sources of decoherence of the atomic or motional qubit; state preparation error and

expected laser frequency fluctuations are sufficient to explain the loss of fidelity observed in our data. Improving on the demonstrated ≈ 1 ms coherence time requires further stabilization of the power and frequency of the qubit laser. This can be accomplished with well known techniques, and does not present a significant challenge.

We note that this implementation of the CNOT gate would fail in the fabricated traps at room temperature. The total length of the gate is on the order of 250 µs. At the measured room temperature heating rate of $\approx$ 4000 s^{-1}, the ion's motional state is expected to decohere during the gates duration. For the best 6 K heating rates, though, the expected number of quanta picked up during the gate execution is 0.001.

Current fidelity values allow for execution of a few gates, suggesting further experimental effort to be placed on scaling the experiment to a larger number of qubits. The next section is devoted to one possible approach to scaling the system to a few qubits.

7.3 Individual Ion Addressing

All of the experiments discussed so far made use of a single trapped ion and its motional state. To scale these experiments up, two ion operations are required, accomplished by co-trapping the ions in the same zone and utilizing the shared motional mode to interact them. Non-trivial algorithms require both two qubit and single qubit operations. The co-trapped ions are spaced by $O(10\ \mu m)$, thus requiring either very precise laser focusing [NLR+99], or separating the ions further apart, to separate trap zones [BCS+04] in order to perform the desired single qubit operations. The former presents significant experimental challenges, while the latter requires time and precise control over trap voltages.

Close proximity of the ion chain to the trap electrodes, together with the magnetic field sensitivity of the qubit transition allows for a novel solution. By etching parts of the electrodes away, a current path can be defined generating a position dependent magnetic field, separating the qubit transitions and allowing for addressing of the ions by adjusting the laser frequency. The required field sensitivity, however, can become a source of decoherence if the magnetic fields fluctuate. In this section, both a method for stabilizing the magnetic fields as well as a design and characterization of a gradient loop are presented.

A similar approach has been discussed in literature[WMI+98, MW01], and applied to selectively read-out the ion state[JBT+08]. This section presents the first application of this method to single qubit rotations on a selected ion in an ion crystal, and the first gradient coil design integrated in the trap structure.

7.3.1 Magnetic Field Stabilization

Consider a uniform noise field with a value $\vec{B}(t)$, a reasonable approximation for distant sources. The strong bias field $\vec{B}_0$ used to split the Zeeman levels and define a quantization axis (cf. Section 2.6.1) points along the $\hat{z}$ direction. Noise fields in the $\hat{x} - \hat{y}$ plane tilt the polarization axis, but are not expected to dephase the ion significantly. The $\hat{z}$ component, however, is crucial to stabilize.

The low temperature environment of the cryogenic ion trap suggests the use of a superconductive material for stabilizing the magnetic fields. Superconductive loops, in particular, can be used to trap flux for as long as the superconductivity of the loop is maintained. However, stable flux is not equivalent to a stable field at the ion's position, except in special cases.

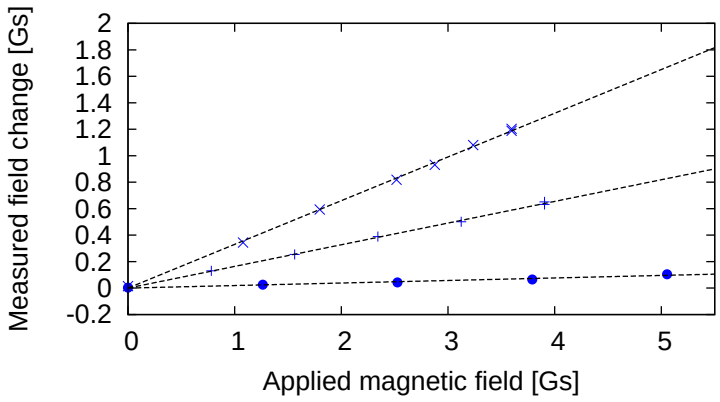

Figure 7-7: Two superconductive discs, one below and one above the trapped ion, stabilize the magnetic field in the $\hat{z}$ direction. The three curves correspond to the field fluctuation suppression due to the top disc only ($\times$), the bottom disc only ($+$) and both discs. When both discs are used, field changes are suppressed 50-fold.

For a uniform field in $\hat{z}$ direction, two superconductive discs accomplish such feat. The first ring has an inner radius of 1 mm and an outer radius of 5 mm and is placed 1 mm below trap center. The second has an inner radius of 5 mm and an outer radius of 25 mm and is placed 7 mm above trap center. Numerical calculation of the current and field distributions in this arrangement of superconductors promise a 96% suppression of the magnetic field fluctuations $\vec{B}(t) \cdot \hat{z}$ at the ion [BC03].

The experimental verification of the theoretical prediction is shown in Figure 7-7. The magnetic field is measured by observing the splitting of the Zeeman lines of the ion against the external applied field. In case of a single ring, either above or below the trap, a modest suppression is observed, by a factor of $3-6$. When both of the rings are employed, however, the external field is suppressed 50 fold, slightly exceeding the theoretical prediction.

7.3.2 Magnetic Field Gradient

The magnetic field at a distance d away from a current wire falls off as $1/d$, with the field gradient scaling as $1/d^2$. Large splitting of the qubit frequencies will require positioning the gradient creating wires as close as possible to the ion. At the same time, to simplify fabrication, the design should not to call for additional metal layers or changes in the fabrication process.

Figure 7-8 shows the required changes to the ground electrode. The coil, driven with a current I, is designed to provide a gradient of 6 $\frac{I}{100\ \mathrm{mA}}$ Gs/mm, and to minimize the absolute value of the field at the center of the trap, with the expected field of $B = (0.16\hat{x} - .01\hat{y} + 0.002\hat{z})\ \frac{I}{100\ \mathrm{mA}}$ Gs. The low residual field should reduce decoherence due to fluctuations in the gradient current.

Actual gradient values can be measured by trapping two ions in the trap, and observing the relative positions of the qubit transitions. The distance between two co-trapped ions is

$$s = 2^{1/3} \left(\frac{e^2}{4\pi\epsilon_0 m \omega_z^2} \right)^{1/3} \tag{7.5}$$

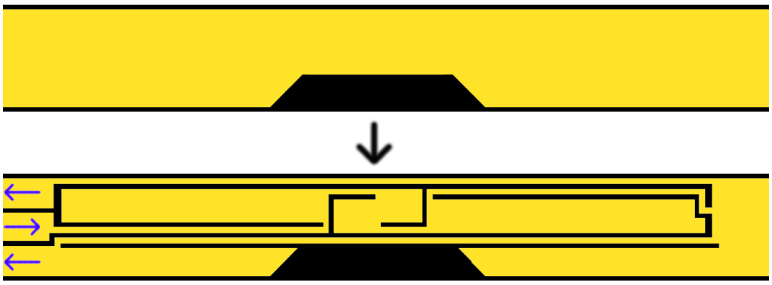

Figure 7-8: Changes required to introduce the gradient field coil to the trap. (top) Original design of the center ground electrode (yellow). (bottom) Revised design, with parts of the electrode etched away during fabrication (black lines), defining current traces. Blue arrows designate the current flow.

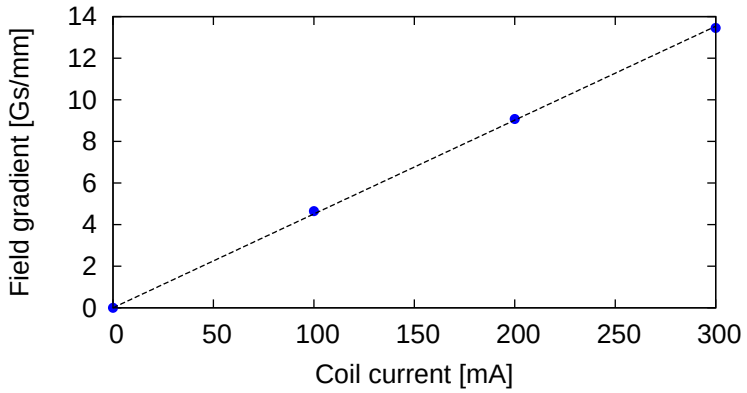

Figure 7-9: Observed gradient field as a function of the applied current. Slope of the fit equals 4.5 $\frac{\text{Gs}}{\text{mm}} \frac{I}{100\ \text{mA}}$.

where ω_z is the axial common-mode vibrational frequency, m the mass of the ion and e its charge. The frequency shift of the qubit transition, taking into account the g-factors of ground and excited states, equals to $2\mu_B B$. For a measured qubit frequency splitting of Δf, the field gradient equals,

$$\frac{\partial B}{\partial x} = \frac{\Delta f}{2s\mu_B} \tag{7.6}$$

Figure 7-9 shows the measured gradient values for a range of applied currents. The experimental value at 100 mA is somewhat smaller than expected, at 4.5 Gs/mm. A refined model of the gradient loop current distribution may explain the observed difference. The $\hat{z}$ projection of the field at the center of the ion crystal depends acutely on the compensation voltages, which shift the entire crystal with respect to the trap, but is typically smaller than 0.01 Gs at 100 mA.

The splitting of the qubit lines for a trap running at 1 MHz equals $\Delta f = 2s\mu_B \frac{\partial B}{\partial x} \approx 12 \frac{\partial B/\partial x}{\mathrm{Gs/mm}}$ kHz. At $I = 500$ mA, the frequency splitting is approximately 275 kHz.

7.3.3 Individual Addressing of Ions

Preliminary data demonstrating the ability to perform a Rabi flop on one of the two qubits is shown in Figure 7-10. The state of both ions is measured after the applied rotation, and the populations with zero, one or two ions in the state $|\downarrow\rangle$ are counted. No effort was made to identify which of the ions was in the $|\downarrow\rangle$ state in the case of a single ion in each of the $|\uparrow\rangle$, $|\downarrow\rangle$ states. The plot demonstrates the transitions between a configuration with both ions in the $|\downarrow\rangle$ state to a configuration with only one ion in this state. The configuration with both ions in the $|\uparrow\rangle$ state remains relatively unpopulated. Therefore, it can be concluded that the Rabi rotation affects only one of the ions.

In this experiment, the Rabi frequency was lowered to avoid exciting of the second ion, and experimentally measured at $\Omega = 35$ kHz. The half width of the Gaussian envelope is ≈ 170 µs, allowing for ≈ 10 π rotations on the carrier. The initial contrast of the Rabi oscillations is 97%. These values are significantly lower than those observed in the single ion experiments, possibly a result of poor ground state cooling of the stretch and common vibrational modes of the ions.

The coherence time of the atomic qubit in presence of the gradient field was measured using Ramsey spectroscopy. The observed values decreased from the initial value of ≈ 550 µs at zero current to ≈ 400 µs at 500 mA. This reduction was observed with both a single ion and two ions trapped in the trap. Further experiments are needed to determine the source of this decoherence.

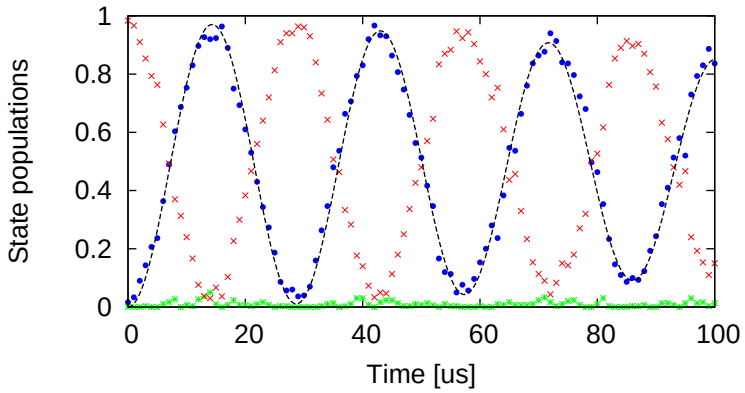

Figure 7-10: Rabi oscillations observed on one of the two co-trapped ions. Three populations are plotted, corresponding to a state with both ions in $|\downarrow\rangle$ state (red $\times$), one ion each in $|\downarrow\rangle$ and $|\uparrow\rangle$ states (blue $\bullet$) and both ions in $|\uparrow\rangle$ state (green $*$). The fit to the second dataset is shown (dashed line), with fitted Rabi frequency $\Omega = 35$ kHz. The envelope is fitted to a Gaussian, yielding HWHM of 170 µs and initial contrast of 97%.

Chapter 8

Conclusions and Future Work

The motivation for this thesis was provided equally by the great success enjoyed by the trapped ion quantum computing community, and the continuous questions regarding its tenability. Ion traps hold the record for readout fidelity, single and two qubit operations and achieved algorithms. At the same time, the solid state qubits, patterned using well established microfabrication techniques, are often considered to provide an easier way to scaling to a large number of qubits. A successful marriage of trapped ion's coherence and microfabrication techniques seemed questionable due to the observed decoherence near the surface.

The successful demonstration of low decoherence and quantum operations in a sub-100μm microfabricated trap may be the most lasting impact of this thesis. Cryogenic cooling of trap surfaces can reduce the electric field noise, which causes decoherence of the motional state, by up to 7 orders of magnitude. Such dramatic improvement can increase motional state coherence to the level of atomic state coherences, and allow for quantum operations in ions as close as 10 μm to the trap surface. At such length scales, the qubit size and achievable gate speeds become comparable to those observed in solid state systems, alleviating the concerns of scalability. Long lifetimes achievable in cryostats, with demonstrated value of 10 hours and published values of months, may make such systems as robust as the lithographically defined qubits. Implementation of a Cirac-Zoller type CNOT gate between the ion and its motional state fully validates surface electrode ion traps for quantum information experiments. Other techniques developed, including the monolithic filtered laser system and the pulse sequencer were invaluable to the success of the core experiments, but certainly do not constitute the only way of accomplishing their respective goals.

Frequently, during the course of experiments, more questions arise than are answered. This was certainly the case in this work. While the motional heating was suppressed to values low enough not to constitute a major concern, the experimental data exhibited a number of baffling characteristics. Strong dependences on the fabrication process, observed in silver traps, together with the extremely high decoherence rates observed at room temperature remain mysterious. Variability of the measured noise with temperature cycling and cleaning in laboratory solvents measured in gold traps demonstrates a strong sensitivity of measured values to the details of fabrication and handling, making even qualitative comparisons between processes and traps difficult. Lastly, the measured temperature dependence of the noise does not extrapolate to 0 at 0 K, indicating either extremely small activation barriers or a tunneling process, neither of which was expected prior to this work.

The noise is characterized by a $1/f$ dependence and, unfortunately, seems as difficult to track down as similar noise sources in bulk metallic and semiconductive materials, which remain actively studied.

Some underdeveloped ideas presented in this thesis warrant further exploration. Superconductive ion traps promise hybrid quantum systems, integrating solid state and trapped ion qubits. High quality superconductive resonant circuits could also provide a new way of interacting trapped ions held in separate trap zones, providing a "quantum wire" between any pairs of ions. These ideas are currently being investigated for coupling of polar molecules; the strong interaction of the ion's unshielded charge may allow for even stronger couplings. The magnetic field gradient structures presented at the thesis' end may simplify experimental implementations of a few ion quantum processors. Similar ideas, using static and oscillating fields and their gradients, are concurrently being explored for addressing and gate operations by a number of groups.

The holy grail in the field of experimental quantum computing is a simple, scalable architecture for a physical realization of a quantum processor. While that goal was not achieved, this thesis provided a few more building blocks which may eventually be used in such a machine. Equally likely, though, this work will be made obsolete by advances in solid state quantum information processors, room temperature ion traps or classical computers. In either case, having the opportunity to construct a state of the art experiment from the ground up, and look at a mysterious process nobody has a handle on has been a gratifying experience.

Bibliography

[ADD+06] A. Andre, D. DeMille, J. M. Doyle, M. D. Lukin, S.E. Maxwell, P. Rabl, R. J. Schoelkopf, and P. Zoller. Polar molecules near superconducting resonators: a coherent, all-electrical, molecule-mesoscopic interface. *Nature Physics*, **2**, 636, 2006.

[ALB+07] Marco Anderlini, Patricia J. Lee, Benjamin L. Brown, Jennifer Sebby-Strabley, William D. Phillips, and J. V. Porto. Controlled exchange interaction between pairs of neutral atoms in an optical lattice. *Nature*, **448**, 452, 2007.

[AMK+] J. Alnis, A. Matveev, N. Kolachevsky, T. Wilken, Th. Udem, and T. W. Haensch. Sub-Hz line width diode lasers by stabilization to vibrationally and thermally compensated ule fabry-perot cavities. preprint available at http://arxiv.org/pdf/quant-ph/0801.4199v1.

[BB84] C. H. Bennet and G. Brassard. Quantum cryptography: Public key distribution and coin tossing. In *IEEE International Conference on Computers, Systems and Signal Processing*, p. 175, Bangalore India, December 1984.

[BB02] D. J. Berkeland and M. G. Boshier. Destabilization of dark states and optical spectroscopy in zeeman-degenerate atomic systems. *Phys. Rev. A*, **65**, 033413, 2002.

[BC03] A. A. Babaei Brojeny and J. R. Clem. Magnetic-field and current-density distributions in thin-film superconducting rings and disks. *Phys. Rev. B*, **68**, 174514, 2003.

[BCJD99] G. K. Brennen, C. M. Caves, P. S. Jessen, and I. H. Deutsch. Quantum logic gates in optical lattices. *Phys. Rev. Lett.*, **82**, 1060, 1999.

[BCL+07] K. R. Brown, R. J. Clark, J. Labaziewicz, P. Richerme, D. R. Leibrandt, and I. L. Chuang. Loading and characterization of a printed-circuit-board atomic ion trap. *Phys. Rev. A*, **75**, 015401, 2007.

[BCS+04] M. D. Barrett, J. Chiaverini, T. Schaetz, J. Britton, W. M. Itano, J. D. Jost, E. Knill, C. Langer, D. Leibfried, R. Ozeri, and D. J. Wineland. Deterministic quantum teleportation of atomic qubits. *Nature*, **429**, 737, 2004.

[BDL+00] P. A. Barton, C. J. S. Donald, D. M. Lucas, D. A. Stevens, A. M. Steane, and D. N. Stacey. Measurement of the lifetime of the 3d $D_{5/2}$ state in $^{40}Ca^{+}$. *Phys. Rev. A*, **62**, 032503, 2000.

[Ber02] D. J. Berkeland. Linear paul trap for strontium ions. *Rev. Sci. Inst*, **73**, 2856, 2002.

[BHI+89] J. J. Bollinger, D. J. Heinzen, W. M. Itano, S. L. Gilbert, and D. J. Wineland. Test of the linearity of quantum mechanics by rf spectroscopy of the $^{9}Be^{+}$ ground state. *Phys. Rev. Lett.*, **63**, 1031, 1989.

[BHI+91] J. J. Bollinger, D. J. Heinzen, W. M. Itano, S. L. Gilbert, and D. J. Wineland. A 303-Mhz frequency standard based on trapped Be^{+} ions. *IEEE Trans. Instr. Meas.*, **40**, 126, 1991.

[BKRB08] J. Benhelm, G. Kirchmair, C. F. Roos, and R. Blatt. Towards fault-tolerant quantum computing with trapped ions. *Nature Physics*, **4**, 463, 2008.

[BLW+06] M. Brownnutt, V. Letchumanan, G. Wilpers, R. C. Thompson, P. Gill, and A. G. Sinclair. Controlled photoionization loading of $^{88}Sr^{+}$ for precision ion-trap experiments. *Appl. Phys. B*, **87**, 411, 2006.

[BMB+98] D. J. Berkeland, J. D. Miller, J. C. Bergquist, W. M. Itano, and D. J. Wineland. Minimization of ion micromotion in a paul trap. *J. Appl. Phys.*, **83**, 5025, 1998.

[BP01] S. Brouard and J. Plata. Heating of a trapped ion by random fields: The influence of the micromotion. *Phys. Rev. A*, **63**, 043402, 2001.

[BPIW85] J. J. Bollinger, J. D. Prestage, W. M. Itano, and D. J. Wineland. Laser-cooled-atomic frequency standard. *Phys. Rev. Lett.*, **54**, 1000, 1985.

[BSW82] R. Blatt, H. Schnatz, and G. Werth. Ultrahigh-resolution microwave spectroscopy on trapped $^{171}Yb^{+}$ ions. *Phys. Rev. Lett.*, **48**, 1601, 1982.

[CBB+05] J. Chiaverini, R. B. Blakestad, J. Britton, J. D. Jost, C. Langer, D. Liebfried, R. Ozeri, and D. J. Wineland. Surface-electrode architecture for ion-trap quantum information processing. *Quantum Inf. Comput.*, **5**, 419, 2005.

[CC01] A. M. Childs and I. L. Chuang. Universal quantum computation with two-level trapped ions. *Phys. Rev. A*, **63**, 012306, 2001.

[CCW+03] O. Cherniavskaya, L. Chen, V. Weng, L. Yuditsky, and L. E. Brus. Quantitative noncontact electrostatic force imaging of nanocrystal polarizability. *Journal of Physical Chemistry B*, **107**, 1525, 2003.

[CDB91] J. B. Camp, T. W. Darling, and R. E. Brown. Macroscopic variations of surface potentials of conductors. *J. Appl. Phys.*, **69**, 7126, 1991.

[CDB92] J. B. Camp, T. W. Darling, and R. E. Brown. Effect of crystallites on surface potential variations of au and graphite. *J. Appl. Phys.*, **71**, 783, 1992.

[CDT+06] L. Childress, M. V. Gurudev Dutt, J. M. Taylor, A. S. Zibrov, F. Jelezko, J. Wrachtrup, P. R. Hemmer, and M. D. Lukin. Coherent dynamics of coupled electron and nuclear spin qubits in diamond. *Science*, **314**, 281, 2006.

[CFR+08] A. S. Clark, J. Fulconis, J. G. Rarity, W. J. Wadsworth, and J. L. O'Brien. An all optical fibre quantum controlled-not gate. prerint available at http://arxiv.org/abs/0802.1676v1, 2008.

[Chu36] A. Church. An unsolvable problem of elementary number theory. *Am. J. Math.*, **58**, 345, 1936.

[CLS+04] J. Chiaverini, D. Leibfried, T. Schaetz, M.D. Barrett, R.B. Blakestad, J. Britton, W.M. Itano, J.D. Jost, E. Knill, C. Langer, R. Ozeri, and D.J. Wineland. Realization of quantum error correction. *Nature*, **432**, 602, 2004.

[CVZ+98] I. L. Chuang, L. M. K. Vandersypen, X. Zhou, D. W. Leung, and S. Lloyd. Experimental realization of a quantum algorithm. *Nature*, **393**, 143, 1998.

[CZ95] J. I. Cirac and P. Zoller. Quantum computations with cold trapped ions. *Phys. Rev. Lett.*, **74**, 4091, 1995.

[DBIW89] F. Diedrich, J. C. Bergquist, W. M. Itano, and D. J. Wineland. Laser cooling to the zero-point energy of motion. *Phys. Rev. Lett.*, **62**, 403, 1989.

[Deh67] H. G. Dehmelt. Radiofrequency spectroscopy of stored ions I: Storage. *Adv. At. Mol. Phys.*, **3**, 53, 1967.

[Deu85] D. Deutsch. Quantum theory, the church-turing principle and the universal quantum computer. *Proc. Roy. Soc. London Ser. A*, **400**, 97, 1985.

[DFWG99] I. Dorofeyev, H. Fuchs, G. Wenning, and B. Gotsmann. Brownian motion of microscopic solids under the action of fluctuating electromagnetic fields. *Phys. Rev. Lett.*, **83**, 2402, 1999.

[DH81] P. Dutta and P. M. Horn. Low-frequency fluctuations in solids: 1/f noise. *Rev. Mod. Phys.*, **53**, 497, 1981.

[DHD87] B. Dahmani, L. Hollberg, and R. Drullinger. Frequency stabilization of semiconductor-lasers by resonant optical feedback. *Opt. Lett.*, **12**, 876, 1987.

[DHL+05] E. A. Donley, T. P. Heavner, F. Levi, M. O. Tataw, and S. R. Jefferts. Double-pass acousto-optic modulator system. *Rev. Sci. Instr.*, **76**, 063112, 2005.

[DiV95] D. P. DiVincenzo. Quantum computers, factoring, and decoherence. *Science*, **270**, 255, 1995.

[DLC+05] R. S. Decca, D. López, H. B. Chan, E. Fischbach, D. E. Krause, and C. R. Jamell. Constraining new forces in the casimir regime using the isoelectronic technique. *Phys. Rev. Lett.*, **94**, 240401, 2005.

[DNBP94] F. DiFilippo, V. Natarajan, K. R. Boyce, and D. E. Pritchard. Accurate atomic masses for fundamental metrology. *Phys. Rev. Lett.*, **73**, 1481, 1994.

[DOS+06] L. Deslauriers, S. Olmschenk, D. Stick, W. K. Hensinger, J. Sterk, and C. Monroe. Scaling and suppression of anomalous heating in ion traps. *Phys. Rev. Lett.*, **97**, 103007, 2006.

[DUB+01] S. A. Diddams, Th. Udem, J. C. Bergquist, E. A. Curtis, R. E. Drullinger, L. Hollberg, W. M. Itano, W. D. Lee, C. W. Oates, K. R. Vogel, and D. J. Wineland. An optical clock based on a single trapped $^{199}Hg^{+}$ ion. *Science*, **293**, 825, 2001.

[DW68] H. G. Dehmelt and F. L. Walls. "Bolometric" technique for the rf spectroscopy of stored ions. *Phys. Rev. Lett.*, **21**, 127, 1968.

[ESL+07] R. J. Epstein, S. Seidelin, D. Leibfried, J. H. Wesenberg, J. J. Bollinger, J. M. Amini, R. B. Blakestad, J. Britton, J. P. Home, W. M. Itano, J. D. Jost, E. Knill, C. Langer, R. Ozeri, N. Shiga, and D. J. Wineland. Simplified motional heating rate measurements of trapped ions. *Phys. Rev. A*, **76**, 033411, 2007.

[Fey82] R. P. Feynman. Simulating Physics with Computers. *Intl. J. Theor. Phys.*, **21**, 467, 1982.

[Fis76] J. R. Fisk. Helical-resonator design techniques. *QST*, p. 11, 1976.

[FNTU05] T. Furukawa, J. Nishimura, U. Tanaka, and S. Urabe. Design and characteristic measurement of miniature three-segment linear paul trap. *Jpn. J. Appl. Phys.*, **44**, 7619, 2005.

[For93] Norval Fortson. Possibility of measuring parity nonconservation with a single trapped atomic ion. *Phys. Rev. Lett.*, **70**(16), 2383–2386, Apr 1993.

[GGJM+06] N. Gaillard, M. Gros-Jean, D. Mariolle, F. Bertin, and A. Bsiesy. Method to assess the grain crystallographic orientation with a submicronic spatial resolution using kelvin probe force microscope. *Appl. Phys. Letters*, **89**, 154101, 2006.

[Gho95] P. K. Ghosh. *Ion Traps*. Clarendon Press, Oxford, 1995.

[GJ91] C. Guet and W. R. Johnson. Relativistic many-body calculations of transition rates for Ca^+, Sr^+, and Ba^+. *Phys. Rev. A*, **44**, 1531, 1991.

[GMS91] P. Goldberg, P. W. Milonni, and B. Sundaram. Theory of the fundamental laser linewidth. *Phys. Rev. A*, **44**, 1969, 1991.

[GPQ+95] G. Gabrielse, D. Phillips, W. Quint, H. Kalinowsky, G. Rouleau, and W. Jhe. Special relativity and the single antiproton: Fortyfold improved comparison of $\bar{p}$ and p charge-to-mass ratios. *Phys. Rev. Lett.*, **74**, 3544, 1995.

[Gro96] L. K. Grover. A fast quantum mechanical algorithm for database search. In *Proceedings of the 28th Annual ACM Symposium on the Theory of Computing*, p. 212. ACM, New York, NY, 1996.

[Hay02] K. Hayasaka. Frequency stabilization of an external-cavity violet diode laser by resonant optical feedback. *Opt. Comm.*, **206**, 401, 2002.

[HB97] F. N. Hooge and P. A. Bobbert. On the correlation function of 1/f noise. *Physica B*, **239**, 223, 1997.

[Hen82] C. Henry. Theory of the linewidth of semiconductor lasers. *IEEE J. Quantum Electron.*, **18**, 259, 1982.

[Hen86] C. Henry. Theory of spontaneous emission noise in open resonators and its application to lasers and optical amplifiers. *J. Light. Tech*, **4**, 288, 1986.

[HGH+07] R. J. Hendricks, D. M. Grant, P.F. Herskind, A. Dantan, and M. Drewsen. An all-optical ion-loading technique for scalable microtrap architectures. *Appl. Phys. B*, **88**, 507, 2007.

[HGR+03] H. Häffner, S. Gulde, M. Riebe, G. Lancaster, C. Becher, J. Eschner, F. Schmidt-Kaler, and R. Blatt. Precision measurement and compensation of optical stark shifts for an ion-trap quantum processor. *Phys. Rev. Lett.*, **90**, 143602, 2003.

[HHR+05] H. Häffner, W. Hänsel, C.F. Roos, J. Benhelm, D. Chek al kar, M. Chwalla, T. Körber, U.D. Rapol, M. Riebe, P.O. Schmidt, C. Becher, O. Gühne, W. Dür, and R. Blatt. Scalable multi-particle entanglement of trapped ions. *Nature*, **438**, 643, 2005.

[HMJ+90] A. Hemmerich, D. H. McIntyre, D. Schropp Jr., D. Meschede, and T. W. Hänsch. Optically stabilized narrow linewidth semiconductor-laser for high-resolution spectroscopy. *Opt. Commun.*, **75**, 118, 1990.

[HMO+06] Y. Hashimoto, L. Matsuoka, H. Osaki, Y. Fukushima, and S. Hasegawa. Trapping laser ablated Ca^+ ions in linear pual trap. *Jpn. J. Appl. Phys.*, **45**, 7108, 2006.

[HN49] C. Herring and M. H. Nichols. Thermionic emission. *Rev. Mod. Phys.*, **21**, 185, 1949.

[HOS+06] W. K. Hensinger, S. Olmschenk, D. Stick, D. Hucul, M. Yeo, M. Acton, L. Deslauriers, C. Monroe, and J. Rabchuk. T-junction ion trap array for two-dimensional ion shuttling, storage, and manipulation. *Appl. Phys. Letters*, **88**, 034101, 2006.

[HUW00] K. Hayasaka, S. Urabe, and M. Watanabe. Laser cooling of Ca^+ with an external-cavity ultraviolet diode laser. *Jpn. J. Appl. Phys.*, **39**, L687, 2000.

[HW99] C. Henkel and M. Wilkens. Heating of trapped atoms near thermal surfaces. *Europhys. Lett.*, **47**, 414, 1999.

[Jam98] D. F. V. James. Quantum dynamics of cold trapped ions with applications to quantum computation. *Appl. Phys. B*, **66**, 181, 1998.

[JBT+08] M. Johanning, A. Braun, N. Timoney, V. Elman, W. Neuhauser, and Chr. Wunderlich. Individual addressing of trapped ions and coupling of motional and spin states using rf radiation. preprint available at http://arxiv.org/abs/0801.0078, 2008.

[JPD87] R. S. Van Dyck Jr., P. B. Pschwinberg, and H. G. Dehmelt. New high-precision comparison of electron and positron g-factors. *Phys. Rev. Lett.*, **59**, 26, 1987.

[JPM90] G. R. Janik, J. D. Prestage, and L. Maleki. Simple analytic potentials for linear ion traps. *J. Appl. Phys.*, **67**, 6050–6055, 1990.

[Kan98] B. E. Kane. A silicon-based nuclear spin quantum computer. *Nature*, **393**, 133, 1998.

[KBT+06] F. H. L. Koppens, C. Buizert, K. J. Tielrooij, I. T. Vink, K. C. Nowack, T. Meunier, L. P. Kouwenhoven, and L. M. K. Vandersypen. Driven coherent oscillations of a single electron spin in a quantum dot. *Nature*, **442**, 766, 2006.

[KLM06] S. Kuehn, R. F. Loring, and J. A. Marohn. Dielectric fluctuations and the origins of noncontact friction. *Phys. Rev. Lett.*, **96**, 156103, 2006.

[KMW02] D. Kielpinski, C. Monroe, and D. J. Wineland. Architecture of a large-scale ion trap quantum computer. *Nature*, **417**, 709, 2002.

[Kni81] R. D. Knight. Storage of ions from laser-produced plasmas. *Appl. Phys. Letters*, **38**, 221, 1981.

[KPM+05] J. Kim, S. Pau, Z. Ma, H. R. McLellan, J. V. Gates, A. Kornblit, R. E. Slusher, R. M. Jopson, I. Kang, and M. Dinu. System design for large-scale ion trap quantum information processor. *Quantum Inf. Comput.*, **5**, 515–537, 2005.

[Kwo89] Victor H. S. Kwong. Production and storage of low-energy highly charged ions by laser ablation and an ion trap. *Phys. Rev. A*, **39**, 4451, 1989.

[Lam97] S. K. Lamoreaux. Thermalization of trapped ions: a quantum perturbation approach. *Phys. Rev. A*, **56**, 4970, 1997.

[LCB89] Ph. Laurent, A. Clairon, and Ch. Breant. Frequency noise-analysis of optically self-locked diode-lasers. *IEEE J. Quantum Electron.*, **25**, 1131, 1989.

[LCL+07] D. R. Leibrandt, R. J. Clark, J. Labaziewicz, P. Antohi, W. Bakr, K. R. Brown, and Isaac L. Chuang. Laser ablation loading of a surface-electrode ion trap. *Phys. Rev. A*, **76**, 055403, 2007.

[LD98] D. Loss and D.P. DiVincenzo. Quantum computation with quantum dots. *Phys. Rev. A*, **57**, 120, 1998.

[LDM+03] D. Leibfried, B. DeMarco, V. Meyer, D. Lucas, M. Barrett, J. Britton, W. M. Itano, B. Jelenkovic, C. Langer, T. Rosenband, and D. J. Wineland. Experimental demonstration of a robust, high-fidelity geometric two ion-qubit phase gate. *Nature*, **422**, 412, 2003.

[LGA+08] J. Labaziewicz, Y. Ge, P. Antohi, D. Leibrandt, K. R. Brown, and I. L. Chuang. Suppression of heating rates in cryogenic surface-electrode ion traps. *Phys. Rev. Lett.*, **100**, 013001, 2008.

[LGL+08] J. Labaziewicz, Y. Ge, D. Leibrandt, S. X. Wang, R. Shewmon, and I. L. Chuang. Temperature dependence of electric field noise above gold surfaces. 2008.

[LGRS04] V. Letchumanan, P. Gill, E. Riis, and A. G. Sinclair. Optical ramsey spectroscopy of a single trapped $^{88}Sr^{+}$ ion. *Phys. Rev. A*, **70**, 033419, 2004.

[LHN+07] A. D. Ludlow, X. Huang, M. Notcutt, T. Zanon-Willette, S. M. Foreman, M. M. Boyd, S. Blatt, and J. Ye. Compact, thermal-noise-limited optical cavity for diode laser stabilization at 1×10^{-15}. *Opt. Lett.*, **32**, 641, 2007.

[LHW+03] G. P. T. Lancaster, H. Haffner, M. A. Wilson, C. Becher, J. Eschner, F. Schmidt-Kaler, and R. Blatt. Doppler cooling a single Ca^+ ion with a violet extended-cavity diode laser. *Appl. Phys. B*, **76**, 805, 2003.

[LKS+05] D. Leibfried, E. Knill, S. Seidelin, J. Britton, R.B. Blakestad, J. Chiaverini, D.B. Hume, W.M. Itano, J.D. Jost, C. Langer, R. Ozeri, R. Reichle, and D.J. Wineland. Creation of a six-atom 'Schrödinger cat' state. *Nature*, **438**, 639, 2005.

[LLT+06] Huanqian Loh, Yu-Ju Lin, Igor Teper, Marko Cetina, Jonathan Simon, James K. Thompson, and Vladan Vuletić. Influence of grating parameters on the linewidths of external-cavity diode lasers. *Appl. Opt.*, **45**, 9191, 2006.

[LRB+07] J. Labaziewicz, P. Richerme, K. R. Brown, I. L. Chuang, and K. Hayasaka. Compact, filtered diode laser system for precision spectroscopy. *Opt. Lett.*, **32**, 572, 2007.

[Luc07] D. Lucas. Private communication, 2007.

[LWF77] J. M. Lockhart, F. C. Witteborn, and W. M. Fairbank. Evidence for a temperature-dependent surface shielding effect in Cu. *Phys. Rev. Lett.*, **38**, 1220, 1977.

[LWGS05] V. Letchumanan, M. A. Wilson, P. Gill, and A. G. Sinclair. Lifetime measurement of the metastable 4d $^2D_{5/2}$ state in $^{88}Sr^+$ using a single trapped ion. *Phys. Rev. A*, **72**, 012509, 2005.

[Mat79] R. A. Matula. Electrical resistivity of copper, gold, palladium, and silver. *Journal of Physical and Chemical Reference Data*, **8**, 1147, 1979.

[MBCR03] H. J. Mamin, R. Budakian, B. W. Chui, and D. Rugar. Detection and manipulation of statistical polarization in small spin ensembles. *Phys. Rev. Lett.*, **91**, 207604, 2003.

[MBH+04] H. S. Margolis, G. P. Barwood, G. Huang, H. A. Klein, S. N. Lea, K. Szymaniec, and P. Gill. Hertz-level measurement of the optical clock frequency in a single $^{88}Sr^+$ ion. *Science*, **306**, 1355, 2004.

[MBK95] W. Mende, K. Bartschat, and M. Kock. Near-threshold photoionization from the Sr I (5s5p) $^1P_1^0$ state. *J. Phys. B*, **28**, 2385, 1995.

[MCS75] W. F. Meggers, C. H. Corliss, and B. F. Scribner. Tables of spectral-line intensities. *Natl. Bur. Stand. (U.S.), Monograph*, **145**, 1975.

[MGW+03] O. Mandel, M. Greiner, A. Widera, T. Rom, T. W. Hansch, and I. Bloch. Controlled collisions for multi-particle entanglement of optically trapped atoms. *Nature*, **425**, 937, 2003.

[MMK+95] C. Monroe, D. M. Meekhof, B. E. King, W. M. Itano, and D. J. Wineland. Demonstration of a fundamental quantum logic gate. *Phys. Rev. Lett.*, **75**, 4714, 1995.

[MMK+96] D. M. Meekhof, C. Monroe, B. E. King, W. M. Itano, and D. J. Wineland. Generation of nonclassical motional states of a trapped atom. *Phys. Rev. Lett.*, **76**, 1796, 1996.

[MMO+07] D. L. Moehring, P. Maunz, S. Olmschenk, K. C. Younge, D. N. Matsukevich, L.-M. Duan, and C. Monroe. Entanglement of single-atom quantum bits at a distance. *Nature*, **449**, 68, 2007.

[MNAU02] J. M. Martinis, S. Nam, J. Aumentado, and C. Urbina. Rabi oscillations in a large Josephson-junction qubit. *Phys. Rev. Lett.*, **89**(11), 117901, 2002.

[MOL+99] J. E. Mooij, T.P. Orlando, L. Levitov, L. Tian, C. H. v.d. Wal, and S. Lloyd. Josephson persisten-current qubit. *Science*, **285**, 1036, 1999.

[MvdS99] H. J. Metcalf and P. van der Straten. *Laser Cooling and Trapping*. Springer-Verlag, New York, 1999.

[MW01] F. Mintert and Chr. Wunderlich. Ion-trap quantum logic using long-wavelength radiation. *Phys. Rev. Lett.*, **87**, 257904, 2001.

[NC00] M. A. Nielsen and I. L. Chuang. *Quantum Computation and Quantum Information*. Cambridge University Press, Cambridge, UK, 2000.

[NHTD78] W. Neuhauser, M. Hohenstatt, P. Toschek, and H. Dehmelt. Optical-sideband cooling of visible atom cloud confined in parabolic well. *Phys. Rev. Lett.*, **41**, 233, 1978.

[NLR+99] H. C. Nägerl, D. Leibfried, H. Rohde, G. Thalhammer, J. Eschner, F. Schmidt-Kaler, and R. Blatt. Laser addressing of individual ions in a linear ion trap. *Phys. Rev. A*, **60**, 145, 1999.

[NOW91] M. Nonnenmacher, M. P. O'Boyle, and H. K. Wickramasinghe. Kelvin probe force microscopy. *Appl. Phys. Letters*, **58**, 2921, 1991.

[NPT99] Y. Nakamura, Y. A. Pashkin, and J.S. Tsai. Coherent control of macroscopic quantum states in a single-Cooper-pair box. *Nature*, **398**, 786, 1999.

[NRV+87] J. Neukammer, H. Rinneberg, K. Vietzke, A. Knig, H. Hieronymus, M. Kohl, H.-J. Grabka, and G. Wunner. Spectroscopy of rydberg atoms at n=500: Observation of quasi-Landau resonances in low magnetic fields. *Phys. Rev. Lett.*, **59**, 2947, 1987.

[OCK+06] S. Oh, K. Cicak, J. S. Kline, M. A. Sillanp, K. D. Osborn, J. D. Whittaker, R. W. Simmonds, and D. P. Pappas. Elimination of two level fluctuators in superconducting quantum bits by an epitaxial tunnel barrier. *Phys. Rev. B*, **74**, 100502, 2006.

[OHDG06] B. Odom, D. Hanneke, B. D'Urso, and G. Gabrielse. New measurement of the electron magnetic moment using a one-electron quantum cyclotron. *Phys. Rev. Lett.*, **97**, 030801, 2006.

[OK85] M. Ohtsu and S. Kotajima. Linewidth reduction of a semiconductor-laser by electrical feedback. *IEEE J. Quantum Electron.*, **21**, 1905, 1985.

[OS92] S. Ohshima and H. Schnatz. Optimization of injection current and feedback phase of an optically self-locked laser diode. *J. Appl. Phys.*, **71**, 3114, 1992.

[OWC07] J. M. Obrecht, R. J. Wild, and E. A. Cornell. Measuring electric fields from surface contaminants with neutral atoms. *Phys. Rev. A*, **75**, 062903, 2007.

[OWN+01] K. Okada, M. Wada, T. Nakamura, I. Katayama, L. Boesten, and S. Ohtani. Cryogenic ion trap for minimization of trapped ion loss. *Jpn. J. Appl. Phys.*, **40**, 4221, 2001.

[Pau90] W. Paul. Electromagnetic traps for charged and neutral particles. *Rev. Mod. Phys.*, **62**, 531–540, 1990.

[PBIW96] M. E. Poitzsch, J. C. Bergquist, W. M. Itano, and D. J. Wineland. Cryogenic linear ion trap for accurate spectroscopy. *Rev. Sci. Instr.*, **67**, 129, 1996.

[Pet79] K. Petermann. Calculated spontaneous emission factor for double-heterostructure injection lasers with gain-induced waveguiding. *IEEE J. Quantum Electron.*, **15**, 566, 1979.

[PJT+05] J. R. Petta, A. C. Johnson, J. M. Taylor, E. A. Laird, A. Yacoby, M. D. Lukin, C. M. Marcus, M. P. Hanson, and A. C. Gossard. Coherent manipulation of coupled electron spins in semiconductor quantum dots. *Science*, **309**(5744), 2180–2184, 2005.

[PLB+06] C. E. Pearson, D. R. Leibrandt, W. S. Bakr, W. J. Mallard, K. R. Brown, and I. L. Chuang. Experimental investigation of planar ion traps. *Phys. Rev. A*, **73**, 032307, 2006.

[PS53] W. Paul and H. Steinwedel. Ein neues massenspektrometer ohne magnetfeld. *Z. Naturforsch. A*, **8**, 448, 1953.

[RBB+06] N. A. Robertson, J. R. Blackwood, S. Buchman, R. L. Byer, J. Camp, D. Gill, J. Hanson, S. Williams, and P. Zhou. Kelvin probe measurements: investigations of the patch effect with applications to ST-7 and LISA. *Class. Quant. Grav.*, **23**, 2665, 2006.

[RHR+04] M. Riebe, H. Häffner, C.F. Roos, W. Hänsel, J. Benhelm, G.P.T. Lancaster, T.W. Körber, C. Becher, F. Schmidt-Kaler, D. F. V. James, and R. Blatt. Deterministic quantum teleportation with atoms. *Nature*, **429**, 734, 2004.

[RHS+08] T. Rosenband, D. B. Hume, P. O. Schmidt, C. W. Chou, A. Brusch, L. Lorini, W. H. Oskay, R. E. Drullinger, T. M. Fortier, J. E. Stalnaker, S. A. Diddams, W. C. Swann, N. R. Newbury, W. M. Itano, D. J. Wineland, and J. C. Bergquist. Frequency ratio of Al^+ and Hg^+ single-ion optical clocks; metrology at the 17th decimal place. *Science*, **319**, 1808, 2008.

[RKS+06] M. Riebe, K. Kim, P. Schindler, T. Monz, P. O. Schmidt, T. K. Körber, W. Hänsel, H. Häffner, C. F. Roos, and R. Blatt. Process tomography of ion trap quantum gates. *Phys. Rev. Lett.*, **97**, 220407, 2006.

[RLCB+03] S. Gulde M. Riebe, G. P. T. Lancaster, J. Eschner H. Hffner F. Schmidt-Kaler C. Becher, I. L. Chuang, and Rainer Blatt. Implementation of the Deutsch-Jozsa algorithm on an ion-trap quantum computer. *Nature*, **421**, 48, 2003.

[RO92] F. Rossi and G. I. Opat. Observations of the effects of adsorbates on patch potentials. *J. Phys. D*, **25**, 1349, 1992.

[RWE+95] L. Ricci, M. Weidemuller, T. Esslinger, A. Hemmerich, C. Zimmermann, V. Vuletic, W. Konig, and T. W. Hansch. A compact grating-stabilized diode laser system for atomic physics. *Opt. Commun.*, **117**, 541, 1995.

[RYB+00] R. J. Rafac, B. C. Young, J. A. Beall, W. M. Itano, D. J. Wineland, and J. C. Bergquist. Sub-dekahertz ultraviolet spectroscopy of $^{199}Hg^{+}$. *Phys. Rev. Lett.*, **85**, 2462, 2000.

[SBC+93] C. I. Sukenik, M. G. Boshier, D. Cho, V. Sandoghdar, and E. A. Hinds. Measurement of the Casimir-Polder force. *Phys. Rev. Lett.*, **70**, 560, 1993.

[SCR+06] S. Seidelin, J. Chiaverini, R. Reichle, J. J. Bollinger, D. Liebfried, J. Britton, J. H. Wesenberg, R. B. Blakestad, R. J. Epstein, D. B. Hume, J.D. Jost, C. Langer, R. Ozeri, N. Shiga, and D. J. Wineland. Microfabricated surface-electrode ion trap for scalable quantum information processing. *Phys. Rev. Lett.*, **96**, 253003, 2006.

[SHM08] M. Schlosshauer, A. P. Hines, and G. J. Milburn. Decoherence and dissipation of a quantum harmonic oscillator coupled to two-level systems. *Phys. Rev. A*, **77**, 022111, 2008.

[Sho94] P. W. Shor. Algorithms for quantum computation: Discrete log and factoring. In S. Goldwasser, editor, *Proceedings of the 35th Annual Symposium on the Foundations of Computer Science*, p. 124, IEEE Computer Society, Los Alamitos, CA, 1994.

[Sho95] P. W. Shor. Scheme for reducing decoherence in quantum memory. *Phys. Rev. A*, **52**, 2493, 1995.

[SHO+06] D. Stick, W. K. Hensinger, S. Olmschenk, M. J. Madsen, K. Schwab, and C. Monroe. Ion trap in a semiconductor chip. *Nature Physics*, **2**, 36, 2006.

[Sie86] A. E. Siegman. *Lasers*. University Science Books, Sausalito, CA, 1986.

[SKHR+03] F. Schmidt-Kaler, H. Häffner, M. Riebe, S. Gulde, G. P. T. Lancaster, T. Deuschle, C. Becher, Ch. Roos, J. Eschner, and Rainer Blatt. Realization of the Cirac-Zoller controlled-NOT quantum gate. *Nature*, **422**, 408, 2003.

[SLH+04] R. W. Simmonds, K. M. Lang, D. A. Hite, S. Nam, D. P. Pappas, and John M. Martinis. Decoherence in Josephson phase qubits from junction resonators. *Phys. Rev. Lett.*, **93**, 077003, 2004.

[Slu06] R. E. Slusher. Scalable ion traps with monolithically integrated Cmos controls, 2006. 20th International Conference on Atomic Physics, Innsbruck, 2006.

[SM99] A. Sørensen and K. Mølmer. Quantum computation with ions in thermal motion. *Phys. Rev. Lett.*, **82**, 1971, 1999.

[SMHS06] H. Stoehr, F. Mensing, J. Helmcke, and U. Sterr. Diode laser with 1 Hz linewidth. *Opt. Lett.*, **31**, 736, 2006.

[SMS+01] B. C. Stipe, H. J. Mamin, T. D. Stowe, T. W. Kenny, and D. Rugar. Noncontact friction and force fluctuations between closely spaced bodies. *Phys. Rev. Lett.*, **87**, 096801, 2001.

[SNBT86] Th. Sauter, W. Neuhauser, R. Blatt, and P. E. Toschek. Observation of quantum jumps. *Phys. Rev. Lett.*, **57**, 1696, 1986.

[SNY85] S. Saito, O. Nilsson, and Y. Yamamoto. Frequency modulation noise and linewidth reduction in a semiconductor laser by means of a negative frequency feedback technique. *Appl. Phys. Letters*, **46**, 3, 1985.

[SO90] C. Shin and M. Ohtsu. Stable semiconductor-laser with a 7-Hz linewidth by an optical-electrical double-feedback technique. *Opt. Lett.*, **15**, 1455, 1990.

[ST58] A. L. Schawlow and C. H. Townes. Infrared and optical masers. *Phys. Rev.*, **112**, 1940, 1958.

[ST03] C. C. Speake and C. Trenkel. Forces between conducting surfaces due to spatial variations of surface potential. *Phys. Rev. Lett.*, **90**, 160403, 2003.

[Ste96] A. M. Steane. Error correcting codes in quantum theory. *Phys. Rev. Lett.*, **77**, 793, 1996.

[Ste03] A. M. Steane. Overhead and noise threshold of fault-tolerant quantum error correction. *Phys. Rev. A*, **68**, 042322, 2003.

[TKK+00] Q. A. Turchette, D. Kielpinski, B. E. King, D. Liebfried, D. M. Meekhof, C. J. Myatt, M. A. Rowe, C. A. Sackett, C. S. Wood, W. M. Itano, C. Monroe, and D. J. Wineland. Heating of trapped ions from the quantum mechanical ground state. *Phys. Rev. A*, **61**, 063418, 2000.

[TKOU06] K. Toyoda, Y. Kubota, T. Okano, and S. Urabe. Ultraviolet diode laser system based on the resonant optical feedback method with the capability of fast continuous sweep. *Appl. Phys. B*, **82**, 25, 2006.

[TMU+01] K. Toyoda, A. Miura, S. Urabe, K. Hayasaka, and M. Watanabe. Laser cooling of calcium ions by use of ultraviolet laser diodes: Significant induction of electron-shelving transitions. *Opt. Lett.*, **26**, 1897, 2001.

[TOPS87] B. Tromborg, H. Olesen, Xing Pan, and S. Saito. Transmission line description of optical feedback and injection locking for fabry-perot and Dfb lasers. *IEEE J. Quantum Electron.*, **23**, 1875, 1987.

[TRBZ04] L. Tian, P. Rabl, R. Blatt, and P. Zoller. Interfacing quantum-optical and solid-state qubits. *Phys. Rev. Lett.*, **92**, 247902, 2004.

[Tur36] A. M. Turing. On computable numbers, with an application to the entscheidungsproblem. *Proc. London Math. Soc.*, **42**, 230, 1936.

[VC05] L. M. K. Vandersypen and I. L. Chuang. Nmr techniques for quantum control and computation. *Rev. Mod. Phys.*, **76**, 1037, 2005.

[VSB+01] L.M.K. Vandersypen, M. Steffen, G. Breyta, C.S. Yannoni, R. Cleve, and I.L. Chuang. Experimental realization of Shor's quantum factoring algorithm using nuclear magnetic resonance. *Nature*, **414**, 883, 2001.

[WDW78] D. J. Wineland, R. E. Drullinger, and F. L. Walls. Radiation-pressure cooling of bound resonant absorbers. *Phys. Rev. Lett.*, **40**, 1639, 1978.

[WEL+07] J. H. Wesenberg, R. J. Epstein, D. Leibfried, R. B. Blakestad, J. Britton, J. P. Home, W. M. Itano, J. D. Jost, E. Knill, C. Langer, R. Ozeri, S. Seidelin, and D. J. Wineland. Fluorescence during Doppler cooling of a single trapped atom. *Phys. Rev. A*, **76**, 053416, 2007.

[WI79] D. J. Wineland and W. M. Itano. Laser cooling of atoms. *Phys. Rev. A*, **20**, 1521, 1979.

[WI81] D. J. Wineland and W. M. Itano. Spectroscopy of a single Mg^+ ion. *Phys. Lett.*, **82**, 75, 1981.

[WIBH87] D. J. Wineland, W. M. Itano, J. C. Bergquist, and R. G. Hulet. Laser-cooling limits and single-ion spectroscopy. *Phys. Rev. A*, **36**, 2220, 1987.

[Wim94] S. Wimperis. Broadband, narrowband, and passband composite pulses for use in advanced nmr experiments. *J. Magn. Reson. B*, **109**, 221, 1994.

[Win06] D. Wineland. Private communication, 2006.

[WMI+98] D. J. Wineland, C. Monroe, W. M. Itano, D. Leibfried, B. E. King, and D. M. Meekhof. Experimental issues in coherent quantum-state manipulation of trapped atomic ions. *J. of Res. of the National Inst. of Standards and Technology*, **103**, 259, 1998.

Appendix A

How to Run an Entire Lab on Python and Field Programmable Gate Arrays

Data collection requires simultaneous control over a number of instruments, with widely varying interfaces and response times. Unsatisfied with the capabilities of Matlab and LabView, I experimented with a python based data acquisition system, called DAQ. The project was a success, and resulted in a broad framework encompassing virtually all instruments in the lab.

In every experiment, there are tasks which can be difficult, or very expensive, to accomplish using off-the-shelf components. In such cases, one is forced to design and build custom instruments. Often, these designs can be simplified using digital logic, with analog-to-digital and digital-to-analog converters on the inputs and outputs as necessary. The recently popularized field programmable gate array (FPGA) development boards provide powerful control logic and a consistent interface to a PC, leading to their extensive use in this project. The flexibility of FPGAs allowed us to use the same board for a wide variety of projects, simplifying development and use.

This appendix describes both of these projects in detail.

A.1 DAQ

DAQ is schematically depicted in Figure A-1. The application is divided into three threads, which handle data input from the command line ("Command Line" box), user interface drawing and operation ("User Interface" box) and interaction with hardware ("Worker" box). To avoid collisions, hardware requests are serialized using an execution queue protected with a global mutex. The "worker" thread removes requests from the queue and executes them.

Most of the application code is written in python, and executed by an embedded python interpreter (red box). Access to the execution queue is provided by extending the C application, and importing it in python. To reduce the number of commands passing through the queue, frequently used scans are defined in the worker thread, and can be initialized with appropriate parameters and executed with a single command.

The design is made highly modular by its rather restrictive structure. The interaction with hardware is abstracted using input and output modules ("I/O"), specific to each instru-

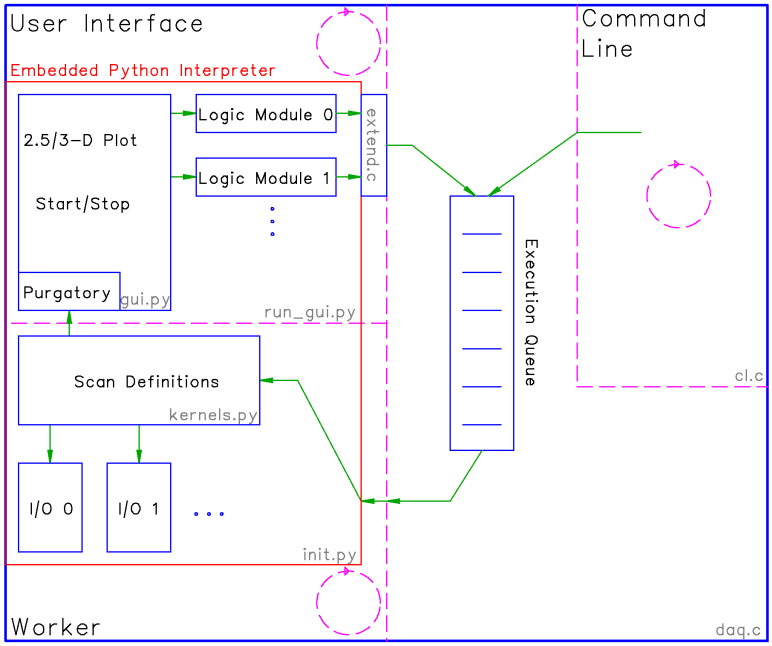

Figure A-1: Schematic of DAQ. Threads are indicated with a circle and arrow, with boundaries in pink dashed lines, The embedded python code is shown as red box, with green arrows indicating information flow.

ment. Each of the I/O modules exports read and write functions, with each read function returning only a single value, and each write function passed a single value to set. While very restrictive, the architecture results in a complete separation of input/output functions from the scan logic. Only a small number of scan routines operating on abstract input and output functions is necessary, and included in the user interface via the logic modules. The I/O and logic modules are independent of each other, and each of the experiments in the lab choose only the desired pieces.

Not all scan types are well served by an abstract scan logic. In case of very specialized, or multi-stage scans, the scan is written up as a python script and the name of the script passed to the worker thread to execute. This entire thesis relied on 7 logic modules, 15 I/O modules and 8 scripts for specialized scans (Rabi frequency measurement, Ramsey scans, process tomography etc.).

A.2 FPGA Control

FPGAs are an ideal tool where rapid response to a digital stimuli (photon counting and photon correlation), digital signal processing (digital PID loops) and complex control of other instruments (sequencing of RF pulses using direct digital synthesis boards) are required. To facilitate PC control of the FPGA, we use OpalKelly boards, which provide libraries for USB communication to the FPGA. A small python wrapper encapsulates this interface, and provides control and display of the instruments settings. A network server listens for control commands, allowing other programs, such as DAQ, to read and set experimental values.

This software stack was used for each of the 4 lasers described in Section 4.1, where the

FPGA implements the equivalent of two frequency synthesizers, two lock-in amplifiers and two PID loops, necessary for stabilization of the optical feedback. Digital control over the laser allowed for remote tuning of the laser and conditional switching of the lock dither on and off at will.

Photon counting and photon correlation to the RF phase are accomplished using a single FPGA, with its input stage clocked at 330 MHz. The 3 ns timing resolution is sufficient for our experiments, with trap RF frequency below 50 MHz.

The pulse sequencer, which controls the lasers during experimental runs, is the most complex of the projects implemented using an FPGA, and will be described in more detail in the next section.

A.2.1 Pulse Sequencer Software Stack

The pulse sequencer is designed to switch the laser frequencies and amplitudes, with the actuation accomplished using acousto-optic modulators (AOM). The RF pulses driving the AOMs are generated by direct digital synthesis (DDS) development boards (AD9858), with the FPGA tasked with control over those boards.

There are a number of possible implementations of the pulse sequencer. In one extreme, the desired RF pulses are saved in memory, with the sequencer simply reading out these values and streaming them to the hardware. In another extreme, the sequencer has an extensive internal state and the ability to execute complicated programs. Our implementation tends towards the latter, due to its perceived flexibility and the possibility for complex feed-back on external inputs.

The FPGA implements a von Neumann stack machine, with a 32-bit wide, 4000 deep memory. The state machine iterates over the program counter PC, executing instructions at memory address PC. Two additional global registers, W and INDF, complete the state of the machine. Each instruction takes at least 2 cycles, with frequency and phase switch commands taking up to 15 cycles. The FPGA is clocked at 62.5 MHz, synchronized to the DDS clock. The synchronization is required to ascertain stable switching of the DDS board (cf. Section 4.3).

The instruction set can be divided into three categories.

- Other
  - NOP - do nothing
  - DIGOUT #n - set the value of the digital outputs
  - END - finish execution
- DDS control
  - DDSFRQ #n, addr - set the DDS#n frequency to value stored at memory address addr
  - DDSAMP #n, addr - set the DDS#n amplitude to value stored at memory address addr
  - DDSPHS #n, addr - set the DDS#n phase to value stored at memory address addr, corrected for Stark shifts
  - DDSCOR #n, addr - set the DDS#n Stark shift correction register to value stored at memory address addr

  - DDSTZR - zero global time reference counter

- Timing control
  - COUNT addr - fetch x from memory address addr, count photons for x cycles
  - DELAY addr - fetch x from memory address addr, delay execution for x cycles

- Logic, arithmetics
  - LDWR addr - load value from memory address addr into W
  - LDWI addr - load value from memory address INDF into W
  - STWR addr - store W into memory address addr
  - STWI - store W into memory address INDF
  - LDINDF - load value from memory address addr into INDF
  - SWAPWI - swap the values in W and INDF
  - ANDW addr - fetch x from memory address addr, W=W&x
  - ADDW addr - fetch x from memory address addr, W=W+x
  - INC addr - fetch x from memory address addr, W=x+1
  - DEC addr - fetch x from memory address addr, W=x−1
  - CLRW - set W= 0
  - CMP addr - fetch x from memory address addr, if W>x, W=W else W= 0

- Flow Control
  - JMP addr - set program counter PC to addr
  - JMPZ addr - set program counter PC to addr only if W== 0
  - JMPNZ addr - set program counter PC to addr only if W! = 0
  - FJMP addr - push registers W, INDF, and (PC + 1) onto stack, set program counter PC to addr
  - FRET - pop W, INDF, and PC from stack

The "DDSPHS" and "DDSCOR" instructions require further explanation. Stark shift correction, described in Section 2.3.3 and Section 2.3.4 requires knowledge of the pulse start time and duration of all the previous pulses. These variables are most conveniently stored in the hardware, removing the necessity to compute them for each pulse sequence. After "DDSCOR" command sets the correction register to the physical Stark shift, the "DDSPHS" command will adjust following phase requests appropriately, to remove the phase errors. Note that all frequency adjustments are performed "phase-coherently," as described in Section 4.3.

The instructions and data are uploaded to the FPGA from a python program, which also allows for manual control of the synthesized RF frequencies, phases and amplitudes and displays current state of the sequencer. To simplify code writing, a simple compiler processes the code prior to upload. The compiler supports function calls (with arguments passed by value), arrays, pointers, "#define" and "?" operator, multiple source files and local namespaces.

Appendix B

Ion State Simulation Codes

The following pages include printouts of the Mathematica code used to derive some of the results of Chapter 2.

Three state Sr ion simulation

Density matrix equation of motion in Lindblad form

Hamiltonian and operators. State vector is |S, P, D>

```
H[δeg_, δem_, Ωeg_, Ωem_] := {{δeg, Ωeg/2, 0}, {Ωeg/2, 0, Ωem/2}, {0, Ωem/2, δem}};

L[Γeg_, Γem_] := {{{0, Sqrt[Γeg], 0}, {0, 0, 0}, {0, 0, 0}}, {{0, 0, 0}, {0, 0, 0}, {0, Sqrt[Γem], 0}}};

ρinit = {{1, 0, 0}, {0, 0, 0}, {0, 0, 0}};

domains =
  Element[{ρmm, ρee, ρgg, ρgmr, ρgmi, ρemr, ρemi, ρger, ρgei, δeg, δem, Ωeg,
     Ωem, Γeg, Γem}, Reals] && Γeg > 0 && Γem > 0 && Ωeg > 0 && Ωem > 0 && δeg ≠ δem &&
   δeg ≠ 0 && δem ≠ 0;
```

Explicit matrix with real coeffs

```
ρmat := {{ρgg, ρger + i ρgei, ρgmr + i ρgmi}, {ρger - i ρgei, ρee, ρemr + i ρemi}, {ρgmr - i ρgmi, ρemr - i ρemi, ρmm}};
```

Decoherence Operator

```
γ[ρ_, Γeg_, Γem_] :=
 Simplify[
  Sum[L[Γeg, Γem][[i]].ρ.L[Γeg, Γem][[i]]† -
    (L[Γeg, Γem][[i]]†.L[Γeg, Γem][[i]].ρ + ρ.L[Γeg, Γem][[i]]†.L[Γeg, Γem][[i]])/
     2, {i, 1, 2}], domains]
MatrixForm[γ[ρmat, Γeg, Γem]]
```

$$\begin{pmatrix} \Gamma eg\,\rho ee & -\frac{1}{2} i\,(\Gamma eg+\Gamma em)\,(\rho gei - i\,\rho ger) & 0 \\ \frac{1}{2} i\,(\Gamma eg+\Gamma em)\,(\rho gei + i\,\rho ger) & -(\Gamma eg+\Gamma em)\,\rho ee & -\frac{1}{2} i\,(\Gamma eg+\Gamma em)\,(\rho emi - i\,\rho emr \\ 0 & \frac{1}{2} i\,(\Gamma eg+\Gamma em)\,(\rho emi + i\,\rho emr) & \Gamma em\,\rho ee \end{pmatrix}$$

Equation of Motion

```
ρdot[ρ_, δeg_, δem_, Ωeg_, Ωem_, Γeg_, Γem_] :=
  -i (H[δeg, δem, Ωeg, Ωem].ρ - ρ.H[δeg, δem, Ωeg, Ωem]) + γ[ρ, Γeg, Γem];
ρdotmat[δeg_, δem_, Ωeg_, Ωem_, Γeg_, Γem_] =
  FullSimplify[ρdot[ρmat, δeg, δem, Ωeg, Ωem, Γeg, Γem], domains];
MatrixForm[ρdotmat[δeg, δem, Ωeg, Ωem, Γeg, Γem]]
```

$$\begin{pmatrix} \Gamma eg\,\rho ee - \rho gei\,\Omega eg & -\frac{1}{2} i\,((\Gamma eg- \\ \frac{1}{2} i\,((\Gamma eg+\Gamma em-2\,i\,\delta eg)\,(\rho gei + i\,\rho ger) + \rho ee\,\Omega eg - \rho gg\,\Omega eg + i\,\rho gmi\,\Omega em - \rho gmr\,\Omega em) & -(\Gamma eg+\Gamma em \\ \frac{1}{2}\,(2\,(\delta eg-\delta em)\,(\rho gmi + i\,\rho gmr) + \rho emi\,\Omega eg + i\,\rho emr\,\Omega eg - (\rho gei + i\,\rho ger)\,\Omega em) & \frac{1}{2} i\,((\Gamma eg+ \end{pmatrix}$$

TIME DEPENDENT SOLUTION

Numerical integration

```
time = .5;
sol =
  NDSolve[
   {ρ[0] == {{1, 0, 0}, {0, 0, 0}, {0, 0, 0}} &&
     ρ'[t] == ρdot[ρ[t], -2 Pi 10., 2 Pi 20., 2 Pi 20., 2 Pi 10., 2 Pi 20., 2 Pi 1.]},
   ρ, {t, 0, time}, MaxSteps → 100 000];
MatrixForm[Part[ρ[time] /. sol, 1]];
```

Plot evolution of the states, as a check

```
Plot[Norm[Part[ρ[t] /. sol, 1, 1, 1]], {t, 0, time}, PlotRange -> Full,
 AxesLabel → {"Time [μs]", "S population"}, AxesOrigin → {0, 0}]
```

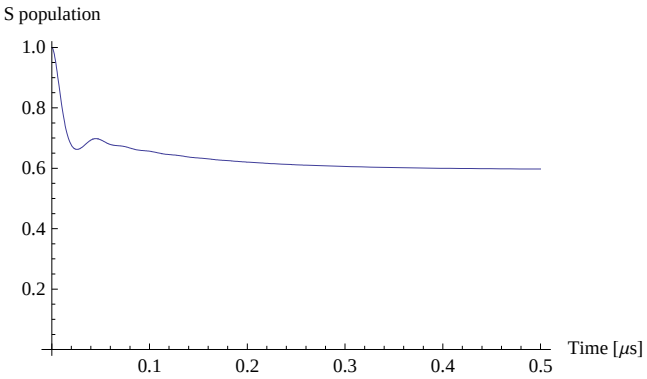


```
Plot[Norm[Part[ρ[t] /. sol, 1, 2, 2]], {t, 0, time}, PlotRange -> Full,
 AxesLabel → {"Time [μs]", "P population"}, AxesOrigin → {0, 0}]
```

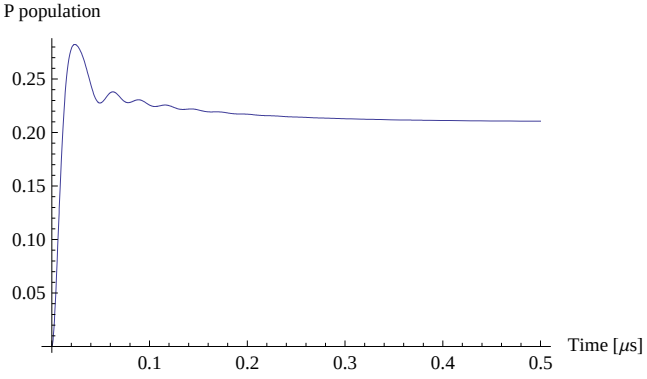

```
Plot[Norm[Part[ρ[t] /. sol, 1, 3, 3]], {t, 0, time}, PlotRange -> Full,
 AxesLabel → {"Time [μs]", "P population"}, AxesOrigin → {0, 0}]
```

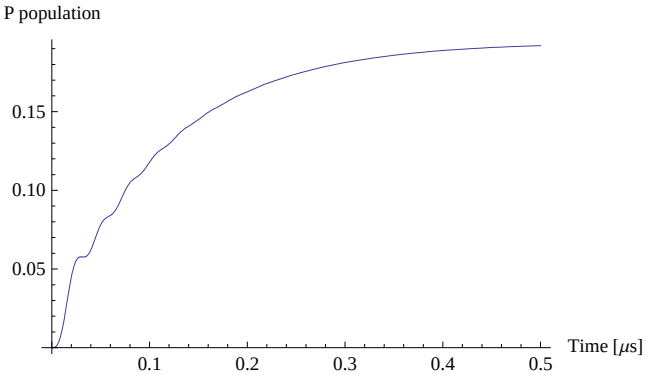

EVOLUTION USING A PROPAGATOR

First, write a linear operator that we can exponentiate. This speeds up the computations a lot. Even though I don't get a closed form for the propagator, it's still fast

```
v[ρgg_, ρee_, ρmm_, ρger_, ρgei_, ρgmr_, ρgmi_, ρemr_, ρemi_] :=
 {ρgg, ρee, ρmm, ρger, ρgei, ρgmr, ρgmi, ρemr, ρemi}
```

Vector to matrix transforms

$$\text{vtorho[v\_List]} := \begin{pmatrix} \text{v[[1]]} & \text{v[[4]]} + i\,\text{v[[5]]} & \text{v[[6]]} + i\,\text{v[[7]]} \\ \text{v[[4]]} - i\,\text{v[[5]]} & \text{v[[2]]} & \text{v[[8]]} + i\,\text{v[[9]]} \\ \text{v[[6]]} - i\,\text{v[[7]]} & \text{v[[8]]} - i\,\text{v[[9]]} & \text{v[[3]]} \end{pmatrix}$$

```
rhotov[rho_List] := {rho[[1, 1]], rho[[2, 2]], rho[[3, 3]],
  (rho[[1, 2]] + rho[[2, 1]]) / 2, i (rho[[2, 1]] - rho[[1, 2]]) / 2,
  (rho[[1, 3]] + rho[[3, 1]]) / 2, i (rho[[3, 1]] - rho[[1, 3]]) / 2,
  (rho[[2, 3]] + rho[[3, 2]]) / 2, i (rho[[3, 2]] - rho[[2, 3]]) / 2}
```

Propagator defined by $\partial_t \rho = A.\rho$

```
basisvec = IdentityMatrix[9];
MatrixForm[A[δeg_, δem_, Ωeg_, Ωem_, Γeg_, Γem_] =
   FullSimplify[
    Chop[
     Transpose[
      Table[rhotov[ρdot[vtorho[basisvec[[i]]], δeg, δem, Ωeg, Ωem, Γeg, Γem]],
       {i, 1, 9}]]]]];
evolverho[rhoinit_, operator_] := vtorho[operator.rhotov[rhoinit]];
renorm[v_List] := v / (v[[1]] + v[[2]] + v[[3]]);
Simplify[MatrixForm[Factor[A[δeg, δem, Ωeg, Ωem, Γeg, Γem]]]]
```

$$\begin{pmatrix}
0 & \Gamma eg & 0 & 0 & -\Omega eg & 0 & 0 & 0 & 0 \\
0 & -\Gamma eg - \Gamma em & 0 & 0 & \Omega eg & 0 & 0 & 0 & -\Omega \\
0 & \Gamma em & 0 & 0 & 0 & 0 & 0 & 0 & \Omega \\
0 & 0 & 0 & \frac{1}{2}(-\Gamma eg - \Gamma em) & \delta eg & 0 & -\frac{\Omega em}{2} & 0 & 0 \\
\frac{\Omega eg}{2} & -\frac{\Omega eg}{2} & 0 & -\delta eg & \frac{1}{2}(-\Gamma eg - \Gamma em) & \frac{\Omega em}{2} & 0 & 0 & 0 \\
0 & 0 & 0 & 0 & -\frac{\Omega em}{2} & 0 & \delta eg - \delta em & 0 & \frac{\Omega}{2} \\
0 & 0 & 0 & \frac{\Omega em}{2} & 0 & -\delta eg + \delta em & 0 & -\frac{\Omega eg}{2} & 0 \\
0 & 0 & 0 & 0 & 0 & 0 & \frac{\Omega eg}{2} & \frac{1}{2}(-\Gamma eg - \Gamma em) & -\delta \\
0 & \frac{\Omega em}{2} & -\frac{\Omega em}{2} & 0 & 0 & -\frac{\Omega eg}{2} & 0 & \delta em & \frac{1}{2}
\end{pmatrix}$$

Check that we didn' t make a mistake

```
Simplify[ρdot[ρmat, δeg, δem, Ωeg, Ωem, Γeg, Γem] -
   vtorho[A[δeg, δem, Ωeg, Ωem, Γeg, Γem].rhotov[ρmat]], domains] ==
 {{0, 0, 0}, {0, 0, 0}, {0, 0, 0}}
```

```
True
```

Plots and tests

```
NullSpace[A[-2 Pi 10., 2 Pi 20., 2 Pi 20., 2 Pi 10., 2 Pi 20., 2 Pi 1.]][[1]]
```

```
{-0.829005, -0.292344, -0.27021, 0.250581,
 -0.292344, -0.0417635, 0.0584688, 1.73577 × 10^-16, 0.0292344}
```

```
Simplify[renorm[FullSimplify[NullSpace[A[δ, δ, Ωeg, Ωem, Γeg, Γem]][[1]]]]]
```

$$\left\{\frac{\Omega em^2}{\Omega eg^2 + \Omega em^2}, 0, \frac{\Omega eg^2}{\Omega eg^2 + \Omega em^2}, 0, 0, -\frac{\Omega eg\,\Omega em}{\Omega eg^2 + \Omega em^2}, 0, 0, 0\right\}$$

```
exΓeg = 2 Pi 1.;
exΩeg = exΓeg / Sqrt[2];
exΩem = exΓeg;
exΓem = exΓeg / 20;
f3[x_, y_, z_] :=
 renorm[NullSpace[A[exΓeg x, exΓeg y, exΩeg, exΓeg z, exΓeg, exΓem]][[1]]][[2]]
tbl3 = Table[{{x, y, z}, f3[x, y, z]}, {x, -5, 5, .05}, {y, -5, 5, .05}, {z, 0, 3, .2}];
g3 = Interpolation[Flatten[tbl3, 2]];
```

Plot the values. Find optimum cooling parameters

```
NMaximize[{g3[x, y, z], 0 < y < 5, -5 < x < 0, 0 < z < 3}, {x, y, z}]
sol1 = NMaximize[{g3[x, y, 1], 0 < y < 5, -5 < x < 0}, {x, y}][[2, 2]]
sol3 = NMaximize[{g3[x, y, 3], 0 < y < 5, -5 < x < 0}, {x, y}][[2, 2]]
Plot[{f3[x, y, 1] /. sol1, f3[x, y, 3] /. sol3,
   (exΩeg)^2 / ((exΓeg)^2 + 2 (exΩeg)^2 + (2 × 2 Pi x)^2)}, {x, -5, 5}, PlotRange -> Full,
 AxesLabel -> {"δeg [Γ]", "ρee population"}, AxesOrigin -> {-5, 0},
 LabelStyle -> {FontSize -> 12}]
```

```
{0.215904, {x → -0.594082, y → 3.25317, z → 3.}}
```

```
y → 1.15592
```

```
y → 3.25316
```

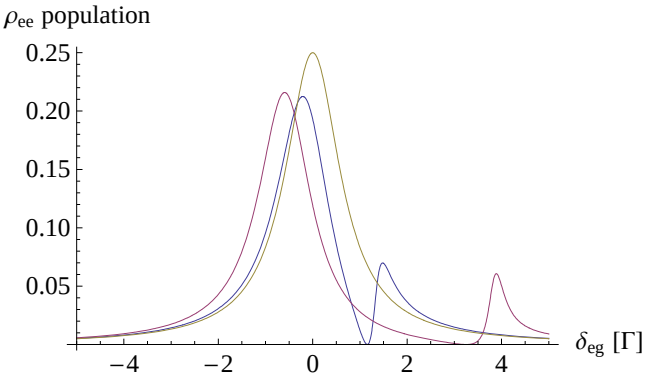


```
DensityPlot[f3[x, y, 1], {x, -4, 4}, {y, -6, 6}, PlotRange -> All, Axes → False,
 ColorFunction → GrayLevel, FrameLabel -> {"δeg [Γ]", "δem [Γ]"}, Mesh -> None,
 PlotPoints -> 100, LabelStyle -> {FontSize -> 12}]
```

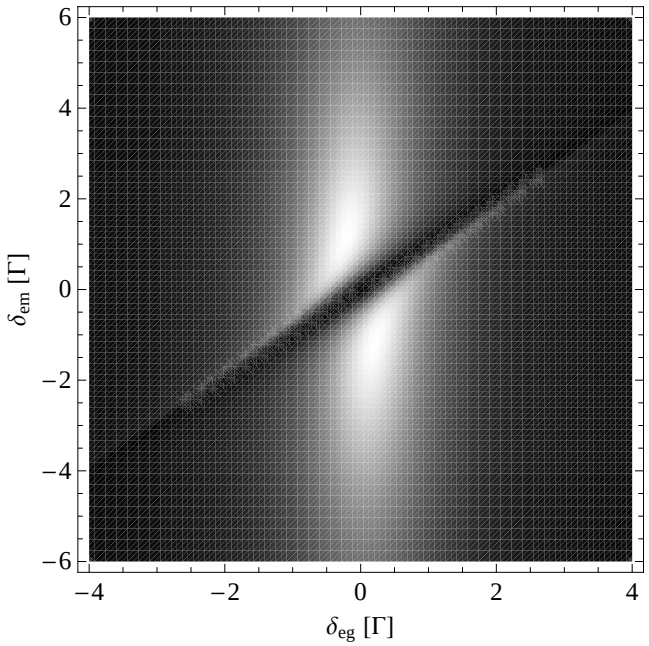

Structure:
Write the Hamiltonian, exponentiate, investigate gates

Derive gate ops

```
ClearAll[Evaluate[Context[] <> "*"]]
```

Experimental values. Note the sec frq is a bit higher here. We'll have to push it there to avoid talking on carrier

```
exΩ = Pi / 3.64;
exωsec = 2 Pi 1.18;
exη =
  2 Pi Sqrt[1.05457148 × 10^-34 / (2 exωsec (88 × 1.67262158 × 10^-27))] /
    (674.0 × 10^-6);
```

Derivation of the Hamiltonian

Necessary definitions

```
CircleTimes[U_, V_] := KroneckerProduct[U, V];
```

Atom operators

$$\sigma_z = \frac{1}{2}\begin{pmatrix} 1 & 0 \\ 0 & -1 \end{pmatrix};$$

$$\sigma_x = \frac{1}{2}\begin{pmatrix} 0 & 1 \\ 1 & 0 \end{pmatrix};$$

$$\sigma_y = \frac{1}{2}\begin{pmatrix} 0 & -i \\ i & 0 \end{pmatrix};$$

$$\sigma_+ = \sigma_x + i\,\sigma_y;$$

$$\sigma_- = \sigma_+^\dagger;$$

$$\sigma_0 = \begin{pmatrix} 1 & 0 \\ 0 & 1 \end{pmatrix};$$

Motional state operators

$$a = \begin{pmatrix} 0 & 1 & 0 \\ 0 & 0 & \sqrt{2} \\ 0 & 0 & 0 \end{pmatrix};$$

```
ida = IdentityMatrix[Dimensions[a]];
```

Hamiltonian definition with RWA. States are | D0 D1 D2 S0 S1 S2 >

$$H_{rest}[\omega 0\_, \omega sec\_, \eta\_, \Omega\_, \omega\_, \phi\_, t\_] = \omega 0\,\sigma_z \otimes ida + \omega sec\,\sigma_0 \otimes a^\dagger.a + \frac{\Omega}{2}\left(\sigma_+ \otimes ida\, Exp[-i(\omega t - \phi)] + \sigma_- \otimes ida\, Exp[i(\omega t - \phi)]\right) + \frac{i\eta\Omega}{2}\left((\sigma_+ \otimes a + \sigma_+ \otimes a^\dagger)\, Exp[-i(\omega t - \phi)] - (\sigma_- \otimes a^\dagger + \sigma_- \otimes a)\, Exp[i(\omega t - \phi)]\right);$$

Frames of reference − the quantum comp one, where states don't rotate and the laser one, where we can compute ops

```
Hqc[ω0_, ωsec_] = ω0 σz ⊗ ida + ωsec σ0 ⊗ a†.a;
Hlaser[ω0_, ωsec_, δ_] = (ω0 + δ) σz ⊗ ida;
```

Interaction hamiltonians in these frames

```
Vqc[ωsec_, η_, Ω_, δ_, ϕ_, t_] =
  Simplify[MatrixExp[i Hqc[ω0, ωsec] t].
    (Hrest[ω0, ωsec, η, Ω, ω0 + δ, ϕ, t] - Hqc[ω0, ωsec]).
    MatrixExp[-i Hqc[ω0, ωsec] t]];
Vlaser[ωsec_, η_, Ω_, δ_, ϕ_] =
  Simplify[MatrixExp[i Hlaser[ω0, ωsec, δ] t].
    (Hrest[ω0, ωsec, η, Ω, ω0 + δ, ϕ, t] - Hlaser[ω0, ωsec, δ]).
    MatrixExp[-i Hlaser[ω0, ωsec, δ] t]];
```

Change of basis from laser frame to QC frame

```
Ulasertoqc[ωsec_, δ_, t_] =
  Simplify[MatrixExp[i Hqc[ω0, ωsec] t].
    MatrixExp[-i Hlaser[ω0, ωsec, δ] t]];
```

Rotating the laser phase,is equivalent to rotating the D states. This is useful, as laser phase control is the only control we have.

```
Uphase[ϕ_] = DiagonalMatrix[Exp[-i {ϕ, ϕ, ϕ, 0, 0, 0}]];
Vlaser[ωsec, η, Ω, δ, ϕ] == Uphase[-ϕ].Vlaser[ωsec, η, Ω, δ, 0].Uphase[ϕ]
```

```
True
```

The matrices look as follows

```
MatrixForm[Hrest[ω0, ωsec, η, Ω , ω, ϕ, t]]
```

$$\begin{pmatrix} \frac{\omega 0}{2} & 0 & 0 & \frac{1}{2} e^{-i (-\phi+t \omega)} \Omega & \frac{1}{2} i e^{-i (-\phi+t \omega} \\ 0 & \frac{\omega 0}{2} + \omega sec & 0 & \frac{1}{2} i e^{-i (-\phi+t \omega)} \eta \Omega & \frac{1}{2} e^{-i (-\phi+t \omega)} \\ 0 & 0 & \frac{\omega 0}{2} + 2 \omega sec & 0 & \frac{i e^{-i (-\phi+t \omega)} \eta \Omega}{\sqrt{2}} \\ \frac{1}{2} e^{i (-\phi+t \omega)} \Omega & -\frac{1}{2} i e^{i (-\phi+t \omega)} \eta \Omega & 0 & -\frac{\omega 0}{2} & 0 \\ -\frac{1}{2} i e^{i (-\phi+t \omega)} \eta \Omega & \frac{1}{2} e^{i (-\phi+t \omega)} \Omega & -\frac{i e^{i (-\phi+t \omega)} \eta \Omega}{\sqrt{2}} & 0 & -\frac{\omega 0}{2} + \omega sec \\ 0 & -\frac{i e^{i (-\phi+t \omega)} \eta \Omega}{\sqrt{2}} & \frac{1}{2} e^{i (-\phi+t \omega)} \Omega & 0 & 0 \end{pmatrix}$$

```
MatrixForm[V_qc[ωsec, η, Ω , δ, ϕ, t]]
```

$$\begin{pmatrix} 0 & 0 & 0 & \frac{1}{2} e^{i (-t \delta+\phi)} \Omega \\ 0 & 0 & 0 & \frac{1}{2} i e^{i (\phi+t (-\delta+\omega \\ 0 & 0 & 0 & 0 \\ \frac{1}{2} e^{i (t \delta-\phi)} \Omega & -\frac{1}{2} i e^{-i (\phi+t (-\delta+\omega \sec))} \eta \Omega & 0 & 0 \\ -\frac{1}{2} i e^{-i (\phi-t (\delta+\omega \sec))} \eta \Omega & \frac{1}{2} e^{i (t \delta-\phi)} \Omega & -\frac{i e^{-i (\phi+t (-\delta+\omega \sec))} \eta \Omega}{\sqrt{2}} & 0 \\ 0 & -\frac{i e^{-i (\phi-t (\delta+\omega \sec))} \eta \Omega}{\sqrt{2}} & \frac{1}{2} e^{i (t \delta-\phi)} \Omega & 0 \end{pmatrix}$$

```
MatrixForm[V_laser[ωsec, η, Ω, δ, ϕ]]
```

$$\begin{pmatrix} -\frac{\delta}{2} & 0 & 0 & \frac{1}{2} e^{i \phi} \Omega & \frac{1}{2} i e^{i \phi} \eta \Omega & 0 \\ 0 & -\frac{\delta}{2}+\omega \sec & 0 & \frac{1}{2} i e^{i \phi} \eta \Omega & \frac{1}{2} e^{i \phi} \Omega & \frac{i e^{i \phi} \eta \Omega}{\sqrt{2}} \\ 0 & 0 & -\frac{\delta}{2}+2 \omega \sec & 0 & \frac{i e^{i \phi} \eta \Omega}{\sqrt{2}} & \frac{1}{2} e^{i \phi} \Omega \\ \frac{1}{2} e^{-i \phi} \Omega & -\frac{1}{2} i e^{-i \phi} \eta \Omega & 0 & \frac{\delta}{2} & 0 & 0 \\ -\frac{1}{2} i e^{-i \phi} \eta \Omega & \frac{1}{2} e^{-i \phi} \Omega & -\frac{i e^{-i \phi} \eta \Omega}{\sqrt{2}} & 0 & \frac{\delta}{2}+\omega \sec & 0 \\ 0 & -\frac{i e^{-i \phi} \eta \Omega}{\sqrt{2}} & \frac{1}{2} e^{-i \phi} \Omega & 0 & 0 & \frac{1}{2} (\delta+4 \omega \sec) \end{pmatrix}$$

```
MatrixForm[U_lasertoqc[ωsec, δ, t]]
```

$$\begin{pmatrix} e^{-\frac{1}{2} i t \delta} & 0 & 0 & 0 & 0 & 0 \\ 0 & e^{-\frac{1}{2} i t (\delta-2 \omega \sec)} & 0 & 0 & 0 & 0 \\ 0 & 0 & e^{-\frac{1}{2} i t (\delta-4 \omega \sec)} & 0 & 0 & 0 \\ 0 & 0 & 0 & e^{\frac{i t \delta}{2}} & 0 & 0 \\ 0 & 0 & 0 & 0 & e^{\frac{1}{2} i t (\delta+2 \omega \sec)} & 0 \\ 0 & 0 & 0 & 0 & 0 & e^{\frac{1}{2} i t (\delta+4 \omega \sec)} \end{pmatrix}$$

Unitary evolution due to laser field

Gates are computed in laser frame, and projected onto quantum computing frame. T0 is gate start time

```
U[ωsec_, η_, Ω_, δ_, ϕ_, T_, T0_] :=
  U_lasertoqc[ωsec, δ, T + T0].MatrixExp[-i V_laser[ωsec, η, Ω , δ, ϕ] T].
   U_lasertoqc[ωsec, δ, -T0];
fixglobalphase66[U_] := Exp[-i Mod[Arg[U[[6, 6]]], 2 Pi]] U;
fixglobalphase11[U_] := Exp[-i Mod[Arg[U[[1, 1]]], 2 Pi]] U;
```

The gate above does not work due to phase shifts. Need to correct it.
Uc and Um are the corrected gates. Carrier needs no correction, but sideband gates need two corrections − for stark shift, and for the change in motional sideband frequency when laser is off.
The extra phase gate sticking in front will have to be propagated all the way to end of pulse sequence in real code *)

```
ϕcorr[δ_, Ω_, T_] := (δ - Sqrt[δ^2 + Ω^2]) T;
Uc[ωsec_, η_, Ω_, δ_, ϕ_, T_, T0_] := U[ωsec, η, Ω, δ, ϕ, T, T0]
Um[ωsec_, η_, Ω_, δ_, ϕ_, T_, T0_] :=
 U_phase[-ϕcorr[δ, Ω, T + T0]].U[ωsec, η, Ω, δ, ϕ, T, T0].
  U_phase[ϕcorr[δ, Ω, T0]]
```

Let's define some actions on state vector starting in S0 state. We'll use these to test whether things worked

```
v0[ωsec_, η_, Ω_, δ_, ϕ_, T_] :=
  Uc[ωsec, η, Ω, δ, ϕ, T, 0].{0, 0, 0, 1, 0, 0};
```

Ramsey on carrier and sidebands

```
vcramsey[ωsec_, η_, Ω_, δ_, ϕ_, TR_] :=
  Uc[ωsec, η, Ω, δ, ϕ , Pi/(2Ω), TR + Pi/(2Ω)].
   Uc[ωsec, η, Ω, δ, 0, Pi/(2Ω), 0].{0, 0, 0, 1, 0, 0};
vsramsey[ωsec_, η_, Ω_, δ_, ϕ_, TR_] :=
  Um[ωsec, η, Ω, δ, ϕ, Pi/(2ηΩ), TR + Pi/(2ηΩ)].
   Um[ωsec, η, Ω, δ, 0, Pi/(2ηΩ), 0].{0, 0, 0, 1, 0, 0};
```

Stark shift forces us to phase shift the last gate. I guessed the necessary shift, but it seems to work well as shown later in notebook

```
vstark[ωsec_, η_, Ω_, δ_, ϕ_, T_, T0_] :=
  Uc[ωsec, η, Ω, 0, ϕ, Pi/(2Ω), T0 + Pi/(2Ω)].
   Um[ωsec, η, Ω, δ, 0, T, Pi/(2Ω)].
   Uc[ωsec, η, Ω, 0, 0, Pi/(2Ω), 0].{0, 0, 0, 1, 0, 0};
```

Projection operators. Will be useful later.

```
ps[v_] := Norm[v[[4]]]^2 + Norm[v[[5]]]^2 + Norm[v[[6]]]^2;
pd[v_] := Norm[v[[1]]]^2 + Norm[v[[2]]]^2 + Norm[v[[3]]]^2;
```

Test simple rotations

Scan of the entire line.

```
Plot[pd[v0[exωsec, exη, exΩ, 2 Pi x, 0, Pi/(exη exΩ)]],
 {x, -1.05 exωsec/(2 Pi), 1.05 exωsec/(2 Pi)}, PlotRange → Full,
 AxesLabel -> {"δ [ωsec]", "D state population"}, AxesOrigin -> {0, 0},
 LabelStyle -> {FontSize -> 12}]
```

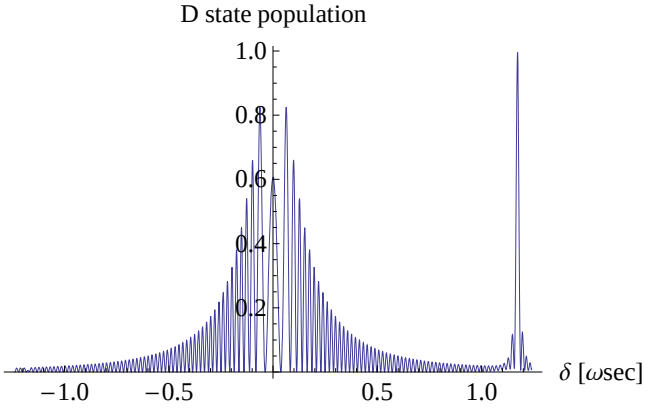

Rabi and Rabi on sideband plots

```
Plot[{pd[v0[exωsec, exη, exΩ, 0, 0, x]],
  pd[v0[exωsec, exη, exΩ, √(exωsec^2 - exΩ^2), 0, x]]},
 {x, 0, 4 Pi / (exη exΩ)}, PlotRange → Full,
 AxesLabel -> {"τ [μs]", "D state population"}, AxesOrigin -> {0, 0},
 LabelStyle -> {FontSize -> 12}]
```

D state population

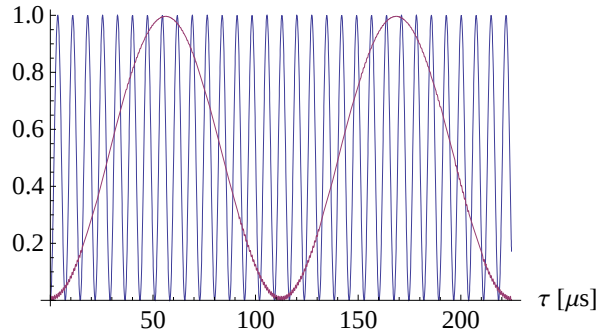

Ramsey with Pi/2 phase shift. Expect flat line if phase corrections are good

```
Plot[pd[vcramsey[exωsec, exη, exΩ, 2 Pi 0, Pi / 2, x]], {x, 0, 100},
 PlotRange → {Full, {0, 1}},
 AxesLabel -> {"τ [μs]", "D state population"}, AxesOrigin -> {0, 0},
 LabelStyle -> {FontSize -> 12}]
```

D state population

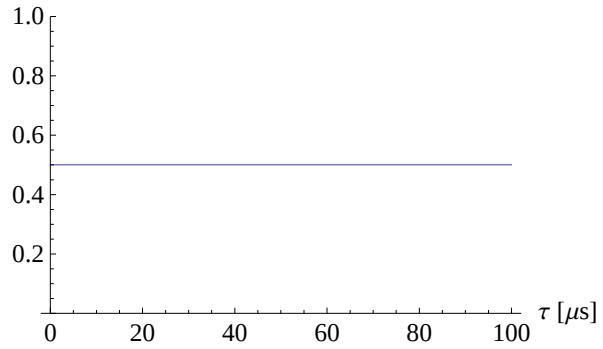

Ramsey on S0−D1 state with Pi/2 phase shift. Expect flat line if phase corrections are good

```
Plot[pd[vsramsey[exωsec, exη, exΩ, √(exωsec^2 - exΩ^2), Pi / 2, x]],
 {x, 0, 100}, PlotRange → {Full, {0, 1}},
 AxesLabel -> {"τ [μs]", "D state population"}, AxesOrigin -> {0, 0},
 LabelStyle -> {FontSize -> 12}]
```

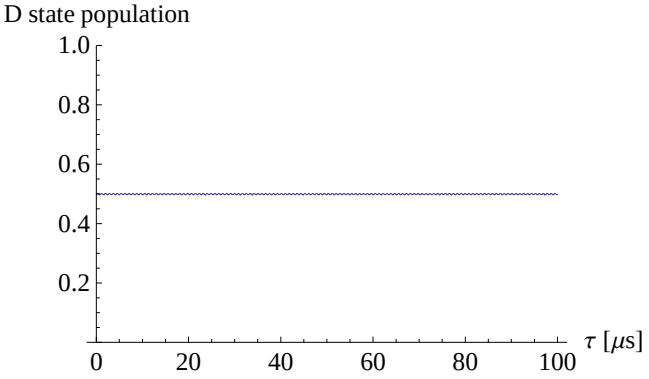

Stark shift of the carrier would cause the Rabi on S0−D1 to destroy coherence, but the phase shift saves the day. Expect 1 period (due to sign change after 2 π rotation)

```
Plot[
 {pd[vstark[exωsec, exη, exΩ, 1 √(exωsec^2 - exΩ^2), 0, x,
    4 Pi / (exη exΩ)]],
  pd[vstark[exωsec, exη, exΩ, 1.2 √(exωsec^2 - exΩ^2), Pi / 2, x,
    4 Pi / (exη exΩ)]],
  pd[vstark[exωsec, exη, exΩ, .8 √(exωsec^2 - exΩ^2), Pi / 2, x,
    4 Pi / (exη exΩ)]]}, {x, 0, 4 Pi / (exη exΩ)}, PlotRange → Full,
 PlotPoints → 200, AxesLabel -> {"τ [μs]", "D state population"},
 AxesOrigin -> {0, 0}, LabelStyle -> {FontSize -> 12}]
```

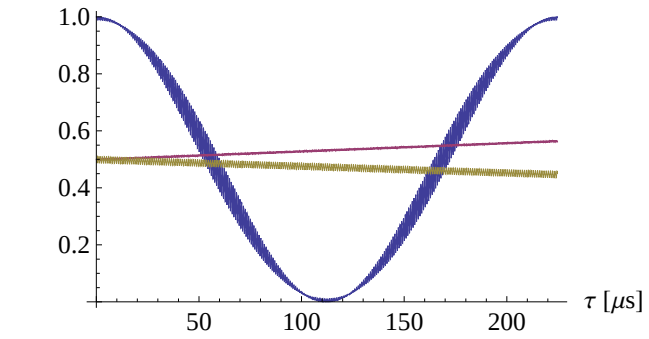

```
Tg0 = Pi / (2 exΩ); T0g0 = 0;
Tg1 = Pi / (exη exΩ); T0g1 = Tg0 + T0g0;
Tg2 = Pi / (√2 exη exΩ); T0g2 = Tg1 + T0g1;
Tg3 = Pi / (exη exΩ); T0g3 = Tg2 + T0g2;
Tg4 = Pi / (√2 exη exΩ); T0g4 = Tg3 + T0g3;
Tg5 = Pi / (2 exΩ);
T0g5 = Tg4 + T0g4;

badUcnot[δ_, ϕ_] := U_phase[Pi].U[exωsec, exη, exΩ, δ, ϕ - Pi / 2, Tg5, T0g5].
   U[exωsec, exη, exΩ, δ + √(exωsec^2 - exΩ^2), ϕ + Pi / 2, Tg4, T0g4].
   U[exωsec, exη, exΩ, δ + √(exωsec^2 - exΩ^2), ϕ, Tg3, T0g3].
   U[exωsec, exη, exΩ, δ + √(exωsec^2 - exΩ^2), ϕ + Pi / 2, Tg2, T0g2].
   U[exωsec, exη, exΩ, δ + √(exωsec^2 - exΩ^2), ϕ , Tg1, T0g1].
   U[exωsec, exη, exΩ, δ, ϕ - Pi / 2, Tg0, T0g0];

Ucnot[δ_, ϕ_] := U_phase[Pi].U[exωsec, exη, exΩ, δ, ϕ - Pi / 2, Tg5, T0g5].
   Um[exωsec, exη, exΩ, δ + √(exωsec^2 - exΩ^2), ϕ + Pi / 2, Tg4, T0g4].
   Um[exωsec, exη, exΩ, δ + √(exωsec^2 - exΩ^2), ϕ, Tg3, T0g3].
   Um[exωsec, exη, exΩ, δ + √(exωsec^2 - exΩ^2), ϕ + Pi / 2, Tg2, T0g2].
   Um[exωsec, exη, exΩ, δ + √(exωsec^2 - exΩ^2), ϕ , Tg1, T0g1].
   U[exωsec, exη, exΩ, δ, ϕ - Pi / 2, Tg0, T0g0];
```

Did it work?

```
NumberForm[
 MatrixForm[Chop[fixglobalphase11[badUcnot[0, 0]], Sqrt[10^-3]]], 3]
NumberForm[
 MatrixForm[Chop[fixglobalphase11[Ucnot[0, 0]], Sqrt[10^-3]]],
 3]
```

$$\begin{pmatrix} 0.159 & 0.0319\,i & 0 & 0.705 + 0.688\,i & 0 \\ 0 & 0.668 + 0.727\,i & 0.0701\,i & -0.0418 & 0.0415 - 0 \\ 0 & -0.0617\,i & -0.14 + 0.04\,i & 0 & 0.0548 \\ 0.527 + 0.832\,i & 0.0321 & 0 & 0.0332 - 0.156\,i & 0.0488\,i \\ -0.0505 & 0.121 & -0.0386 & 0 & 0.593 + 0.\ \\ 0 & 0.0604 & -0.541 - 0.823\,i & 0 & -0.0586\,i \end{pmatrix}$$

$$\begin{pmatrix} 0.995 & 0 & 0 & -0.074 & 0.0325 + 0.0351 \\ 0.0344\,i & 0.0724 & -0.0381 & 0 & 0.986 - 0.111\,i \\ 0 & 0.0323 - 0.061\,i & -0.995 & 0 & -0.0438 \\ 0.0725 & 0.0324 & 0 & 0.959 - 0.263\,i & 0 \\ 0 & 0.975 - 0.18\,i & 0.0446 + 0.0523\,i & 0.0426\,i & -0.0672 \\ 0 & -0.0531 & 0 & 0 & -0.0641\,i \end{pmatrix}$$

Looks correct

Is the phase shift used above best?

Let's look at sideband gate, with an additional phase correction, to see if I can make things better.

```
testU[T_, ϕ_, δ_] :=
  fixglobalphase66[U_phase[ϕ].Um[exωsec, exη, exΩ, δ, Pi / 2, T, 0]];
```

With no extra phase correction, the gate looks as follows

```
Chop[testU[Pi / (exη exΩ), 0, √(exωsec^2 - exΩ^2)], Sqrt[2 * 10^-3]] //
 MatrixForm
```

$$\begin{pmatrix}
0.996534 & 0.0569311\,i & 0 & -0.0583084\,i & 0 & 0 \\
0.0581588 & 0 & 0.0451557\,i & 0.996539\,i & 0 & 0 \\
0 & 0.0461603 & -0.604352 & 0 & 0.792981\,i & 0.05667 \\
-0.0568179 & 0.996539\,i & 0 & 0 & 0.0581588 & 0 \\
0 & 0 & 0.792981\,i & -0.0566753\,i & -0.603629 & 0.04616 \\
0 & 0 & -0.0504446\,i & 0 & -0.0450131\,i & 0.99704
\end{pmatrix}$$

Calculate the optimal extra phase correction by looking at the necessary ϕ to make the 1,1 matrix element real

```
f[T_, ϕ_] :=
 Simplify[
  PowerExpand[Chop[Im[Log[testU[T, ϕ, √(exωsec^2 - exΩ^2)][[1, 1]]]]]],
  Element[ϕ, Reals]]
sol[T_] := Solve[f[T, ϕ] == 0, ϕ][[1]]
```

Plot of ϕ It's slowly increasing, but close to 0 for the entire range

```
Plot[Mod[ϕ + 1, 2 Pi] - 1 /. sol[x], {x, 0, 4 Pi / (exη exΩ)}]
```

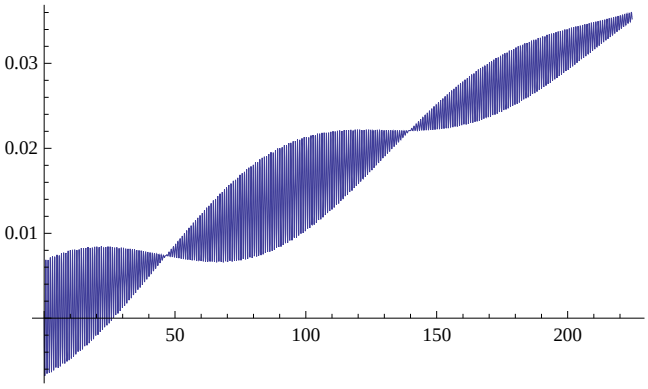

The extra phase shift is very small, so our original correction is good.